Water Vapour Radiometers for the Australia Telescope Compact Array

Balthasar Tobias Indermühle

Submitted in fulfilment of the requirements of the degree of
Doctor of Philosophy

School of Physics
University of New South Wales
September 2011

THE UNIVERSITY OF
NEW SOUTH WALES

SYDNEY • AUSTRALIA

ABSTRACT

In the millimetre wavelength regime of the electromagnetic spectrum used in radio astronomy, poorly mixed pockets of precipitable water vapour cause a change in the refractive index of the atmosphere, thereby inducing an excess path that the signal must travel through. This results in a phase delay for antennae receiving an astronomical signal. In an interferometer such as the Australia Telescope Compact Array (ATCA), variations in phase delay between the antennae thus lead to degradation in the image quality obtainable due to signal decorrelation. This phase fluctuation induced noise increases both with frequency and baseline length. It therefore also puts upper limits on the usable length of baselines without experiencing significant decorrelation, thus limiting the spatial resolution of the interferometer.

I have developed Water Vapour Radiometers (WVRs) for the ATCA that are capable of determining excess path fluctuations by virtue of measuring small temperature fluctuations in the atmosphere using the 22.2 GHz water vapour line for each of the six antennae. By measuring the line of sight variations of the water vapour, the induced path excess and thus the phase delay can be estimated and corrections can then be applied during data reduction. This reduces decorrelation of the source signal. I demonstrate how this recovers the telescope's efficiency and image quality as well as how this improves the telescope's ability to use longer baselines at higher frequencies, thereby resulting in higher spatial resolution.

The design process of the WVRs is discussed, including a review of three other WVR systems for comparison with our system design. A detailed site characterisation is provided with emphasis on millimetre observing conditions and it is determined to what extent WVRs can improve telescope data. A thorough examination of the frequency space used for the WVRs follows in order to avoid and detect radio frequency interference of both terrestrial and orbital origin. A detailed description of the WVR hardware design is given and concludes with a detailed account of the atmospheric modelling and water vapour retrieval mechanisms I have developed. The thesis concludes with a list of future opportunities and developments to improve the existing WVR system.

ORIGINALITY STATEMENT

'I hereby declare that this submission is my own work and to the best of my knowledge it contains no materials previously published or written by another person, or substantial proportions of material which have been accepted for the award of any other degree or diploma at UNSW or any other educational institution, except where due acknowledgement is made in the thesis. Any contribution made to the research by others, with whom I have worked at UNSW or elsewhere, is explicitly acknowledged in the thesis. I also declare that the intellectual content of this thesis is the product of my own work, except to the extent that assistance from others in the project's design and conception or in style, presentation and linguistic expression is acknowledged.'

Signed: .....

Date: .....

Prologue and Acknowledgments

This chapter is going to be a little longer, and a lot more poetic than is deemed normal for a physics thesis. That's perfectly fine though because I'm a bit older than the average PhD graduate and my life took a few squiggly lines before I arrived at this milestone. Keeping my audience in mind, most of the people I really care for are only going to read this prologue anyway, so I might as well give those readers something worth their while.

In the year 1999, I spent a few months in the south of France finishing up lose ends on a software project for a client in Switzerland. I had done that many times before and found the isolation of the pretty little town of Uzès productive. I was a celebrity consultant – both in the sense of whom I catered to as well as far as my own reputation went. Numerous large corporations as well as government departments hired my expertise for both writing code and managing projects (often more adequately referred to as nightmares). Sometimes I would also be hired for simple tasks like IT support that needed that extra degree of professionalism. No line of work was too menial for me, as long as the price was right. Amongst those less interesting but more curious projects were the first internet chat of a Swiss president I provided the infrastructure for in 1998 (President Flavio Cotti), or during the time of crisis in the mid 1990's when Ambassador Borer, who was representing Swiss interests in the dormant accounts and holocaust victim assets litigation, required special around the clock expertise with IT matters and secure communications. It was a good life and I enjoyed the reputation of a skilled code craftsman and IT

project troubleshooter. There was nothing else I should have wished for.

But while in that lovely town in France, every night after dusk, I was sitting on the roof terrace of my familys house, a glass of red wine from the Caves du Midi in my hand, and I'd gaze at the stars, feeling strangely unfulfilled and bothered by the endless cycle I found myself trapped in of reinventing software 'wheels' for my clients and fixing mundane problems.
It was on one of those nights that I decided I was going to leave the service industry life behind me and dedicate the rest of my work life to the furtherance of science. I wanted to make a difference in a world where everybody was pulling on the same rope. I would of course have to abandon my cash cow to help mankind, the same mankind I didn't really care about. That seemed a bit contrary to my convictions, until I remembered the principles Star Trek is based on: Everyone is working for the betterment of mankind, and not for money. I thought I had hit the Jackpot, at least in terms of the meaning of life! Astrophysics was the perfect subject, not only because I had been having a serious amateur interest for many years, but also because it had a proven track record of not being centered around such unexciting things as money, power and influence. At least two generations of TV series were testament to this – in the Star Fleet, there's complete absence of the corruption I came to loathe so much. I would finally be on track to lead a life far removed from people doing things for money.

And so I set sail with only the stars to guide me, without regard to any pecuniary potential (or lack thereof). I removed the words 'money' and 'income' from my vocabulary and struck any references to my previously high life activities such as piloting airplanes and drinking pre 1980's Bordeaux's of the Premier Cru Classé variety. I was thrilled at the possibility of interacting with fellow enthusiasts whose only priorities in life were the selfless advancement of science, advertisement free television and benign dictatorships (of a benevolent, communist nature, of course). Needless to say, things didn't quite evolve as planned.

First of all, love intervened. And it hit me with the weight[1] of a freight train impacting at full speed. Sometime in summer of 2003, at a client's party celebrating the completion of a project, I found this beautiful girl standing next to a barbecue grill. That in itself is not too unusual a picture were it not for the Swiss, and thus miniature, size of the cooking platform and the thick clouds of heavy white smoke that emanated through a stack of chicken that had been piled on in layers several carcasses deep. It was a grisly sight indeed. The pretty girl's facial expression disclosed she was in a state of great emotional distress, her left hand grasping tightly on to a wooden spoon she'd been handed minutes ago. The gentleman who was hosting the event, as I witnessed earlier, had emptied the entire contents of a large bucket of poultry onto the grill and put that girl in charge. I knew she was not in catering, as we had been introduced earlier. Her name was Alyssia and she had created the 3D animations used with the software I wrote for this client. I decided that a culinary train wreck in progress would be a perfect opportunity to strike up a conversation. So I made my way over to her and offered rescue, which she gladly accepted with a smile on her face. The rest is history, we got married less than a year later, and moved to Australia months after exchanging rings. I of course didn't know the first thing about barbecuing and having assumed control of the smoking stack of chooks[2] was not the best of ideas. To this day, and probably as a result of psychological injuries received from this event, I have not mastered the art of barbecuing things. It didn't help that I was further traumatised while living in the bush when my 15 year old (female) work experience student shooed me away from the barbie, told me I had no idea what I was doing and doubled up by demasculatingly bringing me a glass of red wine[3] and assuming control of the utensils.

Departure for Australia wasn't easy. Both Alyssia and I left everyone we knew, including job security, behind. What made it even more difficult was the deteriorating mental health of my dad, Toby. His mental capa-

[1] Ok, this is a physics thesis, the correct term to use is **mass**, not weight, even if it takes the magic out of it…I'm a scientist, not a magician. Or am I…?

[2] Every now and then I have to provide evidence of our prolonged stay in Australia, particularly the four years we spent living in the bush on our little 30 acre farm. A chook, in bush lingo, is a chicken.

[3] Real men in the Australian bush do not drink wine.

bilities had been going downhill for quite a few years, since before I had even decided to become a puritan in science's service. First came the loss of short term memory, then the difficulties in speaking and forming coherent thought. Doctors at various university hospitals showed interest as the symptoms appeared to point at an Alzheimer type dementia, but that, at the time, was a post mortem diagnosis.
When we left in 2005, he was still able to express ideas and expressing them he did! Every time we met, he would point at us, laugh, and move his hands in a motion so as to indicate a departing airplane and making a loud "Swoooooshh!!" noise! He clearly was very excited for us. I'm convinced he understood much more than he was able to verbalise. My mom Susan did everything to the very best of her abilities to take care of him, and when that no longer sufficed, she found him an excellent caretaker. I went to visit them numerous times in the first year and a half of our time in Australia, until he passed away in October 2006.

So what have I learnt along the way? Fundamentally, people appear to be just people, regardless of what they do. And there are only two kinds: weasels and the other kind, and you can't always tell the weasels by their tail. But that's another subject I'll at some point have to fill a book about. There is not much hope for the betterment of mankind, except through processes of natural selection. There is no selflessness in science, no common goal everyone is working towards, and indeed I had in my boundless optimism misinterpreted the world altogether. I found that people in the sciences are behaving the exact same way as they are in business, only fighting with different means. While most of us are living the lives of pecuniary paupers (measured by the degree of education), many are wielding intellects (and egos) as sharp as razors, an essential utensil in the competition for funds in a minefield of politics, favouritism and ulterior motives. I soon came to liken my position to that of a developmental aid worker, who, in the Swiss tradition of the good samaritan decided it was time to help the poor only to find that there are no poor, and even worse, that it works just fine the way it is even though everybody is complaining about it and that whatever my contribution is going to be in the grand scheme of things is of a minimal, almost negligible nature.

This is not a dissertation about the sociology of science, fortunately. It's about improving the performance of an existing instrument that will enhance our ability to see a lot of cool new stuff never seen before. The instrument, you've guessed it, is the Australia Telescope Compact Array (ATCA), a radio telescope consisting of 6 antennae that are up to 6 km apart. My contribution to this is a machine that corrects for some of the effects that the atmosphere inflicts on the signals we receive from the objects in space. Simply put, I have built glasses for ATCA. How befitting of a 40 year old! It was a leap for one man, but a small step for mankind...

Please forgive me if I sound pessimistic. You see, my generation is not the generation that sent a man to the moon, where one small step for that man was one giant leap for mankind. I'm of the leaking O-ring generation[4], built by the lowest bidder. We outsource everything, perhaps even to a pathological degree, all in the name of creating better results, when all it creates is better opportunities for little western oligarchs to embezzle the rest of us without any regard to what they leave behind. This is much like Australian mining today: raping and pillaging an entire continent for the benefit of a handful of billionaires. My generation has seen more selfishness than any other, more government spending than any other, more wealth inequality than any other, more privatisation of profit and nationalisation of debt than any other, and last but not least, more idiocracy than any other. The only thing we have seen much less of than any other is the enthusiasm of an entire nation standing behind a common goal as a collective, supporting (for example) a space flight programme and being part of something grand. We have never learnt to dream, we've only ever had programmes shut down due to restructuring and cutting cost, yet copious funds are always available to be wasted in the senseless friction of administrations we have built. For example, occupational health and safety would have you believe that every step taken contains risks rather than opportunities. I wonder what the psychological impact of this will be on an entire population? Sadly, and in short, our generation did not build the Concorde, we mothballed it.

Star Trek obviously is not real, this much I have learnt along the way. Sorry,

[4]The leaking O-ring brought down the Challenger Space Shuttle in 1986.

Gene, but Douglas Adams came a lot closer. Vogons[5] appear to be very real, alive and well. I've met and worked for quite a few of them over the years. But not all is lost. On this journey I have also met a number of wonderful people I would never have had the privilege of meeting or working with in my previous life. I may still be no philanthropist, but I've grown a lot more tolerant.

* * *

I would not have been able to complete this work had it not been for the generous help of many people around me. I would like to thank all of you, in no particular order, you all deserve credit for having supported, encouraged, helped and endured me for all those years!

Michael Burton, you have encouraged me to take on this challenge and guided me with your critical thinking and passion for your work. Your relentless attention to detail was always extremely helpful and appreciated, and your simultaneous awareness of the big picture impressive. I can only conclude you bear the marks of a great scientist!

Alyssia, my wonderful wife, you have been patient and encouraging with me. You've made the ultimate sacrifice: you gave up your well established career in Switzerland for a life of following me around the planet. For that, and all your other good deeds I am indebted to you until we'll drive the short bus to where it's hot and sticky!

Phil Edwards, even though co-supervising only for the last half year of this project, you have been my boss at work for many years now. Amongst the many things you taught me, the meaning of the word "circumspect" was probably the hardest for me to comprehend, culturally. That deserves credit!

[5] From Wikipedia: The Vogons are a fictional alien race from "The Hitchhiker's Guide to the Galaxy". They're responsible for the destruction of the Earth in order to facilitate an intergalactic highway construction project. Vogons are described as mindlessly bureaucratic, aggressive, having "as much sex appeal as a road accident" and are the writers of "the third worst poetry in the universe". They are employed as the galactic government's bureaucrats.

Susan, my dear mom, and my late dad Toby, thank you! You have always encouraged me to follow my dreams. You knew early on it would be an exercise in futility to try and make me follow a traditional way of life, you never gave me a hard time for doing everything in reverse. For that I love you, even if that makes you hippies! Thank you also for your generous support during the beginning of this adventure, without which it would have been much more difficult. Many thanks also to Paul for taking such great care of my Mom.

* * *

Susan, you gave me Oliver Twist when others read Superman, you fed me granola bars when others got Mars bars, now I give you this for your bedside table. Enjoy, and remember to keep challenging yourself. And if that gets boring, challenge someone else!

* * *

Contents

Chapter 1

Introduction

1.1 Overview

The Australia Telescope Compact Array (ATCA) is a radio interferometer capable of observing in the centimetre and millimetre wavelength regime of the electromagnetic spectrum. It has for over 20 years been the only centimetre wavelength radio interferometer in the southern hemisphere offering full horizon to horizon coverage apart from the Large Baseline Array (LBA) and for a little over a decade the only millimetre interferometer in the southern hemisphere. Interferometry is the measurement of the same incoming wavefront emitted by an object using separated antennae. It is a central concept to the field of radio astronomy. The technique allows images to be built up of astronomical sources, with a resolution equivalent to that of a telescope whose diameter is equal to the separation of its antennae. This can be many times better than that achieved using a single antenna, since the best spatial resolution obtainable by a telescope is given by its diffraction limit, which is inversely proportional to its diameter, or to the spacing of the antennae for an interferometer:

$$R = 1.22\frac{\lambda}{D} \tag{1.1.1}$$

where R is the diffraction limited resolution in radians, D the diameter of the telescope and λ the observing wavelength (both in the same units). The difference in arrival time of the wavefront between two antennae results from the path difference between the source and the separated antennae. This in turn is related to a difference in phase for the wavefront.

By tracking the change in the phase difference as a source moves across the sky, the technique of synthesis imaging allows a picture of it to be obtained.

During the course of an observing session, small phase corrections have to be applied to the phase differences to correct for the refractive index of the atmosphere, as well as for instrumental drifts. At centimetre wavelengths the atmosphere is nearly transparent to radiation, and so phase correction is readily obtained by periodically observing a bright calibrator source (which must also be an unresolved point source to be useful for amplitude calibration), in between measurements of the source of interest, and by adjusting for the relative position of the source in the sky in relation to the antennae. At millimetre wavelengths the atmospheric component can no longer be this easily corrected for because water vapour in the troposphere changes its refractive index, thus causing delays in the propagation of the wavefront of the incoming signal. The effect of these delays is inversely proportional to the observed wavelength. At centimetre wavelengths they are tiny in proportion to the wavelength, but at millimetre wavelengths they become significant.

Variations in the water vapour content along the lines of sight from the source being observed to each antenna lead to fluctuations in the refractive index, and so to the delays and the phase fluctuations. At millimetre wavelengths, these fluctuations are rapid, requiring frequent measurement of a calibrator source in order to be followed. Frequent calibrator scans means every 5-10 minutes, depending on weather conditions, observations have to be interrupted to observe a calibrator in order to follow the phase variations induced by the atmosphere. This can consume up to 25% of the observing time. The water vapour induced phase variations also increase with the length of the baseline between antennae. With the Australia Telescope Compact Array, the largest useable baseline is found to be ~300m for measurements made in the 3 mm waveband (frequencies around 100 GHz). Yet the maximum baseline separation of the five antennae is 3km, and this is used regularly at centimetre wavebands. If this could be used at millimetre wavelengths it would result in up to a factor of ten improvement in the spatial resolution for millimetre

imaging.

Before WVRs were installed, observations on long baselines were only possible for exceptionally bright sources, which can provide their own phase referencing, a process referred to as self calibration (also called "selfcal") because the object being observed serves as its own phase calibrator. This is limited to observing bright sources, e.g. the luminous, massive star η Carinae. However, there is a means of determining the phase corrections directly. The water vapour which causes the phase delays also emits radiation, causing small fluctuations in the sky brightness temperature. The signal this produces depends on the amount of water vapour present. Therefore, by measuring the fluctuations it is possible to calculate the phase correction needed between two antennae. This is what water vapour radiometers (WVRs) can do. By measuring the changes in temperature arising from fluctuations in the emission from an atmospheric water vapour line, WVRs make it possible to calculate the extra path length travelled by the signal. This quantity can then be used to calculate the phase delays induced, and apply those corrections to the measured phases during the data reduction of the interferometer data.

1.2 Motivation

In order for ATCA to remain at the forefront of astronomical research, continued development and improvement of its systems is essential. In optical and infrared Astronomy, substantial efforts have gone into compensating for effects the troposphere is having on the signal received. Adaptive optics systems are a result of these efforts. They allow a telescope to obtain data much closer to, or even at, its diffraction limit. In millimetre wave radio astronomy, the troposphere plays an equally important role in degrading the signal received. As outlined in the Overview, the mechanism is a different one and will be discussed in detail in chapter 6.2.1, but the effect remains the same as for optical Astronomy: The image obtained from the degraded signal has lower contrast and more noise. Indeed, because the image is synthesised in interferometry, the atmosphere can degrade the observed phase data so badly that no image information can be restored because the phase has decorrelated. This happens when

the phase variations are larger than one wavelength during one integration cycle: Phase wrapping occurs, and the true phase can no longer be determined. At 3.3 mm wavelength, this happens when the water vapour fluctuates by more than about 0.44 mm, or about 440 μm as we will show in the site characterisation in chapter 3. We will also show that the path length fluctuations encountered at Narrabri are on average well suited for 3 mm observing. During daytime both in winter and summer, the Water Vapour Radiometers (WVRs) however can help. By independently tracking the water vapour responsible for the path variations and thus phase delays, image quality can be substantially improved and phase information can be recovered. The ability to correct for excessive phase delays that would cause decorrelation under normal circumstances has implications for the longest baselines usable at millimetre wavelengths with the ATCA. By increasing the largest baselines, the angular resolution increases as well, enabling new science.

As will be shown in chapter 6.2.1, for atmospheric conditions at Narrabri, measurements of the water vapour line need to be based on the 22.2 GHz frequency (i.e. in the 12mm waveband). Two prototype water vapour radiometers were built for the Australia Telescope Compact Array for this purpose in 1999, they however were used on one baseline only for a small number of test observations[49]. These units used four filters spread out over the water vapour line between 16 GHz to 26 GHz, in order to separate out the signal arising from fluctuations in the water vapour content alone, as opposed to fluctuations of other components of the emission (e.g. from liquid water in the atmosphere, which produces a stronger signal but does not cause significant phase delays). When this project was revived in 2006, the new Water Vapour Radiometer design was based on this existing design, further optimising the filter frequencies for what appeared a better match. The same manufacturer who built the first two units, Astrowave Pty Ltd (Jonathan Crofts) was then charged with building five new units and refurbishing the two old units with new filters and components to deliver a total of seven units, six of which were mounted on the six antennae of the Australia Telescope Compact Array. The seventh unit is kept as a spare but could potentially be put to use at another millimetre telescope, e.g. Mopra, 100 km south of the ATCA.

The accuracy requirements, details of which will be elaborated in chapter 6.2.2, demand measurement of the phase differences to at least 48 degrees. This corresponds to a path difference of $\lambda/7.5$; i.e. when observing at 3mm, an electrical path excess of ~0.4mm needs to be detectable, which in turn is a difference in precipitable water vapour of just under 0.07 mm between two antenna sight lines. This is equivalent to measuring the temperature difference to an accuracy of about 0.1 K at the peak of the water line. At the continuum end of the water line, it corresponds to about 12 mK, an even more stringent requirement. This is one part in 10^4 of the actual signal from the atmosphere and telescope and needs to be achieved within an integration period of a few seconds. While this is a stringent requirement, the system does not, however, need to have long term temperature stability, since the measurements will be regularly checked by comparing to a calibrator every few minutes. Figure 1.2.1 shows a sample measurement with measured phase, WVR phase and phase residual (the difference between the two). The observing frequency was set to 22.9 GHz (λ = 13.1mm) and the baseline corresponds to 872 m in length. The lower curve shows the phase difference between these determinations (in terms of the path delay from an unperturbed wavefront) also called the "residual phase". The atmospheric water vapour deduced phase changes are seen to track the phase fluctuations observed with the science receiver well. The residuals are shown in the lower plot; their standard deviation is 34.1 degrees, or about 1.14mm, which is well within the 2 mm or $\frac{\lambda}{7.5}$ needed for phase correction to provide a gain in performance.

At present, observing in the 3mm band is only conducted on baselines of ~350m or less (with the exception of sources like η Carinae, which is bright enough to allow observations up to 3km baselines since it can be self-calibrated in phase). Thus, the angular resolution of 3mm observations in 350m configurations is poorer than 12mm observations on 3km baselines. The correction of raw interferometric phases with WVR data has the potential to allow 3mm, and also 7mm, observations on longer baselines, improving the angular resolution by a factor of up to 10. On shorter baselines the improved phase stability will improve the signal to

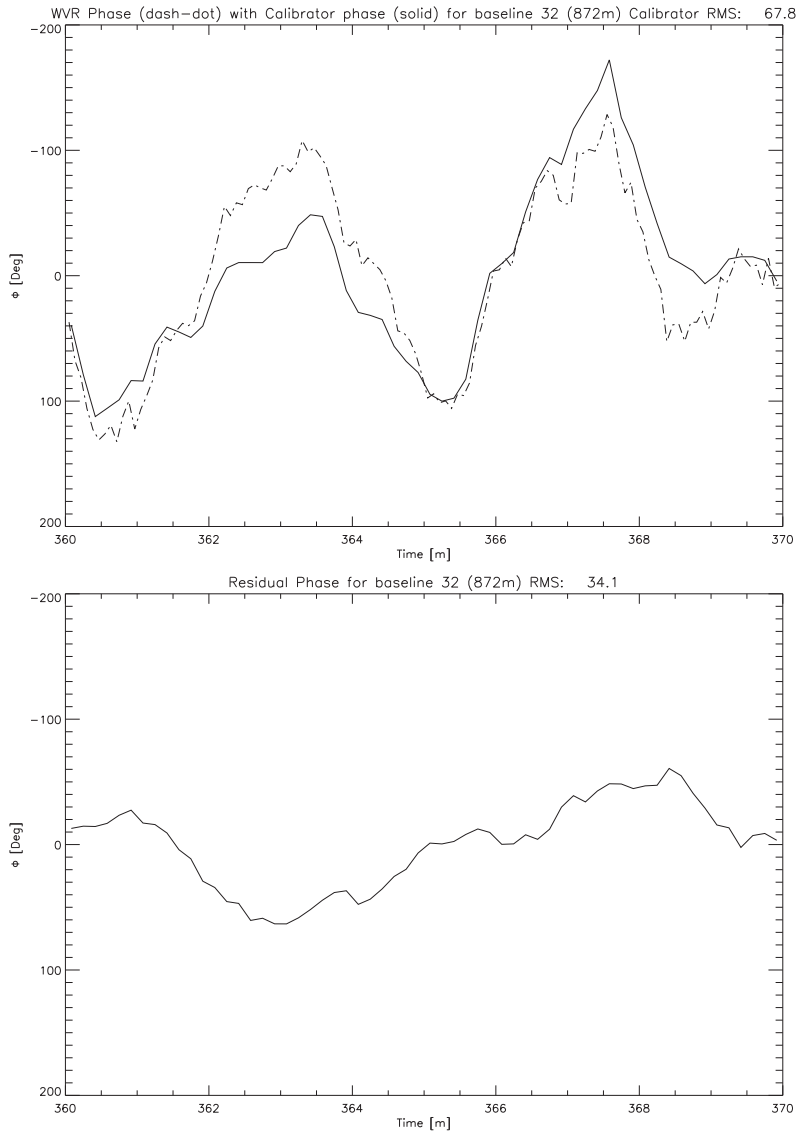

Figure 1.2.1: Example tracking the calibrator 2223–052: Shown are the measured phase, the WVR derived phase and the difference between the two, the residual phase, as a function of time. This data was taken on January 4, 2011 in mediocre weather conditions on a 872 m baseline. The Australia Telescope Compact Array seeing monitor displayed a path noise that fluctuated between 500μm – 1500μm for the time of these observations over a 230 m baseline.

noise ratio of millimetre-wave observations.

Observing at millimetre wavelengths currently is largely restricted to the winter months, although Water Vapour Radiometers may allow the mm season to start earlier and end later. In 2006, 33% of proposals in the April semester involved observations at 3mm: in 2007 the figure was 25%. In 2008, 37% of Australia Telescope Compact Array proposals requested 3mm observing, and fully 45% requested 3mm and/or 7mm observations. These figures are comparable throughout the years up until the April 2011 semester. The interest in millimetre observing has remained strong with the installation and commissioning of the Compact Array Broadband Backend (CABB) in 2009.

The Australia Telescope Compact Array is no longer the only millimetre-wave interferometer operating in the southern hemisphere. The Atacama Large Millimetre Array (ALMA) has already produced the first science results and with its expected completion in 2013, new science will be enabled. ALMA will work mostly at shorter wavelengths than the Australia Telescope Compact Array, in the sub-millimetre bands. An enhanced ATCA would be able to better feed ALMA projects to undertake.

1.3 The Atmosphere

The various constituents of the atmosphere all have an effect on the transmission of signals from space. In the millimetre region of the electromagnetic spectrum (between about 16 GHz to 300 GHz), the main contributors to atmospheric attenuation are O_2 and H_2O, the latter in its gaseous form as water vapour. Below $\lambda \leq 1.5$ cm, the optical depth of the troposphere thus increases and becomes significant, leading to increased system temperatures due to atmospheric emission [8]. The refractivity of water vapour at these frequencies is about 20 times greater than in the near-infrared or optical regimes [57]. Figure 6.2.1 provides a good overview of how the sky emission continuum increases with frequency ($\approx \nu^2$) and shows the two water vapour line features at 22.2 and 183.3 GHz. When evaluating the atmospheric conditions, several models were used to characterise the temperature differences encountered for the expected de-

gree of phase delays we need to correct for. This is a result of the several different software packages used for the project. The first such model was the Millimeter Propagation Model (MPM) developed by Liebe in 1985 [35] and implemented in the Miriad software package. This model, while accurate enough for purposes of filter optimisation has been improved upon by Pardo et al. in [45] who developed the Atmospheric Transmission at Microwaves (ATM) model we used to simulate PWV induced excess temperatures. The well characterised VanVleck – Weisskopf (VVW) profiles were also used to determine the model atmosphere parameters for the water vapour calibration factors as well as the weighting coefficients determined in detail in chapter 6.4.3. The same VVW profiles used for the coefficients were also integrated into the ATM model by Pardo et al. in [45].

1.4 Science Motivation

Development and installation of WVRs at ATCA would enable new science that can be pursued with this world class facility. In this introduction, a brief overview is given into some fields in Astronomy that will find advantage in the improved instrument. This section is an updated version of the LIEF grant application used to finance the WVRs.

1.4.1 Massive Star Formation: Protostellar Sources and Cold Dust Cores

Throughout cosmic history star formation has been the principal driver of galactic evolution. Massive stars are at the heart of this process. They provide the bulk of the Galaxy's luminosity. They are responsible for its chemical evolution, through the production of heavy elements in stellar nuclear furnaces and their subsequent dispersal into space. Massive stars form in clusters, though are greatly outnumbered by the lower-mass, solar-type stars that form alongside them. Despite their obvious importance, knowledge about how they form is poor, in contrast to that of low mass star formation [5]. Distance, rarity and rapidity of evolution all contribute to this state of uncertainty. Massive stars form within the coldest environments in the Galaxy, dense cores of dust weighing a few thousand

solar masses, lying within "giant molecular clouds" of up to a million solar masses. To understand where, why and how massive stars form it is first necessary to identify where the cores are, and then which are likely to form stars. We then need to determine their physical characteristics and where the "protostars" are inside them [36]. These objectives can all be met using millimetre-wave observations. Dust masses are given by the strength of the millimetre-wave continuum emission and gas masses from those of molecular lines. Of particular interest is measuring the temperature inside the coldest cores, which can be obtained from ammonia (NH_3) lines at 12mm, sensitive to the temperature in gas below ~20 K. The structure and dynamics within the core may also be examined through observation of the diazenylium ion (N_2H^+) at 3mm, which remains in the gas phase even in the coldest environments. The number and sizes of the individual protostellar condensations can be determined from the 3 millimetre-continuum emitted by their dust. Crucial to all these observations is spatial resolution. The nearest and thus best resolved dust cores where massive star formation is initiated are typically ~30 arcseconds in angular extent, but the protostars inside them are associated with features on the arcsecond scale [21]. Currently it is not possible to probe smaller than ~5 arcseconds at mm wavelengths with the Australia Telescope, but arcsecond resolution would be attainable if the full baseline of the array could be used. This would then allow direct comparison with data obtained at mid-infrared wavelengths using, for instance, the Gemini telescopes, where diffraction-limited imaging, providing sub-arcsecond resolution, is possible. In the infrared the young stars can be seen directly, once they have warmed to temperatures of a few hundred degrees. However, they can only be seen in the millimetre in their earliest manifestations as cold protostars. With improved imaging capability on the Australia Telescope we would be able to compare directly the stellar content (from the infrared) to the gas and dust content (from the mm) inside the cores where massive stars form.

1.4.2 Chemical Clocks on the Evolutionary Route to Massive Star Formation

Massive stars pass through a sequence of stages as they form. Observations have identified easily recognisable tracers of the early stages, such as masers, hot molecular cores, ultracompact ionized regions and infrared dark clouds [62]. What is not known is how these tracers fit into a timeline for massive star formation. For example, it is not clear whether the (cold) infrared dark cloud is the earliest phase, because some contain (hot) ultracompact ionized regions, which are thought to occur in the final phase [61].

The way forward is to examine the emission from complex chemicals that accompany the formation process. Detailed chemical models currently exist, but their productivity is limited by the resolution of the data, which cannot resolve the small regions of complex chemicals surrounding young, massive stars. An increase in resolution by an order of magnitude would allow us to resolve such regions in nearby star formation sites. Such information will allow models of the spatial structure in the star forming cores to be made. From there, we can build a picture of the massive star formation process, providing chemical clocks to place them in the correct time sequence.

1.4.3 The Search for Biologically Relevant Molecules in Space

One of the objectives in the field of interstellar chemistry is to determine whether chemical evolution in space can produce reservoirs of biogenic molecules that may provide the seeds for life to evolve from. Many surprisingly complex organic molecules have been detected in the interstellar medium, including acetic acid, acetone and the sugar glycolaldehyde [24]. Molecules are identified by the detection of their molecular line transitions. The fact that many of the transitions detected by radio telescopes have not been assigned to any molecule suggests that there are many complex molecules yet to be identified. This is, however, much more difficult than identifying their simpler counterparts. Complex species have large numbers of weak transitions, blended amongst a forest of spectral features in the millimetre wavebands. This leads to confusion

between transitions if the spatial and spectroscopic resolution is not high enough. An interferometer is particularly valuable for this situation; if a bright, small-diameter hot core is observed, the interferometer filters out confusing lines from more extended gas, leaving only those lines present in the hot core. The fluxes for lines of interest are also diluted if the core remains unresolved. Thus, imaging on an arcsecond scale, as would be made possible using radiometers, would greatly facilitate the search for biogenic molecules in space. It could lead to increases in brightness of an order of magnitude for many of the lines of interest.

1.4.4 Protoplanetary Disks around Young Stars

We know that planets form out of the dust grains in disks that surround young stars, but the details of how the tiny, micron-sized grains coagulate to form planets, objects $10^{13\text{-}14}$ times larger, are not well understood. To understand planet formation we need to study the earliest stages of the process, when the dust particles begin to grow in size. This can be done with millimetre continuum observations, which probe the cool outer regions of protoplanetary disks where the majority of the mass resides [56]. The flux provides a measure of the disk mass and slope of the energy distribution information on the grain sizes. However, there is a degeneracy between observations of spatially-small, optically thick disks with small grains and spatially-extended, optically thin disks with larger grains, which make them look the same, preventing such deductions being made. This degeneracy can only be broken by resolving the disks. A typical nearby disk, at a distance of ~150pc and with size ~200AU, is only about 1 arcsecond in angular size. This is currently unresolvable but could be resolved if water vapour radiometers were used to increase baselines to the full extent of the Australia Telescope Compact Array. In addition, the sensitivity to detecting emission from disks would also be improved, perhaps by as much as a factor of 10, as the fluxes will no longer be beam diluted.

1.5 The ATCA Water Vapour Radiometers

The WVRs developed for ATCA are an uncooled design based on four filters placed between the frequencies of 16 – 26 GHz, each with 1 GHz of

bandwidth to increase the sensitivity. This allows the WVRs to measure small variations in the spectrum of the 22.2 GHz water vapour emission and derive phase variations based on these measurements. The key elements of the WVRs are their maintenance free operation (there is no cryogenically cooled stage to maintain), they are co-located with the science receivers, hence look through almost the same beam onto the sky, and they operate at frequencies the antennae were designed to perform at. By using a differential water vapour determination method, absolute measurements are not required. Instead, sensitive differential measurements must be executed to determine the minute temperature differences caused by the fluctuations in the water vapour in the lines of sight.

We will now show how the WVRs were developed from examining other existing systems and discuss their shortcomings and design specifications in chapter 2. Then the first site characteristics analysis for the ATCA site near Narrabri with a specific emphasis on millimetre conditions is provided in chapter 3. Then we discuss the implications of radio frequency interference in chapter 4 and how it affected the decisions on where to place the filters to optimally retrieve the water vapour emission at 22.2 GHz, avoiding the increasingly commercial use of this frequency band. We then show the hardware design in chapter 5, derive and discuss in detail the water vapour retrieval algorithm in chapter 6 and we conclude with chapter 7, providing an outlook into future work that can be done to further improve on the WVR system.

Chapter 2

Other Water Vapour Radiometer Systems

In this chapter I provide an overview of what I believe are the three most relevant systems that have been implemented in the field of water vapour radiometry. While this does not necessarily reflect on the merit of the solutions found, especially in the case of the first system, the 225 GHz ATCA WVR, it represents an interesting sample using the three different spectral regimes of 22 GHz, 183 GHz and 225 GHz continuum of the water vapour line. Each of the three systems uses a radically different approach to water vapour retrieval and its application to interferometry.

There are also a number of further WVR systems that have been developed in the past 20 years. A non exhaustive list in roughly chronological order includes:

- The Owens Valley Radio Observatory millimetre array (OVRO) featuring a triple channel 22 GHz WVR system on 6 antennae described in detail in [37].
- The Effelsberg water vapour radiometer is a scanning radiometer that provides absolute PWV measurements for phase correction on single dish measurements. This system has in detail been described in [11] and its design is based in part on the Tahmoush and Rogers design described in [53].
- The WVR developed between 1995 – 1998 for the James Clark Maxwell

Telescope and the Caltech Submillimeter Observatory (JCMT-CSO) on Mauna Kea is the first WVR to use the 183 GHz water line and is described in detail in [64].

2.1 ATCA – Australia Telescope Compact Array

The Australia Telescope Compact Array (ATCA) has already seen the implementation of a prototype water vapour radiometer system in 1998 with the 225 GHz detector system developed by David Abbott and Peter Hall [2]. They used the 225 GHz region depicted in Figure 2.1.1. The temperature difference between 3 mm and 30 mm of PWV is ~200 K. Given this large temperature difference, it appears evident that this should be an excellent position in the spectrum to measure the line emission and infer PWV from that using an adequately stable system. However, at this high a frequency, the liquid water contribution to the emission is inseparable from the water vapour contribution. Because liquid water has hardly any effect on the electrical path length, this is a problem for a total power system in the continuum portion of the spectrum. That issue, however, was not realised at the time. The design called for a small, very accurate reflector mounted co-axially on the front of the subreflector of each ATCA antenna, thus pointing in the same direction as the antenna. The small (0.5m) diameter of the dish, coupled with the receiver wavelength of λ = 1.3mm (225 GHz) samples the near field of the astronomy antenna within the lower 2km of troposphere, which is where PWV induced phase delays originate. The design comprised the following elements:

- 0.5m Cassegrain reflector.
- A conical horn feed with 10°FWHM, responding to one linear polarisation.
- A sub-harmonically pumped 225 GHz Schottky diode mixer.
- A low noise Indium Phosphide (InP) Gunn local oscillator (LO) operating at 112.5 GHz.
- A 20 dB cross-guide coupler for LO-mixer coupling and decoupling.

The total power system was mounted on the Mopra telescope for trials and successfully demonstrated with lunar scans that the half power point is, as predicted by the Rayleigh formula (see equation 1.1.1), 11 arcmin for the 0.5m dish. Measuring the Allan variance of the system it was determined that the system works as an ideal radiometer for a timescale up to several hundred seconds. For timescales exceeding this timespan, long term drift effects start to dominate. The system was further mounted briefly on antenna 4 of the ATCA and used to experimentally determine WVR phase fluctuations on the antenna 4 – 6 baseline of 5.8 km length. It was found to reduce the phase noise on that baseline by a factor of $\sqrt{2}$, as expected when assuming that the atmospheric phase fluctuations on both antennae are uncorrelated. In contrast to the system we have built, this 225 GHz WVR attempts to make an absolute determination of water vapour. The prototype unit remained the only one ever constructed.

There are a number of problems with trying to use total power meters to determine precipitable water vapour: When measuring the total power, the liquid water contribution seriously compromises water vapour determination, as outlined in [63]. Three other WVR efforts, the Plateau de Bure Interferometer [6], the Submillimeter Array (SMA) [3] and the EVLA [10] have described this problem. Liquid water is a strong source of continuum emission ($T_B \propto \nu^2$) but hardly contributes to the electrical path. Total power meters therefore are not well suited to distinguish between water vapour and liquid water contribution in the form of cloud or ice, making them of little use for atmospheric phase correction in an interferometer. An additional difficulty when using an externally housed WVR operating in a frequency domain so vastly different from the science receivers concerns the inability to use the same antenna as the science receiver. The antennae at ATCA were not built to measure emission at a frequency of 225 GHz.

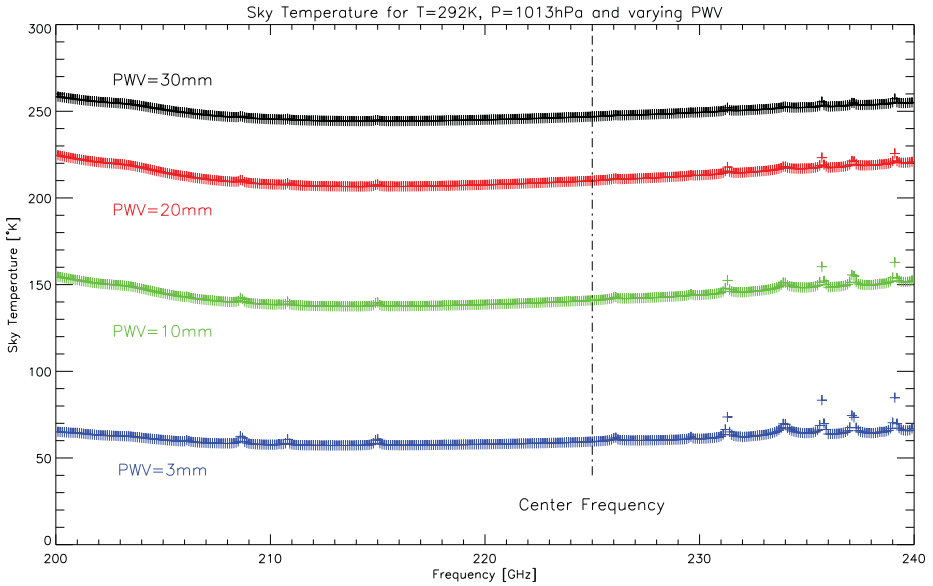

Figure 2.1.1: The continuum around 225 GHz, calculated using the ATM model [45]: The large temperature variations in dependence of precipitable water vapour makes this part of the spectrum an ideal place to measure water vapour, or so it would seem. However, it turns out that the large temperature differences are dominated by liquid water in the continuum end of the spectrum and separating out the water vapour contribution to the signal is not possible. Because liquid water does not affect the electrical path length, the phase delay inducing water vapour cannot be estimated from it, making it an unusable quantity for the purposes of interferometric phase correction. The spectral lines are: O_2 at 234.1 and 235.7 GHz, O_3 at 208.6, 215, 231.3 and 237.1 GHz, H_2O at 210.3 GHz, N_2O at 226.1 GHz. Molecular species are identified from [47].

2.2 ALMA – Atacama Large Millimeter Array

In contrast to the 225 GHz ATCA system described in 2.1, which depends on a simple total power radiometer to measure absolute water vapour, the Atacama Large Millimetre Array (ALMA) water vapour radiometer system measures the brightness of the water line and similarly to our own approach forms differences in water vapour between each line of sight. It depends on the measurement of the line shape using several filters. A good overview is given in [43] and detailed information can be found in [22], [52], [30], [42], [40] and [41]. ALMA is an interferometer that aims to synthesise an antenna with an effective diameter of over 15 km. While this in theory would result in a diffraction-limited resolution of 15 milliarcseconds at 300 GHz, the uncorrected radio seeing at this frequency would typically limit the resolution of images to 700 milliarcseconds if no adaptive optics corrections were applied [19]. This adaptive optics correction is achieved in a similar manner as we have implemented it at ATCA: via direct measurement of atmospheric properties along the line of sight of each of the 54 12–metre diameter antennae using mm-wave radiometers. The ALMA water vapour radiometers, however, measure the emission of the 183 GHz water vapour line, as opposed to our system which measures the 22 GHz water line. This is due to the exceedingly low levels of water vapour present in the troposphere above ALMA: The 22 GHz line is much too weak at PWV levels of just 0.5 – 2 millimetres, with very small temperature differences resulting, too small to be measured by the radiometers.

Even at a very high and dry site like ALMA, changes of up to 50% in the line of sight water vapour can be observed in a matter of minutes. In order to estimate the errors introduced by these fluctuations, each of ALMA's antennae has a water vapour radiometer that measures the 183.3 GHz emission of the $3_{13} \rightarrow 2_{20}$ rotation line of the para water molecules in the atmosphere. This line lies about 200 K above the ground state and so is ideal for tracing water vapour. The principle then is the same as for the 22.2 GHz water line we are using: through well defined atmospheric models, the power received in certain filters set across the water vapour line can be converted into an amount of water vapour which in turn results in an electrical path excess and consequently the phase difference on a any

given baseline. Using these estimates the observed astronomical data can then be corrected for the effect of path fluctuations.

The prototype WVRs for ALMA were developed by a collaboration between the University of Cambridge and Onsala Space Observatory. After successful laboratory and field testing of the prototypes, an industrial partner (Omnisys Instruments AB, Sweden) was contracted for delivery of the production units. The production stage was completed in May 2011 and ALMA has taken delivery of all the radiometers for all 54 of the planned 12–metre antennae.

Utilising the 183 GHz water line poses a few challenges over using the 22 GHz line at a lower frequency: Design and production of the hardware is more complex and expensive, requiring custom components and high precision machining. Also, calibration is more difficult as it needs to be based on very frequent (10 Hz in the case of ALMA) observation of physical internal calibration loads. Even though the site is already very dry, the water vapour line is close to saturation and thus subject to non-linear effects, leading to significantly more complex software requirements. An example of one issue includes making use of just the line wings when the centre of the line becomes saturated.

Since early 2010, extensive testing of the first WVR systems has been carried out at the ALMA site. The preliminary results of these tests suggest that the development and production stage has successfully met these challenges. So far, the units installed on the ALMA antennae appear to be performing well in terms of noise, stability and reliability [41].

The WVRs provide measurements of sky brightness in four filters centered on 176, 177.6, 180 and 182.3 GHz. The system uses a double sideband mixing system, measuring each frequency below the line centre frequency along with its symmetrical upper side band counterpart above the 183.3 GHz water line. The readout frequency from the WVRs can be as high as 5 Hz, although 1 Hz has been determined as fast enough.

The short integration times demand a rather complex system which re-

quires both a calibrated hot and cold load. The stability requirements as per the manufacturers specifications [1] are given as 80 – 100 mK sensitivity in the four separate channels with a stability of 100 mK during a 10 minute time interval and over a 10 degree tilt range. The front end features a low noise corrugated horn antenna with a noise figure of 7.5 dB, an integrated Schottky mixer and LNA providing 30 dB gain, and 50 dB gain over the four detector diodes. Simply by looking at the relative model temperature differences between the 22 GHz and the 183 GHz lines and typical PWV values at site where each would be used, it can be shown that the sensitivity requirements are a factor of ~5 less stringent than for the 22.2 GHz system: The peak temperature for the 183.3 GHz water line, assuming 1 mm of PWV is about 200 K. In contrast, 10 mm of PWV at 22.2 GHz result in a peak water line temperature of ~24 K. Calculating the temperature difference that needs to be measured at the line peak for a path difference of 180 degrees then comes to 0.4 K at 22.2 GHz with 10 mm of PWV and observing at λ = 3 mm. The same calculations for the 183.3 GHz water line with 1mm of PWV and observing at λ = 300 μm requires the WVRs to determine a temperature fluctuation of 2.3 K. A system on the 22.2 GHz water line therefore needs to be ~5 times more sensitive to achieve comparable performance. While the ALMA system has the disadvantage of having to develop higher frequency components, it needs less sensitivity due to the much larger temperature fluctuations measured in the 183 GHz water line at typical conditions.

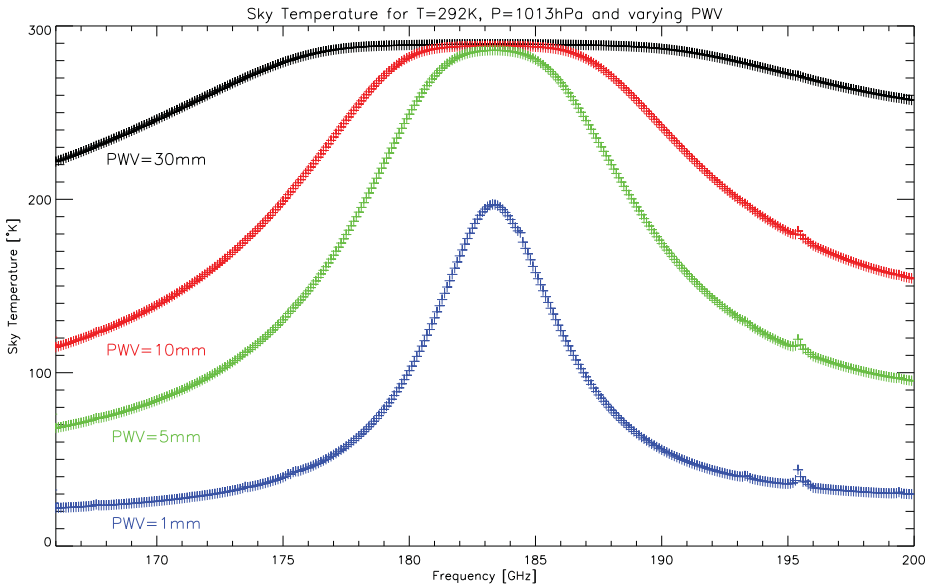

Figure 2.2.1: The water line around 183.3 GHz, calculated using the ATM model [45]: It is immediately evident that for the precipitable water vapour values typically encountered at the ATCA site in Narrabri of >10 mm, this line is completely saturated. At ALMA's site however where the PWV is most of the time <5 mm, this line should provide a good determination of water vapour.

2.3 PdBI – IRAM Plateau de Bure Interferometer (PdBI)

The Institut de Radio Astronomie Millimétrique (IRAM) in Grenoble, France, operates the Plateau de Bure interferometer (PdBI) in the French Alps just north of Gap. The telescope operates at frequencies of 3mm (~100 GHz) to 0.8mm (~340 GHz) and is therefore also highly affected by tropospheric water vapour induced phase noise [66]. This system is described in [6] as well as in a presentation by the same author in [7].

Bremer's description was the first to determine that for the atmospheric phase correction in the presence of clouds, the 22.2 GHz water line seems to be the most favourable part of the spectrum, because at higher frequencies, cloud droplets quickly dominate the atmospheric emission, which makes it difficult to isolate the water vapour contribution needed for the modelling of the atmospheric phase error (liquid water from the cloud droplets does not affect the electrical path length responsible for inducing signal path delays).

Two system designs are discussed, a twin filter and a triple filter system. The classical dual frequency method where one filter is placed on the continuum end of the water vapour line, i.e. in the part of the spectrum where there is minimal contribution from the spectral line, and the other filter is placed onto the water feature at 22.2 GHz is simple and can detect cloud effects such as the increase in continuum temperature caused by the liquid water encountered in cloud. The triple frequency radiometer however proves superior in that it can detect cloud, correct phase at 350 GHz to 30 degrees RMS and it can eliminate the variations in ground pickup which are telescope elevation dependent as well as variations in receiver temperature. The gain stability required for this level of accuracy is determined to be $7.5 \cdot 10^{-4}$ and a frequency separation of at least 3.5 GHz between the highest and lowest monitoring frequencies is required, given a bandwidth of 0.5 GHz and a Tsys of 143 K.

It is interesting to note that even in 1997 when the initial technical report was written which this summary is based on, interference from commercial bands was considered one of the major dangers to using the 22.2 GHz

water line. If one were to stay completely inside the protected bands, the minimum separation between the filters would decrease to a mere 2.5 GHz and rather narrow bandwidth for the filters of between 200 to 0.4 GHz. This in turn would require a Tsys of the receiver of 50.6 K, which would make the system technologically much more challenging to implement and to maintain.

The PdBI triple filter system is also an ambient temperature system and has no cryogenically cooled stages. The filters are 1 GHz wide each and centered on 19.175 GHz, 21.917 GHz and 25.175 GHz. The separation between the observed and monitored axis is 15′ and the WVRs use the same Cassegrain reflectors as the science receivers. For calibration, a noise diode is used as well as a hot load to maintain gain stability.

Chapter 3

Site Characterisation of the ATCA in Narrabri

The Australia Telescope Compact Array is located near the town of Narrabri in northwestern New South Wales, Australia. Its position of S30°18'46.385" E149°33'00.500" [51] has for over 10 years made it the only millimetre interferometer available in the southern hemisphere. The continental climate, the surrounding geography as well as its elevation of 235m above sea level mean that daytime temperatures in the summer average above 30°C. In winter, temperatures still reach above 15°C during the daytime (see Figure 3.1.1). However at night it can drop below freezing and because the weather systems predominantly originate in the west, most air mass reaching the site has been exposed to the dry inner Australian continent, resulting in on occasion quite stable and low water vapour conditions considering the site elevation.

3.1 Meteorological Parameters

Weather conditions at ATCA have been examined from 2006 – 2011 based on weather station data archived in the Monica system. The median hourly temperatures show typical diurnal variations encountered in continental climates with little cloud cover: a sharp rise in the temperature after sunrise with peak temperatures experienced mid to late afternoon followed by a night long period of radiative cooling (see Figure 3.1.1). The hourly median atmospheric pressure (converted to sea level pressure, see Fig-

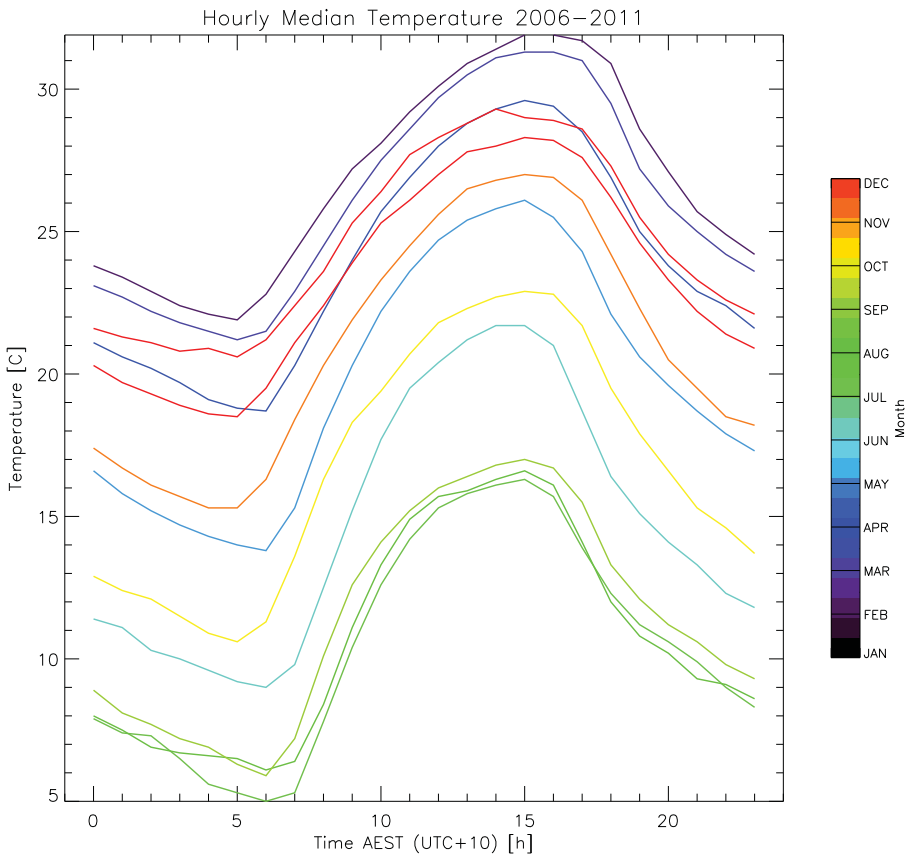

Figure 3.1.1: The hourly median temperatures for 2006 to 2011. In summer, temperatures above 30°C are normal, while winter appears characterised mostly by the July – September temperatures which reach just a little over 15°C at midday. Note the textbook diurnal variations caused by solar heating.

ure 3.1.2) exhibits a typical rise in pressure in the mornings before sunrise with a peak experienced before noon, then a temperature induced pressure drop occurs until solar heating subsides and the pressure gradually rises as the atmosphere cools down. The variations between summer and winter are a fairly steady ~10 hPa.

At winter solstice, the Sun's peak elevation for the Australia Telescope Compact Array's position is ~40°, while at summer solstice, the Sun is al-

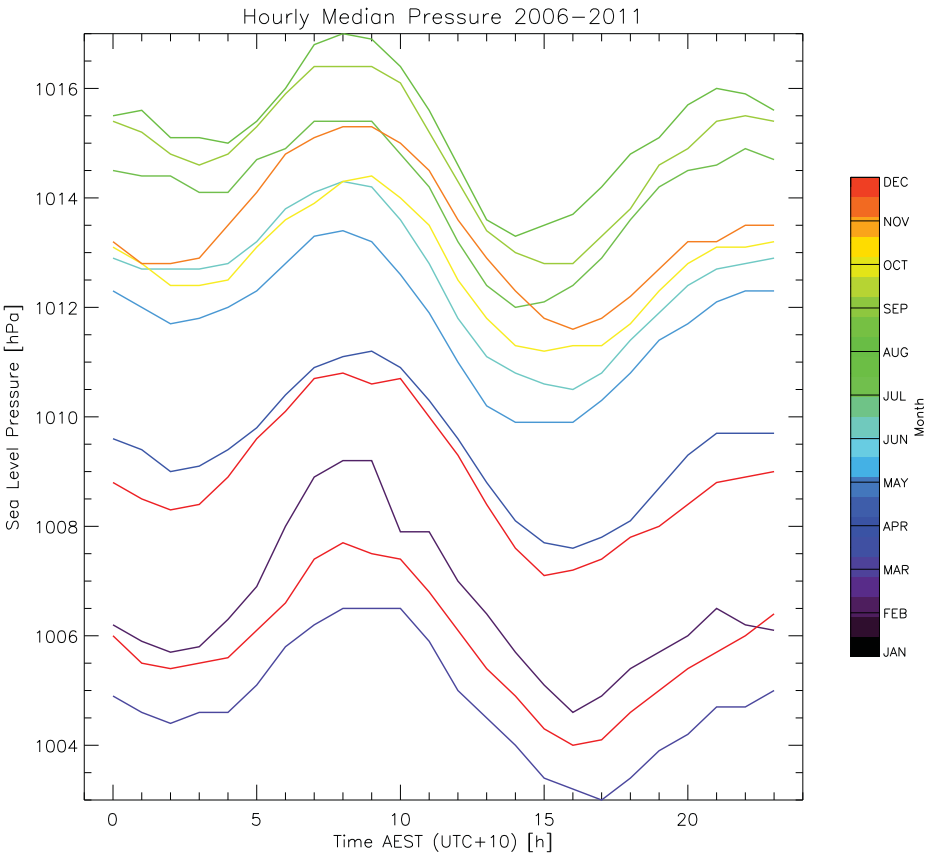

Figure 3.1.2: The hourly median atmospheric pressure for 2006 to 2011. Note the diurnal variations as well as the fairly constant 10hPa pressure differential between summer and winter dominate.

most going through zenith at 83° elevation at midday. Interestingly, the strongest median wind speeds (see Figure 3.1.6) coincide both in summer and winter with the Sun's passing the ~40° elevation mark: This occurs at 8am at summer solstice and 12 noon at winter solstice. Another interesting behaviour concerns the wind direction. Refer to Figure 3.1.3 to see the westward swing of the predominant wind direction that occurs every morning around the same time when the wind speed is increasing. During winter, wind direction is predominantly southern to south easterly at night. In the morning hours, when the wind speed is picking up, this changes around to west south westerly direction. In summer, this swing to the west is also evident in the graph, however, the wind direction is much more varied. Looking at the wind rose diagram in figure 3.1.4 for the full time span from 2006 to 2011, we see that the cardinal wind directions are NNE, SE as well as WSW. These observations are compatible with the presence of the Nandewar Range extending North to South from about 45km to the ENE of the telescope site: Katabatic winds produce the easterly winds measured during night, then once the Sun has started heating the westerly slopes of the Mount Kaputar and the Nandewar Range, updrafts develop and anabatic winds then dominate the remainder of the day.

The wind speeds in Figure 3.1.6 exhibit a distribution that favours two distinct regimes: Daytime and nighttime. The daytime regime in December starts around 6am and goes on through 6pm. In June, the wind doesn't start until 9am and continues until 6pm, much like in summer time. There are a few probable causes for this behaviour: Wind is caused by pressure differences. Thermal heating is one mechanism which creates pressure differences by transferring heat from the ground into the air, causing upward lift resulting in localised low pressure. The amount of time it takes in summer to heat the ground to a temperature high enough to start this mechanism is less than in winter, due to the higher elevation angle of the Sun and thus the more efficient heating. Hence in summer, the wind starts sooner than the difference in Sun rise time: The Sun rises at a steeper angle and thus reaches a higher elevation angle sooner. The probability that

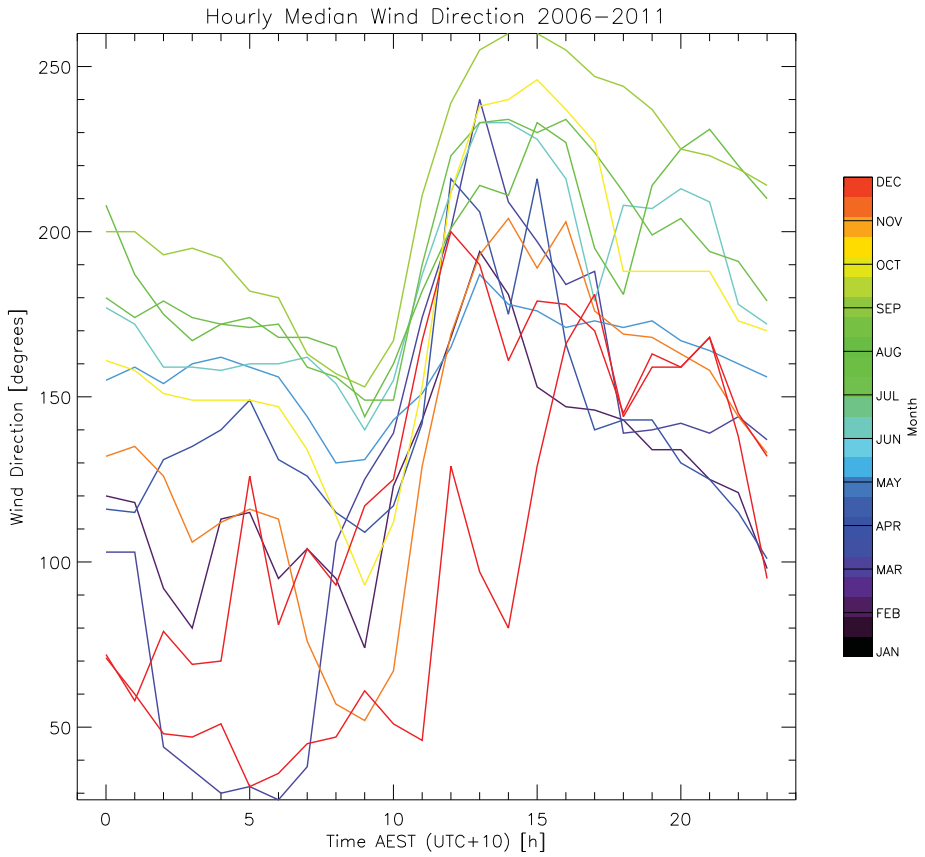

Figure 3.1.3: The hourly median wind direction for 2006 to 2011. Note how the wind direction changes in the same period when the wind speed increases in the morning hours. In winter, the wind direction is predominantly south western during the night, and it swings onto a west south western direction during the day. In summer, the wind direction is much more varied.

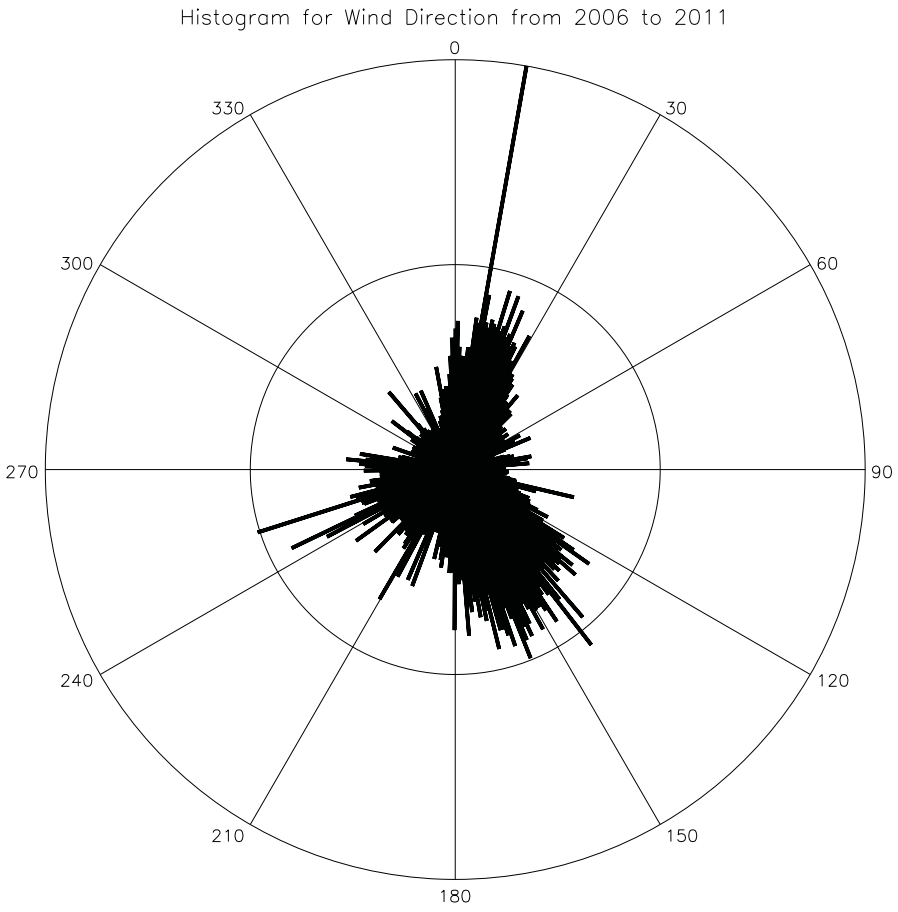

Figure 3.1.4: The wind rose for 2006 to 2011. The three cardinal directions are NNE, SE and WSW.

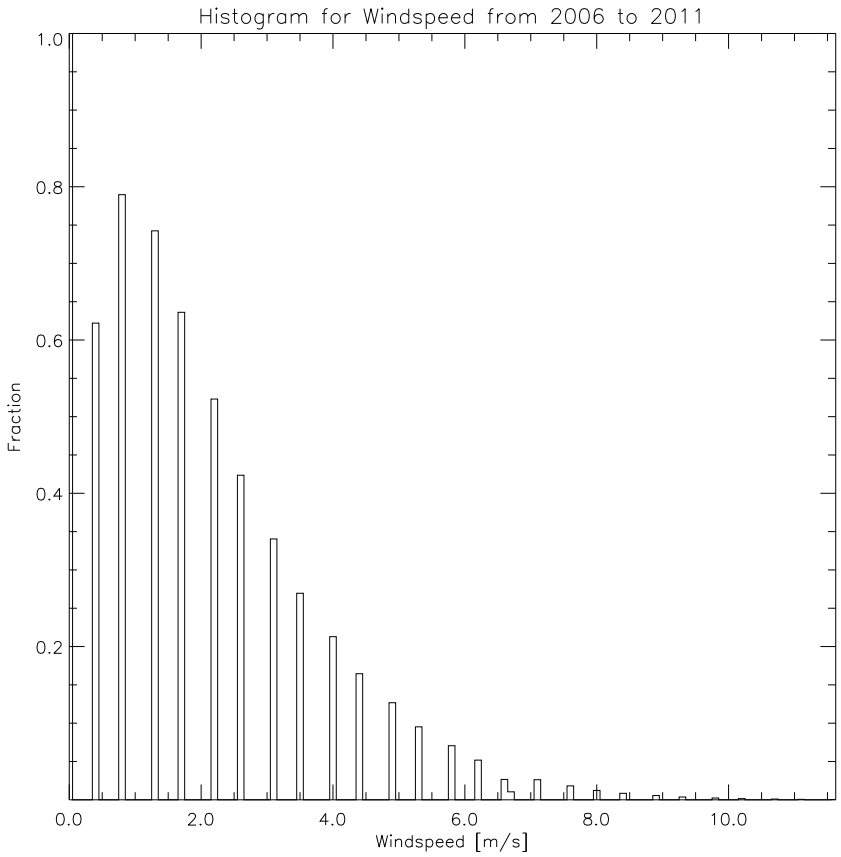

Figure 3.1.5: The wind speed histogram. The wind speeds were normalised to the peak bin (wind still). The second peak occurs at around 0.8 m/s in this typical Weibull distribution. The highest recorded speed from 2004 to 2011 was 23.25 m/s. In order to better read the histogram, it only shows values to half the peak measured, 11.65 m/s. The fraction of bad data which is included in the zero wind speed bin is less than 0.1%.

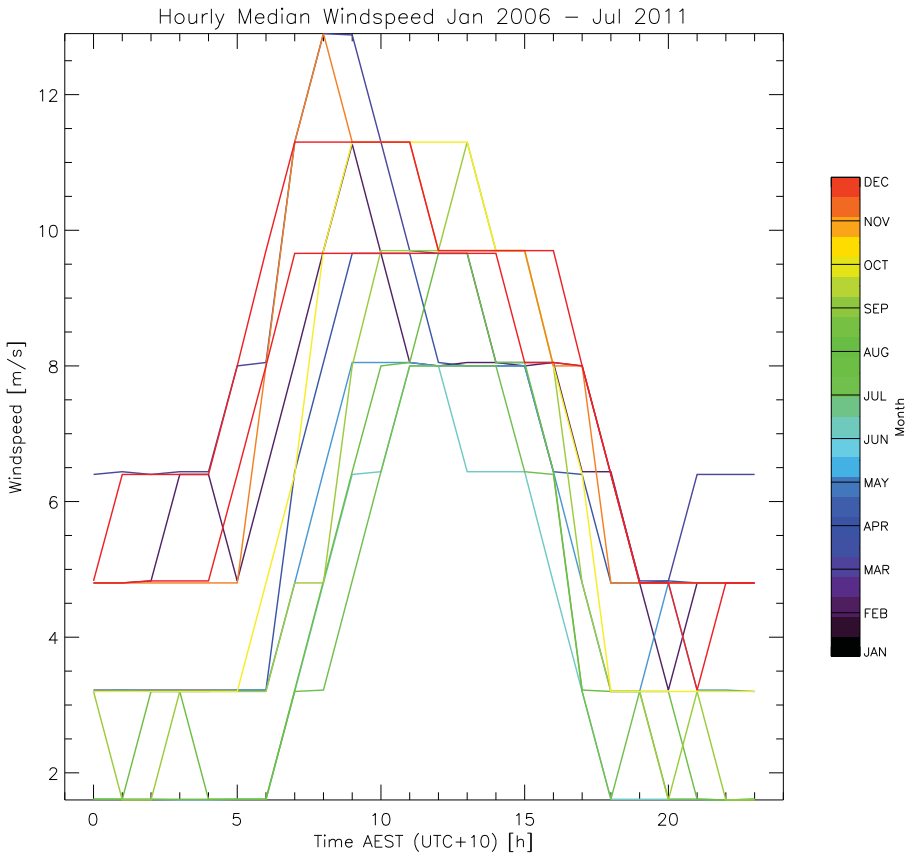

Figure 3.1.6: The hourly median wind speed for 2006 to 2011. Note the generally weaker winds during night time in the winter months. Peak in summer occurs at local morning while during winter, peak occurs closer to midday.

	Windspeed Percentiles	
Month	50% [m/s]	95% [m/s]
All Years	**1.2**	**5.2**
Jan	1.2	5.2
Feb	1.2	5.2
Mar	1.2	4.8
Apr	1.2	4.8
May	1.6	5.2
Jun	1.2	5.2
Jul	1.2	4.8
Aug	1.6	5.2
Sep	1.2	5.2
Oct	1.2	5.2
Nov	1.2	5.2
Dec	1.2	4.8

Table 3.1.1: Shown is a monthly breakdown of windspeed data for 2004-2011. The 50% percentile is 1.2 m/s. 5% of all wind is stronger than 5.2m/s (yearly average). The anemometer has been operational for more than 99.9% of all time. The quantisation of the data into 1.2/1.6 and 4.8/5.2 m/s bins is due to the limited resolution of the anemometer.

the wind exceeds the median yearly wind for a given month has also been examined. The findings are listed in Table 3.1.1. The yearly average wind is below 5.2 m/s during 95% of the time, and below 1.2 m/s 50% of the time. See also Figures 3.1.7 and 3.1.8 for cumulative histograms of the wind speed in June and December respectively. From these Figures it is evident that there is more wind during the daytime than the nighttime, but the seasonal variation is small.

The cumulative histogram distribution for atmospheric pressure in Figure 3.1.9 displays the diurnal variation already seen in Figure 3.1.2: In the afternoon hours when the temperature peaks, the pressure drops due to a combined effect of hot air being less dense than cold air and the creation of a localised low pressure due to thermal uplift of the entire airmass. Other than a constant offset of about 10 hPa, there appears little difference between the June and December histograms (refer to 3.1.9 and 3.1.10). In June, the pressure is in the range of 1010 to 1020 hPa 75% of all

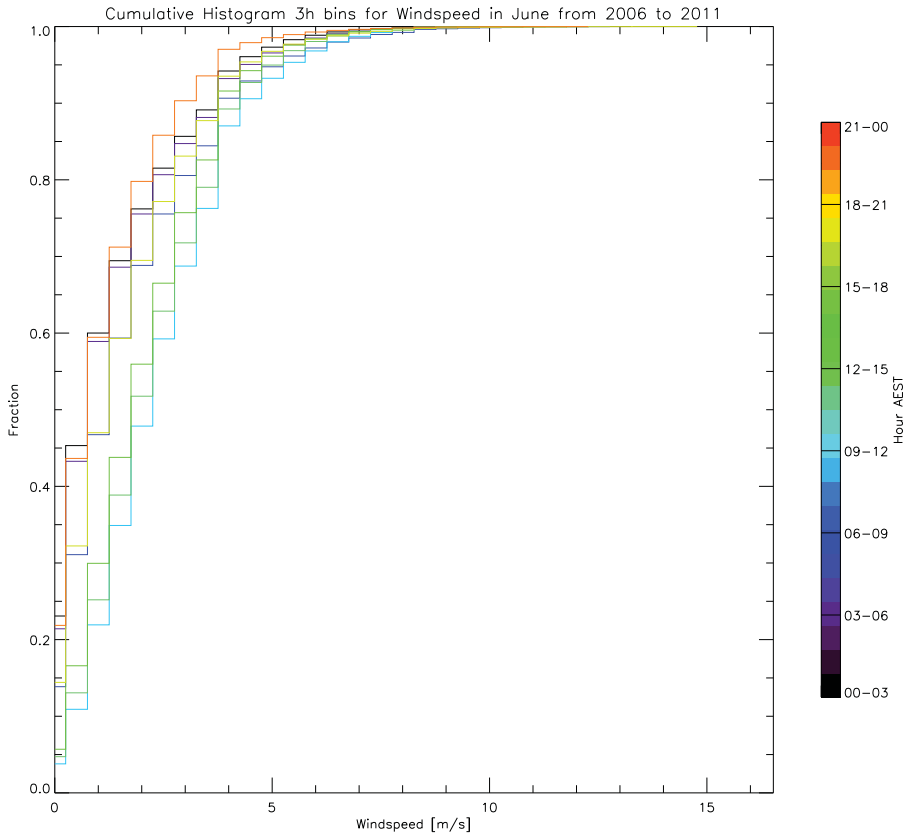

Figure 3.1.7: The cumulative histogram for the wind speed in June. Colour coded is the time of day (AEST) as shown in the colour bar. Two distinctive bands are evident: From 09:00 – 18:00 the probability that the wind speed exceeds 3 m/s is about 25%. During the other times, there is only a 15% chance that winds exceed 3 m/s.

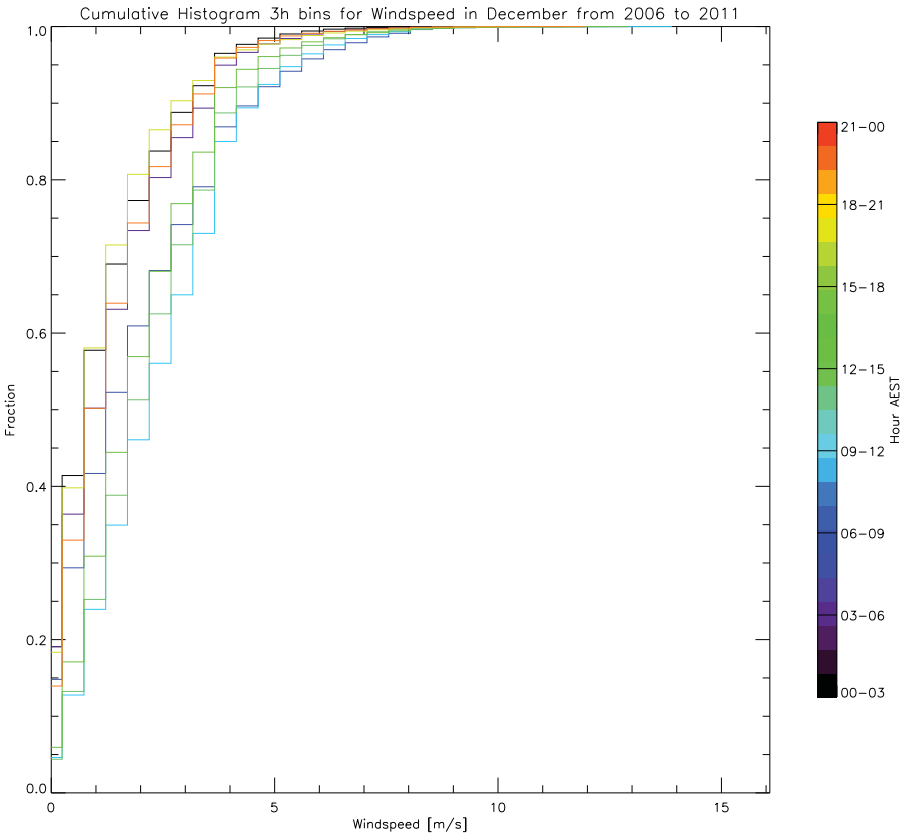

Figure 3.1.8: The cumulative histogram for the wind speed in December. Colour coded is the time of day (AEST) as shown in the colour bar. Two distinctive separated bands are evident: From 06:00 – 18:00 the probability that the wind speed exceeds 3 m/s is about 45%. During the other times, there is only a 15% chance that winds exceed 3 m/s.

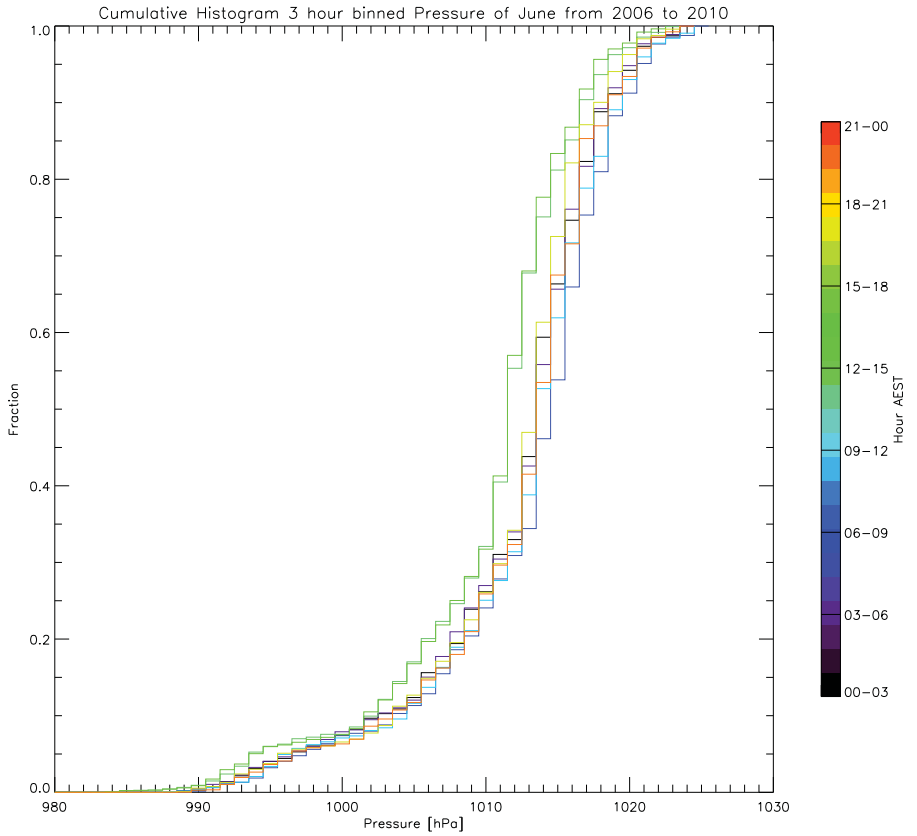

Figure 3.1.9: The cumulative histogram for the pressure in June. Colour coded is the time of day (AEST) as shown in the colour bar. This shows a slight diurnal variation. It is similar to the December histogram in Figure 3.1.10 except that the overall pressure level is raised by about 10 hPa. Note that for a fraction of less than 0.1, the pressure drops off rapidly: This is related to rapid passing of low pressure systems across the site.

time. In December, the same statistic holds true for a pressure range of 1000 to 1010 hPa.

In Figures 3.1.11 and 3.1.12, the temperature distributions are shown. Temperatures in summer are linearly distributed during the daytime hours. At night time, there's a large fraction of 60% where the temperature remains between 18°C to 22°C. During daytime hours the distribution is lin-

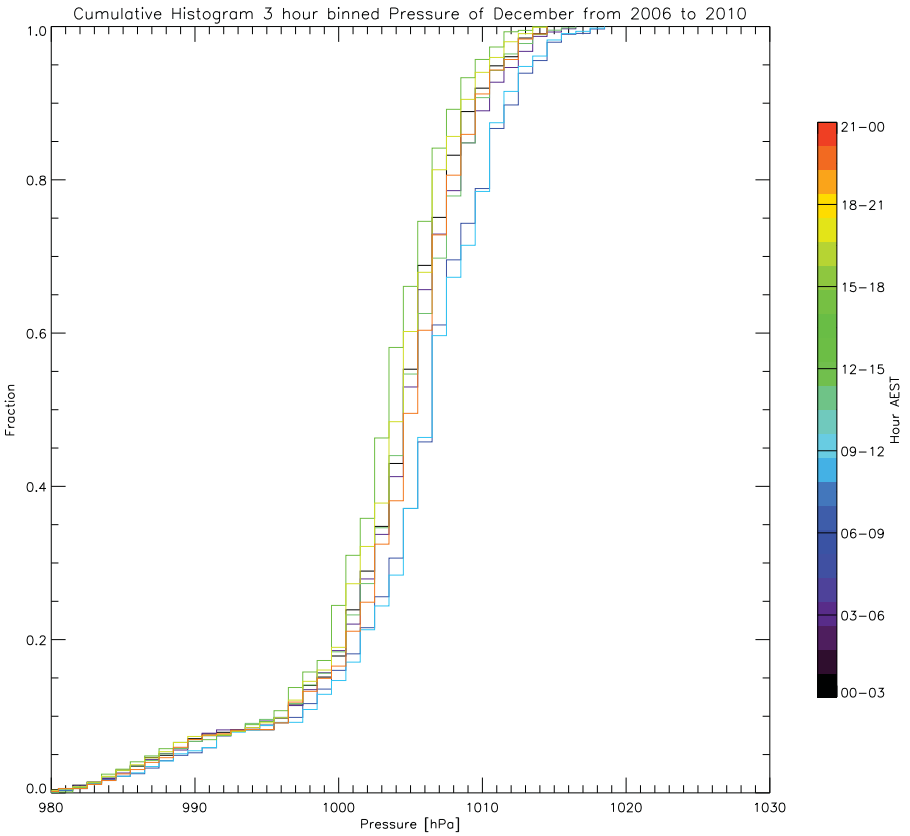

Figure 3.1.10: The cumulative histogram for the pressure in December. Colour coded is the time of day (AEST) as shown in the colour bar. This shows a slightly more pronounced diurnal variation than June. The same dip in fractions of less than 0.1 can be observed as in June, related to the passing of low pressure frontal systems.

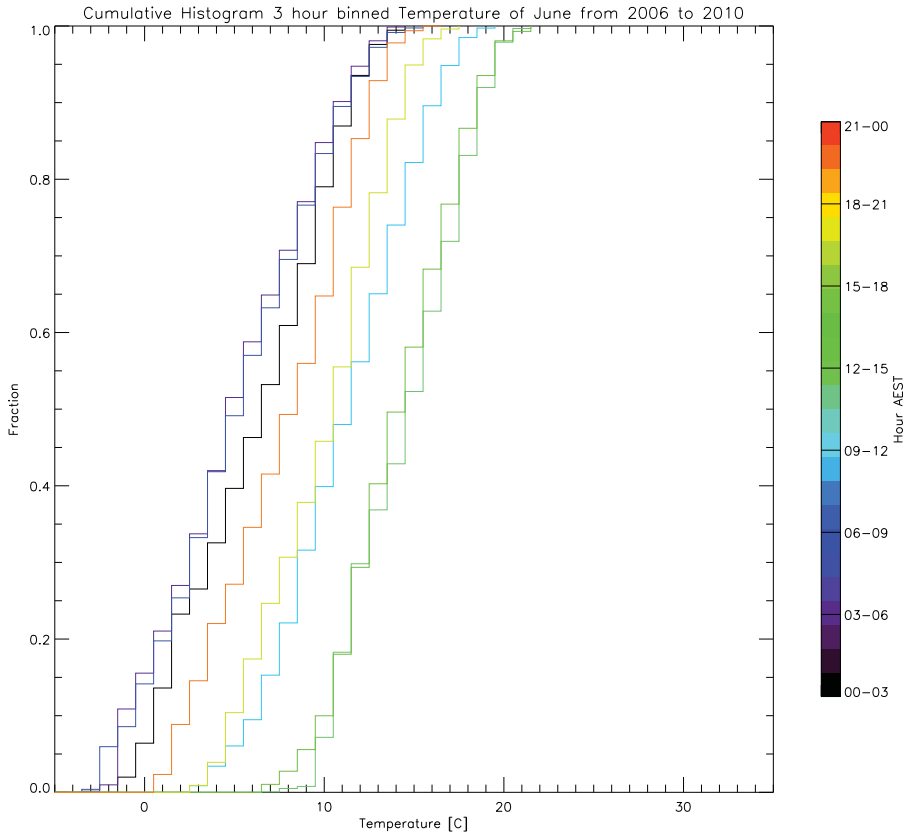

Figure 3.1.11: The cumulative histogram for the temperature in June. Colour coded is the time of day (AEST) as shown in the colour bar. This reveals a linear distribution of both night and daytime temperatures between the minimum and maximum values recorded in each hour range.

ear with 50% of 12:00 – 15:00 temperatures between 20°C to 28°C and the other 50% between 28°C and 33°C. In winter, the temperatures are completely linearly distributed: 50% of 12:00 – 15:00 temperatures are between 8°C to 13°C and the other 50% between 13°C and 21°C. for detailed plots.

The last meteorological parameter examined is rainfall. Total rainfall in the period of January 2006 to July 2011 was 2903 mm, which averages to 634 mm per year. That is in good agreement with the 625 mm of yearly

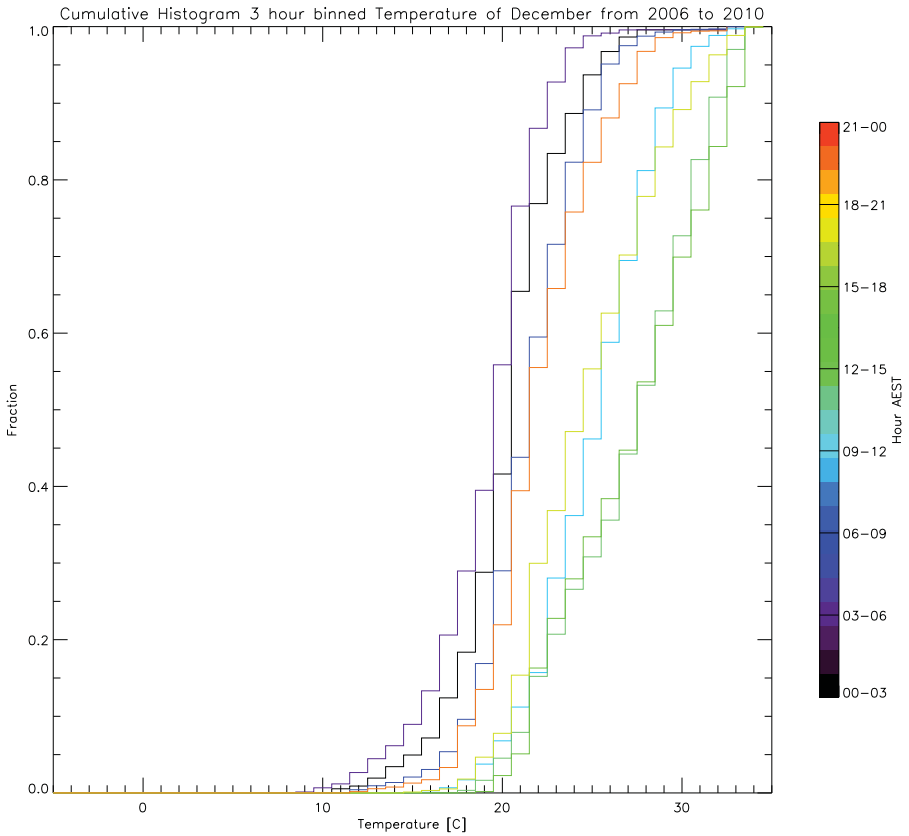

Figure 3.1.12: The cumulative histogram for the temperature in December. Colour coded is the time of day (AEST) as shown in the colour bar. This reveals a symmetrical distribution of night time temperatures. However, it is not a linear distribution unlike in June.

rainfall average from 1981–2010 as reported by the Bureau of Meteorology (BOM) Climate Database for Narrabri. Because of the low rainfall levels, instead of building statistics for just one month in winter and summer, we have combined the graph data over four winter months and four summer months. It is evident from Figure 3.1.13 that especially during the summer months of November – March, the majority of rain occurs in the late afternoon and evening. This is attributed to the increased thunderstorm activity. When rain is present in winter on the other hand, it falls regardless of time of day.

One conclusion we can draw from these basic meteorological parameters is that the ATCA site is not an extreme site: It features moderate to warm temperatures, with moderate wind and strong radiative heating in summer.

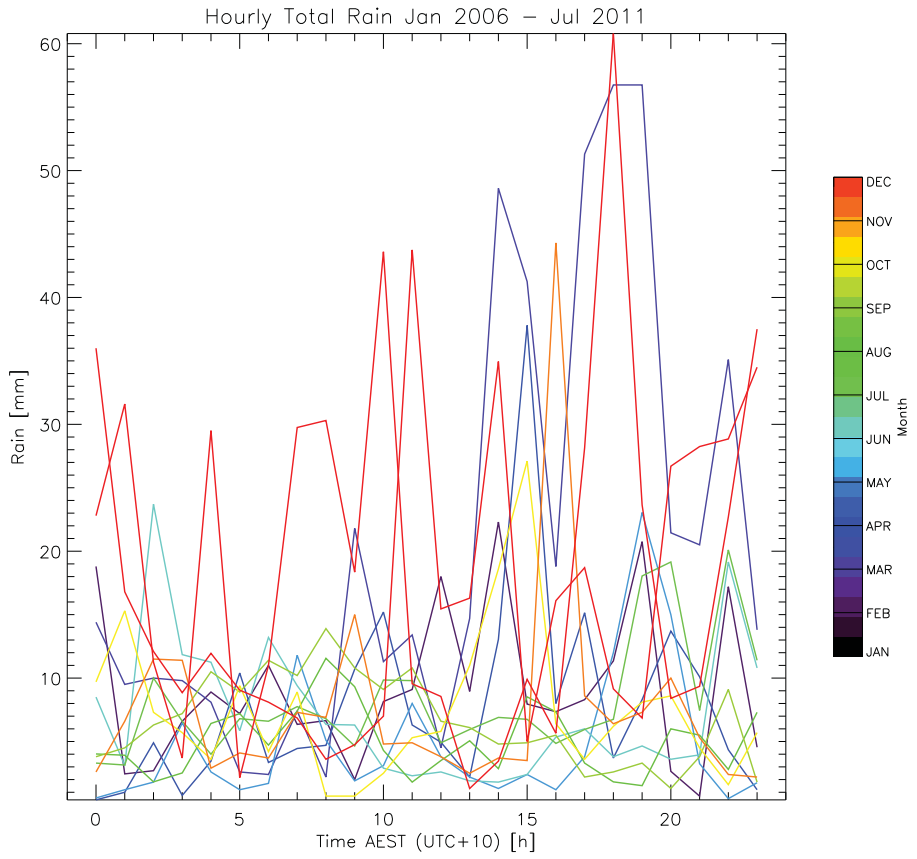

Figure 3.1.13: Total rainfall by hour and month are plotted in this diagram. There appears an increased amount of rain falling from about noon until evening for the months of November – February. This could be due to rainfall originating in thunderstorms rather than frontal systems, the latter we would expect to encounter independently of time of day.

3.2 Theory of Turbulence

In order to understand the movement of an air mass over the aperture of a telescope, some basic theory of turbulence needs to be introduced. Turbulence is a flow regime which is characterised by stochastic properties. Factors that affect turbulence include scale size (e.g. geographical features), boundary layer properties, density, viscosity and relative velocities of the interacting media. Our concern regards air moving over a ground surface with the air itself consisting of pockets of varying amounts of water vapour which is poorly mixed. In 1941, the Russian mathematician Andrey Kolmogorov developed the widely accepted theory [32] that small scale turbulent motions are statistically isotropic and thus do not have any preferential spatial direction. The large scales (which we denote as L, the scale size of the turbulent cell) on the other hand are not isotropic because their behaviour is determined by the shape of the boundary. Kolmogorov's hypothesis starts with the idea that a turbulent flow of velocity V contains large vortices which over time decompose into smaller vortices until they have reached a scale where the remaining kinetic energy is turned into internal energy, e.g. through viscous dissipation. Assuming ϵ_0 is equal to the rate of energy dissipation, this energy cascade can be expressed as:

$$V \propto \epsilon_0^{1/3} L^{1/3} \tag{3.2.1}$$

substituting $L \propto \frac{1}{\kappa}$ to express equation 3.2.1 in spatial frequency space, this turns into

$$V \propto \epsilon_0^{1/3} \kappa^{-1/3} \tag{3.2.2}$$

The kinetic energy field $E(\kappa)$ is proportional to V^2 and can be integrated over $d\kappa$ to obtain the Kolmogorov power law (also referred to as the Kolmogorov power spectrum):

$$E(\kappa) \propto \kappa^{-5/3} \tag{3.2.3}$$

The energy created at the outer scale L_0 cascades down to the inner scale l_0 through the sub-inertial range until it dissipates. Kolmogorov also introduced the structure function in order to describe the fluctuations in

the velocity field as a function of separation r.

3.3 The Phase Structure Function

Tatarski in 1961 [54] describes the spatial structure function over a distance r as:

$$D(r) = \int_{-\infty}^{\infty} dx(f(x) - f(x+r))^2 \tag{3.3.1}$$

which is equivalent to the mean square difference between two points of separation r:

$$D(r) = \langle (f(x) - f(x+r))^2 \rangle \tag{3.3.2}$$

For the purposes of observing through an atmosphere that changes as it is moved across the telescope, the layer containing the eddies of (in our case) water vapour can be regarded as a phase screen moving across the telescope aperture. Taylor in his seminal paper in 1938 [55] found that for a given moving air mass with embedded eddies of varying properties such as temperature, that as long as the velocity of the air mass is "very much greater than the turbulent velocity" (sic), the sequence of changes measured by a probe at a given point simply measures an unchanging pattern of eddies going by. This means the eddies, as related to the probe, are not changing and seen as statically embedded (or "frozen"). This is now referred to as the "frozen screen" or Taylor hypothesis and in our case applies to eddies of water vapour which is poorly mixed in the atmosphere. The velocity of the phase screen is referred to as v_s.

The concept of the frozen screen is now taken and applied to the structure function equation 3.3.2, taking into account that the observation parameter that is modified by water vapour is the phase ϕ. It is further assumed that the phase screen velocity v_s does not change significantly during the time period τ over which the measurement is made, so that τ becomes equivalent to the (fixed) baseline b through the relationship

$$v_s = \frac{b}{\tau} \tag{3.3.3}$$

where the lag time τ is the time it takes for the phase screen to pass over the baseline b. We can then formulate the temporal phase structure function, or lag phase structure function (LPSF):

$$D_\Phi(\tau) = \langle(\phi(t) - \phi(t + \frac{b}{v_s}))^2\rangle \tag{3.3.4}$$

By evaluating the LPSF for a statistically significant amount of time at the ATCA site, statements can be made regarding the scale of the turbulence, as well as the velocity of the phase screen v_s through the following relationship:

$$D_\Phi(\tau) = D_\Phi(b) \mid b = v_s\tau \tag{3.3.5}$$

where D is the size scale of the turbulence, b is the phase screen dimension over which ϕ_{RMS} evolves to its first peak and τ is the corresponding time when that peaks occurs, called the corner time. We illustrate this quantitatively in the next section.

Following Carilli in [9], the square root of the phase structure function corresponds to the RMS phase variation as a function of lag time τ:

$$\Phi_{RMS}(\tau) \equiv \sqrt{D_\Phi(b)} \tag{3.3.6}$$

Expanding on the Kolmogorov turbulence relationship in equation 3.2.3, we can formulate this in a general way to determine a baseline and wavelength dependent term K:

$$\Phi_{RMS}(b) = \frac{K}{\lambda} b^\alpha \tag{3.3.7}$$

where Φ_{rms} is in degrees, λ is in mm, b is the baseline length in km and α is the Kolmogorov exponent. According to Kolmogorov's theory of turbulence, it can be shown that the phase noise vs. baseline relationship should follow equation 3.3.7 with $\alpha = \frac{1}{3}$ for turbulence scales L larger than the baseline b (i.e. their vertical extent h is smaller than the baseline). This case also is referred to as the 2D turbulence case, because the phase screen assumes the statistical properties of a 2 dimensional, thin screen:

$$\left.\begin{array}{l} L > b \\ b > h \end{array}\right\} = \text{2D or thin screen}$$

The other case where the turbulence scale L matches or is smaller than the baseline b results in a Kolmogorov exponent of $\alpha = \frac{5}{6}$. The phase screen then exhibits 3D behaviour and is called the thick screen:

$$\left.\begin{array}{l} L \leq b \\ b \leq h \end{array}\right\} = \text{3D or thick screen}$$

The last relationship that needs to be discussed in this context concerns coherence. The phase variations averaged over a given integration time cause coherence loss in the measured visibility. For a given visibility $V = V_0 e^{i\phi}$ the effect on the measured amplitude due to phase noise in a given averaging time is [9]:

$$\langle V \rangle = V_0 \times \langle e^{i\phi} \rangle = V_0 \times e^{-\phi_{RMS}^2/2} \tag{3.3.8}$$

assuming Gaussian random phase fluctuations of ϕ_{rms} over the averaging time.

3.4 Millimetre Characterisation of the ATCA Site

A quantitative analysis of the site conditions for millimetre astronomy has been facilitated by the installation of a seeing monitor, an interferometer measuring phase variations of the signal from a beacon located on a satellite in geosynchronous orbit. The only baseline available measures 235 m in length and it observes a transmitter beacon on a satellite in the ~15 mm band, the exact frequency is classified as it is colocated with a defence satellite. The seeing monitor, along with some site analysis data for a little over a year's worth of data has been described in detail in [38]. The statistic indicating path length RMS shown in Figure 3.4.1 gives a good indication of the mm observing conditions encountered throughout the seasons. It is interesting to see that during winter, the conditions generally are good enough to permit 3 mm observing 24 hours, while in summer, a window about 3 hours wide around noon during which the 440 μm path length difference limit is exceeded which results in decorrelation for

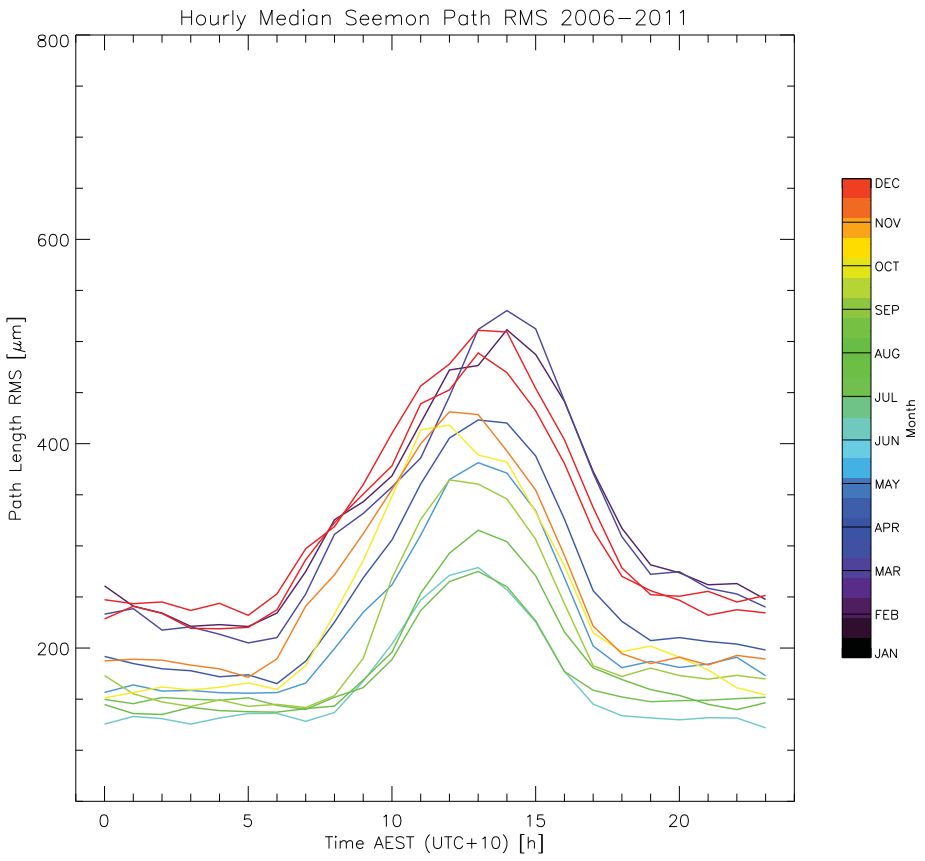

Figure 3.4.1: The path length RMS at Narrabri as a function of time of day and season from 2006 to 2011. During the winter months at night, a path length RMS of 200 μm or better is maintained. During the daytime, conditions remain below 500 μm in winter, allowing 3mm oberving on average to be successful on a 24 hour basis.

3.3 mm observing. This limit comes from the $\frac{\lambda}{7.5}$ figure for a correlation efficiency of ϵ=0.5 which we will derive in equation 6.2.24.

Using the tools derived in the previous section, we now analyse the data to determine the characteristics of the water vapour phase screen typically encountered at ATCA as well as the millimetre seeing limitations. We have examined almost 7 year's worth of data from mid 2004 to mid 2011. Two examples of lag phase structure functions are shown in Figures 3.4.2 and 3.4.3, illustrating the thick screen and thin screen structure func-

tion respectively. Also shown in figure 3.4.4 is an example time series of 60 minutes worth of seeing monitor phase data to derive the lag phase plots. Each of the plots shows a lag time of up to 10 minutes in a lag time interval of 30 minutes length. Each bin contains between 3 and 180 samples. These plots visualise the behaviour of the phase screen as it moves across the baseline. The parameters that can be derived from this include the corner time, which is the time that elapses until the phase noise has peaked for the first time. This is a function of the scale of the turbulence and, knowing both the length of the baseline and how much time has elapsed until the corner time is reached, it directly leads to the velocity of the phase screen v_s (Equation 3.3.3). The gradient fit (in log space) to the ascending phase noise until the corner time then yields the Kolmogorov exponent α. We define the corner time (also referred to as plateau) as the time where two or more successive data points are smaller than the preceding points. See Figure 3.4.5 for a graphical representation of the full date range from 2004 – 2011. June data only is shown in Figure 3.4.6 and December data only is shown in Figure 3.4.7. The overall mean for the Kolmogorov exponent was found to be α=0.763 with σ=0.210. According to the cumulative histograms, and assuming $\alpha \leq 0.4$ to be 2D turbulence, the ATCA site spends less than 5% of the time under a 2D phase screen, about 45% in the transition between 2D and 3D and the remaining 50% under a 3D phase screen. It can thus be said that up to 5% of the time, the phase delay inducing water vapour layer is less than 235 m thick (the baseline of the seeing monitor). There is a clear time of day dependence with a preference towards a larger α during day time hours from 09:00 to 18:00 local time, which is compatible with an agitated troposphere caused by the Sun's thermal heating. This is true both in June and December, however, in December the difference between daytime and nighttime α is larger.

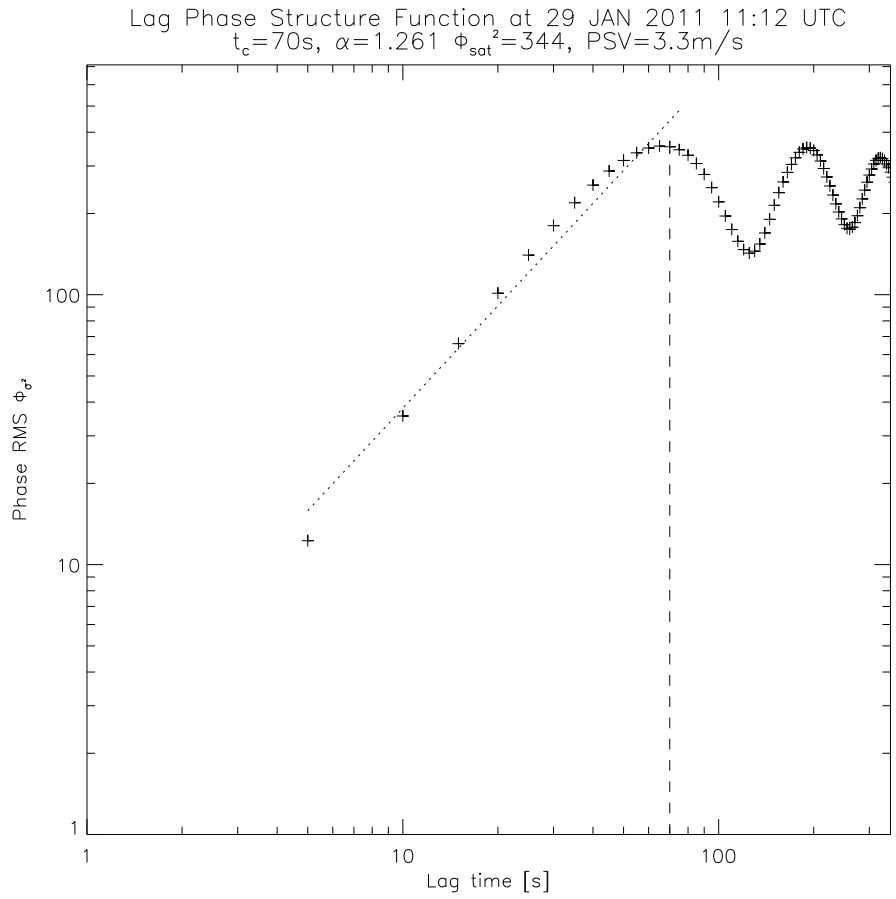

Figure 3.4.2: Seeing monitor data was used to create this plot of the lag phase structure function. Shown is an example of a 3D screen. The corner time t_c is 70 seconds, which translates to a phase screen velocity of 3.3 m/s. The Phase RMS where saturation is reached $\Phi_{\sigma^2,sat}$ is 344 degrees and the slope corresponds to a Kolmogorov exponent of α=1.261, as expected for 3D structure in the phase screen. The vertical dashed line depicts the location of the turnoff corner. The dotted line depicts the fit used to determine the Kolmogorov exponent.

Another important effect caused by tropospheric phase fluctuations

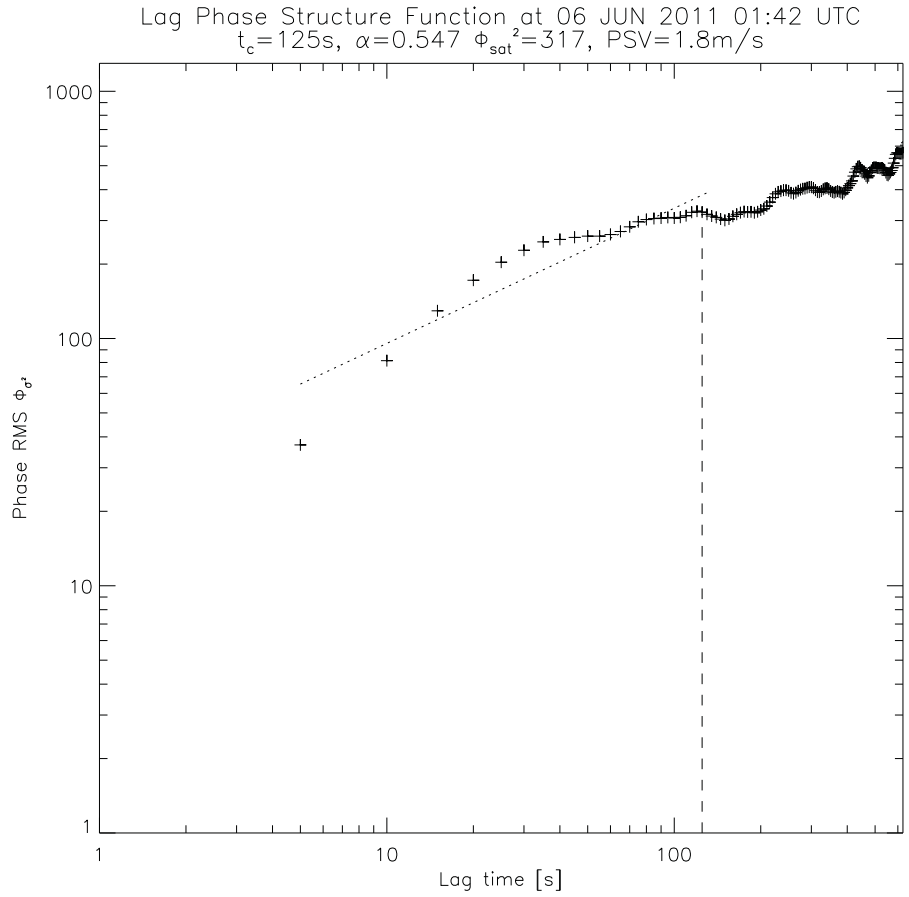

Figure 3.4.3: Seeing monitor data was used to create this plot of the lag phase structure function. Shown is an example of a 2D screen. The corner time t_c is 125 seconds, which translates to a phase screen velocity of 1.8 m/s. The Phase RMS where saturation is reached $\Phi_{\sigma^2,sat}$ is 317 degrees and the slope corresponds to a Kolmogorov exponent of α=0.547. The vertical dashed line depicts the location of the turnoff corner. The dotted line depicts the fit used to determine the Kolmogorov exponent.

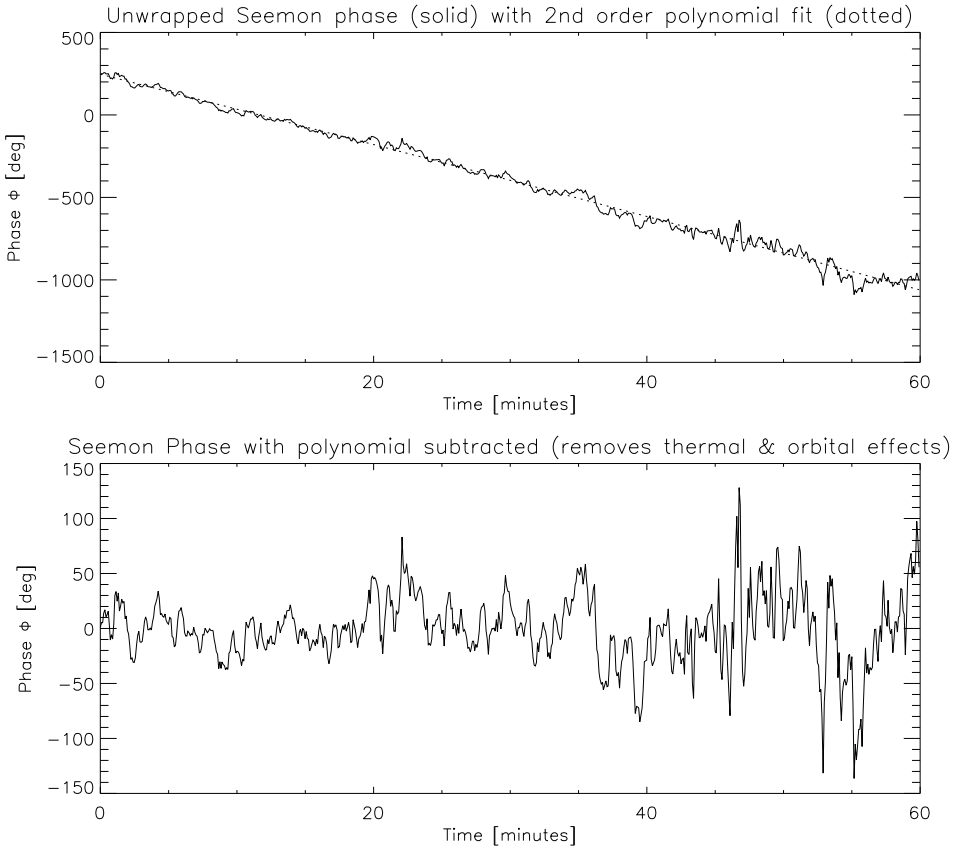

Figure 3.4.4: This plot details the phase data time series used for the lag phase structure function plot in figure 3.4.3. The first panel shows the phase information with just the phase unwrapped but otherwise not corrected data. Because the beacon located on the geosynchronous satellite is moving to and from the observer, large phase fluctuations occur over the course of 24 hours. Another source of large scale fluctuations affecting absolute phase tracking are thermal variations in the seeing monitor enclosures. These, along with the orbital effects, can be removed by subtracting a second order polynomial from the data, the result of which is illustrated in the lower panel. Clearly visible in the figure is the larger amplitude phase turbulence occurring from 45 minutes onward. This turbulence is visible in the structure function in figure 3.4.3 as an increase in phase RMS after having reached the initial phase RMS saturation point.

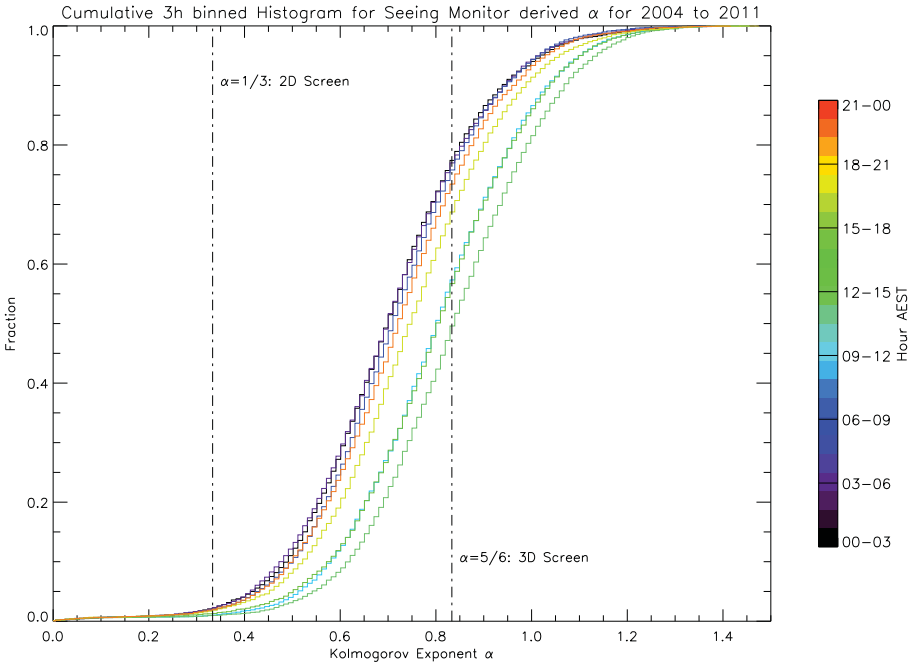

Figure 3.4.5: This cumulative histogram depicts the Kolmogorov exponents encountered as a function of time for the entire data available from the seeing monitor instrument from 2004 until the end of July 2011. The overall mean for α=0.763 and σ=0.210. Note the time of day dependence with a preference towards a larger α during day time hours from 09:00 to 18:00 local time, which is compatible with an agitated troposphere caused by the Sun's thermal heating.

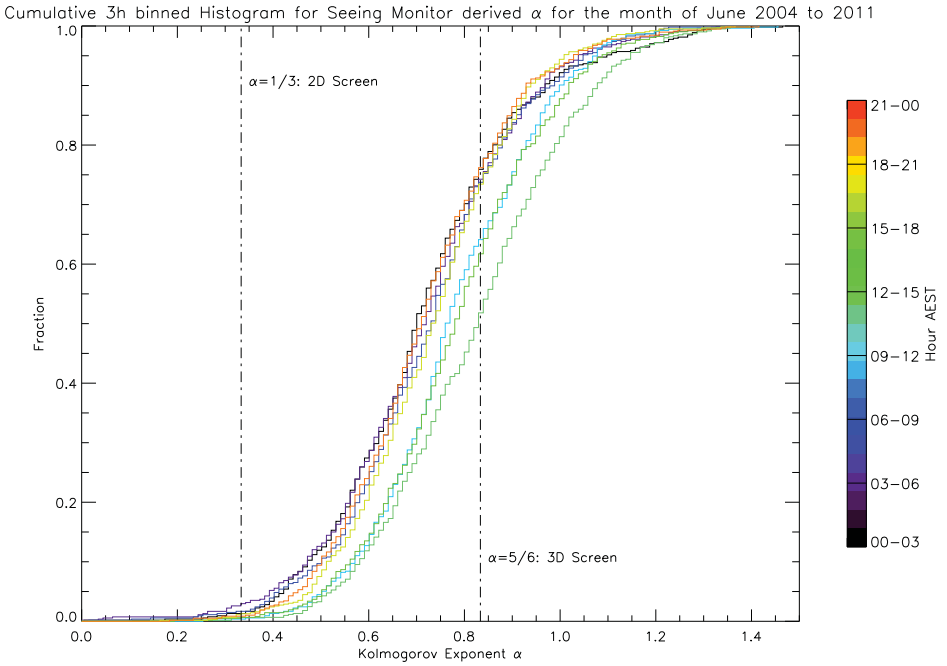

Figure 3.4.6: This cumulative histogram depicts the Kolmogorov exponents encountered as a function of time for the month of June only, from the seeing monitor instrument from 2004 until the end of July 2011. Note the time of day dependence with a preference towards a larger α during day time hours from 09:00 to 18:00 local time, which is compatible with an agitated troposphere caused by the Sun's thermal heating.

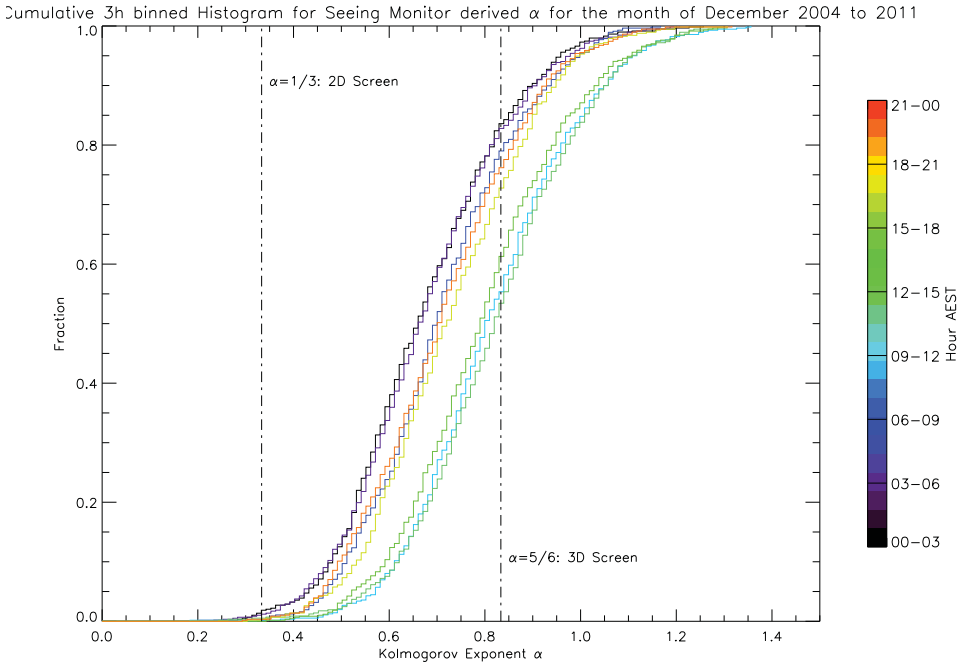

Figure 3.4.7: This cumulative histogram depicts the Kolmogorov exponents encountered as a function of time for the month of December only, from the seeing monitor instrument from 2004 until the end of July 2011. Note the time of day dependence with a preference towards a larger α during day time hours from 09:00 to 18:00 local time, which is compatible with an agitated troposphere caused by the Sun's thermal heating.

is the limitation it imposes on the ability of the telescope to spatially resolve structure. Analogous to the seeing limitations caused by thermal gradients in the optical regime, in the radio regime the water vapour induced phase delays cause a positional variation in the source observed because interferometric phase corresponds to the measurement of a point source [46]. Using equations for the root phase structure function 3.3.7 and equation 3.3.8 for the coherence, we can express the visibility amplitude as a function of baseline length:

$$\langle V \rangle = V_0 \times e^{-(\frac{K' b^\alpha}{\lambda\sqrt{2}})^2} \tag{3.4.1}$$

with the exponent in radians and hence $K' = K\frac{\pi}{180}$. From this, we define the baseline length corresponding to the half power point (half power baseline, HPBL):

$$b_{1/2} = (1.2\frac{\lambda}{K'})^{1/\alpha} \tag{3.4.2}$$

in km, with λ in mm. For example on January 29 2011, the phase structure function parameters were determined in Figure 3.4.2. Using these values to determine K:

$$K = \frac{\Phi_{RMS}\lambda}{b^\alpha} \tag{3.4.3}$$

we obtain $K = 1775$ degrees. From this, $b_{1/2} = 0.181$km which in turn, assuming we were to observe in these conditions at 89 GHz ($\lambda = 3.3$mm), limits the seeing to:

$$\theta[\text{rad}] \approx \frac{\lambda}{b_{1/2}} \approx 3.8\text{”} \tag{3.4.4}$$

Also note that in this equation, λ and $b_{1/2}$ are in the same units. The full range of 2004 to 2011 has been plotted in Figure 3.4.8. The mean seeing for $\lambda = 3.3$mm is 0.9" with $\sigma = 1.0$". Further comparisons have been created between June and December, refer to Figures 3.4.9 and 3.4.10 as well as the hourly seeing breakdown and comparison between June and December in Figure 3.4.11. Also refer to the Table 3.4.1 of mean hourly seeing values. During the night, regardless of whether in winter or summer, the seeing is better by a factor of 2-3, and between the seasons it is evident that summer nights have better seeing than winter days by a factor

of 2.

The half power baseline (HPBL) we calculated from equation 3.4.2 and listed in table 3.4.2 to obtain baseline parameters provides a very interesting metric in itself. We can use the results to determine what length baselines can be used in the pertaining conditions. We have created an analysis for June and December and compared the two. It thus appears that in June, the mean HPBL from Figure 3.4.12 is 2470m, which indicates that the ATCA with its 3000m baseline usable for 3mm observations was well conceived. In December (Figure 3.4.13) conditions are, as expected, much worse and the HPBL is just 1545m. Finally in Figure 3.4.14 we can again compare the winter and summer months against each other.

The conclusion from the millimetre site analysis data is that comparing time of day between winter and summer, winter has better millimetre seeing than summer. However, night time conditions in summer frequently are better than daytime conditions in winter. The data also confirms that the available baselines are at the upper limit of what is useful at mm wavelengths without using water vapour radiometry to correct for the tropospheric phase delays. It is therefore in principle possible to schedule night time millimetre observing in summer much in the same way as daytime millimetre observing is scheduled in winter.

	Seeing θ ["]			
	June		*December*	
Time AEST [h]	$\overline{\theta}$	σ	$\overline{\theta}$	σ
0– 1	0.32	0.34	0.53	0.61
1– 2	0.33	0.36	0.50	0.55
2– 3	0.32	0.34	0.48	0.52
3– 4	0.33	0.37	0.49	0.56
4– 5	0.34	0.37	0.52	0.65
5– 6	0.35	0.45	0.59	0.66
6– 7	0.35	0.45	0.80	0.83
7– 8	0.36	0.45	1.18	1.02
8– 9	0.44	0.43	1.68	1.39
9–10	0.65	0.63	2.13	1.59
10–11	0.91	0.79	2.48	1.76
11–12	1.12	0.91	2.56	1.80
12–13	1.19	0.96	2.53	1.78
13–14	1.10	0.90	2.27	1.65
14–15	0.90	0.80	2.04	1.52
15–16	0.65	0.59	1.69	1.37
16–17	0.49	0.50	1.36	1.24
17–18	0.42	0.42	1.03	1.04
18–19	0.38	0.40	0.78	0.85
19–20	0.38	0.40	0.69	0.80
20–21	0.36	0.34	0.64	0.78
21–22	0.34	0.33	0.64	0.77
22–23	0.33	0.32	0.66	0.83
23–24	0.31	0.29	0.65	0.67

Table 3.4.1: The hourly seeing in arcsec at λ=3.3 mm. Refer to Figure 3.4.11 for a graphical representation.

	Half Power Baseline (HPBL) [m]			
	June		*December*	
Time AEST [h]	$\overline{HPBL}$	σ	$\overline{HPBL}$	σ
0– 1	3137	2279	2365	2082
1– 2	3065	2221	2411	2041
2– 3	3046	2228	2445	2035
3– 4	3050	2213	2430	2042
4– 5	3080	2310	2510	2160
5– 6	3055	2318	2224	2001
6– 7	3082	2432	1777	1768
7– 8	2943	2271	1151	1174
8– 9	2559	2054	793	869
9–10	1902	1652	592	732
10–11	1387	1324	502	647
11–12	1068	1064	491	708
12–13	1023	1121	506	714
13–14	1150	1290	562	747
14–15	1443	1423	629	794
15–16	1786	1471	806	983
16–17	2268	1753	1058	1245
17–18	2593	1932	1443	1560
18–19	2848	2091	1830	1868
19–20	2861	2092	2061	1973
20–21	2895	2129	2125	1987
21–22	2934	2159	2051	1850
22–23	2920	2149	2030	1829
23–24	2963	2153	1968	1747

Table 3.4.2: The hourly half power baseline in metres for λ=3.3 mm. Refer to Figure 3.4.14 for a graphical representation.

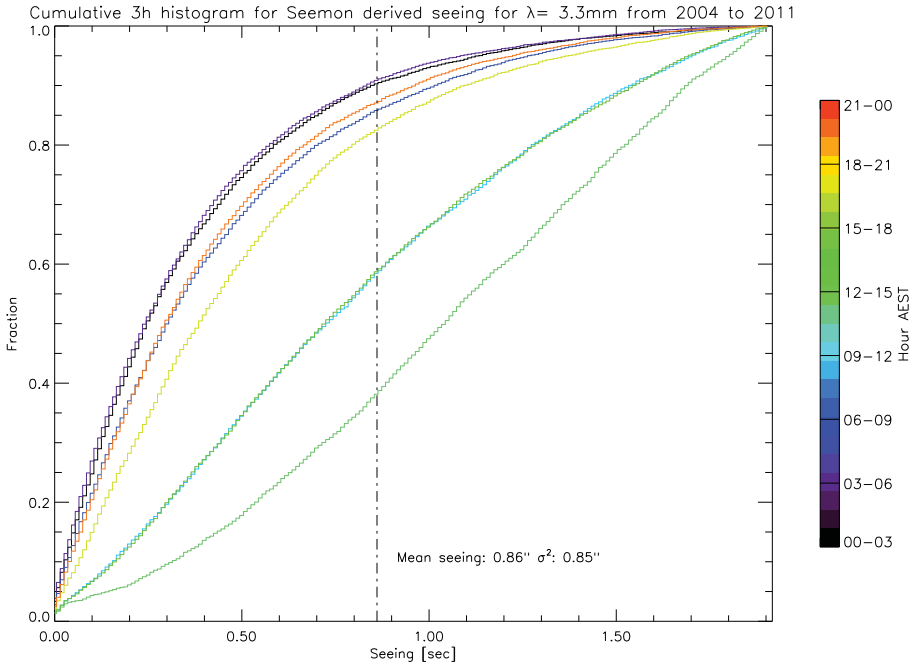

Figure 3.4.8: The cumulative distribution of the seeing measured for the full period from mid 2004 to mid 2011. The seeing is determined for an observing wavelength of 3.3mm (90 GHz) over the period of mid 2004 to mid 2011. The mean seeing was 0.9" with a standard deviation of 1.0". The data has been sigma clipped at a level of 5σ prior to generating the statistics. This however only removed 0.77% of all data.

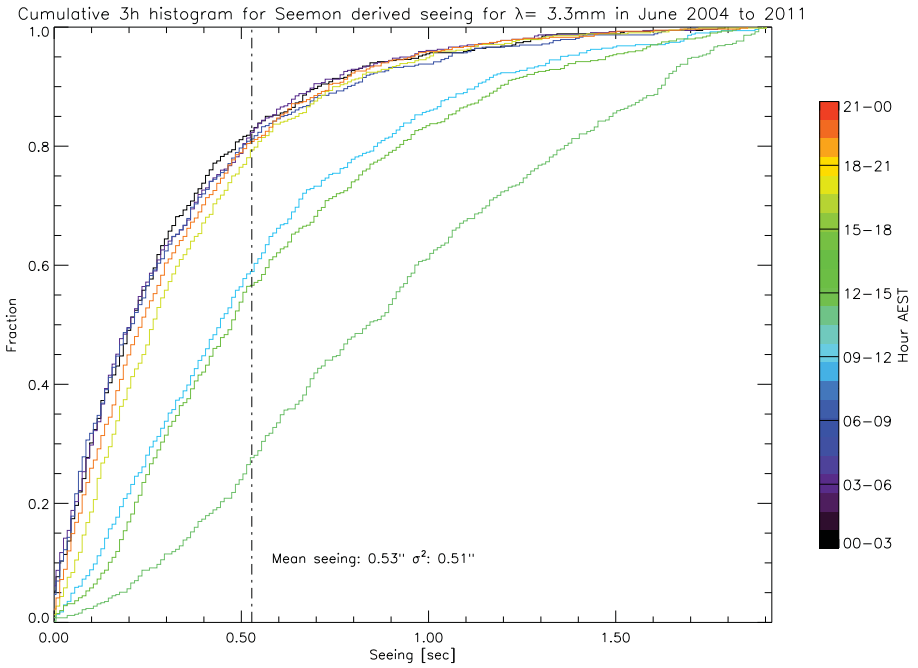

Figure 3.4.9: The cumulative distribution of the seeing measured for the month of June provides a statistical mean of 0.5". During the night time, this is true 80% of the time, whereas during daytime it frequently gets worse than that and the 80% seeing is only better than 1.4".

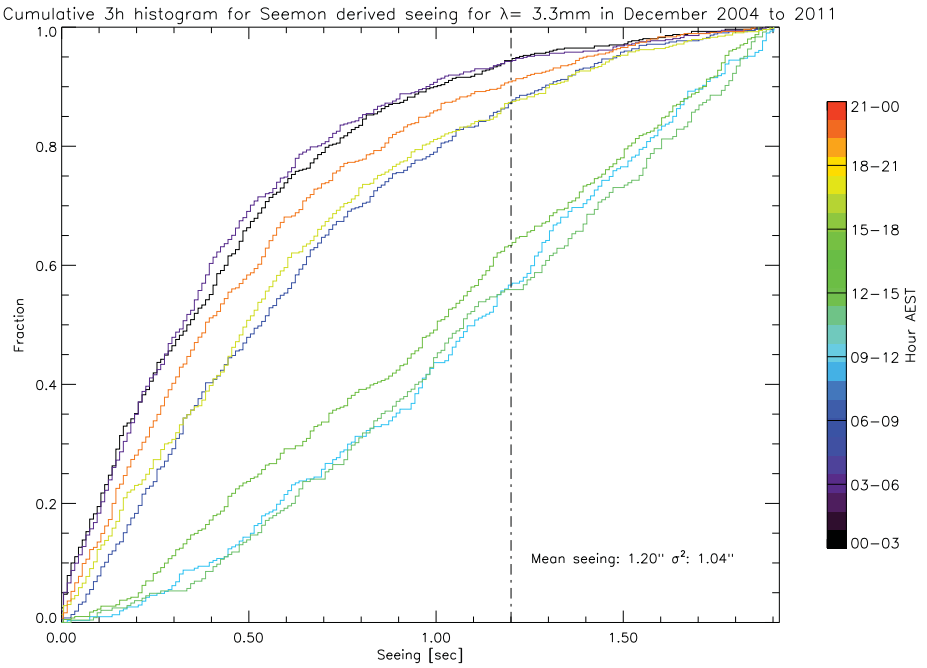

Figure 3.4.10: The cumulative distribution of the seeing measured for the month of December, the mean seeing is 1.2", which during night time is achieved 80% of the time. During daytime, this is true in 60% of the time.

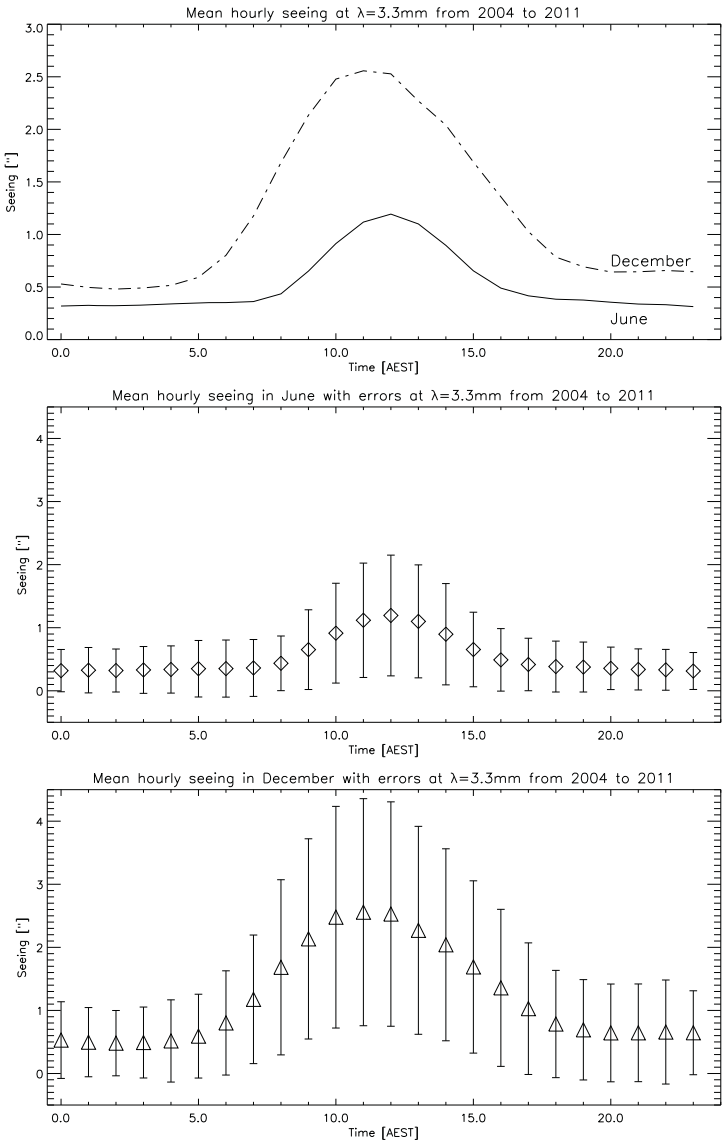

Figure 3.4.11: Shown are the comparison of seeing conditions between June and December on an hourly basis. The top plot shows June and December data on the same scale for comparison. The middle plot shows the same data as the June line (solid) in the top plot but with error bars. The bottom plot shows the same data as the December line (dashed) in the top plot. Note that the adjacent data points are not completely independent of each other, because they are part of a time series. The errors show the standard deviation for a given time over the entire data set, but these values are correlated between adjacent data points. The peak (worst) seeing in December is preceding the June peak by an hour in the top plot.

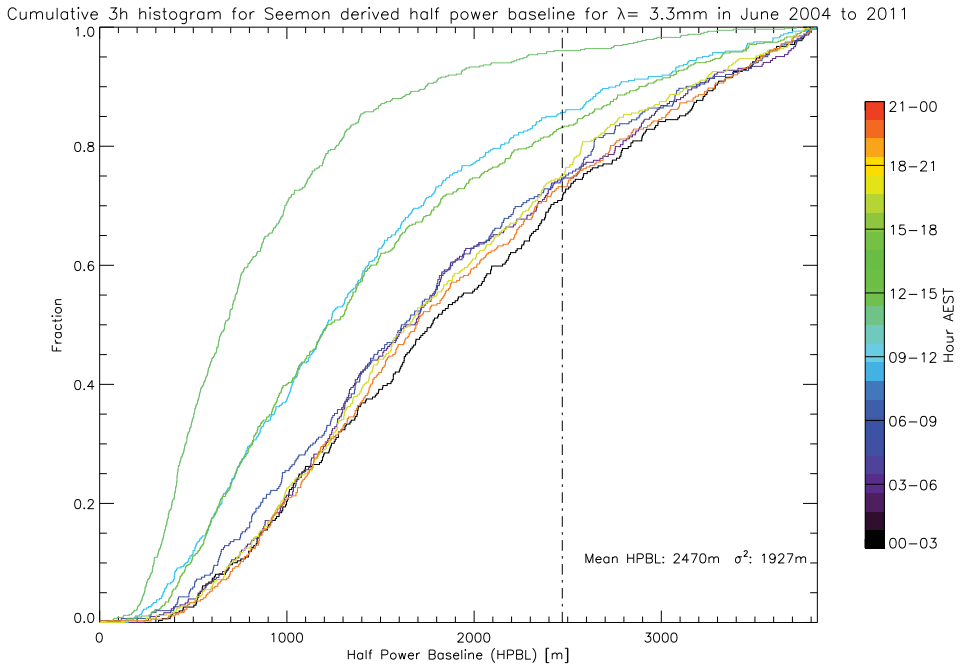

Figure 3.4.12: The half power baseline in June. From this we conclude that it is possible to observe on baselines of 2000m or more about 50% of the time during night time.

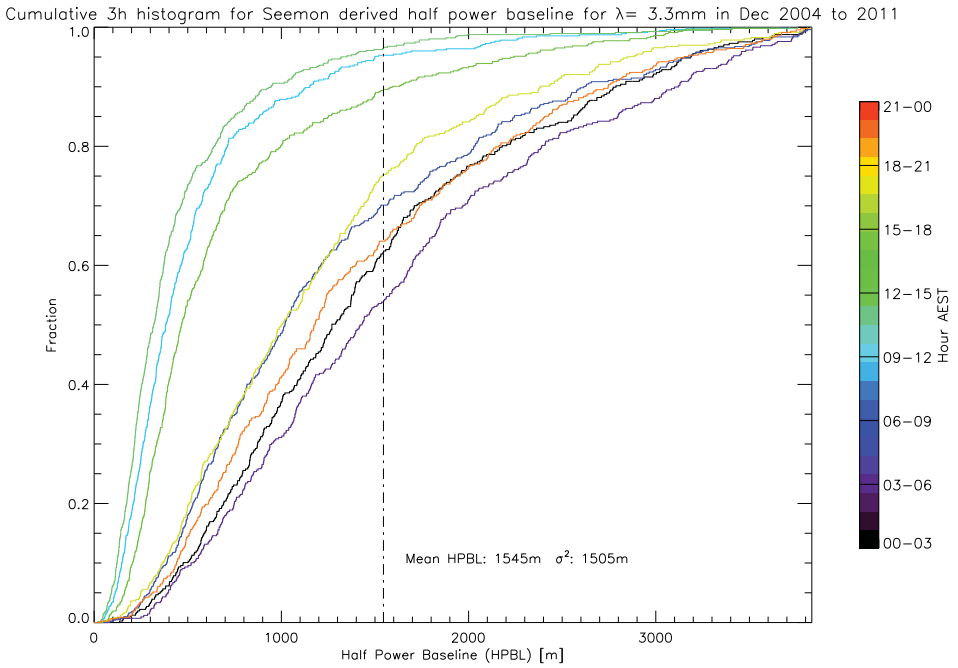

Figure 3.4.13: The half power baseline in December is substantially worse than in June: The median value is 1545m.

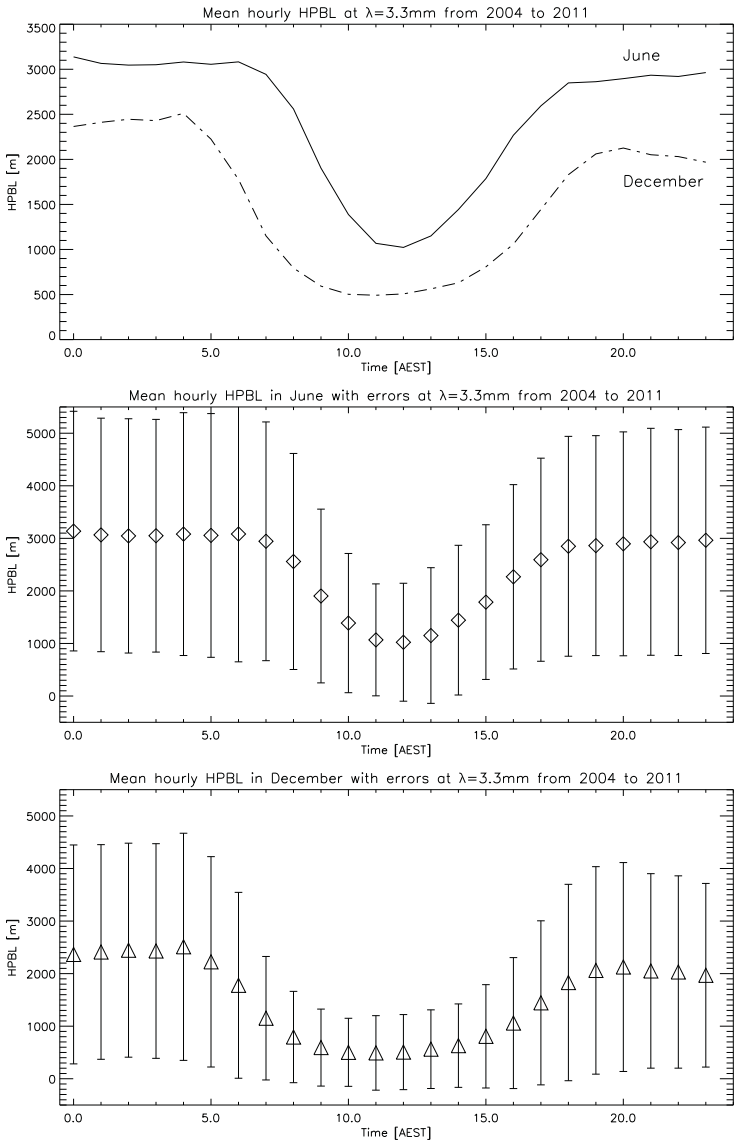

Figure 3.4.14: Shown are the comparison of the half power baselines (HPBL) between June and December on an hourly basis. The top plot shows June and December data on the same scale for comparison. The middle plot shows the same data as the June line (solid) in the top plot but with error bars. The bottom plot shows the same data as the December line (dashed) in the top plot. Note that the adjacent data points are not completely independent of each other, because they are part of a time series. The errors show the standard deviation for a given time over the entire data set, but these values are correlated between adjacent data points. The peak (worst) HPBL in December is preceding the June peak by about two hours in the top plot.

Chapter 4

RFI Survey

4.1 Planning of the filter frequencies

Radio frequency interference (or short: RFI) occurs when electronic components emit radiation either accidentally or purposefully which are in a frequency band that affects receiver systems in such a way that erroneous readings may occur. When building a system like the Water Vapour Radiometers, where the frequencies used to determine water vapour are fixed and there is no tuneable receiver involved, measures need to be undertaken to make sure that the frequencies we select for the filters are free from such RFI. Hence, concurrently with the filter optimisation procedure, a search in the Australian Communications and Media Authority (ACMA) [12] as well ITU frequency allocation databases [31] was conducted. This served two purposes:

1. To ascertain that the filter frequencies chosen profit from at least some protection from harmful radio frequency interference in the future

2. To prevent us from putting the band passes for the optimised filter frequencies near already allocated bands that are likely to cause interference.

The result of this search was combined with several options for the optimised filter frequencies and bandpasses and is shown in Figure 4.1.1 along with a list of excerpts shown in the ACMA database. In ascending

order, the filters chosen, their location in respect to the ITU spectrum allocation as well as any existing RFI sources from the ACMA database are listed here:

Filter 1 is centred at 16.5 GHz and has a bandwidth of about 0.850 GHz. This is halfway in a reserved band for Radio Location (i.e. radar) and deep space communication ES (earth to space). There are a number of Defence owned transmitters listed near that frequency band.

Filter 2 is centred on 18.9 GHz with a bandwidth of 0.9 GHz. This corresponds to a rather busy segment of ES (earth space), SE (space earth) as well as terrestrial data links. The latter appears to be no problem, the nearest datalink is 150km away and has a nominal power of 50mW. The satellite links however are ubiquitous throughout that frequency range: IPSTAR provides broadband data services between 18.25 – 19.7 GHz as do a number of other satellites. It is conceivable, that at some point WVR measurements might be affected in that filter band when observing within a close range to any of those communication satellites.

Filter 3 is centred on 22.9 GHz with a bandwidth of 1 GHz. There are a number of low power communication links according to the ACMA database, however, we could not find any that were located close to the telescope site. The lower part of that filter spectrum is inside a band reserved for Radio Astronomy while the upper part is inside the inter-satellite communications band, also a potential problem depending on slant angles.

Filter 4 is centred on 25.5 GHz and has a bandwidth of 1 GHz also. Earth-Space, Space-Earth as well as inter satellite communications are allowed in this band, again making this potentially vulnerable to satellite induced RFI.

Clearly, before being able to make a definitive choice of filter frequencies, an RFI survey needed to be executed.

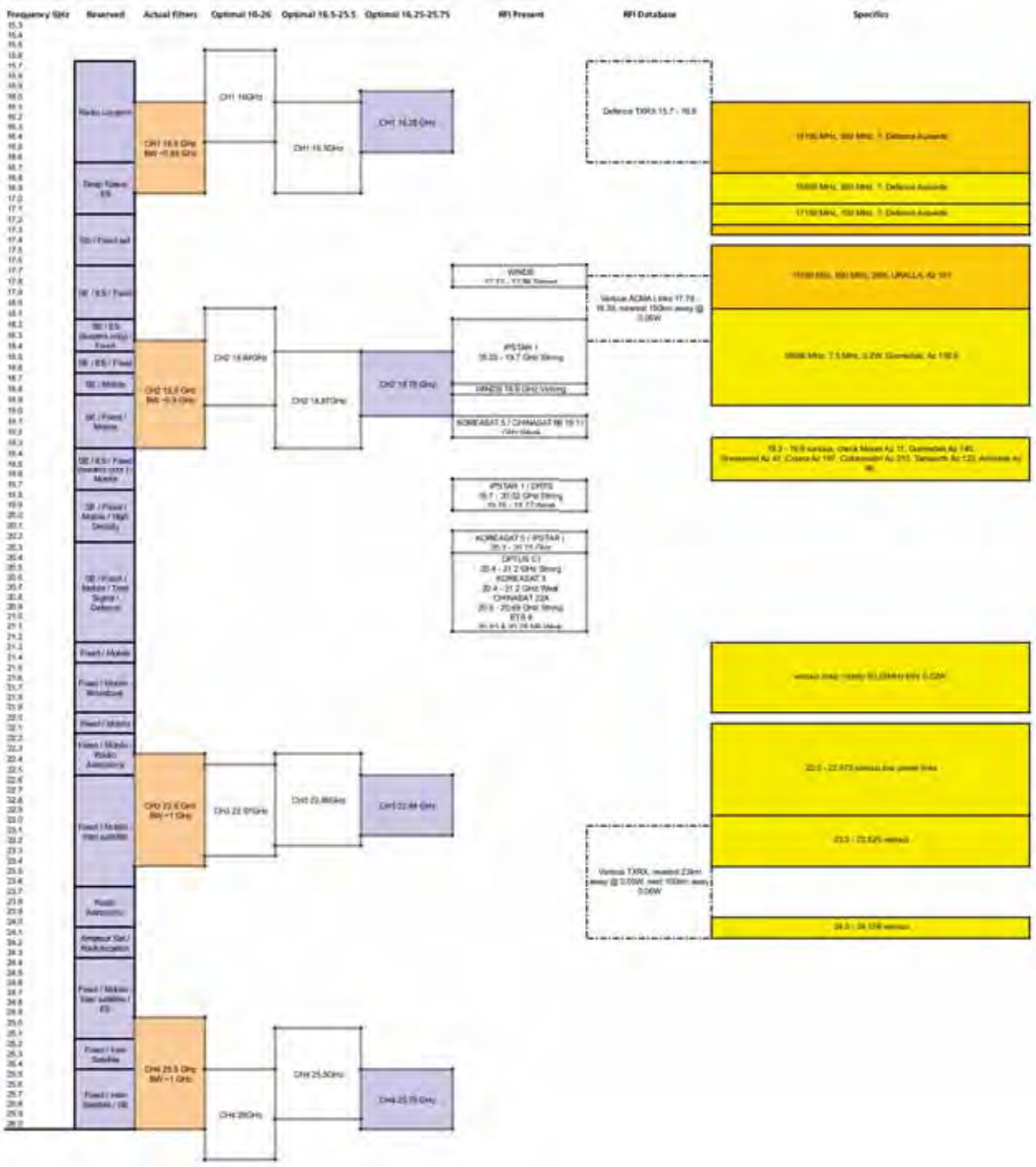

Figure 4.1.1: Listing of all radio spectrum users and allocations. Depicted also are the filters we chose "Actual Filters" as well as three alternative filter optimisation results based on different filter centre frequencies and filter bandwidths, the lower and upper limits as per the title, known RFI emitters, RFI database hits and ACMA database information. See also chapter 5.3 for details on the filter optimisation procedure.

4.2 Known RFI in the sky

Harmful interference in our context refers to interference that would prevent the WVRs from operating correctly, not necessarily destroy them. The number of active transmitters in the sky such as synthetic aperture radar (SAR) satellite missions has increased manyfold in the recent past, posing an increasing problem to the Radio Astronomy community. This is not only because they often cause interference near frequencies of astronomical interest. New to this scenario are transmitters powerful enough to cause physical damage to the receiver systems. The Cloudsat satellite for example already transmits enough power that if it were to be radiating directly inside the high gain lobe of an antenna at ATCA (or Mopra) with a 3mm receiver on axis, enough power would be produced by the low noise amplifiers in the astronomical receivers so as to permanently damage them and burn the MMICs.

While it is possible to calculate threat scenarios for the Cloudsat satellite (such a system has been developed by the author in 2008 and has been in use since then to protect the ATCA as well as Mopra telescopes, see [28] and [27]), the new generation of SAR satellites as well as numerous classified military transmitters have unknown directional emission characteristics, i.e. they radiate at slant angles from their orbital planes that are either unknown or not predictable and often are orbiting in constellations of 2 satellites or more, hence making it impossible to protect the high gain lobes from matching their emission. This has already been observed at 1.6 GHz and 2.5 GHz where the Globalstar and Iridium communications satellite network have traditionally been causing RFI. Another unknown is inter-satellite communication which occurs at slant angles and thus has difficult to predict radiation patterns. While the Globalstar and Iridium constellations have been identified as causal due to the frequencies used, one particular satellite or even orbital plane cannot be blamed because of their omnidirectional emission characteristics, they can be radiating into one of the many side lobes of the ATCA antennas. Other RFI observed includes the weather radars at Moree at 5.625 GHz (old ranging radar, ~120km to the north) and Gunnedah at 2.88 GHz (new doppler weather radar, at a similar distance to the south east).

There are many more mobile emitters from about 5 to 13 GHz, most of which have been impacting ATCA at one point or another, such as airborne weather radar systems (present in every Airliner, they transmit in the 8 – 9.5 GHz range, see e.g. [25]), and also a number of military sources, only some of which are public knowledge.

Fortunately, the 15mm band from 16 – 26 GHz is not very popular with these types of missions. The only known RFI that can impact water vapour determination are the geosynchronous satellites emitting in Ka band from 18 – 21.2 GHz as well as a few terrestrial data links. The WVR system in use at the Plateau de Bure Interferometer in France has encountered this problem already and has a few years worth of data to determine that phase correction is disturbed by "orbital RFI" only for 0.5% of the time as documented in [7]. This of course is a function of the position of the observing targets. In the case of the ATCA, this will only be a problem for observations executed through northerly positions as illustrated in Figure 4.2.1. Geosynchronous satellites can of course become a problem when they have used up their manoeuvring fuel as illustrated in the Earth view (Figure 4.2.2), they then can depart the rather narrow strip of geosynchronous satellites and enter the field of view elsewhere with potentially disruptive radio emission. The author developed a commercial software ("SatWhere", released in 2005, see [29]) which was used to depict the orbital positions of these satellites. One of this software's pioneering features was the object oriented implementation of the SGP4/SDP4 orbital models entirely written in C++. The SGP4 (Simplified General Perturbations) model is used for low earth orbit satellites with orbital periods of generally less than 225 minutes, while the SDP4 (Simplified Deep Space Perturbations) model is used for those with larger orbital periods, details about the algorithms have been published in the Spacetrack Report No. 3, found in [26]. The SGP4/SDP4 models are now superseded by the SGP8/SDP8 models, which provide much better approximations for orbital decay calculations. All these models use the classical TLE (two line element) format to describe the satellite orbital parameters. These elements used to be obtainable by anonymous download from NORAD's SpaceTrack website [44]. With the increased security awareness after the

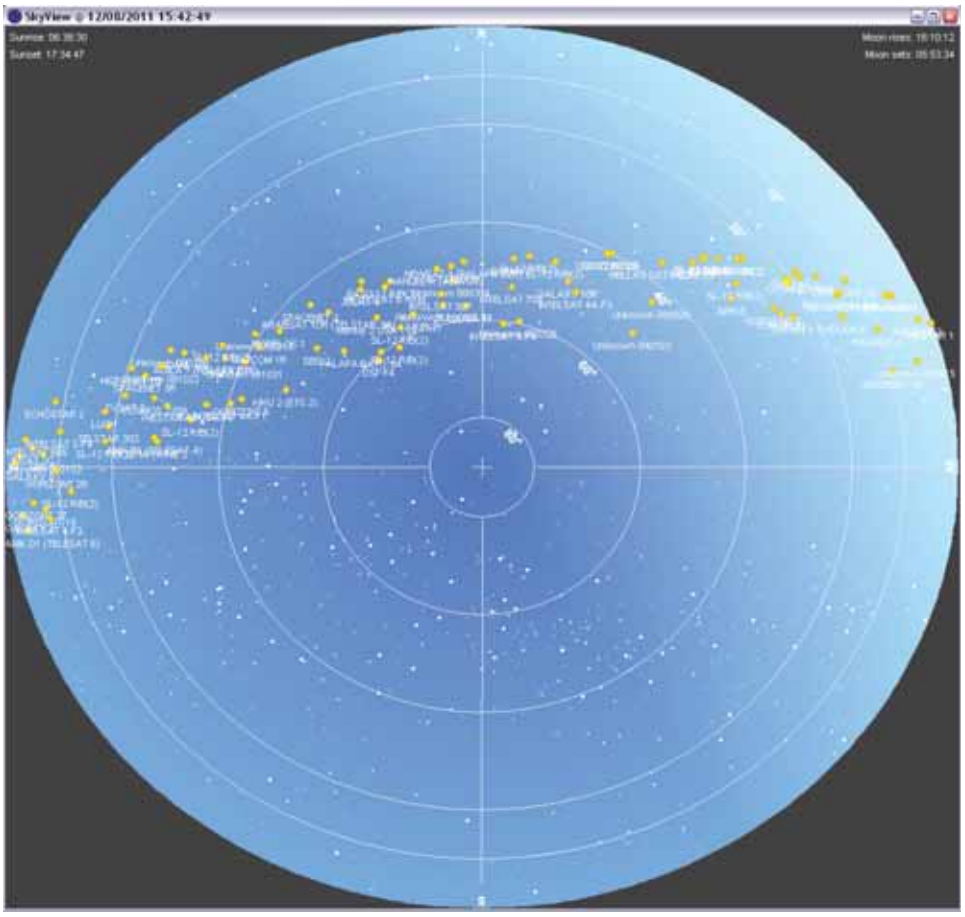

Figure 4.2.1: This is the location of known geosynchronous satellites as seen from the ATCA site. Each yellow dot represents a geosynchronous satellite (although not necessarily a functioning/live one). This serves to illustrate the zone of potential RFI problems with the water vapour radiometers. Screenshot taken from SatWhere, a commercial windows software the author wrote in 2005 [29].

events of 11 September 2001, access has been restricted to registered users who need to demonstrate a need for that data.

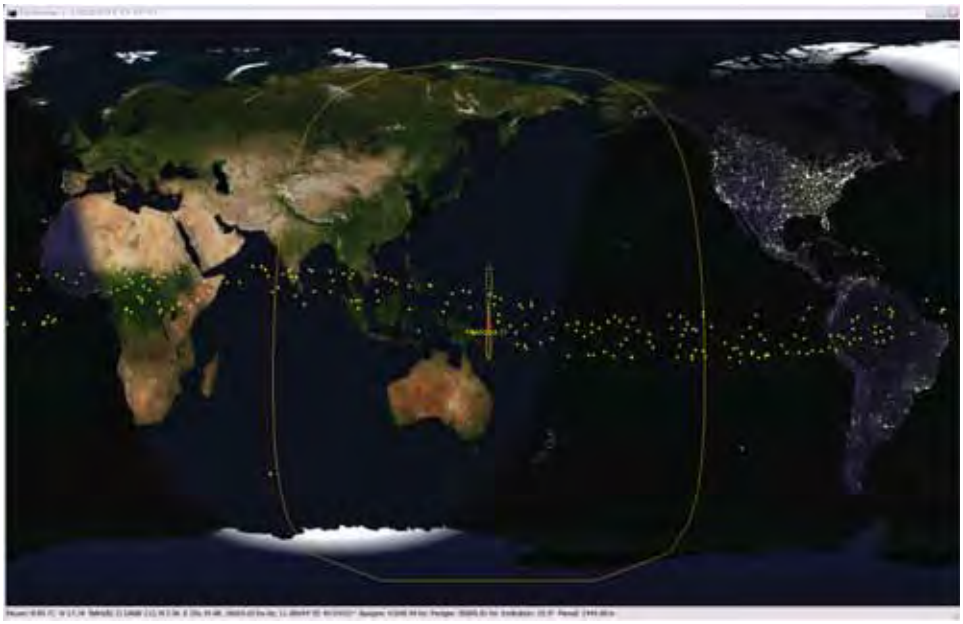

Figure 4.2.2: View of the Earth. Each yellow dot represents a geosynchronous satellite (although not necessarily a functioning/live one). The highlighted satellite is Raduga 12, a Russian communications satellite launched in 1985 and now adrift. The dotted line shows its ground track over a 24 hour period. The yellow line shows the radio horizon of that satellite. Screenshot taken from SatWhere, a commercial windows software the author wrote in 2005 [29].

4.3 RFI scans

Having checked all tentative RFI sources in the ITU frequency allocation and the ACMA databases, direct measurements using the ATCA receiver systems were made. This occurred just at the time when the first CABB (Compact Array Broadband Backend, [65]) upgrades were being installed, so we had the opportunity to check for RFI both with the old receivers and correlator as well as with CABB. This would not only help in showing any other existing external RFI we may not be aware of yet, but also highlight any self generated RFI from inside the vertex room, any parts of the receiver system or even from any of the other antennas. Because the ATCA is already equipped with a receiver system for the 15mm band capable of scanning the full 16 – 26 GHz frequency band, no additional equipment was required.

The method for executing the RFI scan then is relatively simple: Two adjoining antennas are pointing vertically but each offset by 5 degrees from zenith so as not to observe the same area in the sky and to prevent any real sky signal from correlating. The receiver system then steps through the frequency range in 4 GHz intervals (2 GHz IF per receiver) and the correlator then tries to correlate any signal incoming from each pair of receivers. Each frequency is integrated for one minute and the data subsequently analysed. As can be seen in plot 4.3.1, there is only receiver noise present in this frequency range. We have not been able to identify any self generated RFI throughout the entire 15mm band that would be of a potentially disruptive level to the WVRs. The noise level peaks at a flux level of about 80 mJy, well below a level that has any measurable influence on the powers measured over 1 GHz in each of the WVR filter bands.

In January 2009, before the full spectrum scan was undertaken, the old receiver system was used to scan several regions of interest: The satellite uplink station at Uralla is listed in the ACMA database as having a rather strong transceiver, operating at 17.55 GHz with 2kW of power and 0.5 GHz wide. This certainly warranted examination. In Figure 4.3.2, we can see two spikes that at first glance look like they might be caused by interference. However, detailed study of the data revealed that these jumps oc-

cur exactly on 0.128 GHz boundaries of the old receiver bandwidths and are thus artefacts. Figure 4.3.3 shows a scan of the region in the sky where the Thuraya communications satellite is present. While no known downlinks exist on that satellite for the 15mm band, the data uplink is at 21 GHz. This was a test to see whether we might be able to glimpse any radiation bouncing off the satellite. Perhaps surprisingly, given how sensitive the receivers are, we did not detect anything in the expected frequency range. This is assuming that the uplink to the satellite was active at the time, a reasonable assumption given Thuraya is a communication and broadcast satellite which permanently disseminates data. As a last plot, look at Figure 4.3.4 showing the zoomed in spectrum of the Optus C1 satellite, which has known downlinks in the 15mm band. Clearly visible at 20.45 GHz is one of the downlinks. Note the arrows at the top of the graph: They depict each frequency which has a known transmitter. It appears as if those transmitters were not on at the time of our observations, aside from this one exception at 20.45 GHz.

The full band RFI scan was executed using the old ATCA correlator replaced by CABB in 2008. It was used in a 0.128 GHz configuration which does not allow for autocorrelation spectra to be obtained. By pointing the antennae in azimuth / elevation coordinates and each at 5 degrees offset from zenith in opposing directions (so as not to scan the same area in the sky), fringe rotation is automatically inhibited, ensuring that any signal which is stationary in respect to the receivers is not confused.

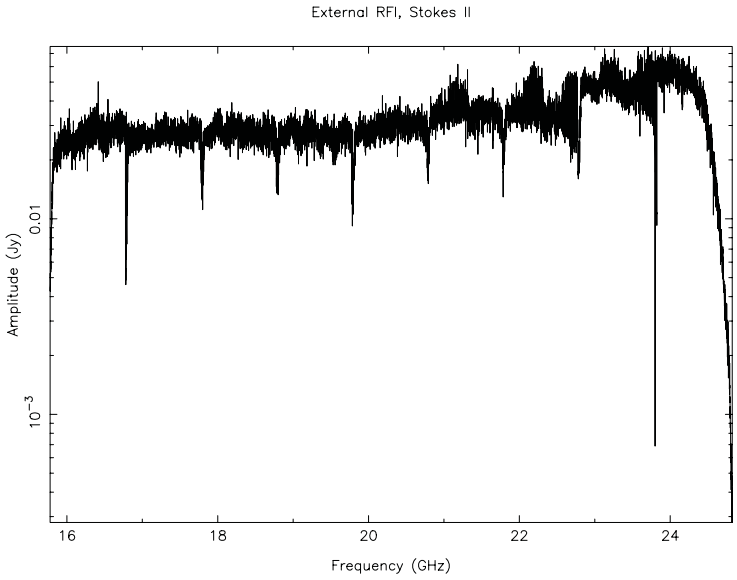

Figure 4.3.1: 15mm RFI spectrum measured in 2009 using the then new CABB backend. From 16 GHz to 26 GHz, there is just receiver noise with the occasional CABB induced birdie. The noise level peaks at flux of about 80mJy. This is a signal level far below anything that could impact the radiometers.

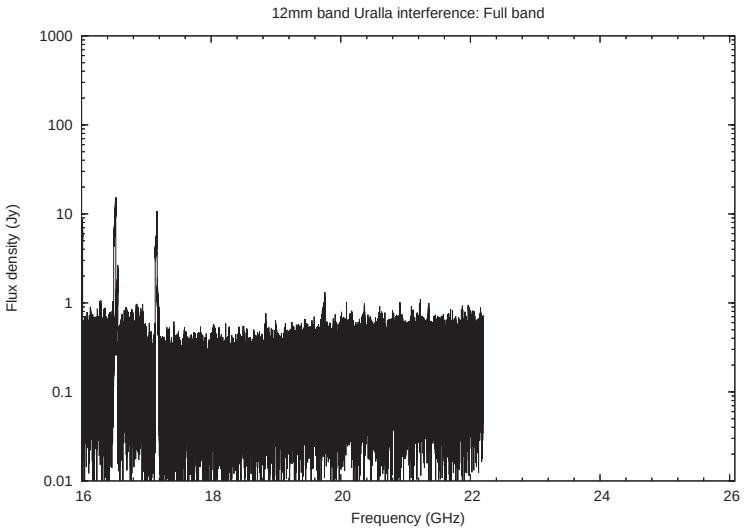

Figure 4.3.2: 15mm RFI spectrum measured in January 2009. Apart from two spikes caused by the old correlators' 0.128 GHz bandpass, no interference is present.

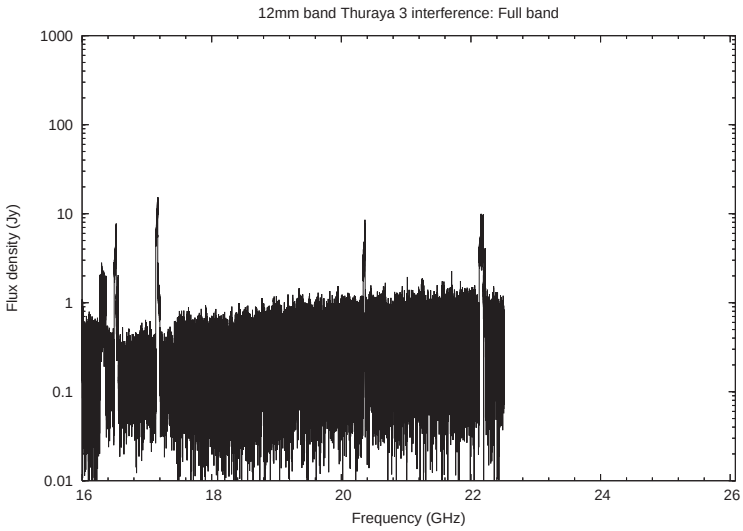

Figure 4.3.3: 15mm RFI spectrum measured in January 2009. A number of correlator bandpass spikes are visible. The communications satellite Thuraya has no known downlink frequencies that should be visible, however, the satellite uplink frequency is at 21 GHz and this was to determine whether we might see a reflection of that signal. No such signal is seen here.

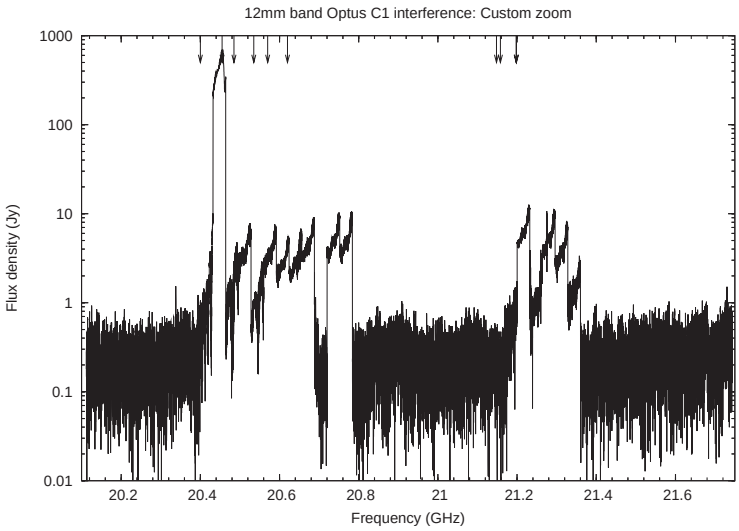

Figure 4.3.4: 15mm RFI spectrum measured in January 2009. Note that this spectrum is zoomed in as opposed to the previous spectra. Again we see several bandpass induced increases in noise level. However, there also is a real interference signal present at 20.45 GHz. This is a known downlink frequency. Note the arrows at the top of the plot, they denote frequency locations of known transmitters on that satellite.

4.4 Conclusion

It is evident from the data gathered through this process that we may see radio frequency interference in bands that are used by our water vapour radiometers originating mainly from satellites. There is no internal RFI that is strong enough to cause radiometer readings that could disturb the water vapour measurement. There is also no terrestrial RFI present in any of the scans, however, the possibility must be entertained that in the future, airborne sources as well as land based transmitters could have an effect on the system.

Chapter 5

Water Vapour Radiometers

5.1 Design Specifications

In order to successfully measure the 22 GHz water line, a radiometer measuring a number of frequencies around that line to a suitable degree of precision is required. In this chapter we determine the design specifications for the WVRs.

The WVR project for ATCA first was initiated in 1998 with two prototype units constructed by Astrowave (Jonathan Crofts) in Melbourne. The specifications for those units were largely based on the triple radiometer design outlined in Bremer's paper [6]. This resulted in two units being built according to a four filter design specified by several instrument scientists at the Australia Telescope National Facility (ATNF). The people initially involved were George Graves, Bob Sault as well as Peter Hall and Graeme Carrad from the receiver lab group [14], [49]. The approach chosen for this instrument was a cost effective one. It is a simple add on to the existing millimetre package and it resides in the vertex room and thus does not require any extra mounting hardware or weather proofing. Its initial design also does not require any cryogenically cooled stages and so does not need a dewar or vacuum system. This makes it a low maintenance system. For the WVRs used here it was decided to stay as close to this original design as possible while improving on the prototype WVRs. The units were then built by Astrowave (Jonathan Crofts).

We will show in chapter 6.2.2 that in order to improve the correlation

efficiency ϵ to better than 0.5 at 95 GHz, we need to be able to determine temperature fluctuations in the water vapour emission profile of 12mK at 95 GHz, 28 mK at 40 GHz and 50 mK at 22 GHz. From this we can obtain the design criteria for the RF electronics by specifying the noise figure this relates to, as we discuss below.

5.2 Determining Noise Limits

The theoretical sensitivity of an ideal total-power radiometer with no gain fluctuations is [60]:

$$\Delta T = \frac{T_a + T_e}{\sqrt{\Delta f \tau}} \tag{5.2.1}$$

where ΔT is the minimum detectable change in the radiometric antenna temperature T_a, T_e is the noise temperature of the entire signal chain, τ is the integration time and Δf is the bandwidth of the system. Note the integration time and bandwidth are both in the divisor: this means that increasing integration time (or bandwidth) also increases sensitivity (by decreasing ΔT). This is illustrated in Figures 5.2.1 and 5.2.2 where a graphical representation of this formula is shown for a number T_a and T_e scenarios. We solve both for the sensitivity (5.2.1) as well as the minimum time required to reach our target sensitivity of 12 mK (5.2.2).

T_e, the total noise temperature, is calculated as a cascaded system taking each component's noise temperature contribution in the signal chain into account. This can be calculated by the Friis formula [34]:

$$T_e = T_{e_1} + \frac{T_{e_2}}{G_1} + \frac{T_{e_3}}{G_1 G_2} + \cdots + \frac{T_{e_N}}{G_1 G_2 \ldots G_N} \tag{5.2.2}$$

Or, more concisely:

$$T_e = T_{e_1} + \sum_{1}^{N} \frac{T_{e_{(N+1)}}}{\prod_1^N G_N} \tag{5.2.3}$$

where T_{e_1} is the noise temperature of the first stage, T_{e_N} and G_N are the noise temperature and the gain of the N$^{\text{th}}$ stage respectively.

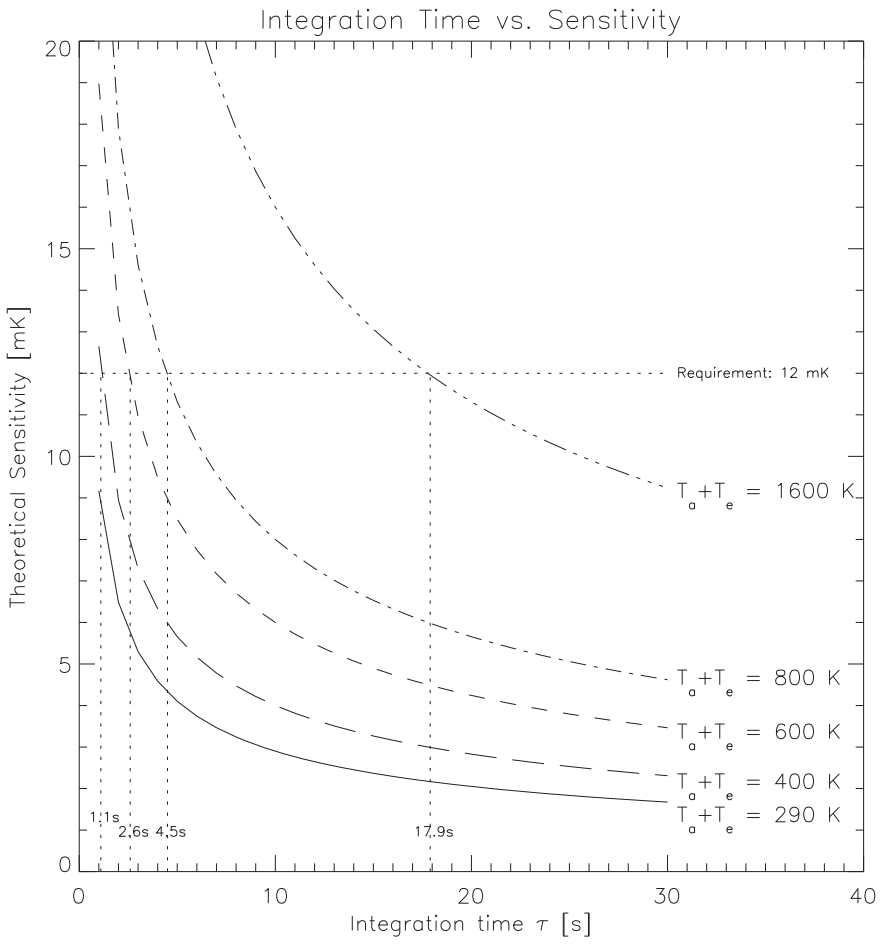

Figure 5.2.1: The theoretical sensitivity of a radiometer with 1 GHz bandwidth. This is a graphical representation of equation 5.2.1 for a range of assumed antenna and noise temperatures.

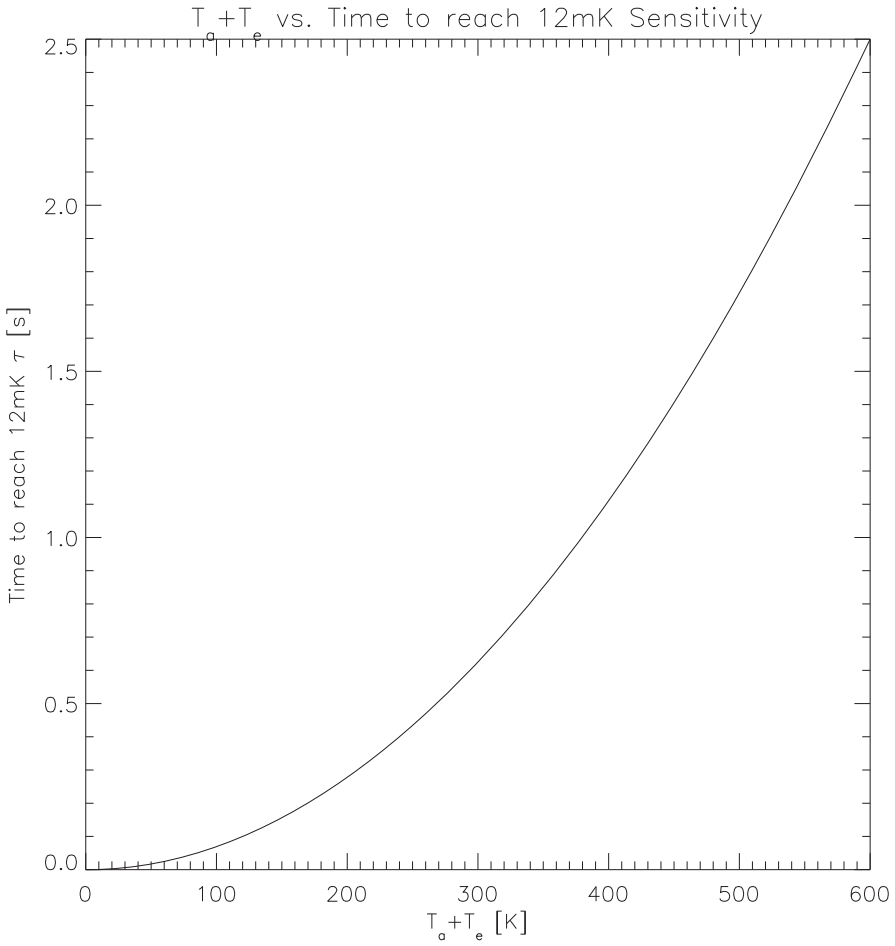

Figure 5.2.2: This Figure shows the integration time required to reach a sensitivity of 12 mK as a function of the $T_a + T_e$ terms.

To specify the noise limitation the fundamental equation determining a radio receiver noise floor is applicable. The power received in watts is determined by:

$$P = kT\Delta f \,[\mathrm{W}] \tag{5.2.4}$$

where k is the Boltzmann constant, T is the temperature in K and Δf is the bandwidth of the receiver in Hz. Note that in high frequency engineering, it is useful to express the power and noise ratios as referenced to 1 milliwatt (abbreviated as dBm). We hence convert P to mW for all calculations. Assuming 290 K for the temperature and 1 GHz of bandwidth, the minimum equivalent input noise of the water vapour radiometer is –83 dBm, this is also noted on the receiver diagram in Figure 5.4.11. We can then determine the noise floor:

$$\text{Noise floor} = -174\,\text{dBm} + \text{NF} + 10 \times \log_{10}(\Delta f)\,[\text{dBm}] \tag{5.2.5}$$

where NF is the noise figure of the system and –174 dBm corresponds to the input noise of 1 Hz of bandwidth at room temperature (290 K). Referring to the noise figures we measured in Table 5.4.1, we can fill in and determine the noise floor for each of the filters and list them in the same Table.

5.3 Optimisation Of The Filter Frequencies

In order to determine the best set of filter frequencies, a dataset containing the radiosonde measurements at Moree from 1 January 1985 to 2 September 1997 was obtained from the Bureau of Meteorology. This provides a good set of parameters to model the vertical troposphere profile and serves to estimate the typical tropospheric water vapour content at Moree which is the nearest site to ATCA that has daily radio sounding measurements taken. Moree's climate as well as geography is identical to ATCA's. For the calculation we assumed that we want to detect a 1 mm water vapour excess between two antennas located 1 km apart. We then iterate through each radiosonde dataset to extract the pressure, temperature and humidity data points and create a brightness temperature profile based on the Liebe atmosphere model [35] code used in the

Miriad software package from the lower to the upper frequency cutoff that corresponds to the radiosonde input parameters. This yields the 22.2 GHz water vapour line shape as it would be present for that given troposphere. We then add 1 mm of water vapour and calculate the line profile again and store the difference (the "excess") temperature. The excess profiles can then be plotted (see Figure 5.3.1) and a least squares fit over the excess profiles with four unknowns is solved. This process yields for every filter combination a sample variance ξ^2. This is used as the metric for the goodness of the fit:

$$\xi^2 = \frac{1}{N}\sum_{i=0}^{N}(\mathcal{T}_i - \overline{T_i})^2 \tag{5.3.1}$$

where $\mathcal{T}_i$ is the "observed" temperature excess, i.e. the value obtained by feeding radio sonde data into the line model. $\overline{T_i}$ is the temperature excess produced by the fit when iterating towards a solution as seen in Figure 5.3.2. N is the number of radiosonde samples, which turned out to be in excess of 3000 samples, counting all weekday soundings in the 12 year span available and discounting about 3 % of the data due to rain. We have adapted a code written originally by Robert Sault for this purpose.

The filter optimisation routine was run with several different parameter sets for lower and upper frequency cut off as well as filter bandwidth. In Figure 4.1.1 these other frequencies and bandwidths that were considered are listed. Ultimately, the filter frequency range from 16.5 GHz to 25.5 GHz was decided on because there is no readily available method to verify freedom from interference below 16 GHz and above 26 GHz than to look for RFI with the ATCA science receivers. The science receivers in turn cannot be tuned to lower or higher frequencies than 16 GHz and 26 GHz respectively. The bandwidth was chosen as a compromise between sensitivity and freedom from both current and potential future interference. 0.5 GHz of bandwidth would have provided the best separation from potential RFI, however, 1 GHz bandwidth gives the best sensitivity when integrating over time as can be seen from equation 5.2.1.

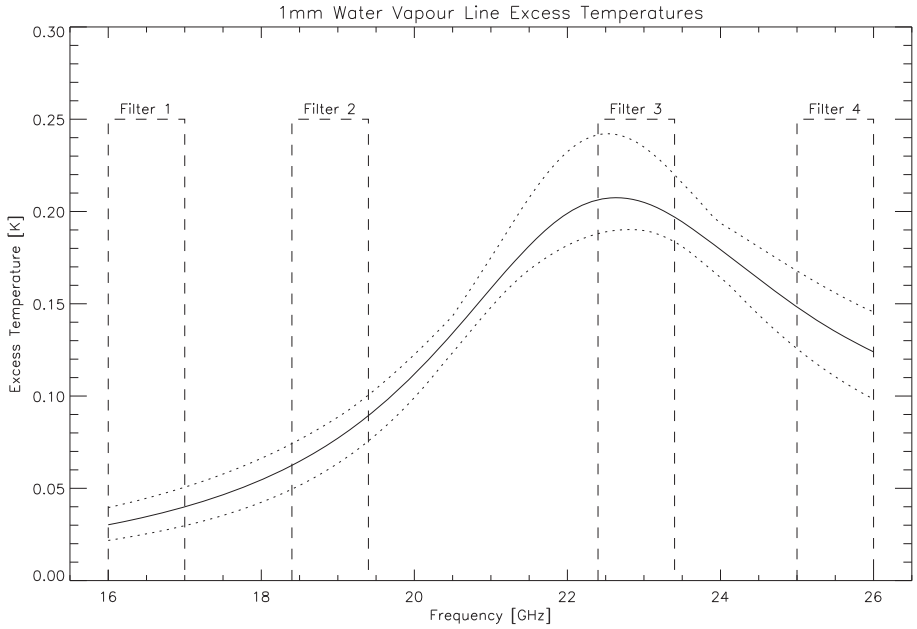

Figure 5.3.1: The combined water vapour line excess profiles derived from Moree radiosonde data. The data spans from January 1 1985 to September 2 1997 and the filter locations are the optimised filter frequencies listed in Table 5.3.1. The dotted lines represent the maximum and minimum values encountered over the 12 years of data while the solid line represents the mean temperature excess for 1 mm of water vapour.

Filter	F1	F2	F3	F4
Frequency [GHz]	16.50	18.87	22.88	25.50

Table 5.3.1: The optimal filter frequencies as determined by the least squares minimisation routine.

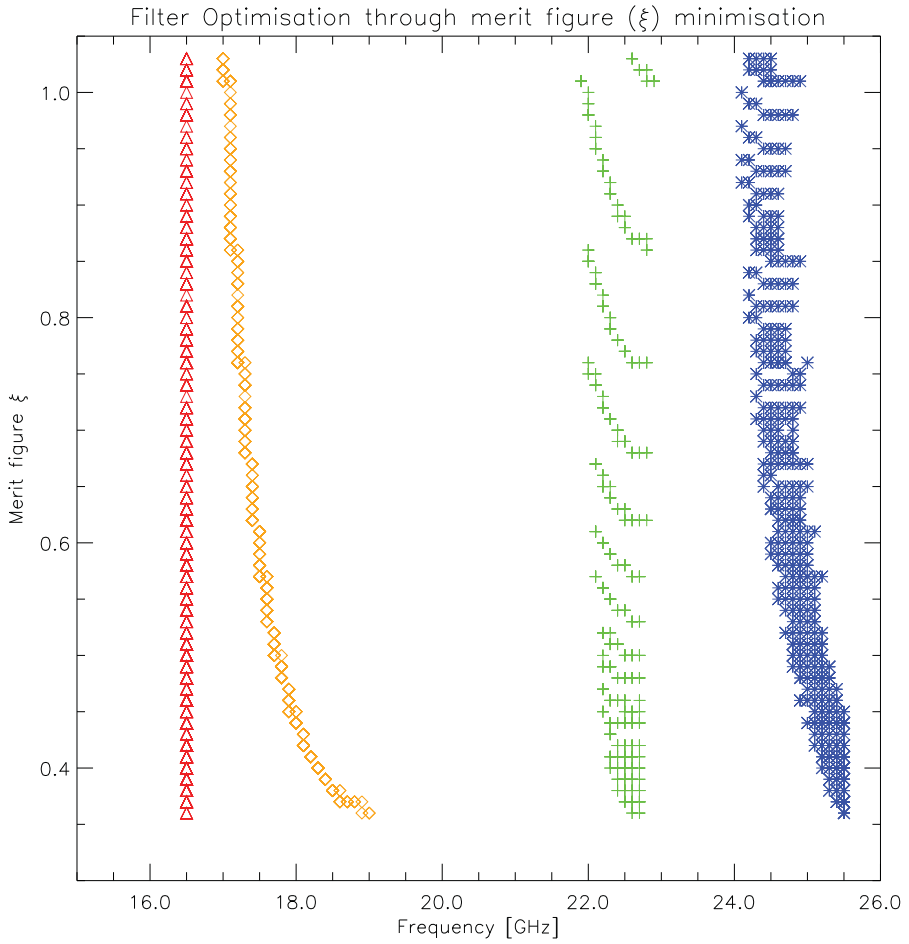

Figure 5.3.2: The filter optimisation process illustrated: Through a least squares fit, the merit figure ξ is minimised and the filter locations are determined. Refer to Table 5.3.1 for the exact filter frequencies obtained through this method. ξ is obtained from equation 5.3.1. The process is started at the top and the three variable filters are moved by the predetermined frequency increment (0.1 GHz in this case). The solution would have converged to an even lower merit figure ξ if the upper cut off was a higher frequency than 25.5 GHz.

5.4 Hardware

The uncooled radiometers are designed to reside inside the vertex room, attached to the millimetre receiver system mounting cage, also referred to as the "millimetre package". The WVR feed horn is situated in such a way that regardless of which mm receiver is on axis, the WVR feed is offset by no more than 12 cm from the axis. This arrangement results in the beams being separated by about 5.8 m at 2 km altitude, below which the majority of PWV induced phase delays originate. For the ATCA antennae with a 22 m diameter, the beams thus overlap by a substantial fraction of >73 %. Refer to Figure 5 in [13] for details on the geometry of the antenna reflector surfaces as well as the size of the focal plane. This means the beams are matched well and sample the same lowest 2 km of the troposphere where most of the water vapour is located.

From the Friis formula (5.2.2) we see that the first stage of the amplifiers is the most important stage where the noise needs to be kept lowest. Any subsequent components add a much lower contribution to the system noise. This is why a LNA (Low Noise Amplifier) is used for the first stage. They have a noise figure of 1.8 to 2.2 dB at room temperature [14]. This is additionally degraded by the feed horn, waveguide and coaxial feed which all contribute their own parts to the total noise. During the design stage, this combined noise was estimated to be around 4 dB at the horn face. Initial measurements when the WVRs were being built at Astrowave in Melbourne have shown the noise figure to be somewhat higher, at around 5.5 dB. The final figures we determined during the calibration on the antennas turned out to be substantially better than that, likely because the dummy load used in laboratory testing and consisting of a coaxial 50Ω load in liquid nitrogen (LN_2), was a poor match at LN_2 temperatures. We have measured the noise figures again during the calibration observations and note that they are indeed better at around 3 dB; see Table 5.4.1 for a comprehensive listing of the noise figures for all filters and units.

Unit	Filter [GHz]	T_{rec} [K]	Noise Figure (NF) [dB]	Noise Floor [dBm]
	16.5	319.2	3.22	–81.43
	18.9	251.4	2.71	–81.84
1	22.9	249.9	2.70	–81.30
	25.5	316.0	3.20	–80.76
	TP	422.4	3.20	–70.80
	16.5	370.3	3.57	–81.13
	18.9	266.8	2.83	–81.48
2	22.9	266.8	2.83	–81.17
	25.5	334.6	3.33	–80.46
	TP	438.3	3.33	–70.67
	16.5	300.8	3.09	–81.51
	18.9	267.0	2.83	–81.48
3	22.9	287.0	2.99	–80.76
	25.5	329.4	3.30	–80.37
	TP	386.1	3.30	–70.70
	16.5	305.0	3.12	–81.58
	18.9	251.8	2.71	–81.70
7	22.9	320.5	3.23	–80.72
	25.5	382.5	3.65	–80.09
	TP	398.1	3.65	–70.35
	16.5	288.8	3.00	–81.81
	18.9	279.3	2.93	–81.48
5	22.9	316.8	3.21	–80.67
	25.5	352.5	3.45	–80.55
	TP	620.8	3.45	–70.55
	16.5	296.8	3.06	–81.64
	18.9	244.2	2.65	–81.76
6	22.9	265.6	2.82	–81.01
	25.5	295.0	3.05	–80.95
	TP	676.5	3.05	–70.95

Table 5.4.1: The receiver temperatures T_{rec}, the noise figure and noise floor for each filter in each of the WVRs. TP is the total power channel, which is 10 GHz wide, from 16 to 26 GHz. Note that Unit 4 (for historical reasons) remained with the manufacturer for extended testing purposes and antenna 4 thus was provided with unit 7 instead.

The required temperature stability was derived from the overall gain stability requirements discussed in the Bremer paper [6] for the original design specifications. The most temperature dependent components in the WVR are the RF amplifiers which have a gain change of about 0.04 dB per 1 K. This gave a temperature control requirement of +/- 1 mK at the RF plate control point. This degree of temperature control was verified by calculating the Allan deviation of the RF Plate temperature control point over an arbitrary time period. As can be seen in the Allan deviation plots in Figures 5.4.1 to 5.4.7, this was achieved with values between 0.1 and 0.4 mK. The Allan deviation is a useful quantity to employ for this kind of data because similarly to a power spectrum it highlights behaviour in the time domain such as temperature control flicker caused by timed activation of the RF plate heaters, or externally caused temperature oscillations e.g. by the vertex room air conditioning system. The Allan deviation is calculated as the square root of the Allan variance, which in turn is one half the time average of the squares of the differences between successive data points of the frequency deviation, sampled over the sampling period. Equation 5.4.2 shows the Allan variance:

$$\sigma_T^2(\tau) = \frac{1}{2}\langle(\overline{T_{N+1}} - \overline{T_N})^2\rangle \tag{5.4.1}$$

and from this the Allan deviation:

$$\sigma_T(\tau) = \sqrt{\sigma_T^2(\tau)} \tag{5.4.2}$$

The Allan deviation is useful to plot activation states of switched elements, such as the heaters we employ inside the WVRs to stabilise the temperatures. The temperatures are very stable as long as no thermal elements are switched. As soon as they do switch however, variations in temperature do appear, as evidenced by the sudden changes in figures 5.4.1 – 5.4.7. While the thermal sensors are extremely sensitive and detect temperature variations to better than 0.5 mK with drift stability of better than 0.08 mK / hour, their absolute temperature points are not calibrated (they don't need to be) and hence each unit has its own characteristic temperatures, it is not sensible to compare absolute values between the units.

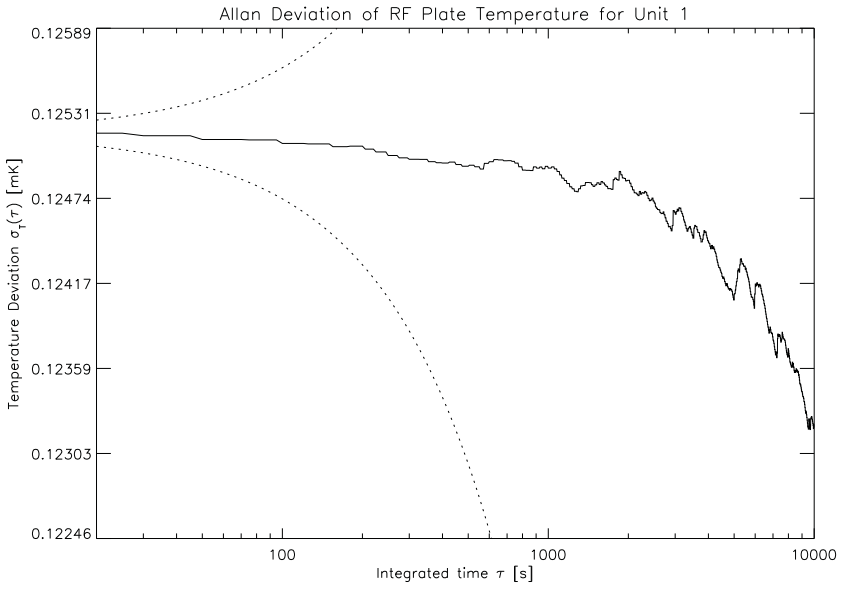

Figure 5.4.1: The Allan deviation of the RF Plate temperature control point for Unit 1 in the evening of August 23 2011. The dotted lines represent the maximum temperature drift as per the design specifications. The temperatures therefore are more stable than the design criteria required by about 3 orders of magnitude for unit 1.

The other temperature stability requirement stated <0.01 K change at the worst case position on the RF components for an ambient change of 10 K. With the already demonstrated temperature stability this is achieved. It is important to note here that this relates to a change in temperature for the vertex room, not of the residual temperature gradients across the RF plate. Some effort has gone into designing WVRs to minimise static temperature gradients as well but this proved to be unnecessary, as long as these gradients remain essentially constant.

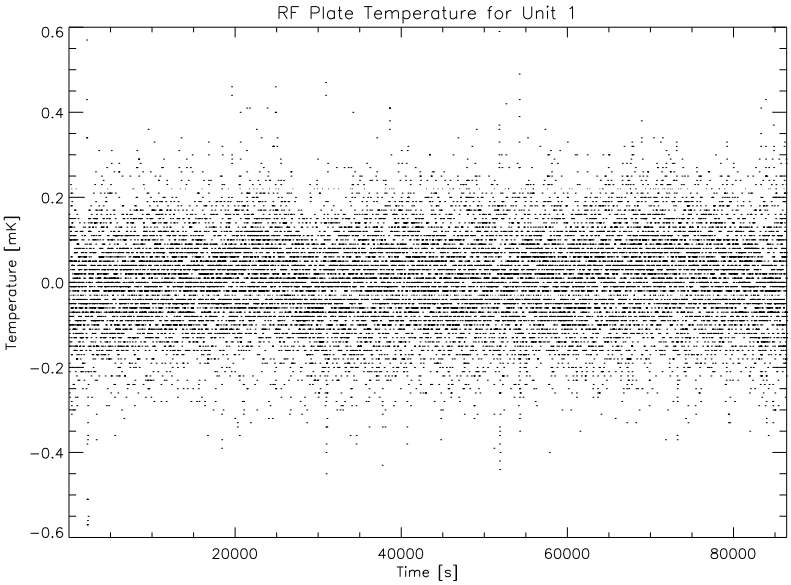

Figure 5.4.2: The raw data of the RF Plate temperature control point for Unit 1 for all of August 23 2011. Note the horizontal striping depicting the digitiser resolution limit for the thermal sensor. The temperature stability is excellent and the behaviour confirms the Allan deviation for the same data which is shown in figure 5.4.1.

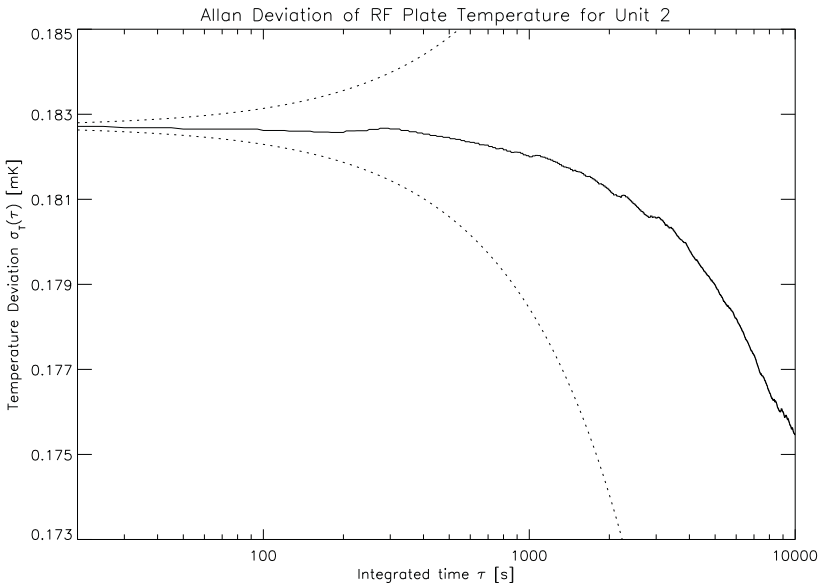

Figure 5.4.3: The Allan deviation of the RF Plate temperature control point for Unit 2 in the evening of August 23 2011. The dotted lines represent the maximum temperature drift as per the design specifications. The temperatures therefore are more stable than the design criteria required by two orders of magnitude for unit 2.

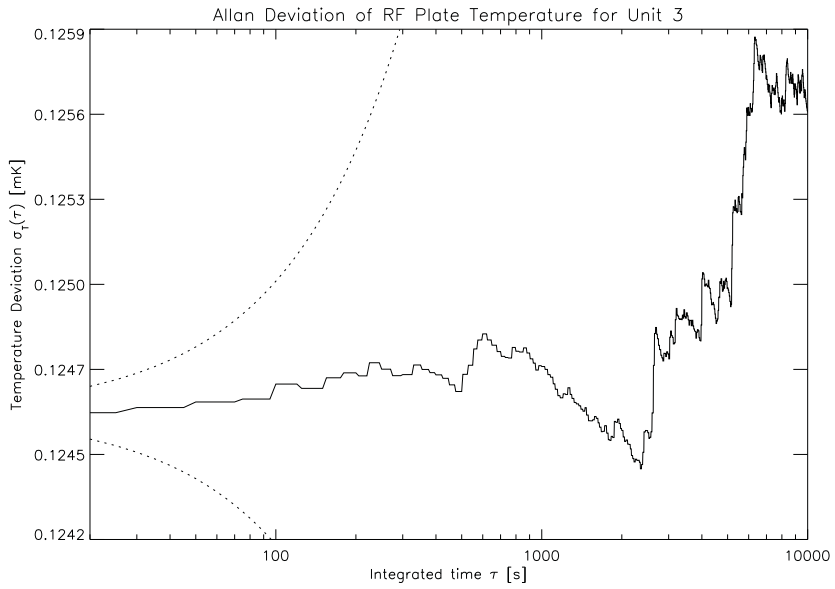

Figure 5.4.4: The Allan deviation of the RF Plate temperature control point for Unit 3 in the evening of August 23 2011. The dotted lines represent the maximum temperature drift as per the design specifications. The temperatures therefore are more stable than the design criteria required by 3 orders of magnitude for unit 3.

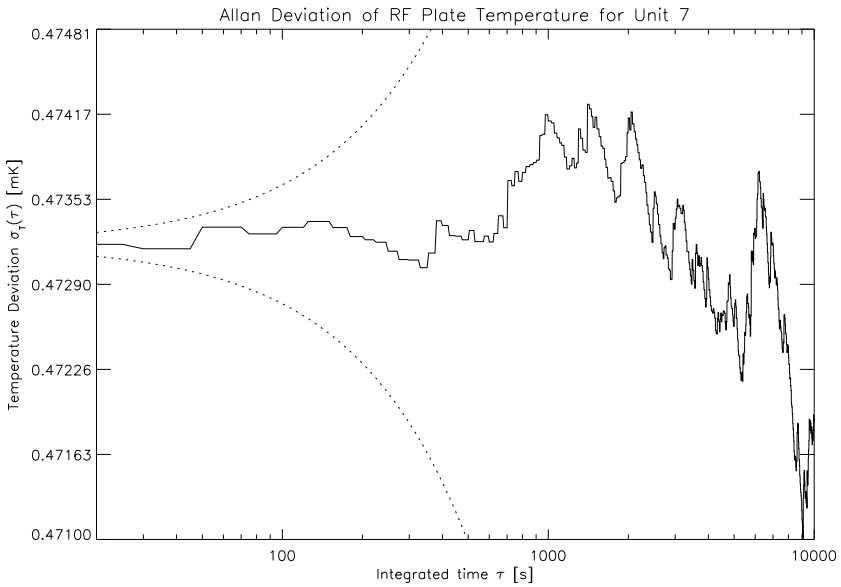

Figure 5.4.5: The Allan deviation of the RF Plate temperature control point for Unit 7 in the evening of August 23 2011. The dotted lines represent the maximum temperature drift as per the design specifications. The temperatures therefore are more stable than the design criteria required by 5 orders of magnitude for unit 7.

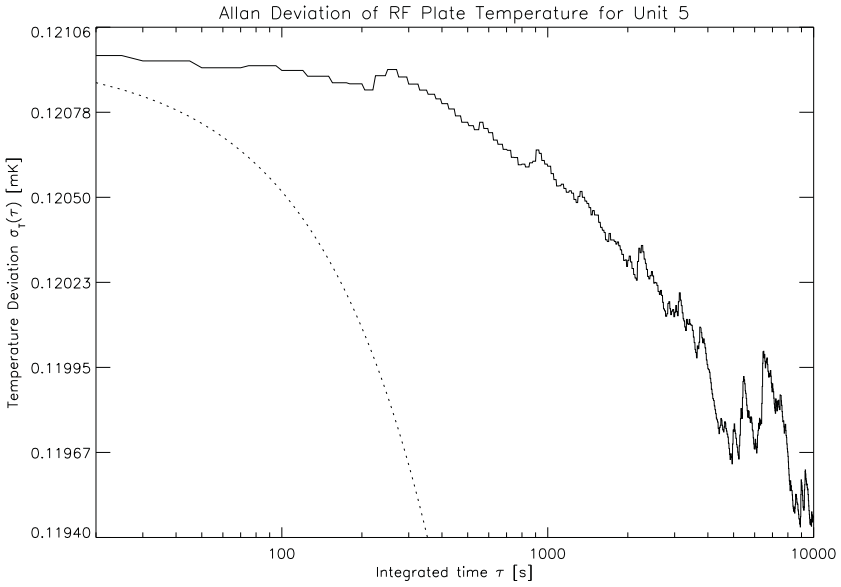

Figure 5.4.6: The Allan deviation of the RF Plate temperature control point for Unit 5 in the evening of August 23 2011. The dotted lines represent the maximum temperature drift as per the design specifications. The temperatures therefore are more stable than the design criteria required by 3 orders of magnitude for unit 5.

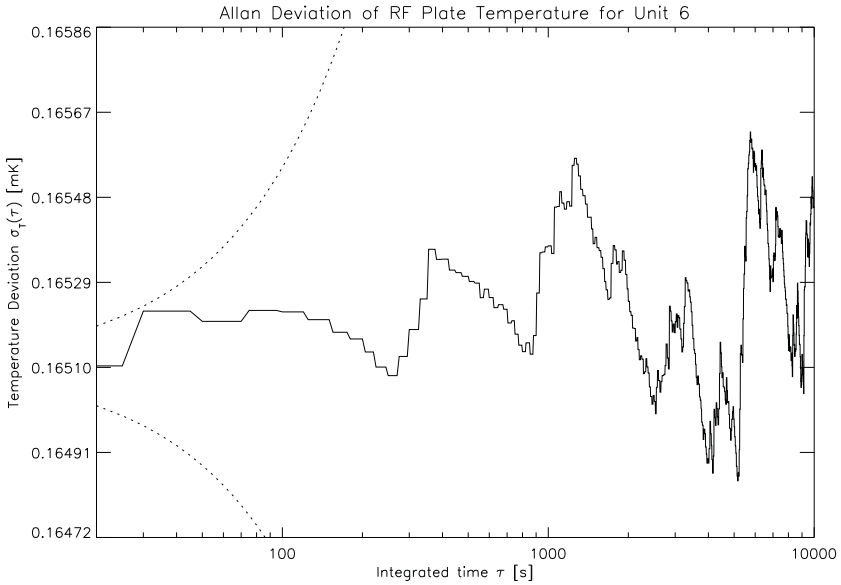

Figure 5.4.7: The Allan deviation of the RF Plate temperature control point for Unit 6 in the evening of August 23 2011. The dotted lines represent the maximum temperature drift as per the design specifications. The temperatures therefore are more stable than the design criteria required by 4 orders of magnitude for unit 6.

To reduce temperature gradient change with ambient temperature change, it is imperative to have multi layered insulation and one, or more, conductive shells completely surrounding the RF plate. These shells also should be temperature controlled. The ideal material is anisotropic with good insulation 'across' the medium and good conductivity 'along' the medium (i.e. around the RF plate). A useful approximation to this is several alternate layers of thermal insulator and conductor. This presents some difficulties, however, when reasonably easy access to the RF plate is to be maintained. A practical solution that also satisfied the required gradient change in a simulation was to build two insulating layers and three conductive (aluminium) layers with the inner two actively temperature controlled. The minimum gradient change was successfully achieved using this method. Refer to Figures 5.4.8 and 5.4.9 which illustrate in cross sections how this was achieved: The top halves of the conducting layers were rendered as a transparent plastic in this visualisation to illustrate the layering. The hollow spaces in between are foam filled in the real units.

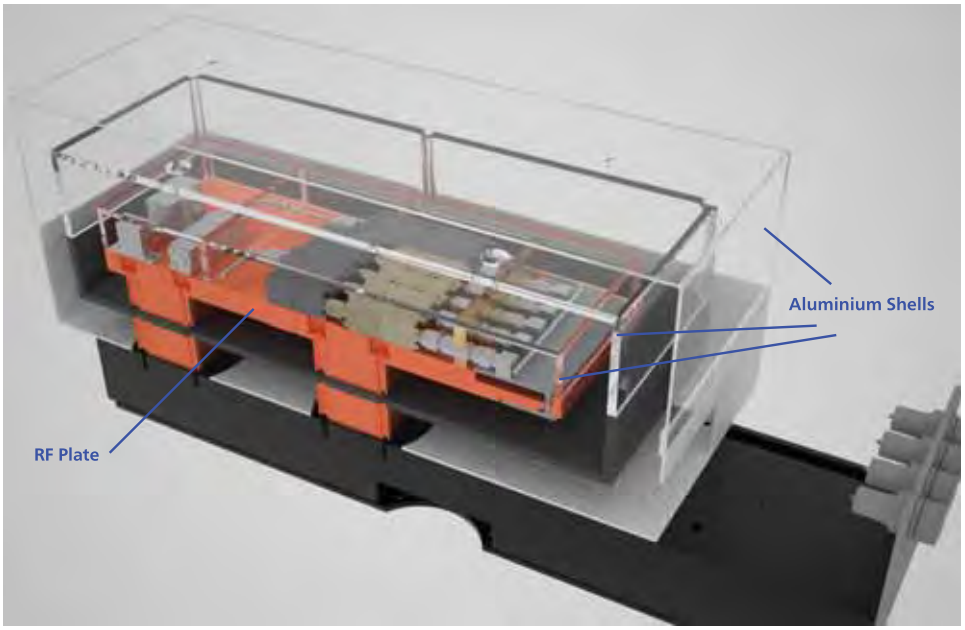

Figure 5.4.8: Cross section render through one of the WVRs. In the centre is the RF plate with some components visible. The RF plate itself is shielded inside a first aluminium enclosure, which itself is surrounded by foam (not shown in the render). Then a second aluminium shell surrounds this with more foam on the outside and finally the outside shell which is not thermally controlled. The outside is however painted white to minimise thermal energy uptake through solar radiation when pointing the antennas near the Sun. Visualised by the author using Maxwell Render [39] based on an AutoCAD model provided by Astrowave (Jonathan Crofts).

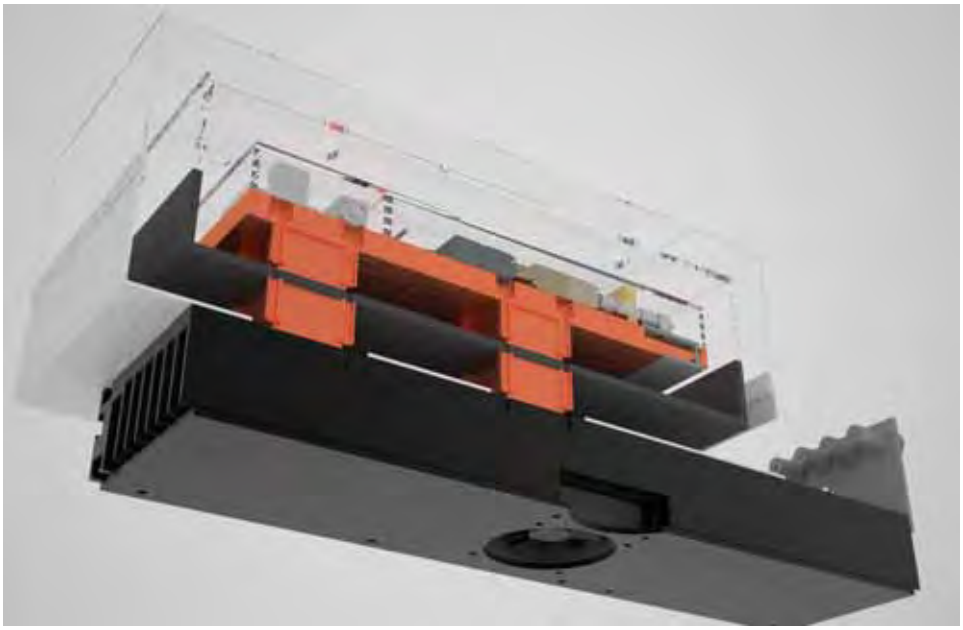

Figure 5.4.9: Cross section render through one of the WVRs, viewed from the bottom. In the centre is the RF plate with some components visible. The RF plate itself is shielded inside a first aluminium enclosure, which itself is surrounded by foam (not shown in the render). The base plate which attaches to the millimetre package on the receiver turret in the vertex room of each antenna features two fans to maintain a baseplate temperature close to ambient. Visualised by the author using Maxwell Render [39] based on an AutoCAD model provided by Astrowave (Jonathan Crofts).

For both gain stability and temperature stability the +10V drive voltage needs to be exceedingly stable, because changes in power dissipation of RF components would change local temperature. Great care was taken to stabilise this using precision voltage references installed on the RF plate PCB. This helped maintain the temperature stabilised environment with all of the control semi-conductors (which all have varying power dissipation) outside of the thermal enclosure directly on the main heat sink.

To thermally isolate the RF plate from the environment, all electrical conductors leading into the RF electronics were fabricated as thin traces on a 200mm long specially manufactured (and flexible) Kapton printed circuit. The input coaxial feed is fabricated from stainless steel for low thermal conductivity, with thin silver layers on the centre conductor and inside of the outer conductor for low electrical loss. This helps reduce thermal leakage but it is still the weakest link in the thermal design because this cable penetrates the shield.

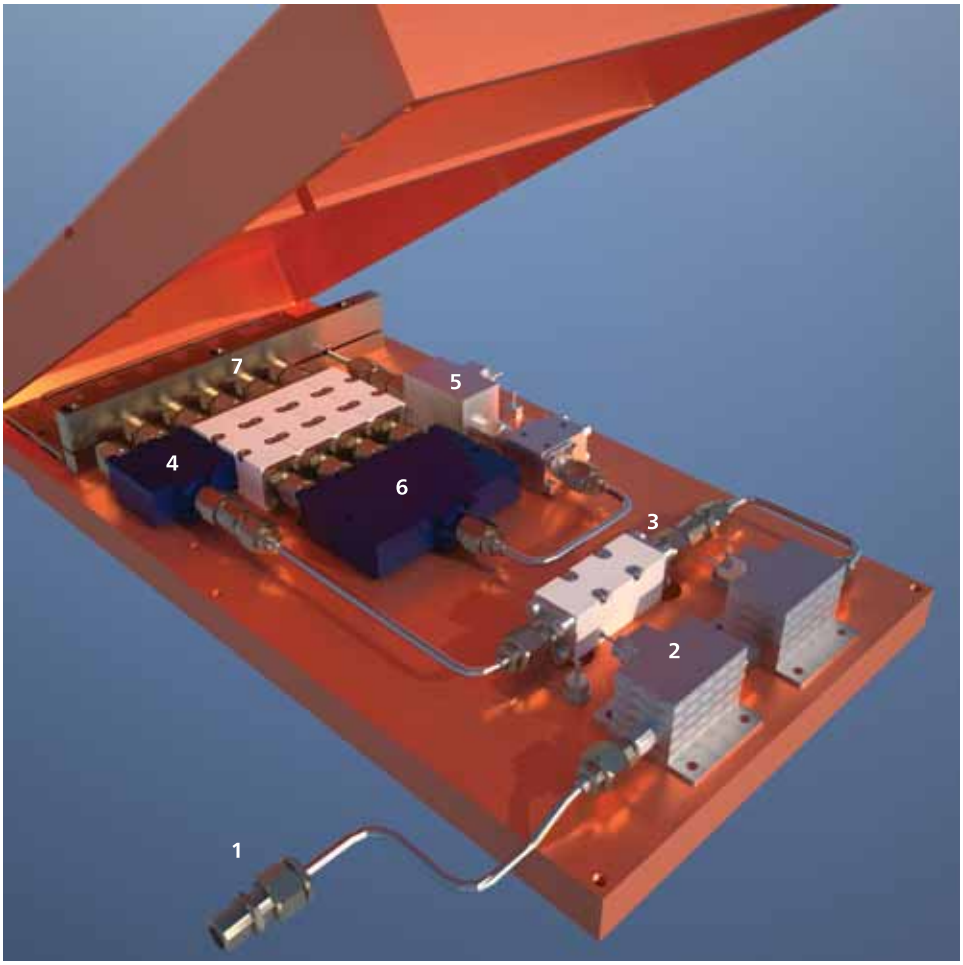

Figure 5.4.10: A render of the RF plate with all components and waveguides. The text follows the signal path in detail. #1: Feed connector, #2: First Miteq LNA, #3: 26 GHz low pass filter, #4: MCLI 2 way splitter, #5: Miteq LNA, #6: MCLI 4 way splitter, #7: tunnel diodes with filters. Visualised by the author using Maxwell Render [39] based on an AutoCAD model provided by Astrowave (Jonathan Crofts).

One of the original requirements was to have sharp cut off filters particularly to minimise overlap between the two closest channels. For that reason, a 7th order Chebychev filter design was chosen as they give the sharpest cut off and the theoretical 1 dB ripple in the pass band is dampened out by the insertion loss. 7th order also gives a rather high insertion loss (5 to 7 dB) but this is at high signal level at the end of the signal channel and we have sufficient gain available so it is not really of concern.

The filters were implemented as Micro-Strip filters etched on 0.25 inch backed 'Duroid' (i.e. ceramic loaded PTFE[1]) substrate. This gave a small physical size, helping keep the overall WVR package small. Also, by keeping the RF plate as small as possible, the temperature gradients induced by a given thermal leakage remain smaller. Further, this makes for a mechanically very solid, stable, filter.

There was some concern regarding thermal stability of this substrate material but bench tests of a completed filter over a 50 K range indicated that the insertion loss had a temperature coefficient of only 0.01 dB / K, or 0.23 parts in 10^4 / 10 mK, which is well within requirements and very well below the RF amplifier's temperature coefficient.

To summarise, the temperature coefficients of the critical components are listed in Table 5.4.2.

[1]PTFE = Polytetrafluoroethylene, more commonly known as the brand name Teflon.

Component	Coefficient	Comments
RF amplifiers	0.04 dB/ K	
Filters	0.01 dB/ K	
Ditom isolator	0.005 dB/ K	
Inmet attenuators	0.0003 dB/ K	This is from theory and the resistor temperature coefficients. The housing and connectors may be somewhat higher than this but in the worst case still $\ll$ 0.001 dB/ K)
DC amplifiers		With high stability resistors, high gain feedback and circuit topology used: $\ll$ than any of the above.
DataSet		No data is known, however, they were designed and made by an engineer (Suzy Jackson) at ATNF and were designed to be at least as stable as the above system. Further to this, the filter data is digitised at the interface to the dataset, it is hence safe to assume that the dataset itself will not have any detrimental effect on the data. It is further located outside the thermal envelope, so any thermal effect it might have will not propagate to the RF components.

Table 5.4.2: The temperature coefficients for all components used in the WVR design. Data and information supplied by Jonathan Crofts (Astrowave Pty Ltd).

To illustrate the signal path and the components involved in this water vapour radiometer as well as to visualise the insulation characteristics of the package, we now walk through the signal path while simultaneously looking at the following four plots:

- The radiometer schematics in Figure 5.4.11, starting at the top,
- the RF plate render in Figure 5.4.10, starting at the feed connector at the bottom left (#1 in the diagram),
- the view onto the "glass" radiometer in Figure 5.4.12, starting at the bottom connector.
- the photo of Unit 1 before it was retrofitted with the new filter frequencies. 5.4.13

We first enter the signal path at the feed horn (only shown on the schematic) where a weak signal of –83 dBm (=dB referenced to milliwatt) at 1 GHz of bandwidth (corresponding to the widest filters we have in the system) is received. The waveguide (numbered 1) then brings this signal into the first two low noise Miteq amplifiers (LNA's, numbered 2) which boost the signal each by +36 dB. The signal continues via an Inmet matching pad through a 26 GHz low pass filter (numbered 3) and another matching pad, introducing a loss of –25 dB. Then the first MCLI splitter is reached (numbered 4) which splits off the total power signal from the other filters. Note that the RF plate render in Figure 5.4.10 depicts a shorter version of this splitter whereas the glass render in Figure 5.4.12 shows a long version. Both kinds have been used in the construction of the WVRs, they are equivalent in their functionality. The total power channel now directly feeds into the Herotek tunnel diode detector and from there into the Analog Devices ultra precision operational amplifiers from where the signal is digitised and fed into the dataset (this last step is not shown). Following the other signal path after the total power splitter, we see another matching pad and by now the signal loss has been too large so another Miteq LNA (numbered 5) amplifies the signal by another +36 dB, then through a Ditom isolator, an MCLI four-way splitter (numbered 6) and into the Astrowave low pass filters (numbered 7), one for each of the filter frequencies of 16.5, 18.9, 22.9 and 25.5 GHz respectively. Then the signal follows the Herotek tunnel diode detectors into

the amplifiers and then into the datasets where the data can be queried by the data bus. The datasets are providing digitisation of the analog signal voltages from the tunnel diodes. They also provide the platform to run the temperature control logic as well as the communication and data interface for the observing system, allowing the WVR channel and monitoring data to be queried.

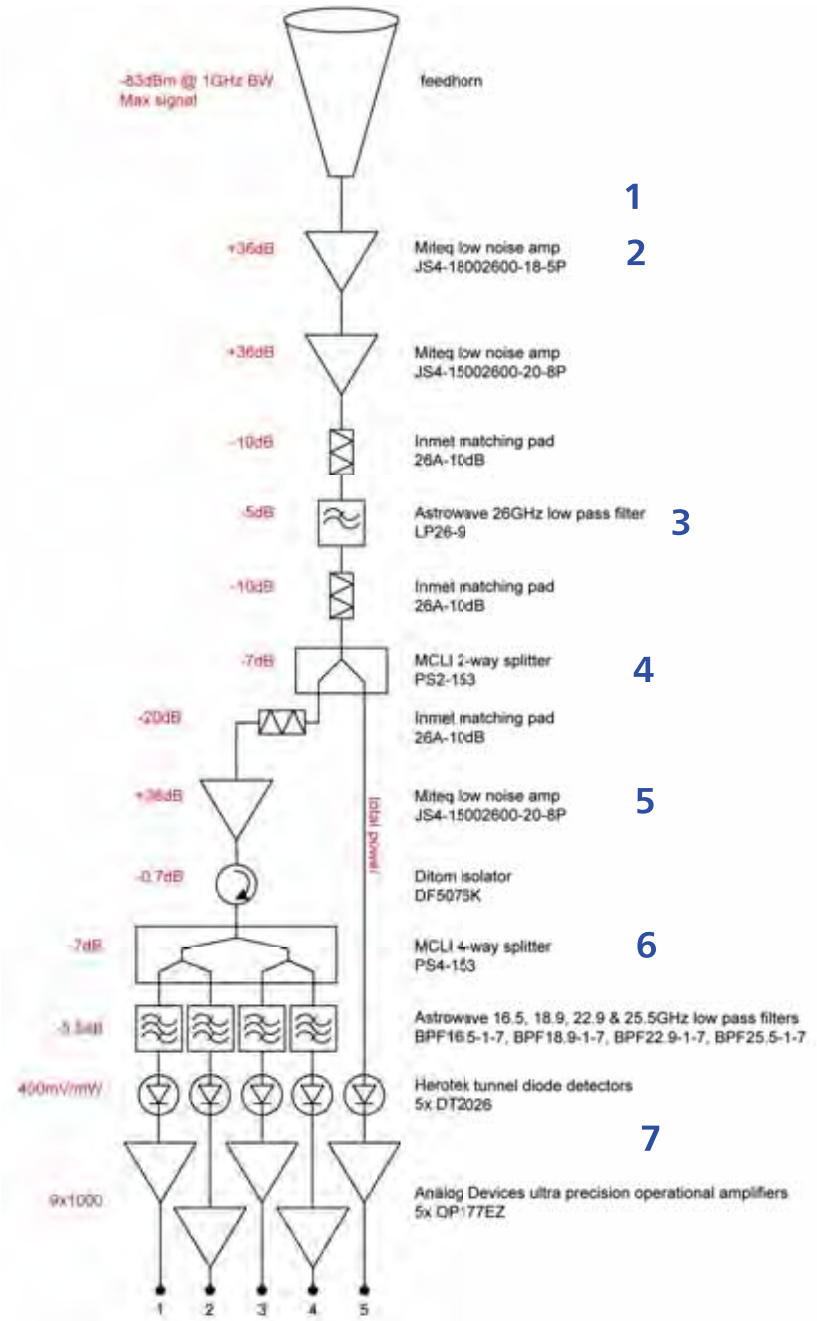

Figure 5.4.11: A schematic diagram of the WVR kindly provided by Christoph Brem (CASS Narrabri) after a hand sketch by Jonathan Crofts (Astrowave). The numbers refer to labels in Figures 5.4.10 and 5.4.12.

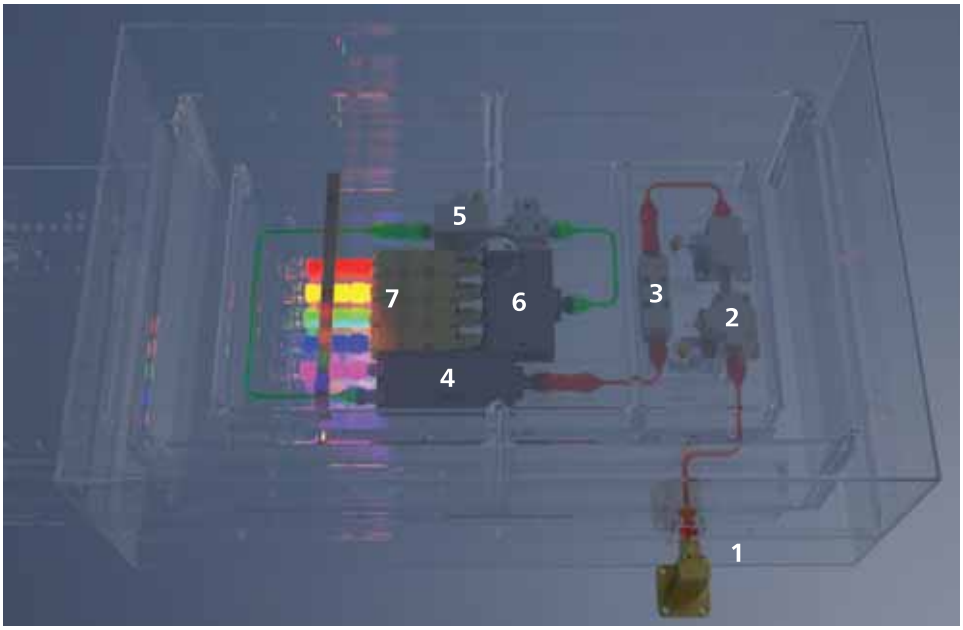

Figure 5.4.12: The WVR unit rendered with all hardware transparent as glass, except for the connectors, waveguides, LNA's, Filters and Diodes. Note the several conducting insulator layers depicted in glass here. In between those layers is foam in the real units. The tunnel diodes have been colour coded: Red is the 16.5 GHz channel, orange is 18.9 GHz, green is 22.9 GHz, blue is 25.5 GHz and magenta is the total power channel. #1: Feed connector, #2: First Miteq LNA, #3: 26 GHz low pass filter, #4: MCLI 2 way splitter, #5: Miteq LNA, #6: MCLI 4 way splitter, #7: tunnel diodes with filters. Visualised by the author using Maxwell Render [39] based on an AutoCAD model provided by Astrowave (Jonathan Crofts).

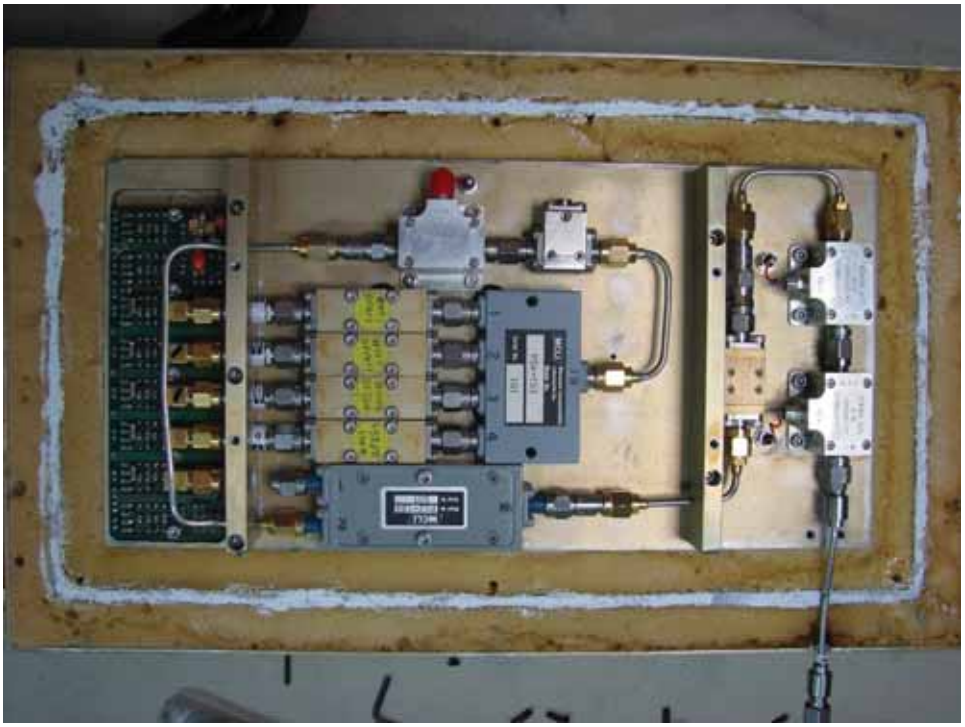

Figure 5.4.13: A photograph of the RF plate of Unit 1. Note that this was taken before the unit was fitted with the new filter frequencies. The foam insulating material is visible as well as all of the components. The components can be identified by comparing to Figure 5.4.10.

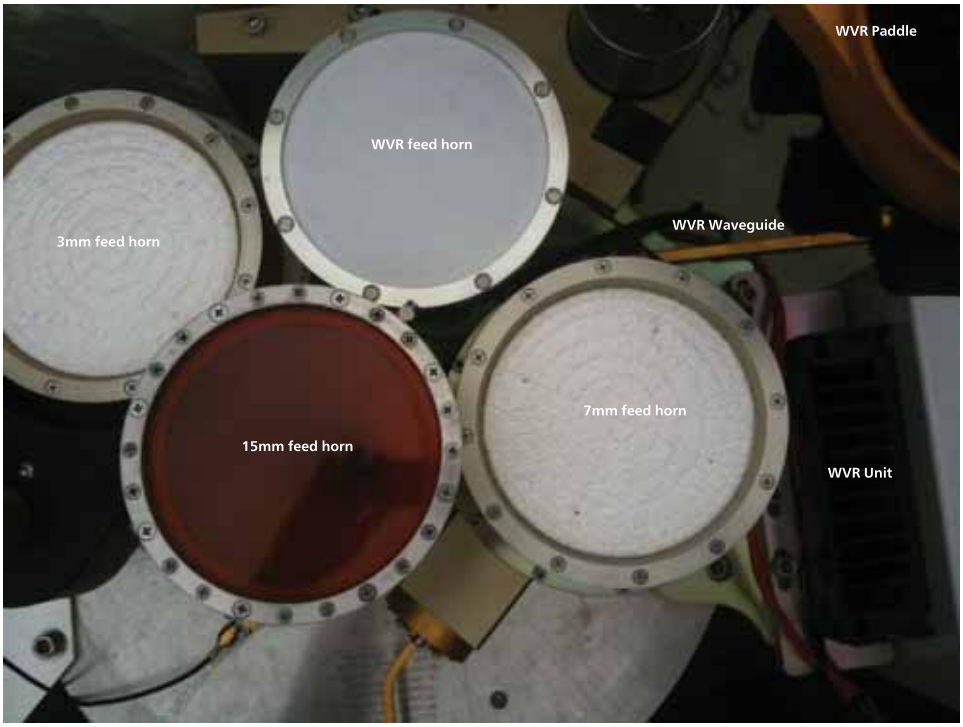

Figure 5.4.14: A photograph of the top of the millimetre dewar with all the feeds visible. Clockwise from the top: WVR feed with gold coloured waveguide leading the sky signal to the WVR box mounted on the right hand side of the mm package. Next is the 7 mm feed, then follows 15 mm and lastly to the left is the 3mm feed which is the only other system that has a paddle. Photo taken by the author in February 2010.

Figure 5.4.15: A side view of the millimetre package with the WVR mounted on the side (the white box). The WVR paddle, feed horn as well as waveguide can be clearly seen. The WVR paddle is in the same position as in Figure 5.4.14, i.e. not obstructing any of the feed horns. Photo by Peter Mirtschin in April 2011.

5.5 Calibration

5.5.1 Initial Calibration

Calibration of the water vapour radiometers is achieved by measuring the individual channel voltage on two known set points. The first set point measures the hot load (or paddle), which simply consists of activating the paddle mechanism and reading the temperature of a probe inside the absorber foam that is mounted on the paddle. There is also a case temperature probe (called T5) on each water vapour radiometer which can be used to indicate the ambient temperature (and thus hot load temperature). The colder set point is achieved by setting a styrofoam box on top of the feed horn with a microwave absorber inside submerged in a sufficient amount of liquid nitrogen so that the absorber along with the LN_2 becomes optically thick.

To measure the water vapour line temperatures we need to convert the voltages that are measured at each tunnel diode behind each filter in the WVRs into sky temperatures for the frequency and bandwidth each filter covers. This is best done by applying this simple linear conversion function:

$$T_{Sys} + T_{Rec} = GV \tag{5.5.1}$$

with

$$T_{Sys} = T_{Sky} + T_{Spillover} \tag{5.5.2}$$

where G is the gain, T_{Sys} is the atmospheric emission (including any astronomical source) and $T_{Spillover}$ (from now on referred to as T_S) is the spillover emission. V is the voltage measured at the tunnel diode. In order to be able to solve this equation, we need to derive the gain G and the receiver temperature T_{Rec} for each filter in each unit to obtain T_{Sys}. We achieve this with calibration measurements and the hot and cold loads. These measurements can be reformed into two equations stating:

$$T_{Hot} + T_{Rec} = G \cdot V_{Hot} \tag{5.5.3}$$

and

$$T_{Cold} + T_{Rec} = G \cdot V_{Cold} \tag{5.5.4}$$

Because during the calibration measurements the feed horn is completely covered by either the microwave absorber submerged in LN_2 or the paddle / hot load, there is no spillover temperature T_S or T_{Sys} to consider. By reforming this algebraically, we can derive what the receiver engineers call the "Y factor":

$$\frac{T_{Hot} + T_{Rec}}{T_{Cold} + T_{Rec}} = \frac{V_{Hot}}{V_{Cold}} = Y \tag{5.5.5}$$

solve for T_{Rec} to obtain:

$$T_{Rec} = \frac{T_{Hot} - YT_{Cold}}{Y - 1} \tag{5.5.6}$$

and

$$G = \frac{T_{Hot} + T_{Rec}}{V_{Hot}} \tag{5.5.7}$$

where V_{Hot} is the tunnel diode voltage measured for the filter with the paddle (also called hot load) in front of the feed horn, V_{Cold} is the voltage measured for the same tunnel diode and filter. The Y factor then is simply the ratio between the hot and cold calibration points. Note that T_{Rec} contains the noise temperature contribution of all feed, receiver and IF components prior to detection.

The gain equation 5.5.7 allows us to correct for gain drift using a hot load only, so by using the paddle at regular intervals, we can always derive the latest gain number under the assumption that the Y factor remains constant. We now examine whether this is the case.

5.5.2 Gain stability

In order to establish longer term gain stability figures, several calibrations were executed and subsequently compared. The first measurement series was executed on 9 November 2010, with subsequent calibration runs on 7 and 8 March and 2011. The data for March 7 can be found in the Table

5.5.1 below, whereas the data for the other calibration runs can be found in the appendix as Tables A.0.1, A.0.2 and A.0.3 respectively.

We have derived the Y factors for each of the calibration runs and are comparing them in Table 5.5.2. The variation of the Y factor between the measurements is consistently less than 1%. The receiver temperature on the other hand varies by up to 3.4%. As long as the Y factor remains stable, we can derive the T_{Rec} from the paddle measurements at any given time, so we are able to correct for the variations observed.

			Radiometer Channel				
Antenna	**Unit**		**16.5 GHz**	**18.9 GHz**	**22.9 GHz**	**25.5 GHz**	**TP**
CA01	1	*Y factor*	1.56	1.68	1.68	1.56	1.44
		Gain [K/V]	77.14	76.93	73.65	95.71	123.97
		T_{Rec} [K]	319.2	251.4	249.9	316.0	422.4
		T_{Sky} [K]	8.8	14.8	45.0	28.6	27.7
CA02	2	*Y factor*	1.50	1.65	1.65	1.54	1.43
		Gain [K/V]	147.98	72.46	70.01	127.60	92.97
		T_{Rec} [K]	370.4	266.8	266.9	334.6	438.3
		T_{Sky} [K]	4.9	12.9	42.6	24.3	24.4
CA03	3	*Y factor*	1.58	1.64	1.61	1.54	1.48
		Gain [K/V]	97.66	167.57	70.88	117.26	80.64
		T_{Rec} [K]	300.9	267.0	287.1	329.5	386.9
		T_{Sky} [K]	8.0	14.6	44.7	26.6	26.9
CA04	7	*Y factor*	1.58	1.67	1.56	1.48	1.47
		Gain [K/V]	75.72	73.68	121.06	133.85	115.56
		T_{Rec} [K]	305.0	251.8	320.5	382.5	398.1
		T_{Sky} [K]	4.1	12.6	45.0	25.7	22.5
CA05	5	*Y factor*	1.61	1.62	1.56	1.52	1.32
		Gain [K/V]	67.33	71.31	76.57	98.42	122.92
		T_{Rec} [K]	288.8	279.3	316.8	352.5	620.8
		T_{Sky} [K]	6.1	13.8	45.9	27.5	23.9
CA06	6	*Y factor*	1.59	1.69	1.65	1.60	1.30
		Gain [K/V]	72.88	70.26	101.19	117.18	140.82
		T_{Rec} [K]	296.8	244.2	265.6	295.0	676.5
		T_{Sky} [K]	9.0	16.0	45.6	28.1	23.3

Table 5.5.1: Calibration result for March 7, 2011.

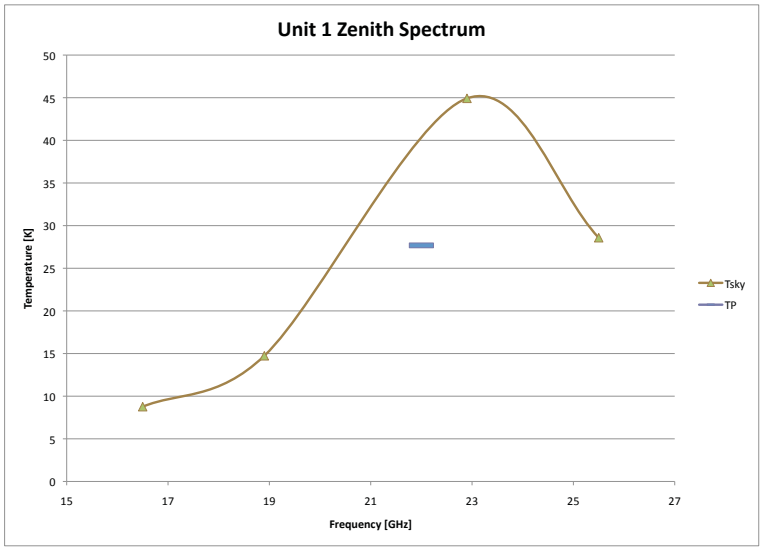

Figure 5.5.1: Zenith sky spectrum for unit 1. The temperature excess reaching above the ν^2 continuum (this is within the Rayleigh-Jeans regime of the spectrum) of the three outside channels is approximately 20 K. Data taken on March 7 2011 in clear skies.

At the end of the calibration series, a zenith sky spectrum was obtained for each antenna. Figure 5.5.1 shows this spectrum for Unit 1. The sky temperatures in the channels follow the model atmosphere as expected and outline the shape of the H_2O line on top of the ν^2 continuum. The sky temperature in the total power channel (spanning the full 16 – 26 GHz) is at a similar level to the highest continuum point at 25.5 GHz, and the shape of the water line is traced in all filter positions. A better representation of this data for all units is shown in Figure 5.5.2. It outlines the same H_2O line spectrum for all of the units, and also displaying the actual filter bandwidths as measured for each filter, refer to Appendix B.0.1 for a complete list of all filter bandwidths. Also shown in 5.5.2 are the ATM derived model atmospheres for 5mm, 50mm and the actual value of 23mm

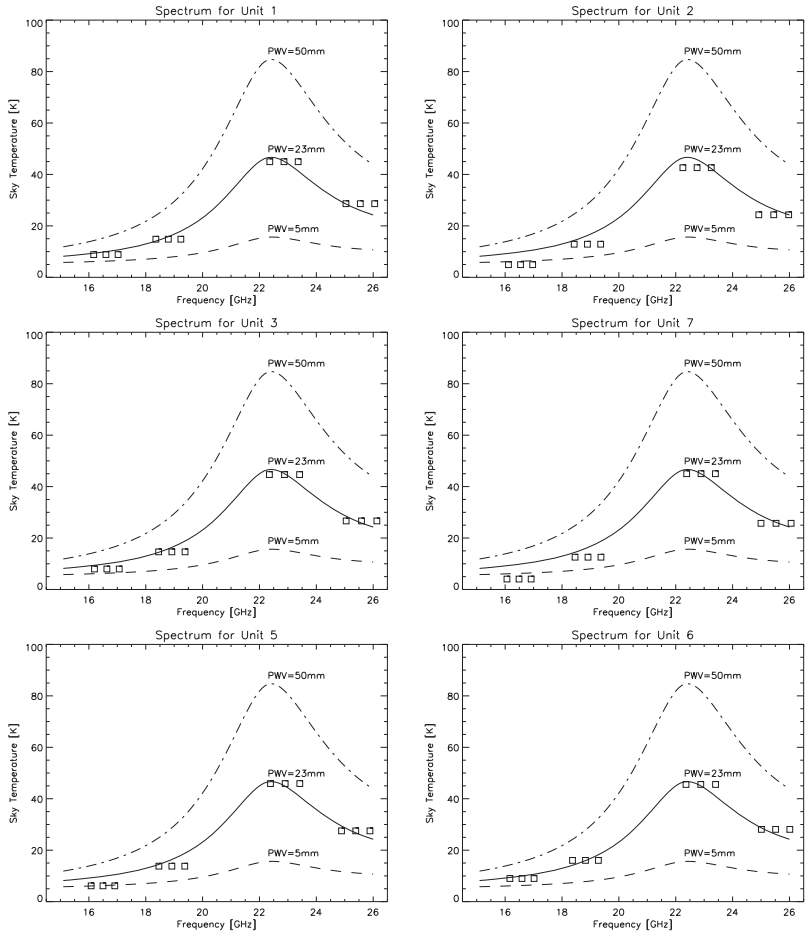

Figure 5.5.2: During the calibration run in March 2011, sky data was recorded and the corresponding sky temperatures are plotted. The three lines are for 5mm, 50mm and 23mm of PWV calculated using the ATM code. The latter corresponds to the tropospheric PWV as it was present during the calibration measurements. Each filter location is marked by three boxes, one in the centre of the band, and one each on the upper and lower limit of the bands. Note that for this plot, the actual filter transmission profiles as documented in appendix B.0.2 were used to display the filter widths.

	16.5 GHz	18.9 GHz	22.9 GHz	25.5 GHz	Total Power
Y Factor Aug 2010	1.582	1.682	1.571	1.506	1.490
Y Factor Nov 2010	1.579	1.677	1.570	1.500	1.476
Y Factor difference	+0.2%	+0.3%	+0.06%	+0.4%	+0.9%
T_{Rec} K Aug 2010	304.1	247.9	311.4	360.9	375.4
T_{Rec} K Nov 2010	306.0	250.3	311.9	366.6	388.3
T_{Rec} difference	1.0%	1.0%	1.0%	–1.5%	–3.4%

Table 5.5.2: Gain comparisons for calibrations executed on Unit 7 in August and November 2010. The Y factor is stable to within better than 1%. This means that with the help of a hot load alone, we should be able to apply gain drift corrections.

precipitable water vapour at the time these measurements were taken.

5.5.3 Sky dips

During the calibration runs, several sky dips were obtained, one of which is depicted in Figure 5.5.3. These are measurements of the sky flux obtained at a number of elevation angles from 90 degrees to 13 degrees in steps of 10 degrees. Based on the skydip data, each channel for each WVR unit had its τ, zenith T_{Sys} as well as its spillover term T_S determined by a least squares fit of equation 5.5.8 to the data.

$$T_{sec(\theta)} = T_S + T_A(1 - e^{(-\tau sec\theta)}) \tag{5.5.8}$$

which, for small τ becomes:

$$T_{sec(\theta)} = T_S + T_A(\tau sec\theta) \tag{5.5.9}$$

This temperature intercept derived in equation 5.5.8 yields the spillover temperature. In the skydip data presented in Figure 5.5.3 we show the measured points at each elevation, connected with a dashed line. The intersect between an imaginary line and the X axis is the spillover temperature. The solid lines depict a linear fit through the skydip points. They do however not always match very well, so we fitted the skydip equation 5.5.8 to the same data: the fitted data is shown in dotted lines. This improved the fit somewhat. Looking at Figure 5.5.4 and Table 5.5.3 we find that all of the spillover temperatures are negative, i.e. the WVRs either underestimate the measured sky temperatures near zenith, or they overestimate the sky temperatures near the horizon. This is greatest for the 22.9 GHz filter in the water vapour line itself, and less for the other filters. These are, however, a small fraction of the ground temperature of ~290 K and amount to between 1% and 7%. It is also possible that the microwave absorber submerged in liquid nitrogen was warmer than the theoretical 77 K, as observed by [18]. This would increase the spillover temperatures, albeit not by a large amount. We have however no independent means of measuring the absorber temperature and therefore decided to rely on the proven methods of the RF engineers.

Furthermore, the variation in receiver temperature, which is assumed constant in this analysis, is also of order 1 – 3.5% (see Table 5.5.2). However, this

result also indicates limitations in the simple $\sec(\theta)$ plus constant atmosphere model assumed to apply to the skydips. For a real atmosphere, the temperature will vary as a function of height. The opacity is determined from the curvature in each skydip. The results from the fit, including the errors, are listed in Table 5.5.3. Further examining τ in Figure 5.5.5 we see that the derived zenith opacities are well behaved when compared to the zenith opacities of the model atmosphere. The data is consistent with typical atmospheric conditions but the variations also indicate that WVR data cannot be used for absolute determination of path lengths through the atmosphere, only the differential path lengths obtained by subtracting the DC offsets can be derived. See the discussion in chapter 6.4.2 for more details on the DC offsets.

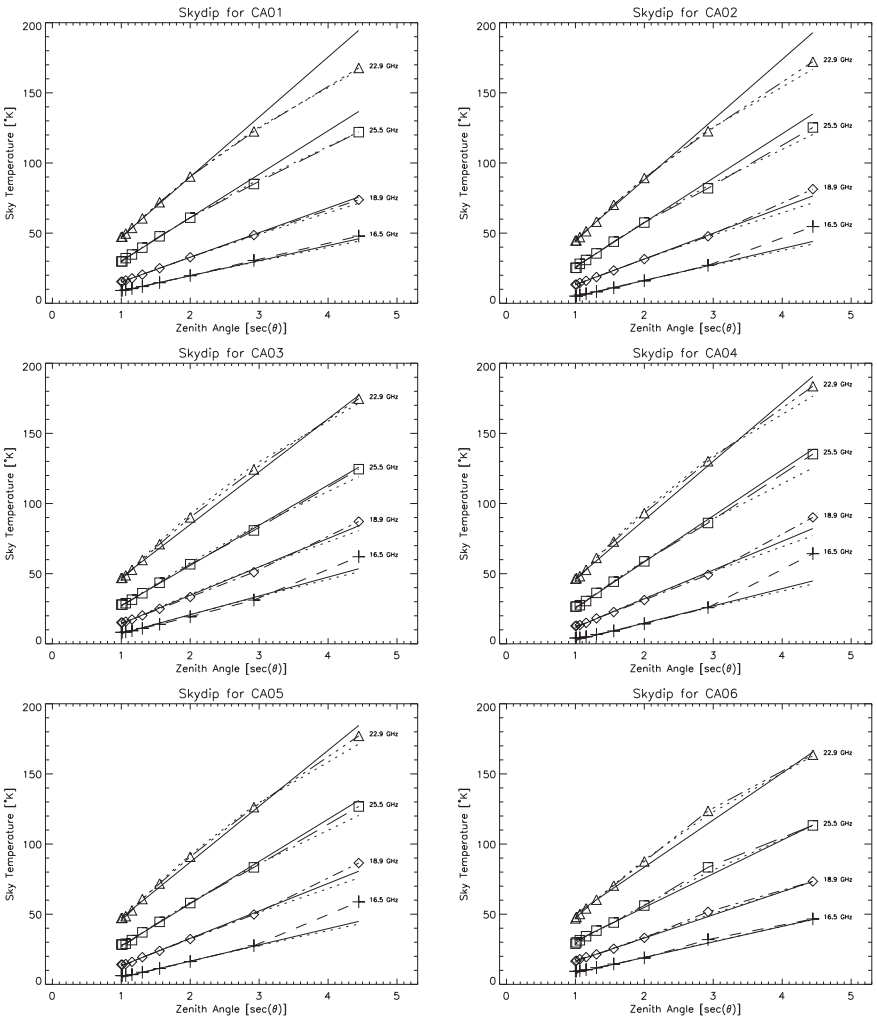

Figure 5.5.3: Skydip functions for all units. Data taken on March 7 2011.

Antenna	Filter [GHz]	T_S[K]	$T_{S,\mathrm{err}}$[K]	τ	τ_{err}
CA01	16.5	–2.4	0.50	0.04	0.001
	18.9	–3.7	0.57	0.07	0.001
	22.9	–6.5	0.95	0.20	0.003
	25.5	–5.6	0.83	0.13	0.002
CA02	16.5	–6.9	0.48	0.04	0.001
	18.9	–6.6	0.56	0.07	0.002
	22.9	–12.1	1.60	0.21	0.005
	25.5	–11.3	1.14	0.13	0.004
CA03	16.5	–7.0	0.47	0.05	0.001
	18.9	–9.0	0.84	0.08	0.002
	22.9	–14.1	2.26	0.23	0.008
	25.5	–8.8	1.37	0.13	0.004
CA04	16.5	–10.3	0.43	0.05	0.001
	18.9	–11.2	0.72	0.08	0.002
	22.9	–21.3	2.35	0.25	0.009
	25.5	–15.1	1.12	0.15	0.003
CA05	16.5	–7.1	0.39	0.04	0.001
	18.9	–8.5	0.69	0.08	0.002
	22.9	–13.7	1.97	0.23	0.007
	25.5	–9.4	1.36	0.13	0.004
CA06	16.5	–4.6	0.23	0.04	0.001
	18.9	–3.7	0.45	0.07	0.001
	22.9	–3.8	1.37	0.19	0.004
	25.5	–2.7	0.75	0.11	0.001

Table 5.5.3: The spillover temperature T_S, spillover error $T_{S,\mathrm{err}}$, zenith opacity τ and opacity error τ_{err} for each antenna and filter. The errors are determined from the fits to derive T_S and τ.

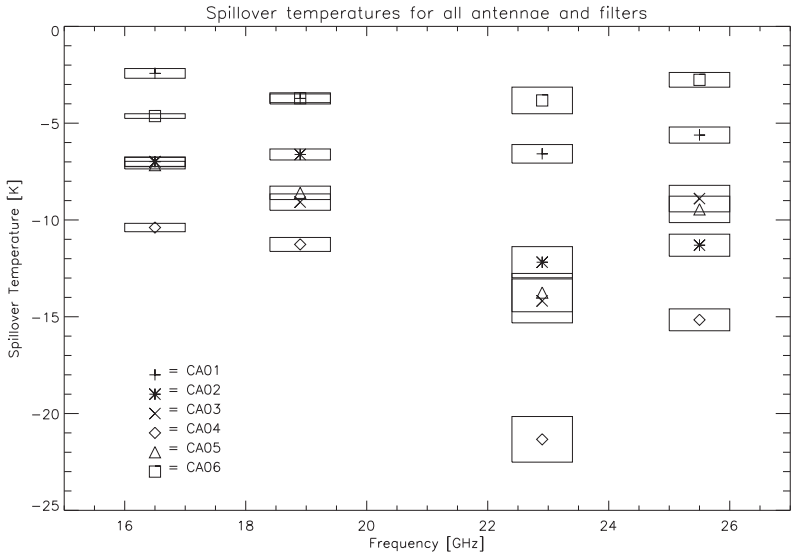

Figure 5.5.4: The spillover temperatures for all antennas and frequencies. Refer to Table 5.5.3 for the values. Each filter is shown as a box of 1 GHz width and $T_{S,\text{err}}$ height. Additionally, the centre point is depicted with a symbol to allow identification of which antenna/WVR the point belongs to.

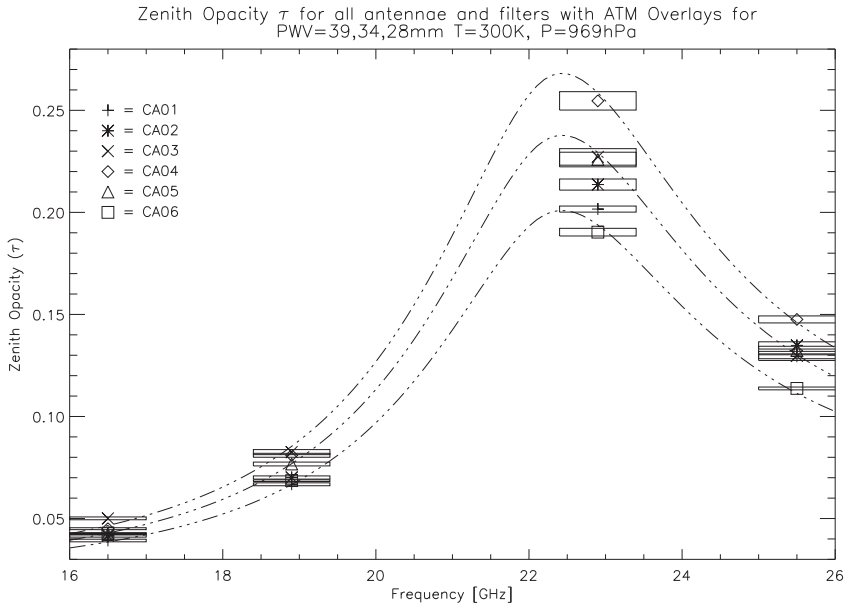

Figure 5.5.5: Zenith opacity τ as determined from the sky dips. Refer to Table 5.5.3 for the values. Each filter is shown as a box of 1 GHz width and τ_{err} height. Additionally, the centre point is depicted with a symbol to allow identification of which antenna/WVR the point belongs to. Over-plotted are three opacities derived from the ATM model atmosphere for PWV values of 28mm (lowest opacity), 34mm (middle line) and 39mm (highest opacity).

5.6 Filter Profile Measurements

Each of the filters for each of the water vapour radiometers was measured for its throughput characteristics prior to mounting them inside the units. Each filter distinguishes itself from the others through the following criteria due to manufacturing tolerances:

- Centre frequency: The exact centre of the peak sensitivity of the bandpass varies.
- Bandwidth: The bandwidth of the 3dB pedestal from either side of the filter peak varies as well.
- Insertion loss: When a filter is inserted into a signal path, it always results in some attenuation and thus loss of power. Insertion loss is the logarithm of the ratio between the power received at the end of the signal chain before and after inserting the filter. Insertion loss is a ratio, and is thus measured in dB or dBm if referring to powers in milliwatts. Because in the WVRs the filters are the last components in the chain, their insertion loss has a very small effect on the measurements as can be seen following the Friis equation 5.2.2.

We have catalogued each of the filter's actual characteristics, see Appendix B.0.2 for the plots and B.0.1 for the detailed numbers. This list provides detailed characteristics of all the filters such as their transmission and response characteristics, their bandwidth and bandpass shape. This information was provided by Astrowave (Jonathan Crofts) using a drift aligned megamac spectrum analyser. Looking at Unit 1 as an example below, we find the detailed filter information for 16.5 GHz in Figure 5.6.1, for 18.9 GHz in Figure 5.6.2, for 22.9 GHz in Figure 5.6.3 and for 25.5 GHz in Figure 5.6.4. Table 5.6.1 lists the filter serial number, the centre frequency, the bandwidth and insertion loss for all the filters in unit 1. Refer to appendix B.0.2 for the other units.

	Serial #	Centre Freq. [GHz]	BW [GHz]	Insertion loss [dB]
Ch1	203	16.599	0.86	–6.5
Ch2	210	18.795	0.88	–7.0
Ch3	222	22.862	1.00	–6.8
Ch4	233	25.548	1.01	–7.6

Table 5.6.1: All filters for Unit 1 characterised: The centre frequency, bandwidth and insertion loss are essential parameters to consider when calibrating the units.

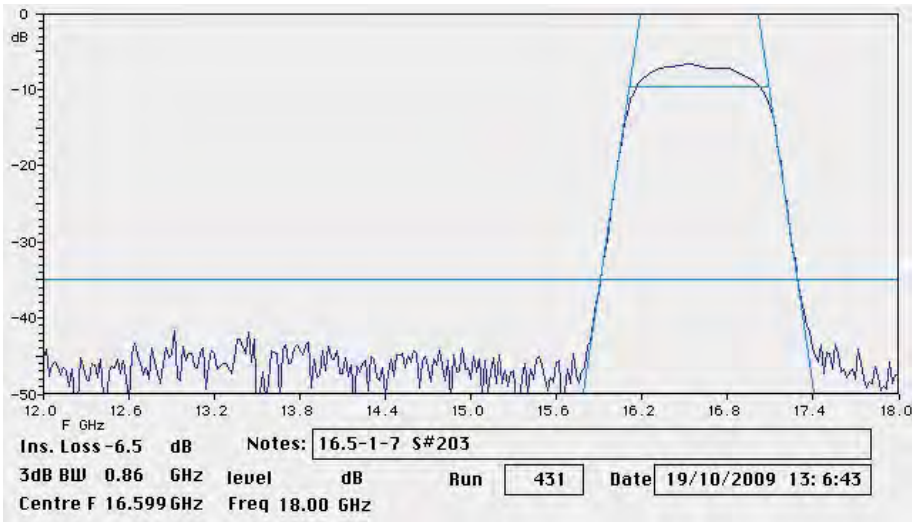

Figure 5.6.1: 16.5 GHz spectrum analyser plot for filter serial number #203 mounted in Unit 1. The x axis is the frequency in GHz, the y axis the signal in dB. The horizontal line near the top of the bandpass is the –10 dB line which corresponds to the –3 dB cut off with the ~–7 dB insertion loss added. This line and another horizontal line at –35 dB (–40 dB for some filters) are then used to determine the diagonal lines which follow the skirts of the response fitted to the data. The intersect between the skirt fits and the –10 dB line is then used to determine the bandwidth of the filter.

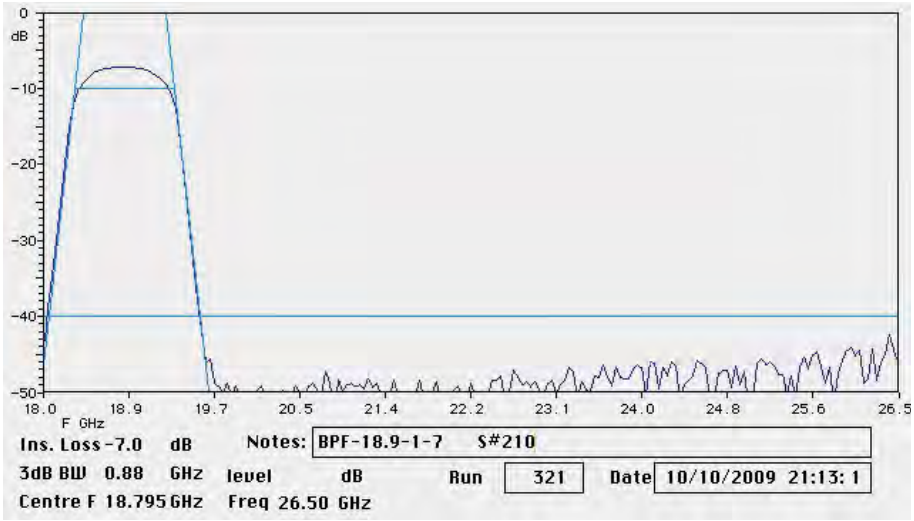

Figure 5.6.2: 18.9 GHz spectrum analyser plot for filter serial number #210 mounted in Unit 1. The x axis is the frequency in GHz, the y axis the signal in dB. The horizontal line near the top of the bandpass is the –10 dB line which corresponds to the –3 dB cut off with the ~–7 dB insertion loss added. This line and another horizontal line at –35 dB (–40 dB for some filters) are then used to determine the diagonal lines which follow the skirts of the response fitted to the data. The intersect between the skirt fits and the –10 dB line is then used to determine the bandwidth of the filter.

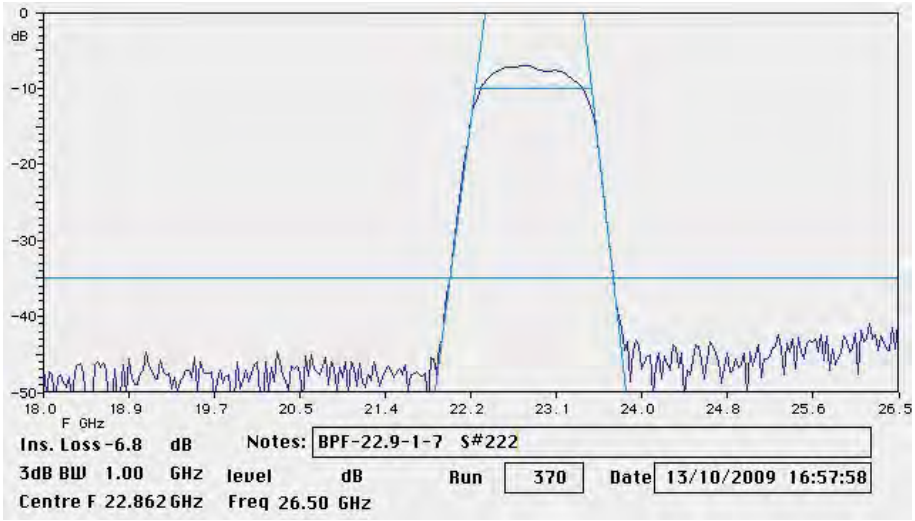

Figure 5.6.3: 22.9 GHz spectrum analyser plot for filter serial number #222 mounted in Unit 1. The x axis is the frequency in GHz, the y axis the signal in dB. The horizontal line near the top of the bandpass is the –10 dB line which corresponds to the –3 dB cut off with the ~–7 dB insertion loss added. This line and another horizontal line at –35 dB (–40 dB for some filters) are then used to determine the diagonal lines which follow the skirts of the response fitted to the data. The intersect between the skirt fits and the –10 dB line is then used to determine the bandwidth of the filter.

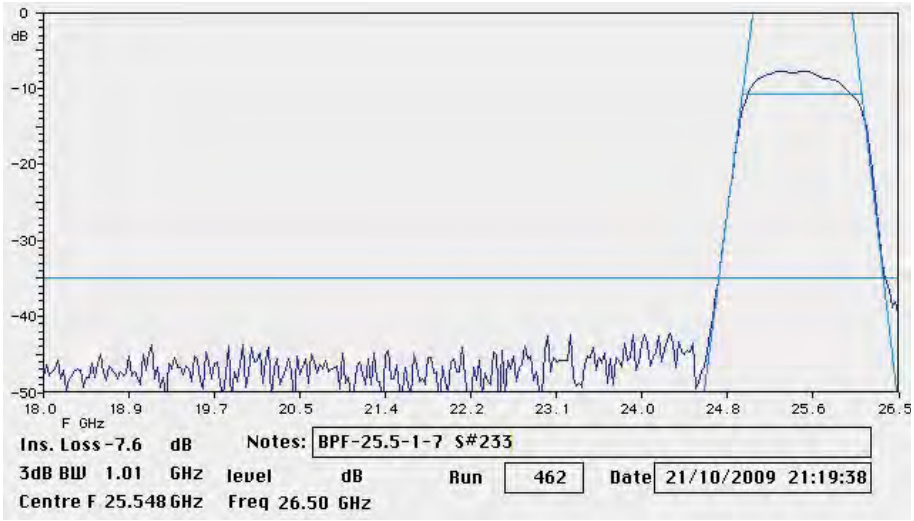

Figure 5.6.4: 25.5 GHz spectrum analyser plot for filter serial number #233 mounted in Unit 1. The x axis is the frequency in GHz, the y axis the signal in dB. The horizontal line near the top of the bandpass is the –10 dB line which corresponds to the –3 dB cut off with the ~–7 dB insertion loss added. This line and another horizontal line at –35 dB (–40 dB for some filters) are then used to determine the diagonal lines which follow the skirts of the response fitted to the data. The intersect between the skirt fits and the –10 dB line is then used to determine the bandwidth of the filter.

Chapter 6

Atmospheric Phase Correction

6.1 Introduction

Because a bright source in the target field of an astronomical source is rarely available, observational data cannot normally be calibrated on source continuously. Observers therefore need to calibrate the data on a nearby source that is bright enough to allow phase information to be measured. This phase information then is interpolated during data reduction: An assumption is made that the phase is linearly changing from its value as determined from the last calibrator to the value measured at the next calibration observation. This works reasonably well at lower frequencies, where the refractive index of the atmosphere caused by water vapour fluctuations is not affecting the phase substantially. But as the frequency is increased into the 15 mm, 7 mm and 3 mm bands, the poor mixing of water vapour with the atmosphere causes fluctuations in the refractive index, leading to path length variations and consequently phase variations that can get so large that the phase can no longer simply be interpolated between calibrator observations: The phase decorrelates. Figure 6.1.1 shows how the poor mixing of water vapour pockets within the atmosphere leads to excess path and phase shifts.

For mm observations in reasonable observing conditions, calibration scans must be executed at between 5 minute (3 mm) to 20 minute (15 mm) intervals if decorrelation between calibrator scans is to be avoided.

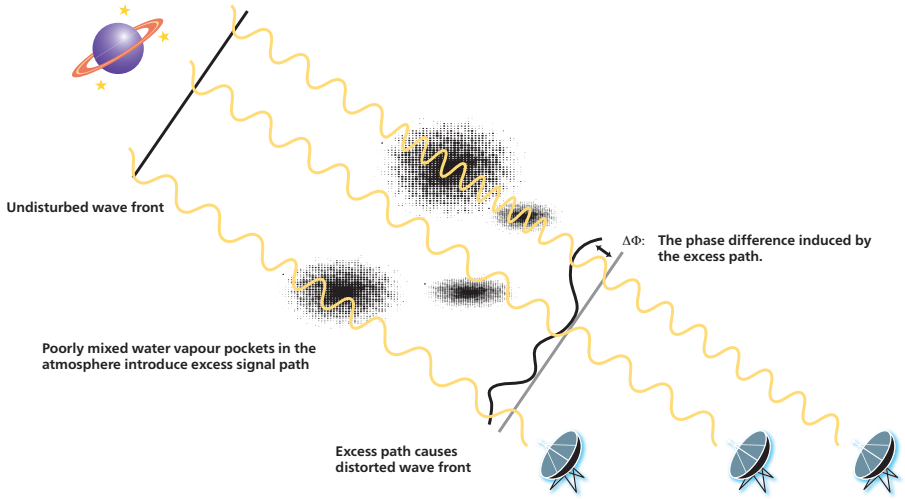

Figure 6.1.1: The incoming wave front of a source being observed with a radio interferometer is distorted due to changes in refractive index caused by the water vapour pockets. This results in an excess path the signal travels through, and hence a shift in phase of the incoming wave front between antennae.

Because water vapour is the main contributor to phase delays in a terrestrial interferometer, by measuring the water vapour's spectral line emission we can estimate the delays induced by it and keep track of the required phase correction. On the following pages, I will detail how we extract this information about the atmosphere using the Water Vapour Radiometers.

6.2 The 22.3 GHz Water Line

6.2.1 Mechanism

The atmospheric emission spectrum from 1 GHz to 200 GHz is depicted in Figure 6.2.1. In this graph, lines are drawn for varying degrees of precipitable water vapour (PWV) while maintaining the other atmospheric parameters at typical values for the site at Narrabri, a pressure of 1000 hPa and a temperature of 290 K. From this variation it is evident that water vapour is responsible for two of the major features visible in this graph: The first one at 22.2 GHz and the second one at 183.3 GHz. The

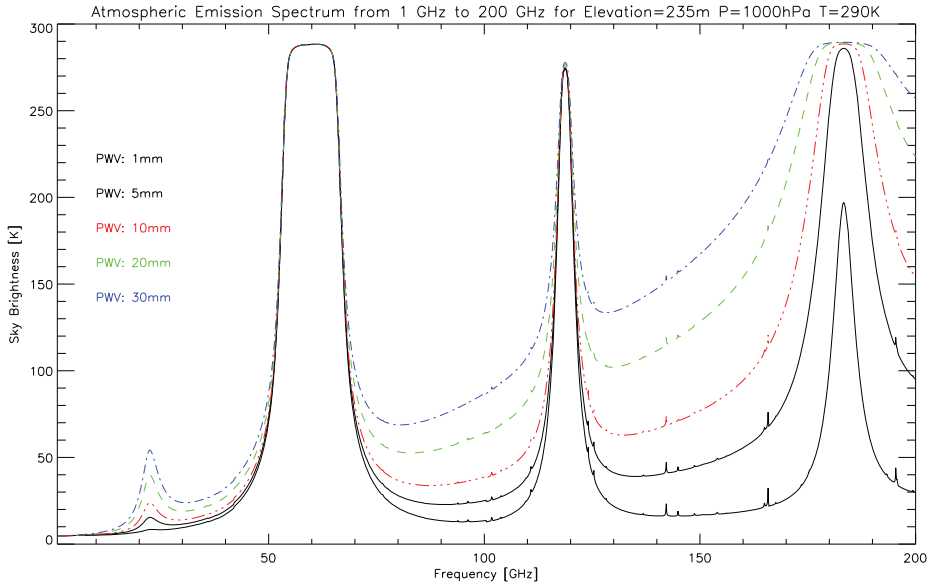

Figure 6.2.1: The atmospheric emission from 1 GHz to 200 GHz for a range of PWV conditions, modelled using the ATM model. Variations in precipitable water vapour (PWV) are shown. The features at 22.2 GHz and 183.3 GHz are the prominent water lines. The 60 GHz and 118 GHz features are caused by O_2. It is immediately evident that for the PWV values of 5 mm to 30 mm encountered at the ATCA site in Narrabri, only the 22.3 GHz line is a viable candidate as the 183.3 GHz line is completely saturated. For locations where the PWV falls below 2 mm, the 183.3 GHz line is the better choice. Note also that the continuum increases as $\approx \nu^2$ [64] [52] [59].

strong emissions from 55 – 65 GHz and 116 – 120 GHz are caused by O_2. The higher frequency water vapour emission is saturated at PWV values typically encountered at Narrabri of 5 mm or more and therefore cannot be used to measure PWV content. The line at 22.2 GHz on the other hand does not saturate. However on dry sites, such as on the Atacama Plateau, this line is too weak to be used to measure PWV.

We describe the line strength of the water vapour emission in units of brightness temperature T_b (we also use the term "sky temperature" interchangeably) instead of using specific intensity I_ν. We define T_b as follows:

$$T_b = \frac{c^2}{2k\nu^2} I_\nu \tag{6.2.1}$$

where ν is the frequency. Since we are in the Rayleigh-Jeans regime ($h\nu \ll kT$ applies), the brightness temperature of a black body is equal to its physical temperature.

Below 30 GHz, absorption and emission is dominated by the weak 6_{16}–5_{23} transition of H_2O [35], [45]. In the following we are concerned only with the description of the mechanism of absorption. To obtain an absorption coefficient which is dependent on temperature, density and total pressure we can write the Van Vleck – Weisskopf profile as follows [57],[53]:

$$\begin{aligned}\alpha = &\left(3.24 \times 10^{-4} e^{\frac{-644}{T}}\right) \frac{\nu^2 P \rho_V}{T^{3.125}} \left(1 + 0.0147 \frac{\rho_V T}{P}\right) \\ &\times \left[\frac{1}{(\nu - 22.235)^2 + \Delta\nu^2} + \frac{1}{(\nu + 22.235)^2 + \Delta\nu^2}\right] \\ &+ 2.55 \times 10^{-8} \rho_V \nu^2 \frac{\Delta\nu}{T^{\frac{3}{2}}} \ [\mathrm{cm}^{-1}]\end{aligned} \tag{6.2.2}$$

$\Delta\nu$ is the half width at half maximum of the line in GHz, given by the equation

$$\Delta\nu = 2.58 \times 10^{-3} \left(1 + 0.0147 \frac{\rho_V T}{P}\right) \frac{P}{(T/318)^{0.625}} \ [\mathrm{GHz}] \tag{6.2.3}$$

where ν is the frequency in GHz, T the temperature in K and P the total pressure in hPa. ρ_V is the water vapour density in g/m^3. Using the Van Vleck – Weisskopf formula, we can obtain α for each frequency.

As we are in the regime where the Rayleigh-Jeans approximation to the Planck function is valid, the intensity of the emission is proportional to the brightness temperature. We therefore can rewrite the equation of radiative transfer as follows:

$$\frac{\mathrm{d}\, T_B}{\mathrm{d}\, y} = -\alpha \left(T_B - T\right) \tag{6.2.4}$$

where T_B is the brightness temperature defined in 6.2.1 and α is the absorption coefficient defined in the Van Vleck – Weisskopf formula 6.2.2. Solving 6.2.4 for radiation propagating along the height axis h, we obtain:

$$T_B(\nu) = T_{B0}(\nu)e^{-\tau_\nu} + \int_0^\infty \alpha(\nu, h)T(h)e^{-\tau'_\nu}dh \tag{6.2.5}$$

where T_{B0} is the brightness temperature in the absence of absorption, i.e. the emission from space,

$$\tau'_\nu(h) = \int_0^h \alpha(\nu, h')dh' \tag{6.2.6}$$

and

$$\tau_\nu(h) = \int_0^\infty \alpha(\nu, h')dh' \tag{6.2.7}$$

Equation 6.2.5 illustrates the fundamental law that absorption always is accompanied by emission: The second term on the right hand side of the equation describes the emission contribution of the atmosphere, while the first term describes absorption. If $T(h)$ remains constant, equation 6.2.5 can be rewritten as

$$T_B(\nu) = T_{B0}(\nu)e^{-\tau_\nu} + T(1 - e^{-\tau_\nu}) \tag{6.2.8}$$

This simplifies equation 6.2.5 so that we only have to estimate opacity τ_ν.

The cause of degraded image quality or even decorrelation for an interferometer is that of path length variations due to changes in the refractive index in the individual lines of sight through the atmosphere above each antenna. Absorption and propagation delay (which leads to the change in refractive index) are intimately linked as they are derived from the real and imaginary parts of the dielectric constant. Those parts are not independent of each other, they are linked by the Kramers-Krönig relation. This is demonstrated in [58] and based on the seminal work in [15] and [33]. The delay aspect of this relation is what translates to a phase shift at the frequency of interest. For wavelengths longer than a few cm, this is a negligible quantity, but in the millimetre bands it can be large.

We continue following [57] to derive the index of refractivity in dependence of atmospheric parameters: From classical work [16] it can be shown that the refractivity of molecules with induced dipole moments varies with pressure and T^{-1}, and the refractivity of molecules with permanent dipole moments varies as pressure and T^{-2}. The atmosphere's main constituents are O_2 and N_2, which, being homonuclear, have no permanent electric dipole moments. H_2O on the other hand does, as well as a number of other constituents present in small quantities. From this we can formulate the general form of the refractivity equation:

$$N = \frac{K_1 p_D}{T\mathcal{Z}_D} + \frac{K_2 p_V}{T\mathcal{Z}_V} + \frac{K_3 p_V}{T^2 \mathcal{Z}_V} \tag{6.2.9}$$

where p_D is the partial pressure of dry air, p_V that of water vapour, $\mathcal{Z}_D$ and $\mathcal{Z}_V$ their respective compressibility factors, and K_1, K_2 and K_3 are constants. The compressibility factors $\mathcal{Z}$ correct for non-ideal gas behaviour. For atmospheric conditions encountered at Narrabri, these factors deviate from unity by less than 0.1% so we assume unity for them ($\mathcal{Z}$=1). The K constants are evaluated from a survey of the dielectric constant of water vapour in [4] on pages 5 and 6 as $K_1 = 77.607 \pm 0.13$ K mbar^{-1}, $K_2 = 71.6 \pm 8.5$ K mbar^{-1} and $K_3 = 3.747 \pm 0.031 \times 10^5$ K^2 mbar^{-1}. With this we can rewrite equation 6.2.9 as:

$$N = 77.6\frac{p_D}{T} + 64.8\frac{p_V}{T} + 3.776 \times 10^5 \frac{p_V}{T^2} \tag{6.2.10}$$

p_D and p_V are given in mBar, T in kelvin. When substituting for total pressure P, the temperature in kelvin for T, and for temperatures around 280K, equation 6.2.10 then becomes the Smith-Weintraub equation [17]:

$$N \simeq \frac{77.6}{T}\left(p + 4810\frac{p_V}{T}\right) \tag{6.2.11}$$

Refractivity N (or the refractive index i, where $N = i - 1$) in a gas is related to the density of its constituents. Using the ideal gas equation, we can substitute the pressure for density. This is achieved by starting out with the ideal gas equation:

$$p = \frac{\rho R T}{M} \tag{6.2.12}$$

where p = the pressure and ρ the density of any of the constituent gases, R = the universal gas constant 8.314 J $mol^{-1}K^{-1}$, T = temperature in K and M is the molecular weight of the gas in g mol^{-1}. For dry air, M_D = 28.96 g mol^{-1}, and for water vapour M_V = 18.02 g mol^{-1} and M_T is the total molar mass of air:

$$M_T = M_V + M_D \tag{6.2.13}$$

Since total pressure p_T is the sum of the partial pressures p_D (dry partial pressure) and p_V (vapour partial pressure), ρ_T is the total density, ρ_D is the dry air density and ρ_V is the water vapour density, we can derive the total molar mass of humid air by starting with these identities:

$$p_T = \frac{\rho_T RT}{M_T} \quad p_D = \frac{\rho_D RT}{M_D} \quad p_V = \frac{\rho_V RT}{M_V}$$

then, stating:

$$p_T = p_V + p_D \tag{6.2.14}$$

and through algebraic reforming we can obtain:

$$\frac{\rho_D}{M_D \rho_T} + \frac{\rho_V}{M_V \rho_T} = \frac{1}{M_T} \tag{6.2.15}$$

Substituting the dry and vapour components of equation 6.2.12 into equation 6.2.10 and setting $\rho_D = \rho_T - \rho_V$, we obtain:

$$N = 0.2228\rho_T + 0.076\rho_V + 1742\frac{\rho_V}{T} \tag{6.2.16}$$

and, because the second term is small in relation to the third term, they can be combined and for T = 280 K we obtain the refractive indices for dry air N_D and water vapour N_V:

$$N \simeq 0.2228\rho_T + 1763\frac{\rho_V}{T} = N_D + N_V \tag{6.2.17}$$

The quantity we are interested in is the electrical path $\mathcal{L}_V$ induced by the water vapour's dipole moment. We can thus integrate the vapour components of equation 6.2.17 (i.e. N_V) over the height of the troposphere and obtain the electrical path (converted to millimetres):

$$\mathcal{L}_V = 1.763 \times 10^{-6} \int_0^\infty \frac{\rho_V(h)}{T(h)} dh \text{ [mm]} \tag{6.2.18}$$

Liquid water does not affect path delays, only the vapour component therefore is of interest. We hence define the vapour component PWV:

$$PWV = \frac{1}{\rho_W} \int \rho_V \tag{6.2.19}$$

Since we are not interested in absolute water vapour determination but in the path difference (or path excess) $\mathcal{L}_{VX}$ between two lines of sight we can rewrite equation 6.2.18 and substitute the difference in the vapour component ΔPWV to yield the excess path $\mathcal{L}_{VX}$ the signal has travelled through between two antenna beams:

$$\mathcal{L}_{VX} = 1.763 \times 10^{-6} \frac{\Delta PWV \rho_W}{T} \text{ [mm]} \tag{6.2.20}$$

where ΔPWV is the difference in the water vapour columns between the two beams. We thus obtain a path length excess in mm, and from this the phase angle difference $\Delta\Phi$ in degrees, with λ in mm:

$$\Delta\Phi = 360 \frac{\mathcal{L}_{VX}}{\lambda} \tag{6.2.21}$$

From equation 6.2.20, we can also establish the simple relationship under the assumption of T = 292 K:

$$\mathcal{L}_{VX} \approx 6.04 \cdot \Delta\text{PWV [mm]} \tag{6.2.22}$$

6.2.2 Required Accuracy

The expected level of decorrelation of the incoming signal can be expressed using the Ruze formula [48] shown in equation 6.2.23. This equation states that for a signal reflected off an antenna surface, the aperture efficiency is A/A_0.

$$A = A_0 e^{-(\frac{4\pi\sigma}{\lambda})^2} \tag{6.2.23}$$

Applying this to interferometry, the phase shift inducing error term which for single dish application is $\frac{4\pi\sigma}{\lambda}$ is halved to $\frac{2\pi\sigma}{\lambda}$ because the locus of the error is above the antenna and the path error is thus induced only

once, whereas in the single dish case, both the incident and exiting angles are contributing to the error. We then substitute to express the required precision as a λ fraction N, and obtain this by setting $\sigma = \lambda/N$. This results in the correlation efficiency figure in equation 6.2.24:

$$A = e^{-(\frac{2\pi}{N})^2} \tag{6.2.24}$$

Plotting this function in Figure 6.2.2 then gives the limits to which we need to be able to correct in order for the WVRs to provide meaningful levels of improvement: Assuming we want to improve to a correlation efficiency of at least $\epsilon = 0.5$, the water vapour phase corrections need to be better than $N_{threshold}$ as expressed in equation 6.2.25:

$$N_{threshold} = \frac{\lambda}{7.5} \tag{6.2.25}$$

This then enables us to determine the required temperature precision to which we must be able to determine the line shape of the 22.2 GHz water line. We look at the behaviour of the water line when introducing the excess electrical path caused by the water vapour pockets, and determine a temperature to water vapour excess ratio.

6.3 Applying WVR Corrections

6.3.1 Simulations

For our simulations, we use the Atmospheric Transmission at Microwaves (ATM) model developed by Pardo et al. [45]. The ATM model has been developed to substantially improve on the older models such as the Millimetre Wave Propagation Model (MPM) developed by Liebe [35] and further extending it through to 10 THz. The differences to MPM at frequencies below 1 THz are very small. The O_2 line at 60 GHz for instance differs by only 0.2% from the MPM model as does the behaviour of the H_2O line, which differs both at 22.235 and 183.31 GHz by less than 0.7% from the ATM model. The Van Vleck – Weisskopf (VVW) profile we have described in equation 6.2.2 and used to derive the absorption coefficients is used also in the ATM model. At frequencies of less than 1.2 THz, ATM and VVW are identical in their description of the H_2O line shape.

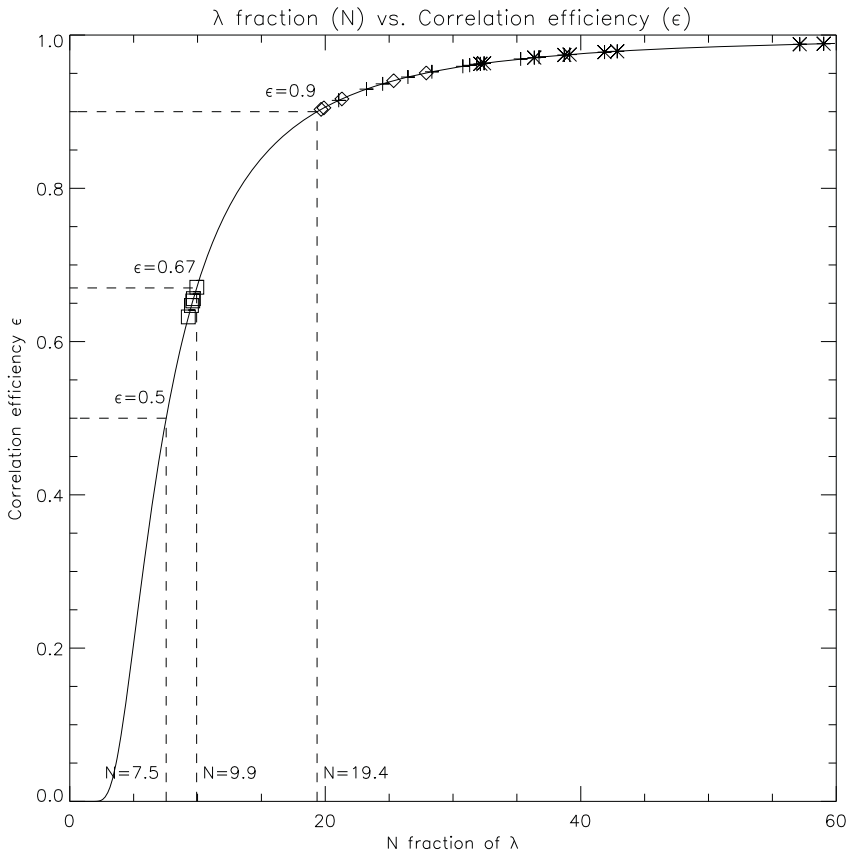

Figure 6.2.2: Plotting the fraction of wavelength corresponding to the path difference $\mathcal{L}_{VX}$ vs. the resulting correlation efficiency: The solid line plots the Ruze formula (see equation 6.2.23). Over-plotted onto that line are shown the resulting correlation efficiency figures derived from the measured phase noise in the test observations undertaken. Stars show short baselines with interpolated data, where correlation efficiency is generally better than 0.95, plus signs show the short baselines with WVR corrections applied. Even though this results in some noise being added and thus a lowered correlation efficiency, it remains above 0.9. On the long baselines, the WVR improvements are substantial: Without corrections, the interpolated data results in efficiencies of about 0.65 (squares), which, when WVR corrections are applied, corrects to better than 0.9 (diamonds).

The line profiles created with the MPM, ATM and VVW models were used in the introduction to show that we need to be using the 22.2 GHz water line at Narrabri (as opposed to the 183.3 GHz water line used for e.g. ALMA). We also determined the anticipated sky temperature fluctuations and thus the required precision to determine the line profile temperatures.

The variations in the simulated sky temperature spectrum obtained by varying the atmospheric pressure, temperature and precipitable water vapour (PWV) has been found to be chiefly dominated by the PWV level itself. The extremes we are interested in are between 5 mm and 30 mm PWV, the lower value representing the lowest values during winter, and the larger value being the cutoff where millimetre observing is discontinued due to excessive sky noise (and temperature). Figure 6.3.1 shows the water line shape for a variety of temperature, pressure and PWV conditions. The labels to the curves indicate (in red) the lines for a pressure of 980 hPa and a set of three values of 5, 15 and 30 mm of PWV, while maintaining constant temperature of 292 K. The blue labels on the right hand side mark the lines depicting the line shape for a pressure of 1030 hPa with otherwise same variations in PWV. It is evident that lower pressure results in an elevated peak temperature at the centre of the water line: 55.1 K is the peak temperature at 980 hPa, while at 1030 hPa the temperature drops to 53.7 K. Table 6.3.3 lists the peak values. Figure 6.3.2 shows the same frame of reference but this time with varying temperature: The lefthand side shows (in red) the 300 K line shapes for 1030 hPa pressure and 5, 15 and 30 mm of PWV, while the right hand side shows the same in blue for 270 K. Table 6.3.3 lists the peak values.

Looking at the model data in more detail, we can show the behaviour of the 22.2 GHz water line by varying atmospheric parameters and making contour plots to illustrate the dependencies in a 3 x 3 grid. In the temperature plot shown in Figure 6.3.3, we show a 3 x 3 grid reflecting atmospheric conditions at Narrabri. In the vertical arrangement of the individual panels, we change the atmospheric pressure from 980 hPa (top)

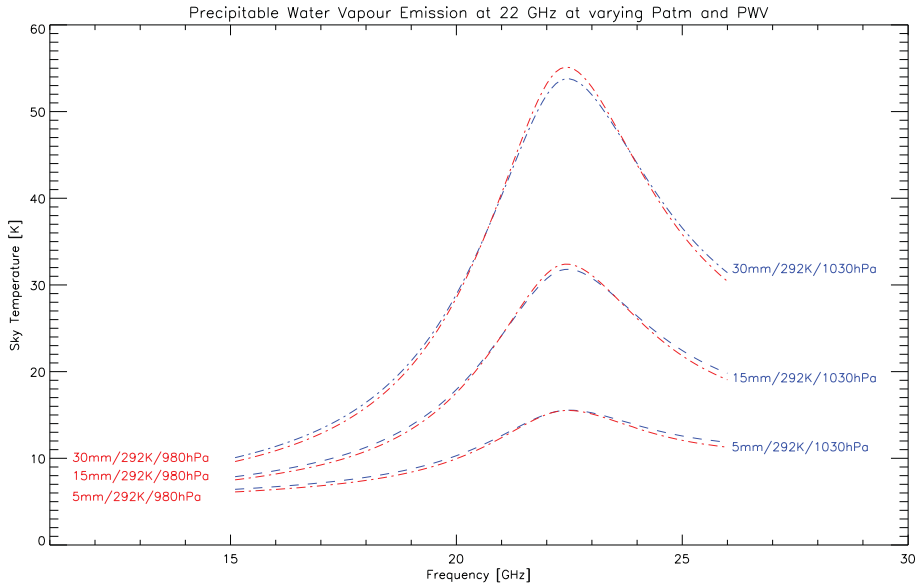

Figure 6.3.1: 22.3 GHz water line as determined by the ATM model with varying pressure and PWV: The pressure is changed from 980hPa to 1030 hPa, the range encountered at Narrabri, whereas the PWV is varied from 5 mm to 30 mm, again reflecting typical values encountered throughout the year at Narrabri. It is evident that the largest influence on the sky temperature is caused by the amount of PWV. The peak values are listed in Table 6.3.3.

PWV [mm]	T_{amb} [K]	P [hPa]	Peak T_{Sky} [K]	Sensitivity [K, hPa]
30	300	1030	55.1	0.17 T_{sky}/T_{amb}
30	292	980	55.1	0.03 T/P
30	292	1030	53.7	0.03 T/P
30	270	1030	49.9	0.17 T_{sky}/T_{amb}
15	300	1030	32.4	0.09 T_{sky}/T_{amb}
15	292	980	32.3	0.01 T/P
15	292	1030	31.8	0.01 T/P
15	270	1030	29.8	0.09 T_{sky}/T_{amb}
5	300	1030	15.7	0.02 T_{sky}/T_{amb}
5	292	1030	15.5	0.000 T/P
5	292	980	15.5	0.000 T/P
5	270	1030	15.0	0.02 T_{sky}/T_{amb}

Table 6.3.1: The peak temperature in dependence of environmental parameters PWV, temperature and pressure, ordered by descending peak temperature. The sensitivity column shows how sensitive the peak sky temperature is to a change in two variable parameters and the third parameter being held constant at the brightest point in the spectrum (at around 22.3 GHz), i.e. $\Delta T_{Sky}/\Delta T_{Amb}$ with P constant, or $\Delta T_{Sky}/\Delta P$ with T_{Amb} constant. The peak temperature changes by about 10% between 270 K and 300 K for high PWV values, about half that for low PWV values.

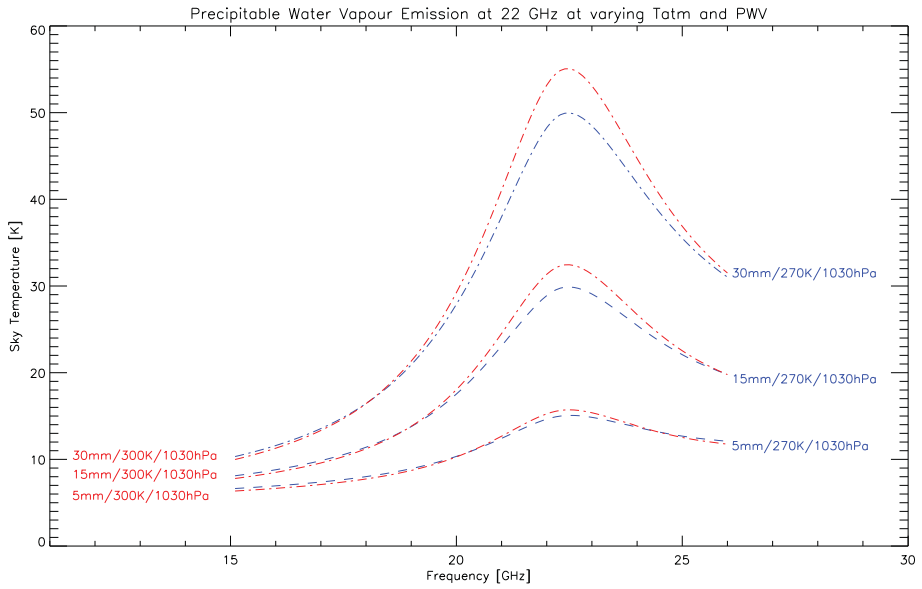

Figure 6.3.2: 22.3 GHz water line as determined by the ATM model with varying atmospheric temperature. The labels to the curves show the variation in PWV. A change in atmospheric temperature from 270K to 300K has a substantial effect on the line, larger than temperature, however, PWV remains by far the most dominant determinant. The peak values are listed in Table 6.3.3.

to 1030 hPa (bottom) with an intermediate step at standard atmospheric pressure of 1013 hPa. We note that the temperature peak at the centre of the water line at 22.2 GHz and 15 mm PWV decreases by about 0.6 K as the pressure is increased to 1030 hPa. In the continuum end of the spectrum around 16 GHz, the temperature increase caused by the pressure increase amounts to ~0.3 K.
In the horizontal arrangement of the panels we vary the PWV from 5 mm to 30 mm with an intermediate step at 15 mm. This variation in PWV, as is immediately obvious, shows much bigger differences in sky temperature: At the line centre of 22.2 GHz at 1013 hPa ambient pressure, the temperature increases from 16 K to 55 K as the PWV is increased from 5 mm to 30 mm. The continuum is also impacted significantly, almost doubling in temperature from ~7 K to ~14 K at 16 GHz as the PWV is increased from 5 mm to 30 mm. It is evident that the isothermal lines are almost vertically aligned. This means that ambient temperature has a small effect on the sky temperature at a given frequency.

In the temperature plot shown in Figure 6.3.4, we again show a 3x3 grid arrangement of panels showing variations in temperature and pressure. In the vertical arrangement, we change the atmospheric temperature from 270 K (top) to 300 K (bottom) with an intermediate step at 287 K. We note that the temperature peak at the centre of the water line at 22.2 GHz increases by about 2 K as the atmospheric temperature is increased to 300 K at a PWV of 15 mm. In the continuum end of the spectrum at 16 GHz, the temperature increase caused by the atmospheric temperature increase amounts to ~0.1 K, a practically negligible amount.
In the horizontal arrangement we again vary the PWV and yield much bigger differences: At the line centre of 22.2 GHz, the temperature increases from 15 K to 53 K as the PWV is increased from 5 mm to 30 mm at an ambient temperature of 287 K. The continuum is also impacted significantly, almost doubling in temperature from ~7 K to ~13 K at 16 GHz as the PWV is increased from 5 mm to 30 mm.

Finally, in the panels shown in Figure 6.3.5, we vary the pressure in the vertical arrangement for a given ambient temperature from 980 hPa (top) to 1030 hPa (bottom) with an intermediate step at 1013 hPa. We see that atmospheric pressure only affects the peak temperature by about

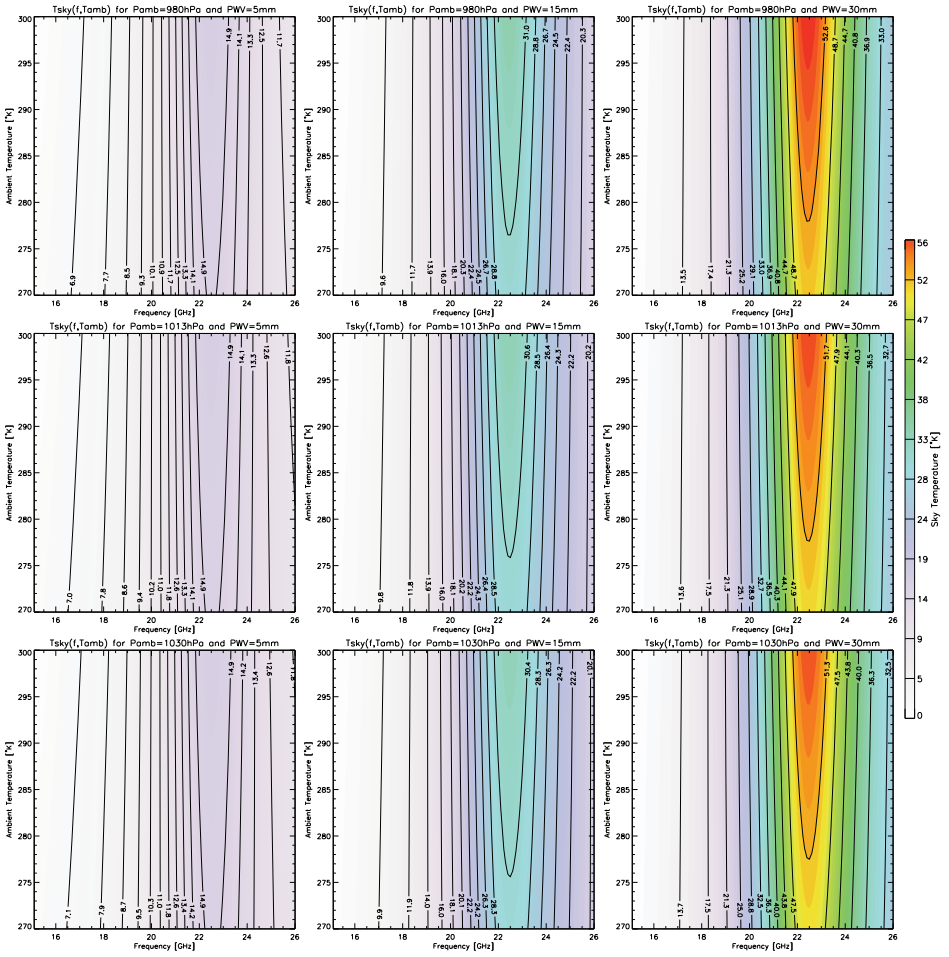

Figure 6.3.3: Sky Temperature as a function of ambient temperature, frequency, PWV and pressure. We show nine contour plots illustrating the sky temperature as a function of ambient temperature and frequency. For each of the panels, the atmospheric pressure is increased from top to bottom. PWV is increased from left to right. We see that the isothermal lines follow an almost vertical profile along the atmospheric temperature axis. This shows that it is primarily frequency that affects sky temperature.

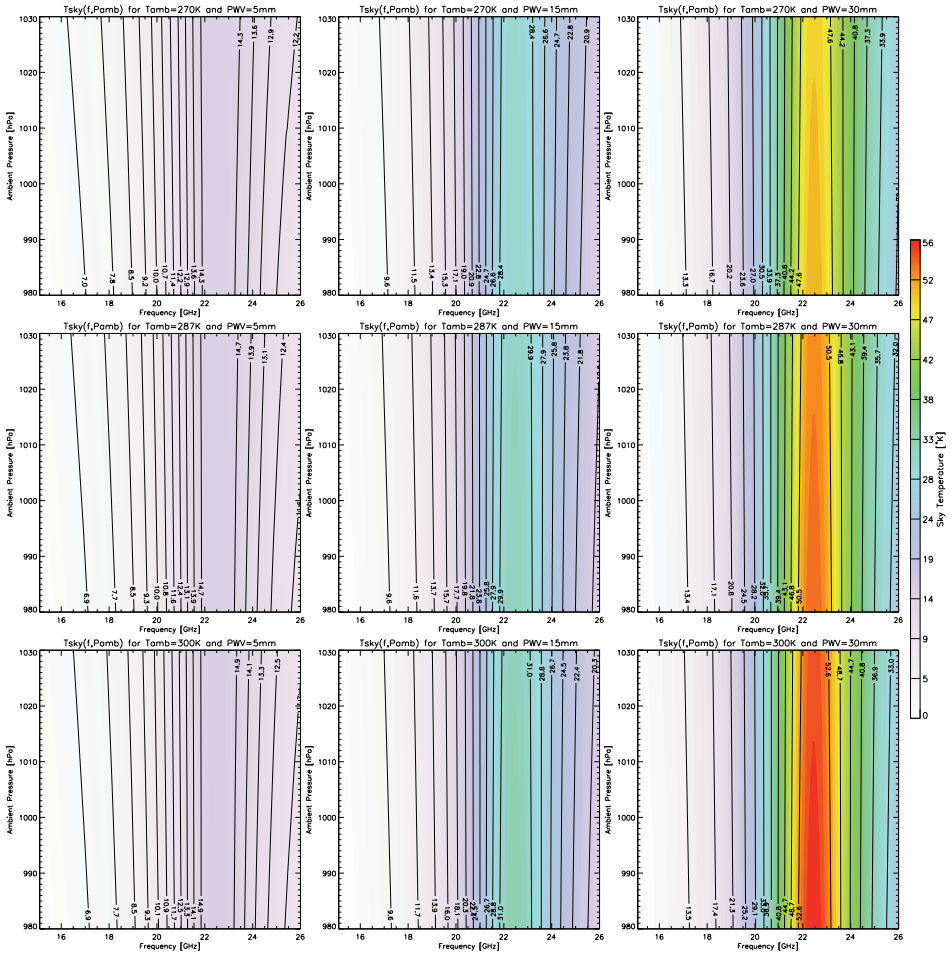

Figure 6.3.4: Sky Temperature as a function of ambient pressure, frequency, PWV and ambient temperature. Here we show 9 contour plots depicting sky temperature as a function of ambient pressure and frequency. Between the panels, ambient temperature is increased from top to bottom, and the PWV is increased from left to right. Note almost vertical isothermal lines, indicating frequency dependence dominates pressure dependence.

2 K, confirming the minimal dependence of the water line sky emission on atmospheric pressure. In the continuum end of the spectrum around 16 GHz, the temperature increase caused by the atmospheric pressure is even smaller and amounts to ~0.1 K, a negligible amount.
In the horizontal arrangement, we vary the atmospheric temperature and yield slightly bigger differences: At the line centre of 22.2 GHz, the peak temperature increases from 51 K to 56 K as the atmospheric temperature is increased from 275 K to 300 K. The continuum around 16 GHz is barely affected with a temperature rise of a little more than 0.6 K.

Figure 6.3.5 illustrates very well the strong dependence of sky temperature on the PWV level. The sky temperature change (the gradient) at the line centre for a given amount of water vapour changes between low and high PWV conditions: At a PWV of 5 mm, the temperature gradient at the line centre amounts to 0.5 mm/K, while at 22 mm PWV, the temperature gradient rises to 0.8 mm/K.

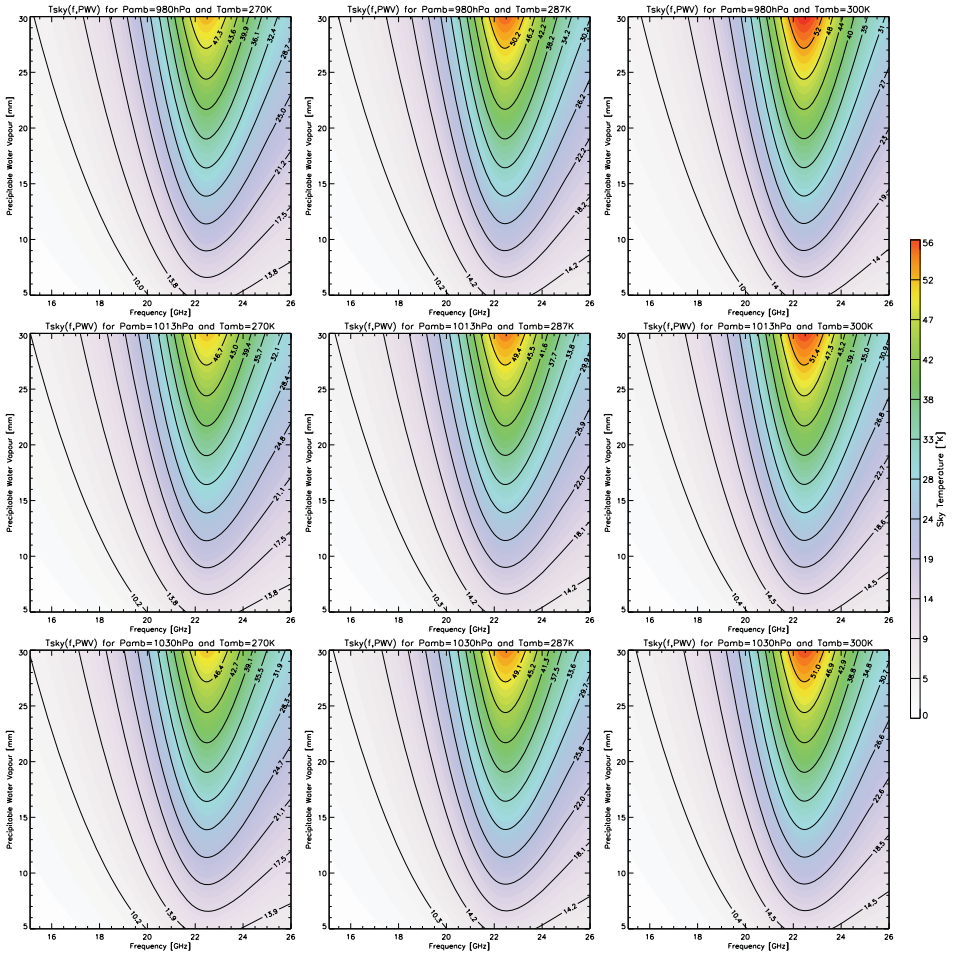

Figure 6.3.5: Sky Temperature as a function of PWV, frequency, ambient temperature and ambient pressure. 9 panels illustrate the contour plots of sky temperature as a function of frequency and PWV. Between the panels, pressure is increased from top to bottom and ambient temperature is increased from left to right. We see that PWV dominates sky temperature. Pressure has a very small effect, but we do note that the highest sky temperature is in the panel that corresponds to the lowest pressure, highest PWV and highest temperature.

Applying what we have learnt about the sky brightness temperatures and its dependence on atmospheric parameters, we can now calculate the level of precision which we need in order to determine the sky temperatures to in the various filter bands for the WVRs. Table 6.3.2 lists the required temperature precision as a function of $N_{Threshold}$. See the Ruze derived correlation efficiency equation 6.2.24 for how ϵ was determined. This then provides the path differences, $\mathcal{L}_{VX}$, which must be measured. From this, ΔPWV is found using the simplified equation 6.2.22. Given ΔPWV we then obtain ΔT from the relation for 16.5 GHz in Figure 6.3.6, which shows the variation in ΔT for a variation of ΔPWV, as calculated using the ATM model, for each of the 4 filter bands. In Table 6.3.2 we show the precision for the 16 GHz filter frequency only, because it displays the least difference in temperature as it is located very close to the continuum portion of the spectrum and so provides the most stringent limits. For all the other filters, the precision required is less by a factor of 2 – 5, as can be seen in the Figure 6.3.6. This plot shows the difference in sky temperature for a given difference in PWV for each of the filters. It is evident that the 22.9 GHz channel for instance shows a broad response to changes in PWV: For a ΔPWV of 1.7 mm, the 22.9 GHz filter will show a ΔT_{sky} of between 1.8 and 2.4 K, depending on the total PWV in the atmosphere. The 16.5 GHz channel on the other hand has a very narrow vertical extent at the same ΔPWV.

Figure 6.3.7 shows the temperature dependence in a more concise fashion: Correcting to $\epsilon = 0.5$ at the highest frequency, the line emission temperature needs at best determined to 12 mK. To correct to $\epsilon = 0.9$ also at the highest frequency, requires the measurement to be a factor of ~3 better and measure temperatures to 4 mK at 16 GHz. This results from using the Ruze and the phase angle difference formulas (see equations 6.2.23 and 6.4.10). The plot shows six pairs of models with the first pair varying pressure, the second pair varying PWV and both of those grouped for one electrical path excess λ/N. This is then repeated for three case scenarios of N (resulting in 2 pairs for 3 scenarios i.e. a total of 6 pairs). The data is calculated using the ATM model in frequency vs. temperature space. Note that because the temperature excesses are small quantities, the vertical axis unit is milli kelvins (mK). Each model shows the temperature differ-

ence the ATM model predicts for changing atmospheric conditions and an introduction of an electrical path excess corresponding to $\lambda/20$, $\lambda/10$, and $\lambda/7.5$, respectively at 3.3 mm (100 GHz). The lowest temperature differences are seen for $\lambda/20$, high atmospheric pressure and high PWV. Refer to Table 6.3.3 which lists the lowest temperature difference for 30 mm of PWV and 1030 hPa of pressure as 36.1 mK. Conversely the highest temperature differential of 123.1 mK is seen where the PWV is 5 mm and the pressure 980 hPa. That pair of models makes up the N=7.5 pair. This means that to correct for N=7.5 (or $\epsilon = 0.5$), ~3.5 times less sensitivity is required in the strongest (22.9 GHz) channel compared to the weakest (16.5 GHz) channel. In this pair, pressure broadening of the line is also nicely visible: At about 20.5 GHz and 24.5 GHz, the lower pressure curve crosses the line of the higher pressure. The temperature peak occurs at a slightly lower frequency and the shoulder of the line is broader.

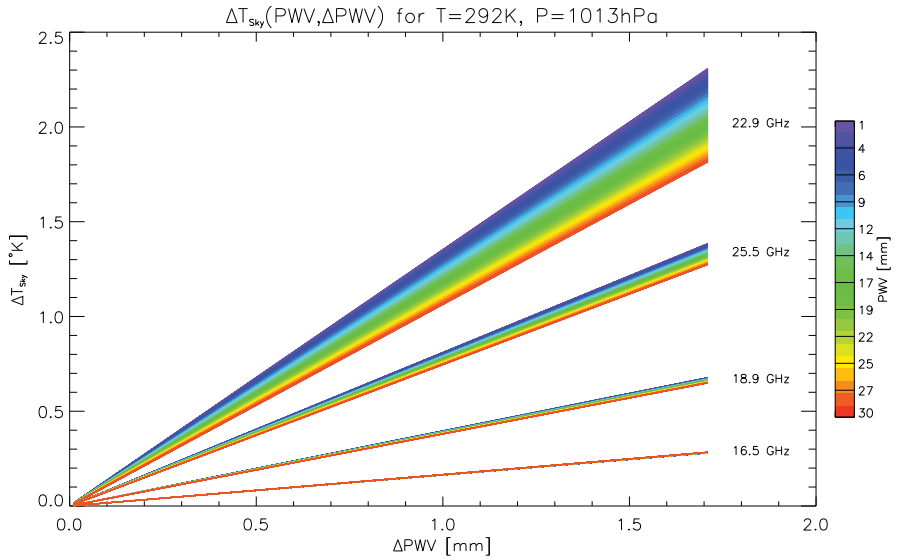

Figure 6.3.6: Using the ATM model atmosphere, we plot the difference in sky temperature for a given difference in PWV for each of the WVR filters, assuming a fixed atmospheric temperature of 292K and pressure of 1013 hPa. This is repeated for the full range of PWV values of 1 to 30 mm, and for ΔPWV's of 0.01 to 1.8 mm on the x-axis. The sky temperatures are integrated over the actual WVR filter widths of between 0.8 to 1 GHz.

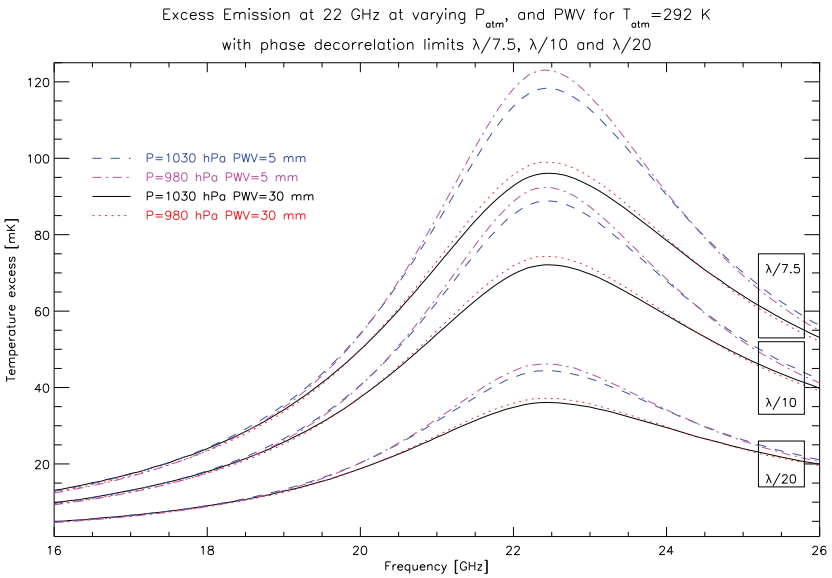

Figure 6.3.7: The 22.3 GHz water line excess measurement sensitivity required for various atmospheric conditions and phase decorrelation limits as determined by the ATM model: The boxes labelling the right hand side of the models comprise each line pair that describes the temperature excess that needs to be measured to correct to the specified fraction of λ. The labels to the left depict the variation in four atmospheric input parameters that were used to calculate the model atmosphere. For example, the solid black line corresponds to a PWV of 30 mm and a pressure of 1030 hPa. Three excess temperatures were then calculated for those parameters: One to correct to $\lambda/7.5$, which peaks at about 90 mK, one at $\lambda/10$ which peaks at about 70 mK, and one for $\lambda/20$ which peaks at about 30 mK.

	$\epsilon = 0.50$			$\epsilon = 0.67$			$\epsilon = 0.90$		
f [GHz]	$\frac{\lambda}{7.5}$ [mm]	ΔPWV [mm]	ΔT [mK]	$\frac{\lambda}{10}$ [mm]	ΔPWV [mm]	ΔT [mK]	$\frac{\lambda}{20}$ [mm]	ΔPWV [mm]	ΔT [mK]
22	1.82	0.30	50	1.36	0.23	38	0.68	0.11	18
40	1.00	0.17	28	0.75	0.12	20	0.37	0.06	10
95	0.42	0.07	12	0.32	0.053	8	0.16	0.027	4

Table 6.3.2: This table shows the required precision in temperature difference ΔT in dependence of $\frac{\lambda}{N}$ (see equation 6.2.24), correlation efficiency ϵ for each observing frequency band taken for the filter frequency with the weakest response, 16.5 GHz. The other filters need to be less precise by a factor of 2 to 5. For example, if we are to obtain corrections at 95 GHz to better than $\epsilon = 0.9$ corresponding to a path difference of $\frac{\lambda}{20}$, we need to be able to detect fluctuations of 4 mK. See equation 6.2.22 to obtain ΔPWV from the λ/N figure. These values are computed for an absolute pressure of 960 hPa, corresponding to ~980 hPa sea level pressure at observatory elevation of 235 m, temperature of 270 K, and PWV of 30 mm. These atmospheric parameters represent the worst case scenario yielding the least excess temperature for a given change in electrical path.

PWV [mm]	P [hPa]	Peak T_{excess} [mK]	N
5	980	123.1	N=7.5
5	1030	118.3	N=7.5
30	980	99.0	N=7.5
30	1030	96.1	N=7.5
5	980	92.4	N=10
5	1030	88.8	N=10
30	980	74.3	N=10
30	1030	72.1	N=10
5	980	46.2	N=20
5	1030	44.4	N=20
30	980	37.2	N=20
30	1030	36.1	N=20

Table 6.3.3: The peak temperature excess differences listed along with the environmental parameters, ordered by descending peak temperature. Low pressure and low PWV yield the highest excess. Pressure dependence is not nearly as pronounced as PWV dependence: The sky temperature difference between highest and lowest pressure only differs by 3% to 4%. The sky temperature difference between the highest and lowest PWV on the other hand differs by over 24%.

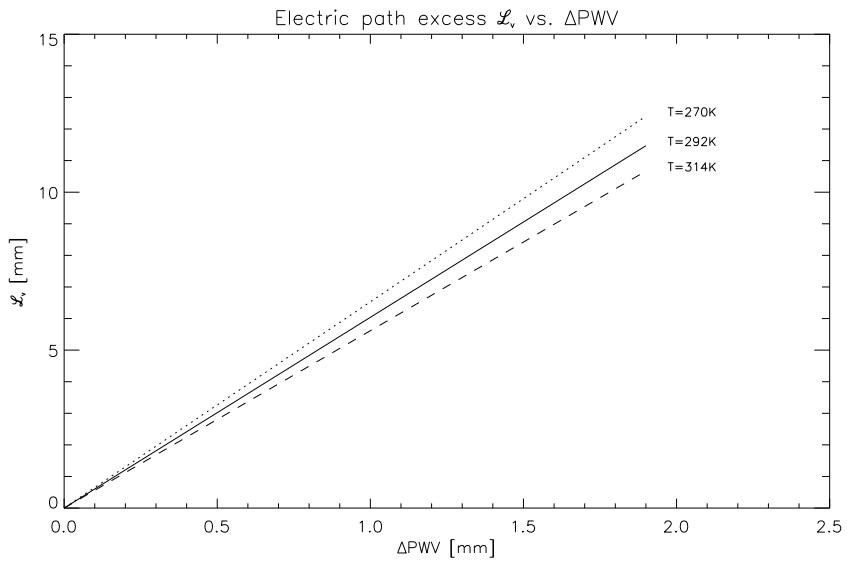

Figure 6.3.8: The relationship between the electrical path excess and the water vapour fluctuations is depicted in this graph. Equation 6.2.20 with w as the water vapour path simplifies to $\mathcal{L}_V = 1763 \cdot \frac{w}{T}$ with T in [K] and w in [mm].

6.4 Extracting Phase

Phase extraction is achieved by measuring the small variations in the line temperatures in each of the four filters at 16.5, 18.9, 22.9 and 25.5 GHz. At present, due to firmware limitations in the datasets used to interrogate the WVRs, the tunnel diode voltages are integrated only in blocks of eight measurements over a 5 ms timespan. Each channel in the WVR is sampled by the dataset sequentially. This includes all 16 signal channels, so also e.g. temperature and supply voltage monitoring points, in addition to the tunnel diode voltages for the filters. The sampling process currently is implemented as follows [23]:

- Initial delay of 15 ms to let the input and electronic components settle.
- Eight samples are taken and averaged, then stored over a timespan of 5 ms.

One channel thus takes a total of 20 ms to sample in this procedure, all 16 channels consequently take 0.32 s to sample. Referring to the required sensitivity discussed in chapter 5.2, this sampling rate is below the rate needed for the target sensitivity of 12 mK. There is room for improvement even when considering the limitations imposed by the current interrogation hardware, the datasets. The datasets have limited memory and processing power and they need to be updated in order to process all the data that can be taken by the WVRs.

6.4.1 Sensitivity

The sensitivity, according to the radiometer sensitivity equation 5.2.1 for a 5 ms readout of one channel assuming a noise temperature of 400 K is ~180 mK. We address this by averaging the samples in the data reduction stage, where at present we calculate a running mean from the average of 35 values to either side of the data point. For a total integration time of 350 ms, this translates into a sensitivity of ~21 mK.

6.4.2 DC Offset

Sensitivity is not the only reason to average data over the time domain. Some of the emission measured includes unwanted signal, such as the spillover and receiver temperatures. This is difficult to estimate and remove, so it is best to work with the differences in signal and assume changes in the quantities are slow compared to the water vapour induced fluctuations so that these terms cancel out in the subtracted quantities. We see in the next section that this indeed allows us to follow the phase variations. After converting the raw voltages into temperatures according to the conversion factors derived in chapter 5.5, we can define the total temperature T_T measured in each filter as:

$$T_T = T_D + T_V + T_S \tag{6.4.1}$$

where T_D is the dry air component, T_V is the H_2O line temperature and T_S is the spillover temperature. T_D will be the same for each antenna looking at the same azimuth and elevation, whereas T_S, the spillover temperature, varies as a function of elevation and is antenna specific. It may also include a component of the receiver temperature if this has varied since its last calibration measurement. The difference between two antennae $a1$ and $a2$ thus becomes:

$$\left.\begin{aligned} T_{T,a1} &= T_{D,a1} + T_{V,a1} + T_{S,a1} \\ T_{T,a2} &= T_{D,a2} + T_{V,a2} + T_{S,a2} \end{aligned}\right\} \text{ with } T_{D,a1} \equiv T_{D,a2} \text{ becomes :}$$

$$\Delta T_T = T_{V,a1} - T_{V,a2} + T_{S,a1} - T_{S,a2} \tag{6.4.2}$$

The key is that the spillover term only varies substantially as elevation changes, which is a slow change while tracking a source. T_V will change rapidly on the other hand. Any drift in receiver temperature since its previous calibration is incorporated into the spillover term. We can remove these drifts and offsets by calculating the differences in a running mean over the time period τ around each measurement with $2N$ points:

$$T_{DC}(\tau) = \frac{\sum_{\tau-N\Delta\tau}^{\tau+N\Delta\tau} T_D + T_V + T_S}{2N} \tag{6.4.3}$$

where $\Delta\tau$ is the time step between each sample, so that the variation between antennae $a1$ and $a2$ becomes defined solely by T_V:

$$\Delta T_T \simeq T_{V,a1} - T_{V,a2} \tag{6.4.4}$$

where these terms are averaged between $\tau - N\Delta\tau$ and $\tau + N\Delta\tau$. From this equation 6.4.4 we can derive numerically for each filter and antenna the amount of water vapour excess in the line of sight, and from that the excess electrical path length and therefore the phase delay the signal has experienced on its way through the lower troposphere. We further combine these by applying a set of weighting coefficients whose derivation we now describe in order to provide the best estimate of the phase difference.

6.4.3 Weighting Coefficients

The conversion from temperature differences in each filter and antenna pair to electrical path length $\mathcal{L}_V$ is achieved by deriving a weighting coefficient C_W for each filter. For this we model the temperatures in the filter frequencies and bandwidths for an assumed standard atmosphere. From that atmospheric model data, we determine the ratio of the filter temperature and total wet path for each filter (the total wet path is obtained using equation 6.2.18) and obtain a water vapour calibration factor K for each filter f:

$$K_f = \frac{T_f}{\mathcal{L}_V} \tag{6.4.5}$$

where $\mathcal{L}_V$ is the total wet path for the model atmosphere, listed in Table 6.4.1 and calculated from equation 6.2.18, and T_f is the temperature measured over the filter bandwidth, obtained by integrating the Van Vleck – Weisskopf profile over the respective filter frequency and bandwidth in equation 6.2.2. The range of values for the water vapour cali-

Atmosphere	Variable	Total wet path $\mathcal{L}_v$
P=1013 hPa T=292 K	PWV 30 mm PWV 1 mm Spread	181.25 mm 6.04 mm 87.6 mm
T=292 K PWV=20 mm	1030 hPa 960 hPa Spread	120.84 mm 120.84 mm 0.00 mm
P=1013 hPa PWV=20 mm	270 K 310 K Spread	130.56 mm 113.91 mm 8.3 mm

Table 6.4.1: The total wet path $\mathcal{L}_v$ for each filter and a variety of atmospheric conditions.

		Water Vapour Calibration Factor K_f [K/mm]			
Atmosphere	Variable	16.5 GHz	18.9 GHz	22.9 GHz	25.5 GHz
P=1013 hPa T=292 K	PWV 30 mm PWV 1 mm Spread	0.0440 0.0426 0.0007	0.0910 0.0914 0.0002	0.2320 0.2591 0.014	0.1636 0.1685 0.0025
T=292 K PWV=20 mm	1030 hPa 960 hPa Spread	0.0441 0.0418 0.0012	0.0917 0.0894 0.0012	0.2386 0.2480 0.005	0.1662 0.1623 0.0012
P=1013 hPa PWV=20 mm	270 K 310 K Spread	0.0411 0.0454 0.0073	0.0829 0.0975 0.0103	0.2071 0.2687 0.031	0.1501 0.1771 0.014

Table 6.4.2: The water vapour calibration factor K_f for each filter and a variety of atmospheric conditions. The spread is half the range in path length for the variation in the relevant variable (column 2). The largest spread occurs in the 22.9 GHz filter and amounts to about 10%.

		Weighting Coefficient C_W			
Atmosphere	Variable	16.5 GHz	18.9 GHz	22.9 GHz	25.5 GHz
P=1013 hPa T=292 K	PWV 30 mm	0.0213	0.0911	0.5929	0.2946
	PWV 1 mm	0.0172	0.0791	0.6353	0.2685
	Spread	0.0021	0.006	0.0212	0.0131
T=292 K PWV=20 mm	1030 hPa	0.0205	0.0886	0.5998	0.2912
	960 hPa	0.0179	0.0818	0.6304	0.2698
	Spread	0.0013	0.0034	0.0153	0.0107
P=1013 hPa PWV=20 mm	270 K	0.0228	0.0930	0.5798	0.3045
	310 K	0.0179	0.0825	0.6272	0.2723
	Spread	0.0025	0.0053	0.0237	0.0161

Table 6.4.3: The weighting coefficients C_W for each filter and a variety of atmospheric conditions. The spread is half the range in path length for the variation in the relevant variable (column 2). The largest spread occurs in the 22.9 GHz filter and amounts to about 3.5%

bration factor K for a variety of atmospheric conditions are listed in Table 6.4.2. From these values it is then possible to determine the relative weighting coefficients C_W for each filter f:

$$C_{W,f} = \frac{K_f^2}{K_{16.5}^2 + K_{18.9}^2 + K_{22.9}^2 + K_{25.5}^2} \tag{6.4.6}$$

with

$$\sum_{f=1}^{4} C_{W,f} = 1 \tag{6.4.7}$$

We have determined the coefficients C_W for a range of atmospheric conditions and listed them in Table 6.4.3. Note the lowest weight coefficient is at 16.5 GHz, which also is the filter that is most sensitive to atmospheric changes, varying by up to 27%. However, because it has the least weight, this variation is also weighted less. The highest weight coefficient is in the 22.9 GHz filter band and varies by only up to 8%. This is not surprising because it is the filter nearest to the peak feature of the 22.3 GHz water line, as we have shown in Figures 6.3.7 and 6.3.6. The emission at the line centre is varying greatly with PWV, and hence results in a high

weight for this coefficient.

For the extraction algorithm, the coefficients from Table 6.4.3 as determined for an atmosphere of P=1013 hPa, PWV=20 mm and T=292 K are used. With the coefficients as well as the emission line's calibration factor K_f determined, we can apply them to the temperature differences obtained from equation 6.4.4. This will yield the excess path $L_{x,f}$ as determined from each filter:

$$L_{x,f} = \frac{T_f}{K_f} \text{ [mm]} \tag{6.4.8}$$

We then build the weighted sum to obtain $\mathcal{L}_{VX}$ with f = filters 1 through 4 using the weighting coefficients derived from the model atmosphere in equation 6.4.6:

$$\mathcal{L}_{VX} = \sum_{f=1}^{f=4} C_{W,f} \cdot L_{x,f} \text{ [mm]} \tag{6.4.9}$$

From this it is trivial to obtain the phase difference $\Delta\Phi$ incurred by the path excess $\mathcal{L}_{VX}$ at observing wavelength λ:

$$\Delta\Phi = 360 \cdot \frac{\mathcal{L}_{VX}}{\lambda} \text{ [degrees]} \tag{6.4.10}$$

where λ and $\mathcal{L}_{VX}$ need to be in the same units of length.

6.5 Demonstrating Phase Correction

The simplest way of showing WVR phase correction at work is to examine a phase plot of an astronomical source and compare it to the measured phases obtained with the water vapour radiometers. A plot of the first data taken with the WVRs is shown in Figure 6.5.1. This simple plot illustrates the calibrator phase fluctuations in red and the WVR derived water vapour fluctuations in blue. It is evident that they follow a similar phase fluctuation. A more sophisticated series of plots follows: Figure 6.5.2 shows a 10 minute span of the short antenna 2 – 1 baseline (92 meters) for the H214 configuration of the ATCA taken on June 4 and 5 2011. The seeing monitor indicates 150 μm to 500 μm RMS for the time

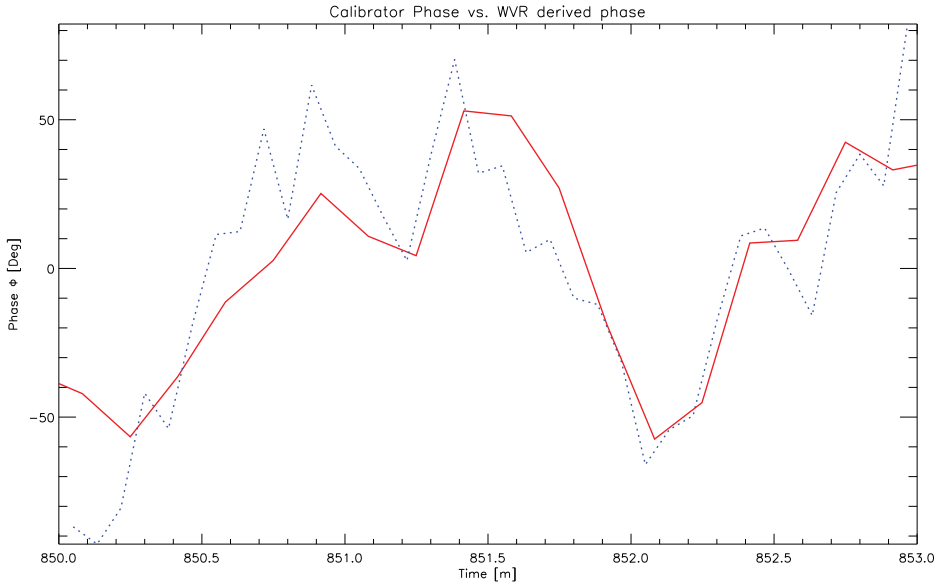

Figure 6.5.1: This is the first WVR data ever taken: In red, the calibrator phase which is seen to track the water vapour phase fluctuations. In blue, the water vapour phase fluctuations as determined by the WVRs. The calibrator data was taken at 22 GHz.

of the observations, which translates to about 12 degrees phase RMS at 15 mm observing frequency and twice that at 7 mm, about 25 degrees phase RMS. The calibrator being observed, 0537-441 is a unresolved point source for the ATCA at all frequencies and baselines. Plot 6.5.3 shows the longest baseline of 4500m formed between antennae 6 and 1. Comparing the phase fluctuations between the WVR corrected data and the interpolated data directly yields a figure of merit for the observations: By comparing the residual phase RMSs we can see whether the WVR corrections have improved the phase determination. The interpolated phase thereby represents the best phase estimate that can be obtained with normal, pre-WVR observing by taking a calibrator phase measurement at the beginning of the scan, one at the end, and using the resulting slope defined by the two phase measurements to interpolate against, hence its name "interpolated phase". This determination makes the assumption that the phase has changed linearly from the starting point to the end

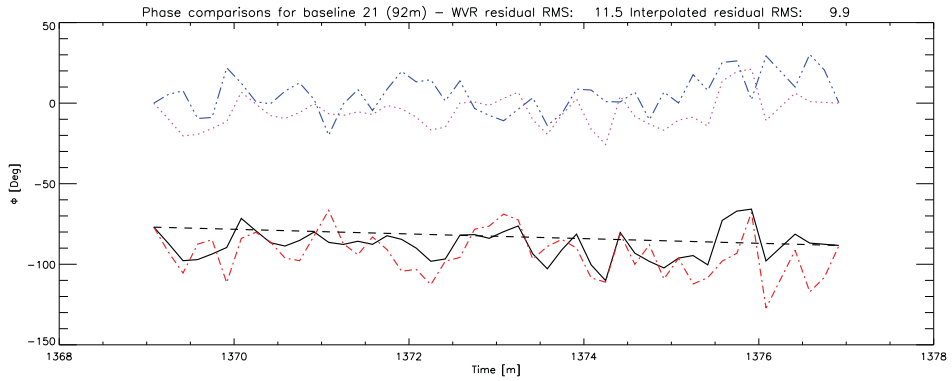

Figure 6.5.2: Phase comparison over a 92 m baseline: Solid: calibrator phase (black), WVR derived phase, dash-dotted (red), Observed phase minus WVR phase Dash-dot-dot (blue), referred to as the "WVR residual phase", and Observed phase minus interpolated phase, dotted (magenta), referred to as the "interpolated residual phase". The quantity we use to assess the merit of the corrections with is the deviation from zero of the residual phases, i.e. their phase RMS. The interpolated phase is simply the linear interpolation between the two bracketing calibrator observations, in this graph between the leftmost and rightmost datapoint, depicted as the black dashed line. The calibrator phase data was taken at 22 GHz.

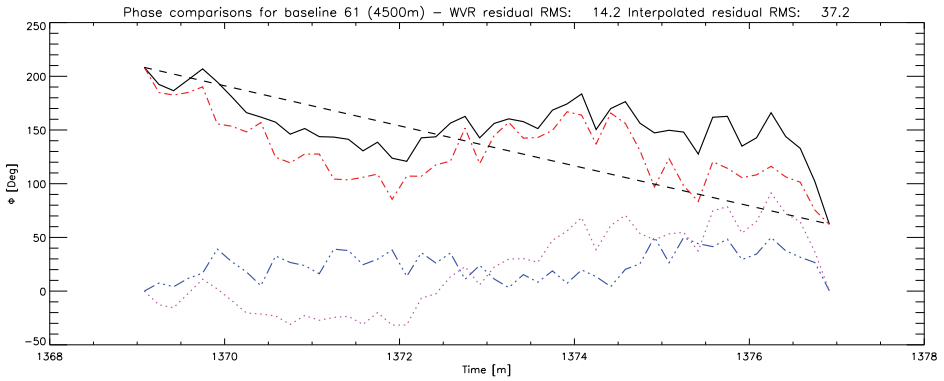

Figure 6.5.3: Phase comparison for the long baselines 61: Solid: calibrator phase (black), WVR derived phase, dash-dotted (red), Observed phase minus WVR phase Dash-dot-dot (blue), referred to as the "WVR residual phase", and Observed phase minus interpolated phase, dotted (magenta), referred to as the "interpolated residual phase". The quantity we use to assess the merit of the corrections with is the deviation from zero of the residual phases, i.e. their phase RMS. The interpolated phase is simply the linear interpolation between the two bracketing calibrator observations, in this graph between the leftmost and rightmost datapoint, depicted as the black dashed line. The calibrator phase data was taken at 22 GHz.

point.

It is immediately evident from comparing the two cases that the WVR derived phases track the calibrator phase on longer time scales (minutes). When looking at smaller timescales however, there is considerable scatter about the true phase values. The WVR derived phase RMS is 13.8 degrees for the short baseline example. When the differences are formed to create the residual phases, the WVR residual is still 11.5 degrees, while the interpolated residual at 9.9 degrees is only slightly worse than the observed data. Refer to Table 6.5.1 for a detailed comparison of the residual phase RMSs.

For the long baseline 6 – 1 in Figure 6.5.3, there is an even better long term tracking between the WVR and the calibrator phases and this is a considerable improvement on the interpolated phase. The WVR residual have corrected to an RMS of 14.2 degrees, whereas interpolated residual remains high at 37.2 degrees. This is a clear improvement of the phase.

Another performance indicator we examine relates to comparing the interpolated residual phase RMS with the WVR corrected residual phase RMS as a function of baseline, as shown in plot 6.5.4. This plot shows that on long baselines, the residual phase error was improved by about 21 degrees, however on the short baselines, it was made worse by 3 degrees, a for all practical purposes negligible amount, refer Figure 6.2.2 why this is the case. It does however hint at a noise floor limitation of about 10 degrees which cannot be improved upon. Table 6.5.1 lists the resulting RMS errors and efficiencies for all baselines. It is evident from that Table that while WVR corrections introduce a small amount of noise in short baselines and reduce correlation efficiency on average by 0.02 for those baselines, on the long baselines their corrections are improving the correlation efficiency to above 0.92 on average. Please refer to appendix C for a list of all plots for all baselines.

Also note that several sets of test observations were made during the testing of the WVR system. We limit discussion to one data set only for brevity and clarity. The other data do not exhibit behaviour that is in any way different from the data presented here.

	Interpolated		WVR Corrected		Improved
Baseline [m]	σ_{Int}	ϵ_{Int}	σ_{WVR}	ϵ_{WVR}	Correlation Efficiency $\Delta\epsilon$
92	9.9	0.97	11.5	0.96	–0.01
230	9.3	0.97	11.3	0.96	–0.01
138	5.5	0.99	11.7	0.96	–0.03
144	6.3	0.98	9.8	0.97	–0.02
82	8.6	0.98	12.7	0.95	–0.03
132	6.1	0.99	10.2	0.97	–0.02
247	11.2	0.96	17.1	0.92	–0.05
216	11.1	0.96	14.7	0.94	–0.03
240	9.2	0.97	13.6	0.95	–0.03
138	8.4	0.98	15.5	0.93	–0.05
4500	37.2	0.65	14.2	0.94	0.28
4408	36.2	0.67	12.9	0.95	0.28
4270	37.4	0.65	16.9	0.92	0.26
4378	38.8	0.63	18.1	0.91	0.27
4383	37.8	0.65	18.3	0.90	0.26

Table 6.5.1: Comparing the figures of merit for each baseline: Listed are the RMS noise σ for the interpolated residual phase and for the WVR residual phase along with their respective efficiencies ϵ. The correlation efficiency of the WVR residual phase (ϵ_{WVR}) is slightly lower than the correlation efficiency of the interpolated residual phase (ϵ_{Int}) for the short baselines, because there is considerable scatter about the true phase. The magnitude however is small, only a few degrees in phase, which is negligible resulting in a decrease of between 0.01 and 0.05 in correlation efficiency. The long baselines however show substantial improvement: The correlation efficiency is improved to above 0.9 for all baselines with the WVR corrections applied. For the interpolated residual phase, the correlation efficiency is only about 0.63. Please refer to appendix C for a list of all plots for all baselines.

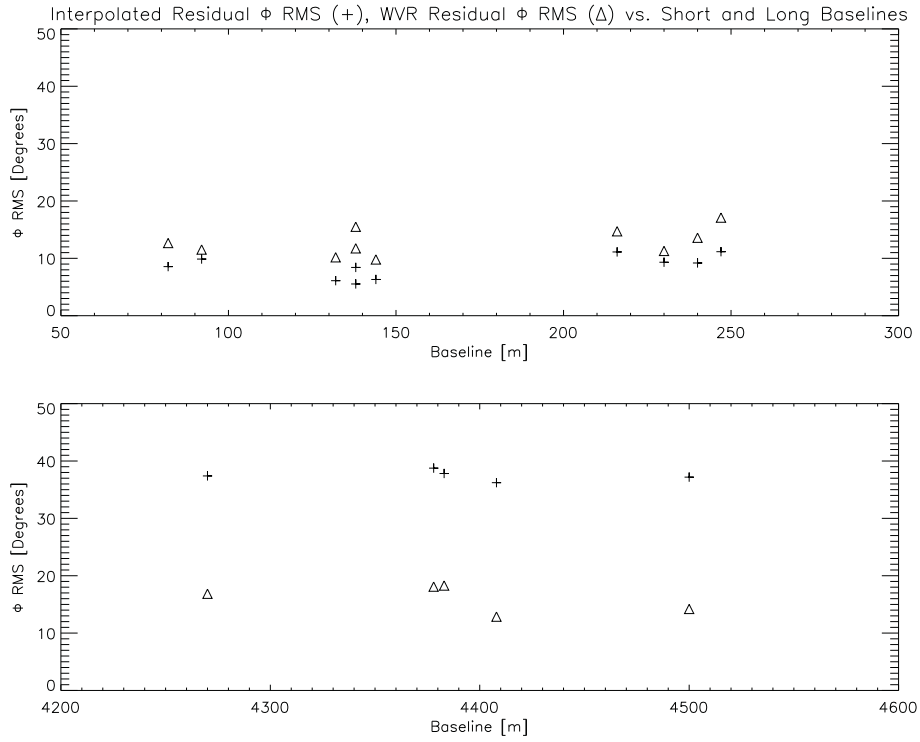

Figure 6.5.4: Residual phase comparison: We show the residual phase RMS for a 10 minute observation in dependence of the baseline. Crosses show the interpolated phase, the triangles show the WVR corrected phase. On the short baselines, the interpolated phase RMS is about 9 degrees while the WVR corrected phase RMS is about 12 degrees.

6.6 Phase Tracking Challenges

One of the challenges that had to be addressed during data reduction concerned the phase drift of the WVRs. This is best illustrated by looking at Figure 6.6.1. This shows a time span of 28 minutes which is long compared to the other data we have shown thus far, which typically spans no more than 10 minutes. For clarity only the calibrator phase (black) and the WVR derived phase (red) are plotted. The phases were matched at the beginning of the data. At the end of the 28 minutes, the WVR phase differs from the calibrator phase by about 80 degrees. The phases are expected to drift due to the measurement uncertainties including drifts in receiver temperature, as well as inaccuracies in the water vapour calibration factors K_f. These phase errors will build up over a long phase tracking period. It is nevertheless evident from the plot that the WVR and calibrator phases are tracking each other over the measured time period. For the data previously shown, the WVR data has been processed in such a manner that the phases match at both the commencement and the end of the phase segment to be corrected with a linear shift to the WVR phases applied to improve the tracking. Under the assumption that the phase is tracked in its entirety this is a valid procedure and results in lowered phase noise over just applying the raw WVR phase data.

Another phase tracking challenge encountered is illustrated in Figures 6.6.2 and 6.6.3. Both plots are also of 28 minutes in length and both feature a baseline including antenna 4. At time 1458.7 minutes a spike occurred in the WVR data which is replicated on both the 4 – 1 and 6 – 4 baselines, thus it must originate in antenna 4 (unit 7). It is not clear at present what caused this spike. It is possible that this is the effect of cloud (i.e. liquid water) in one line of sight only, or it could be an RFI spike in one of the WVR channels whose frequency is not affecting the science receiver frequency at the time. This affects the continuum end of the spectrum. It still is evident that the WVR derived phase is tracking the calibrator phase rather well especially on the shorter 4 – 1 baseline, apart from that one spike.

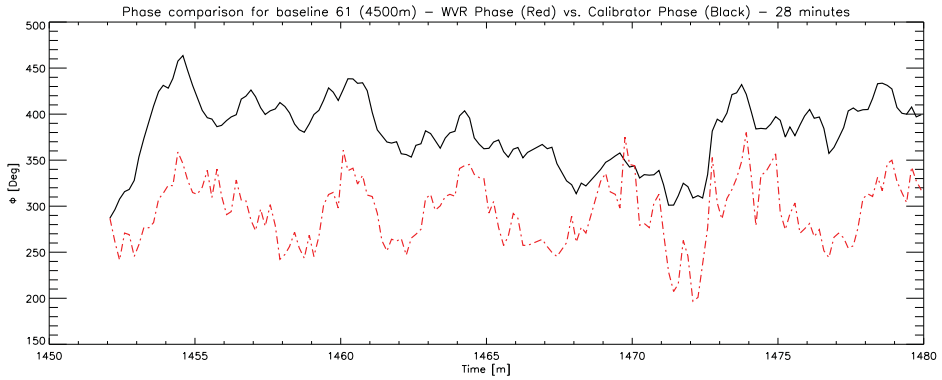

Figure 6.6.1: This phase plot illustrates a dataset of 28 minutes in duration. The calibrator data was taken at 48.3 GHz. Note the phase discrepancy of about 80 degrees at the end of the tracking time between the WVR and calibrator phase. Applying hot load calibration in regular intervals can help in reducing this phase gap.

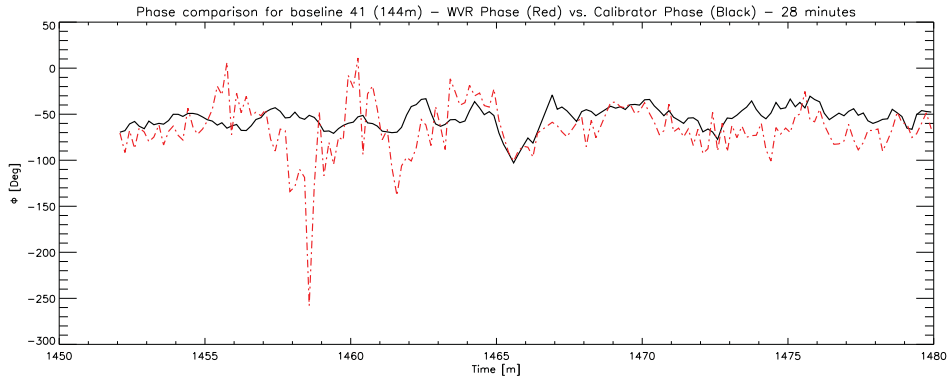

Figure 6.6.2: A 28 minute phase track at 48.3 GHz on the 144m length 4 – 1 baseline. A spike occurs in the WVR data at 1458.7 minutes that is as yet unexplained.

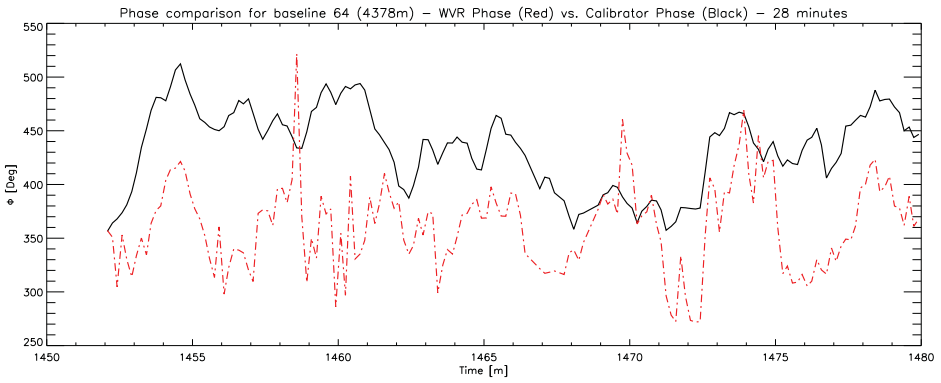

Figure 6.6.3: A 28 minute phase track at 48.3 GHz on the 4378m length 6 – 4 baseline. The same spike in the WVR data at 1458.7 minutes occurs also in the 4 – 1 baseline. The source of this spike thus is WVR unit 7 on antenna 4.

6.7 Demonstrating Phase Correction Efficiency

In order to demonstrate the efficiency of the water vapour radiometer corrections, four dirty maps are created. B. Nicolic has provided a similar demonstration for the ALMA WVRs, published in [43]. We observed the quasar 0537-441 over an hour angle range of about 4 hours in a hybrid H214 array on June 4 and 5 2011 at frequencies of 16.3, 22.3, 47 and 48.3 GHz, where the E – W baselines of the central cluster of antennae 1 – 5 range from 92m to 230m (thus are very compact) and feature short N – S baselines from antenna 4 and 5 of 138m. The E-W baselines to antenna 6 range from 4270m to 4500m. This results in a map that is heterogenous, leading to rapid modulation in a SW – NE direction when the data is limited to short periods of time. This map then has a spatial resolution in two orthogonal directions that is very different. In this configuration, the synthesised beam sizes correspond to 4.46 arcsecs for the inner five antennae and 0.16 arcsecs for the long baselines to antenna 6. The direction of the fringes in the resulting map corresponds to the direction angle between the source hour angle covered and the longest baselines. The data analysis to compare the results has been split into four methods, each using the standard ATNF software packages miriad [50] and kvis, part of the Karma package [20] as well as the WVR phase correction retrieval scripts written by the author.

- The first map shown is the 'perfect' map (selfcal). This has been obtained by calibrating the entire length of the observation using the bright calibrator 0537-441 at the centre of the image. This method will perfectly track any phase fluctuations introduced by the atmosphere.

- The next map (we refer to as the 'fake' map) is made to confirm that the data reduction is working correctly: We use the calibrator phase information that has been extracted from the science receiver data and feed that phase information into the WVR reduction pipeline. Because there are minor gaps in time and thus discontinuities in the calibrator phase that occur when the telescope switches from calibrator to on-source observation, this map is expected to be almost perfect, but not quite as good as the selfcal or 'perfect' map.

- The third map contains the phase corrections extracted from the Water Vapour Radiometers alone, we call this the 'WVR' map. This will be the result we expect for any future science observations and thus the result we need to measure the performance of the WVRs against.

- The last map depicts the quality of the data that can be obtained by interpolating between the calibrator positions, called the 'interpolated' map. This is the best data that the ATCA has been able to produce on a science target to date where there is no strong source at the centre of the field.

The maps in 6.7.1 show an area of about 6x6 primary beam widths. In the top left, we see the 'perfect' map as obtained by the selfcal method: The peak flux goes to 17.9 mJy and the background contains a low level of dispersed power of about –10 mJy. The 'fake' map is almost as good in peak flux, but there is a substantial drop off in contrast: The background has more power in it than the 'perfect' map. The 'WVR' map has again a slightly lower peak flux and slightly worse contrast than the 'perfect' map. It is however similar to within a few percent of the perfect map. Finally the 'interpolated' map is lower by about 20% in peak flux whereas the contrast is much worse with the levels of dispersed power in the background around 4mJy, several times that of the 'WVR' map.

The maps in 6.7.2 provide a zoomed in view of the same maps, in the same arrangement as shown in 6.7.1, showing the central area about two beam widths in diameter only. From these maps it is evident that the central beam in the WVR corrected map receives more power than in the interpolated map, indicating that the phases have been brought into better agreement by using the WVR corrections.

The last performance measure that results from the dirty maps are the ripple profiles shown in Figure 6.7.3. The four panels show a cross section perpendicular to the central peaks in the dirty maps and they show the amplitude of the strongest peak in the centre of the map. The peak intensity of the WVR corrected map compares favourably to the peak flux in the perfect map: it is only about 1% weaker in flux. The interpolated peak flux on the other hand is 22% lower as compared to the perfect map. This illustrates how well the WVRs are able to correct the phase information and to help in keeping more power in the correlated signal than is possible with a system based on interpolated calibrator measurements alone.

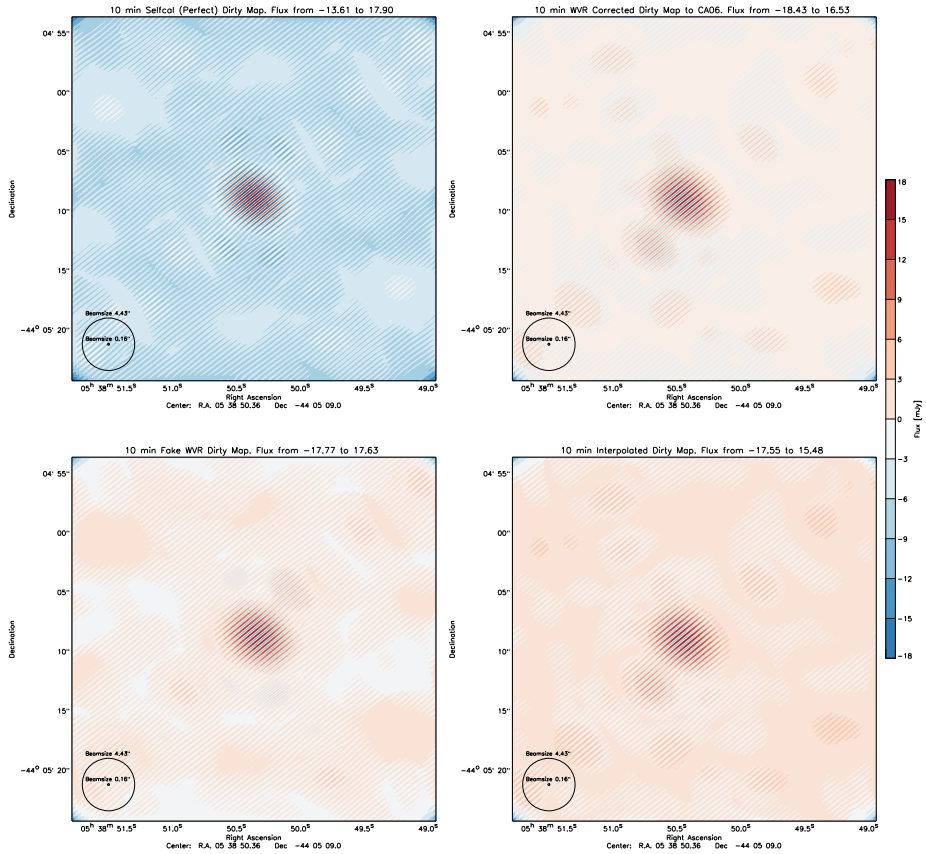

Figure 6.7.1: Large scale dirty maps: These four dirty maps depict an area about 6x6 centre beam widths squared. It depicts the results of (clockwise from top left) the 'perfect' map (using selfcal), the 'WVR' corrected map, the 'interpolated' map as one would obtain pre-WVR and the 'fake' map which introduces measured phase from the calibrator into the WVR data pipeline instead of WVR data.

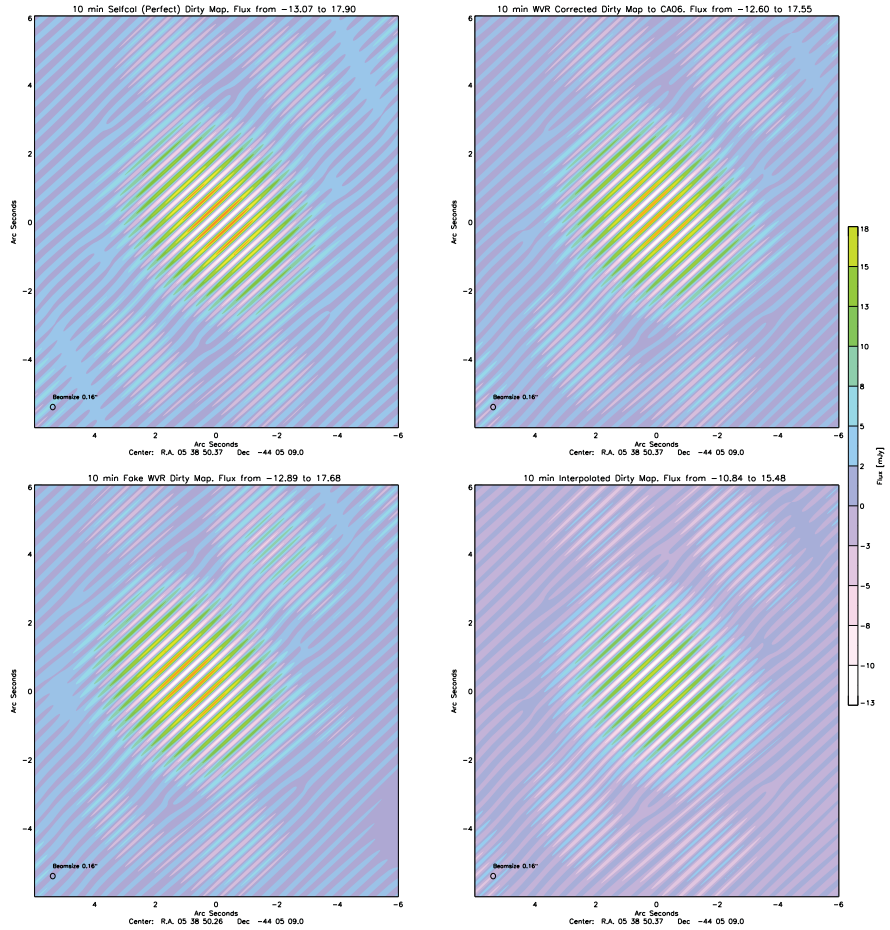

Figure 6.7.2: This zoomed map shows the beam shape representative of the beam for the inner five antennae as well as the peak flux achieved depending on the method of correction. Note that the data still includes all 6 antennae and therefore also the high resolution beam. From top left clockwise: The 'perfect' map (selfcal), the 'WVR' corrected map, the 'interpolated' map without corrections and the 'fake' map which had calibrator data injected into the WVR reduction pipeline.

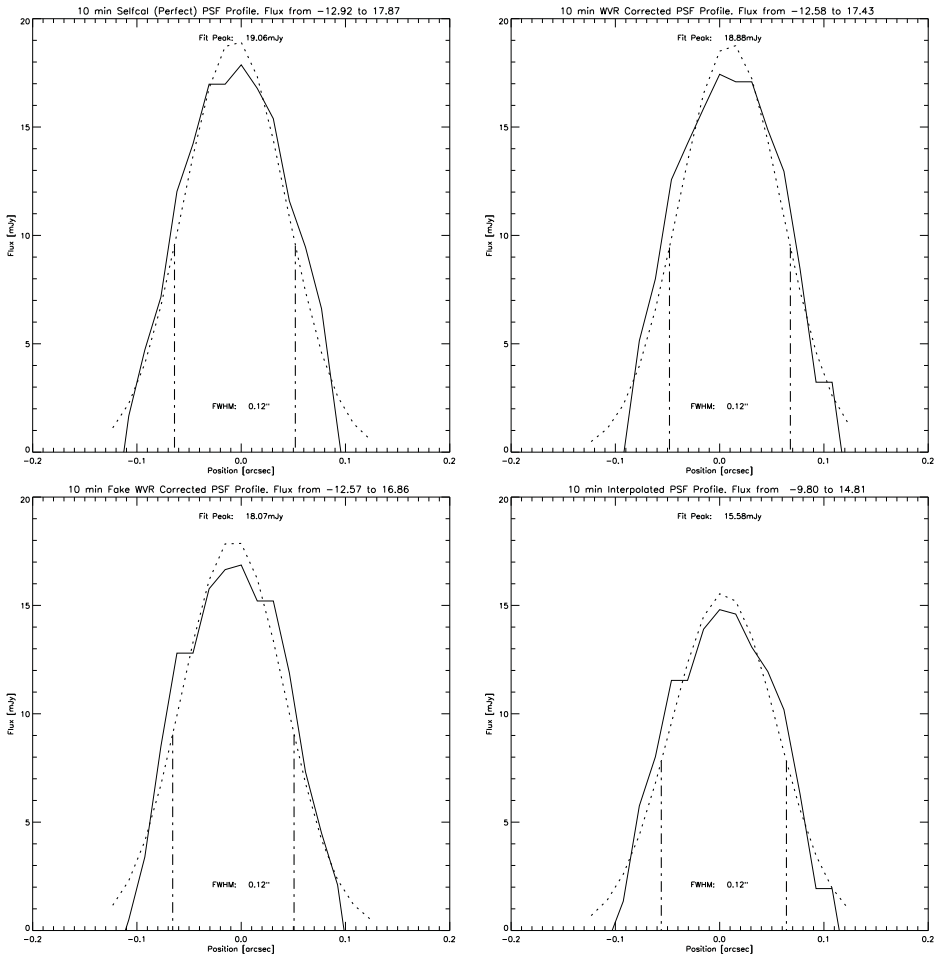

Figure 6.7.3: The beam profile (solid) with a gaussian fitted (dotted) and the FWHM points marked (dash dotted vertical). The fits are made to cuts perpendicular to the central peaks in the above maps. The 'perfect' selfcal map shows the highest peak flux, followed by the 'fake' corrected map, the 'WVR' corrected map and finally the 'interpolated' map. Note that the FWHM remains the same for all maps, but the peak intensity is 22% lower between the selfcal and the interpolated maps. The WVR improvement in peak flux over the interpolated map is 21%.

Chapter 7

Future Developments

In this chapter I would like to provide an outlook on work that is currently ongoing and needs to be completed before the WVRs we have built for the ATCA become part of the standard data reduction pipeline offered to the national facility user community. More importantly, I also would like to discuss some ideas for improvements of the WVR system, some of which have become evident after analysing calibration data taken for this thesis, while other ideas look further into the future.

7.1 Data reduction integration

At present, WVR data is recorded to Monica, the Monitoring system for the Compact Array. All parameters of the WVRs (channel voltages, supply voltages, probe temperatures) are recorded in 5 second intervals. During the data reduction step, the Astronomer has the option to apply the WVR corrections using the 'atwvr' task in miriad. This task has already been implemented, however, it depends on a per-antenna time stamped phase correction input which still needs developed into a stable package ready for public release. Because the WVR data is automatically recorded regardless of which millimetre receiver system is on axis, observers will have the opportunity to go back and re-reduce their data with WVR corrections applied even if the full reduction software is not yet available at the time of this writing.

Another aspect of the data reduction integration concerns the automatic

rejection (flagging) of WVR data that has been affected by RFI. An algorithm will have to be developed that monitors the system metrics such as the receiver noise temperatures and compares these to the RMS levels of the signal measured. If these levels disagree, a RFI situation might be present. This will have to be the subject of further study.

7.2 Integrating channel voltage measurements

The channel voltages retrieved by the Monica system in 5 second intervals are almost instantaneous values, i.e. they are only integrated over a very short timespan of 5 ms. This is the reason the target sensitivity has not yet been reached (see chapter 5). We partially are trying to compensate for this by integrating over almost 6 minutes worth of data during the data reduction process in order to gain enough sensitivity. It is hence an important next step to get the WVRs to integrate these voltages over as large an integration timescale as possible. It is also important in that context that the integrated voltages are obtained on each 5 second boundary which should coincide with the telescope's 10 s integration cycle, otherwise corrections might lag by an offset amounting to the difference between the cycle time boundaries. This is a task requiring the observatory engineers to program the datasets accordingly.

We are assuming that the water line does not change significantly in less than one integration cycle (10 s). For the increased integration requirement, only the tunnel diodes need interrogated. The voltages and monitoring temperatures are sufficiently sampled if we execute one spot measurement for every 5 second cycle. We can thus change the interrogation scheme to continuously sample the tunnel diodes 1 – 4 inside a five second period so as to still allow for a single sampling of all the other 12 channels. 12 channels take 20 x 12 = 240 ms to sample. That leaves 4760 ms to sample filters 1 – 4 in each 5000 ms cycle. This amounts to 1190 ms per filter, a time span long enough to reach our target sensitivity: According to the radiometer equation 5.2.1, the target sensitivity of 12 mK for a T_{Rec} of 400 K will be reached. It also shows that a sensitivity of below 10 mK for T_{Rec} = 290 K can be reached, or, for a worse case of a T_{Rec} of 600K, a sensitivity of 18 mK is still realistic.

7.3 Further characterisations

Depending on the weather conditions, it might be advantageous to only apply long baseline corrections. This has been shown with the test data obtained in very stable conditions, where the short baselines generally were made worse by applying WVR corrections (albeit by a small amount, about 3 – 10 degrees phase) whereas on long baselines phase RMS was able to remain at no worse than 20 degrees RMS, improving the phase by more than 20 degrees in this test data (see chapter 6). The threshold baseline needs to be determined before such a correction scheme may be implemented.

When observers are using the system, they are not afforded the luxury of a metric to determine how well the corrections have worked on each baseline. We can only do that with the test data because it has a strong source in the centre of the field to compare the WVR phases against. Thus one further examination we would like to undertake is to run a series of observations in each ATCA configuration over the course of the next year. This will allow us to constrain the weather conditions under which an advantageous correction can be applied on certain baselines, and, possibly a correlation can be worked out between meteorological parameters such as wind speed and seeing monitor phase noise.

A further interesting test to validate whether the Taylor hypothesis does indeed hold true for the ATCA site consists of taking phase noise measurements over a time period of a few hours on all available baselines, similar to the VLA measurements executed by Carilli in [9] Figure 6. We thus far only have the seeing monitor data to assess whether the turbulence encountered supports a 2D or 3D turbulent screen. This data features only one short baseline (235m), thus substantially increasing the difficulty in measuring behaviour of the atmosphere as it moves across the site. However, in comparison to the VLA, the number and length of the baselines is still small, so this experiment cannot be carried out with the same degree of rigour.

7.4 Using the hot load

One of the limitations with the uncooled system is that the WVRs do not have a stable cold load to calibrate against regularly. The absolute degree of precision with which we can determine sky temperatures is thus only in the range of a few kelvin. In the calibration observations executed with liquid nitrogen and the hot load, it was determined that while the Y factor remains within fractions of a percent between calibration runs, the offset varies by up to a few percent. By using the hot load (which has a known temperature), we are able to calibrate the gain as often as a calibrator scan is initiated by the observing schedule. This data is not used at present by the phase extraction algorithm. The hot load is moved in front of the feed for 20 seconds automatically on every calibrator scan, so the scheme discussed in chapter 6.4.2 can be implemented. However, it depends on the stability of the Y factor for which we have only been able to obtain three measurements to date. These data have shown the Y factor to be stable to within better than 0.5%. It nevertheless would be good to obtain regular calibration runs to verify the continued stability of the Y factors. Another difficulty encountered when calibrating the WVRs revolves around the LN_2 cold load measurements: Because the styrofoam box containing the LN_2 is very cold on the outside, water vapour tends to freeze onto the bottom of the container. This in turn will cause some additional continuum emission during the calibration. While the engineers executing this procedure are aware of that and do their best to wipe the styrofoam clean before setting it on top of the feed, a slow voltage increase in the filter voltages due to this water vapour freezing can be observed in the calibration data.

7.5 Optimising the weighting coefficients

The weighting coefficients determined from the model atmosphere could be optimised empirically with just a few calibration observations by running a least squares fit of ΔT to the phase calibrator. Investigating the changes in weighting coefficients in dependence of weather parameters could then lead to an optimised set of coefficients being used for the path excess calculation based on the prevailing weather conditions.

Chandler et al. found in [10] that the VLA WVR efforts were hampered by variations in the brightness temperature to path length conversion factors that varied by up to 70 % and on short timescales. We have limited the explorations for our conversion factors to the ATM derived model atmospheres outlined in Section 6.4.3, and specifically find in table 6.4.2 that the largest variations are on the order of 10 % of the path length for rapidly changing atmospheric conditions. Once the firmware in our units has been updated, we will be able to experimentally verify the variability of the conversion factors and as outlined above, build a set of empirically derived conversion factors for a range of atmospheric conditions.

7.6 Phase correlation Mopra – ATCA

Seven WVR units have been built. One can either be viewed as a spare, or could be mounted on the Mopra telescope, which is located ~110 km to the south of ATCA near Coonabarabran in the Warrumbungles, next to Siding Spring. Mopra as well as ATCA are used for 15 mm VLBI observations which could profit from using water vapour radiometers. An interesting experiment could be to track a phase calibrator with both Mopra and ATCA and see how the WVR derived phases correlate. Since the water vapour pockets are definitely not correlated on this long a baseline, we could in theory still achieve a phase noise reduction by $\sqrt{2}$.

7.7 Closing Remarks

In the course of this thesis I have demonstrated that the WVRs we developed for the ATCA have substantially improved correlation efficiency on long baselines and thus improved imaging contrast. By virtue of improved correlation efficiency (or lower phase noise), decorrelation at millimetre wavelengths can be reduced on long baselines under average observing conditions. Astronomers are thus able to observe at shorter wavelengths on longer baselines than previously possible. The full 3 km of baseline available at 3 mm can now be used, making use of the WVR corrections. Previously only about 300 m long baselines could reasonably be expected

to work. At 7 mm and 15 mm, it is now possible to use the full 6 km baselines previously only available during the best and most stable of observing conditions. This potentially can improve the spatial resolution of the ATCA in the millimetre observing regime by up to a factor of 10.

This upgrade has further enhanced the world class millimetre facility that ATCA has been for the past 10 years. It has provided a crucial improvement for future projects where instruments like ALMA are not well matched or unavailable.

7.8 Credits

This research was supported under the Australian Research Council's LIEF grant funding scheme (project number LE0882778). The following institutions have provided funding and support for this project:

- University of New South Wales
- University of Sydney
- James Cook University
- Swinburne University of Technology
- Australia Telescope National Facility (CSIRO/ATNF).

Appendix A

Tables

Table A.0.1: Calibration result for March 8, 2011

Antenna	Unit		Radiometer Channel 16.5 GHz	18.9 GHz	22.9 GHz	25.5 GHz	TP
1	1	*Y factor*	1.55	1.67	1.68	1.56	1.44
		Gain [K/V]	78.09	77.76	74.20	96.50	125.71
		T_{Rec} [K]	325.7	256.6	253.4	321.9	429.6
		T_{Sky} [K]	7.5	14.3	47.8	29.5	28.1
2	2	*Y factor*	1.49	1.64	1.65	1.54	1.43
		Gain [K/V]	149.78	73.16	70.46	128.41	93.94
		T_{Rec} [K]	376.4	271.0	269.8	338.3	443.1
		T_{Sky} [K]	4.8	13.4	46.5	26.7	26.1
3	3	*Y factor*	1.58	1.64	1.61	1.54	1.48
		Gain [K/V]	98.22	168.71	71.20	117.87	81.07
		T_{Rec} [K]	303.1	269.6	288.8	331.8	389.7
		T_{Sky} [K]	8.8	16.2	49.1	30.4	29.3
4	7	*Y factor*	1.58	1.68	1.56	1.48	1.47
		Gain [K/V]	75.37	73.27	120.47	133.39	115.05
		T_{Rec} [K]	302.5	249.0	317.9	380.4	395.3
		T_{Sky} [K]	6.0	14.9	46.5	28.8	24.4
5	5	*Y factor*	1.59	1.61	1.55	1.51	1.31
		Gain [K/V]	68.09	72.29	77.32	99.32	124.35
		T_{Rec} [K]	294.2	286.2	322.1	357.7	630.8
		T_{Sky} [K]	4.1	11.1	43.9	26.5	21.8
6	6	*Y factor*	1.59	1.69	1.65	1.60	1.29
		Gain [K/V]	73.18	70.41	101.21	117.14	141.20
		T_{Rec} [K]	297.2	243.9	264.6	293.7	677.4
		T_{Sky} [K]	11.4	19.2	49.6	33.9	26.6

Table A.0.2: Calibration result for November 9, 2011 (first run)

Antenna	Unit		Radiometer Channel 16.5 GHz	18.9 GHz	22.9 GHz	25.5 GHz	TP
1	1	*Y factor*	1.57	1.68	1.68	1.57	1.44
		Gain [K/V]	74.88	74.69	70.85	90.98	122.61
		T_{Rec} [K]	317.3	250.1	248.0	311.8	419.8
		T_{Sky} [K]	89.0	97.2	124.6	110.1	105.3
2	2	*Y factor*	1.50	1.64	1.65	1.54	1.43
		Gain [K/V]	142.38	71.94	69.13	125.84	93.31
		T_{Rec} [K]	366.0	267.1	266.6	334.2	438.7
		T_{Sky} [K]	11.7	22.7	71.0	43.2	39.0
3	3	*Y factor*	1.58	1.64	1.61	1.54	1.48
		Gain [K/V]	96.06	158.71	69.66	114.35	80.75
		T_{Rec} [K]	299.8	267.1	286.3	327.0	386.4
		T_{Sky} [K]	13.4	23.7	70.9	41.5	39.8
4	7	*Y factor*	1.58	1.68	1.57	1.50	1.48
		Gain [K/V]	73.82	70.65	110.78	121.45	111.32
		T_{Rec} [K]	305.5	249.9	311.6	366.3	387.9
		T_{Sky} [K]	8.3	21.2	73.5	41.9	34.6
5	5	*Y factor*	1.61	1.62	1.56	1.52	1.32
		Gain [K/V]	67.18	71.21	76.06	97.27	122.87
		T_{Rec} [K]	286.7	279.0	316.3	350.7	617.2
		T_{Sky} [K]	9.9	21.8	72.8	43.2	35.2
6	6	*Y factor*	1.60	1.69	1.65	1.60	1.30
		Gain [K/V]	69.71	66.21	92.25	106.85	140.04
		T_{Rec} [K]	294.2	242.7	265.4	293.0	670.9
		T_{Sky} [K]	14.2	24.8	71.3	43.9	35.3

Table A.0.3: Calibration result for November 9, 2011 (second run)

Antenna	Unit		Radiometer Channel 16.5 GHz	18.9 GHz	22.9 GHz	25.5 GHz	TP
1	1	*Y factor*	1.56	1.67	1.68	1.56	1.44
		Gain [K/V]	75.67	75.65	71.55	92.35	124.03
		T_{Rec} [K]	323.2	256.5	252.8	320.0	427.4
		T_{Sky} [K]	87.4	95.3	123.5	108.2	103.7
2	2	*Y factor*	1.49	1.63	1.63	1.52	1.42
		Gain [K/V]	143.86	73.02	70.06	128.07	94.61
		T_{Rec} [K]	372.9	275.6	274.4	345.5	449.1
		T_{Sky} [K]	8.6	18.4	67.9	38.5	35.3
3	3	*Y factor*	1.57	1.62	1.59	1.53	1.47
		Gain [K/V]	97.06	161.28	70.68	116.55	81.92
		T_{Rec} [K]	306.1	275.9	294.5	338.5	396.0
		T_{Sky} [K]	10.5	19.6	68.0	37.1	36.4
4	7	*Y factor*	1.57	1.66	1.56	1.48	1.47
		Gain [K/V]	74.84	72.03	112.68	124.26	113.26
		T_{Rec} [K]	313.1	259.9	321.3	380.9	399.0
		T_{Sky} [K]	5.1	16.6	70.4	36.8	30.9
5	5	*Y factor*	1.59	1.60	1.55	1.50	1.31
		Gain [K/V]	67.92	72.36	77.06	99.00	124.79
		T_{Rec} [K]	293.1	288.4	324.8	362.7	631.0
		T_{Sky} [K]	6.8	17.2	69.4	38.3	31.6
6	6	*Y factor*	1.59	1.68	1.64	1.59	1.29
		Gain [K/V]	70.06	66.73	92.93	107.84	140.96
		T_{Rec} [K]	297.5	247.2	269.8	298.9	677.7
		T_{Sky} [K]	12.4	22.3	69.4	41.1	33.2

Appendix B

WVR Filter Characteristics and Plots

B.0.1 Filter lists

	Serial #	Center Freq [GHz]	BW [GHz]	Insertion loss [dB]
Ch1	203	16.599	0.86	-6.5
Ch2	210	18.795	0.88	-7.0
Ch3	222	22.862	1.00	-6.8
Ch4	233	25.548	1.01	-7.6

Table B.0.1: Unit 1 filter characeristics.

	Serial #	Center Freq [GHz]	BW [GHz]	Insertion loss [dB]
Ch1	206	16.524	0.85	-6.8
Ch2	217	18.894	0.93	-6.9
Ch3	224	22.751	1.00	-6.7
Ch4	235	25.446	1.05	-7.6

Table B.0.2: Unit 2 filter characeristics.

	Serial #	Center Freq [GHz]	BW [GHz]	Insertion loss [dB]
Ch1	200	16.633	0.87	-6.4
Ch2	211	18.919	0.93	-6.5
Ch3	221	22.881	1.06	-6.7
Ch4	230	25.590	1.08	-7.0

Table B.0.3: Unit 3 filter characeristics.

	Serial #	Center Freq [GHz]	BW [GHz]	Insertion loss [dB]
Ch1	201	16.592	0.86	-6.5
Ch2	211	18.919	0.93	-6.5
Ch3	223	22.737	0.96	-6.8
Ch4	231	25.634	1.08	-7.2

Table B.0.4: Unit 4 filter characeristics.

	Serial #	Center Freq [GHz]	BW [GHz]	Insertion loss [dB]
Ch1	202	16.496	0.83	-6.6
Ch2	214	18.918	0.91	-6.6
Ch3	225	22.904	1.03	-6.6
Ch4	234	25.386	1.00	-7.7

Table B.0.5: Unit 5 filter characeristics.

	Serial #	Center Freq [GHz]	BW [GHz]	Insertion loss [dB]
Ch1	204	16.592	0.85	-6.6
Ch2	215	18.825	0.91	-6.6
Ch3	226	22.881	1.04	-6.6
Ch4	236	25.513	1.00	-7.3

Table B.0.6: Unit 6 filter characeristics.

	Serial #	Center Freq [GHz]	BW [GHz]	Insertion loss [dB]
Ch1	205	16.489	0.85	-6.6
Ch2	216	18.915	0.91	-6.7
Ch3	227	22.890	1.01	-7.1
Ch4	237	25.528	1.06	-7.1

Table B.0.7: Unit 7 filter characeristics.

B.0.2 16.5 GHz Filters

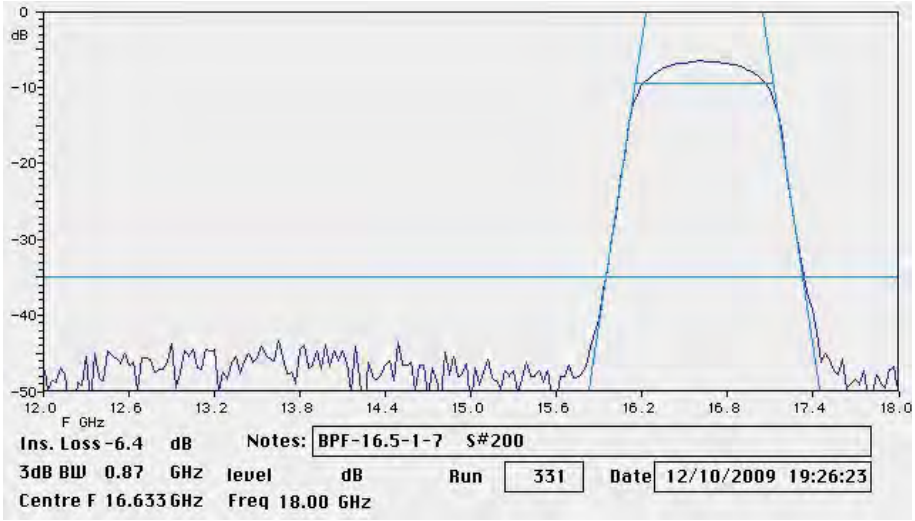

Figure B.0.1: 16.5 GHz spectrum analyser plot for filter serial number #200. This is some additional text to make it wrap in the list of figures.

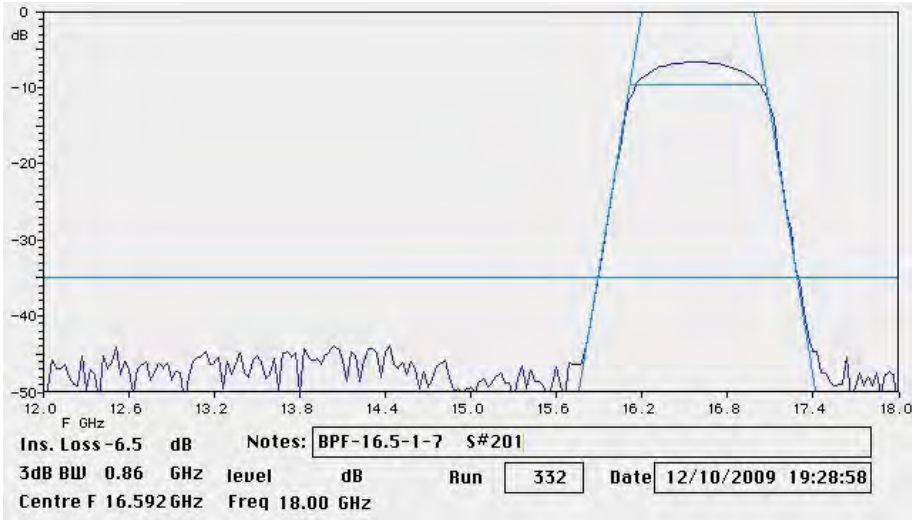

Figure B.0.2: 16.5 GHz spectrum analyser plot for filter serial number #201

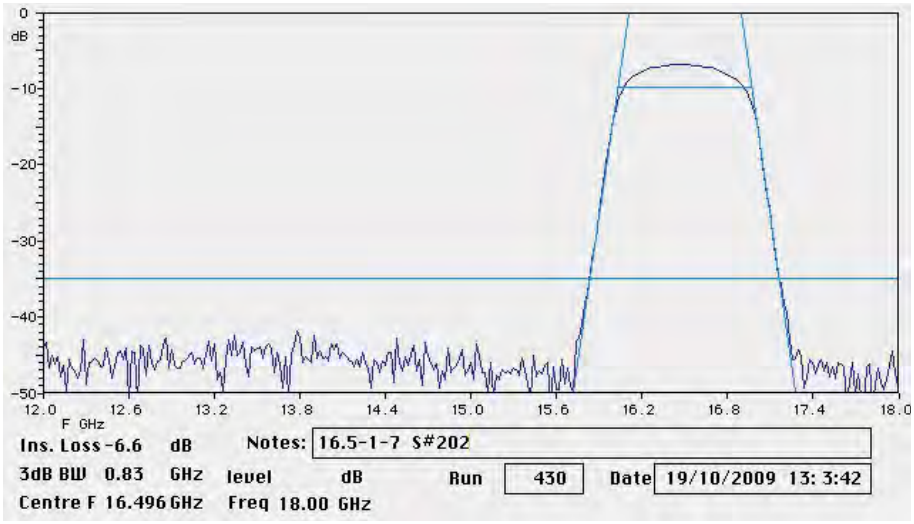

Figure B.0.3: 16.5 GHz spectrum analyser plot for filter serial number #202

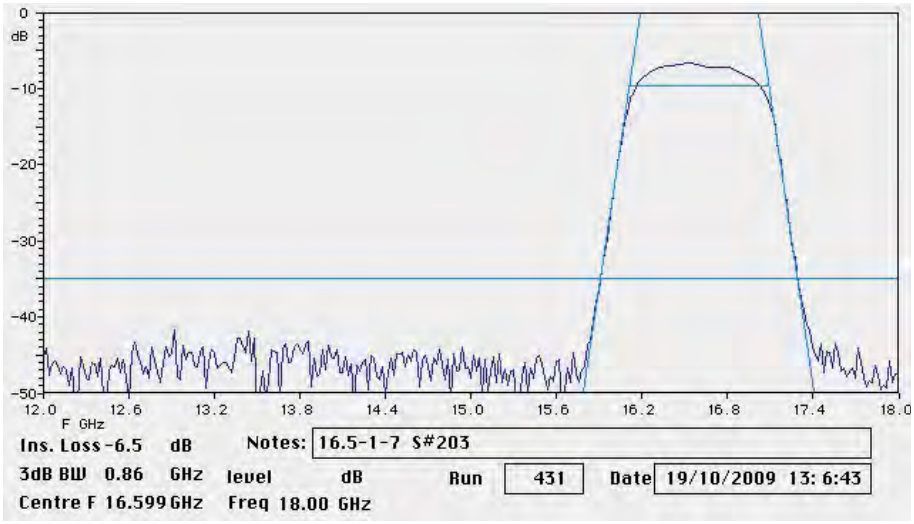

Figure B.0.4: 16.5 GHz spectrum analyser plot for filter serial number #203

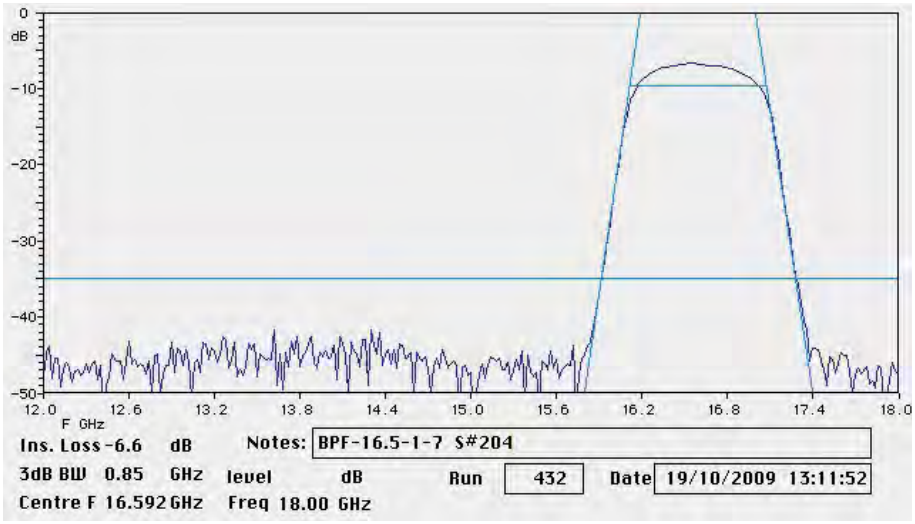

Figure B.0.5: 16.5 GHz spectrum analyser plot for filter serial number #204

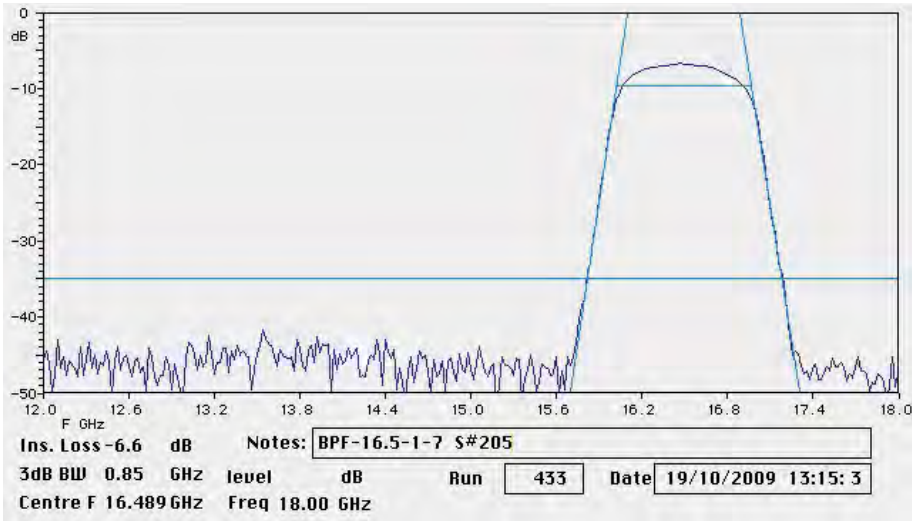

Figure B.0.6: 16.5 GHz spectrum analyser plot for filter serial number #205

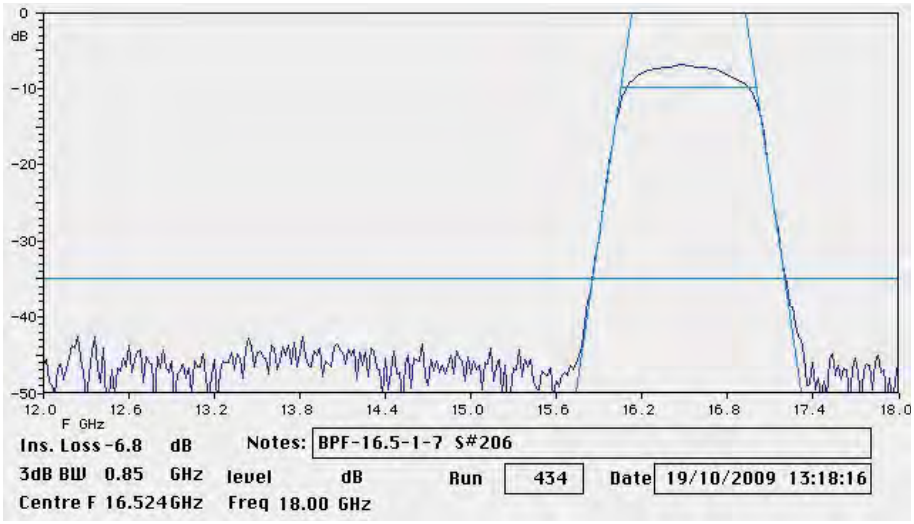

Figure B.0.7: 16.5 GHz spectrum analyser plot for filter serial number #206

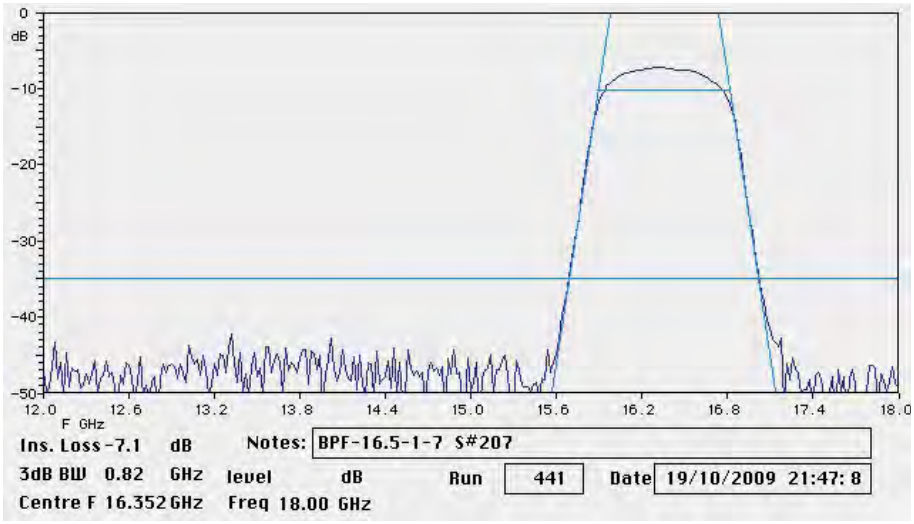

Figure B.0.8: 16.5 GHz spectrum analyser plot for filter serial number #207

B.0.3 18.9 GHz Filters

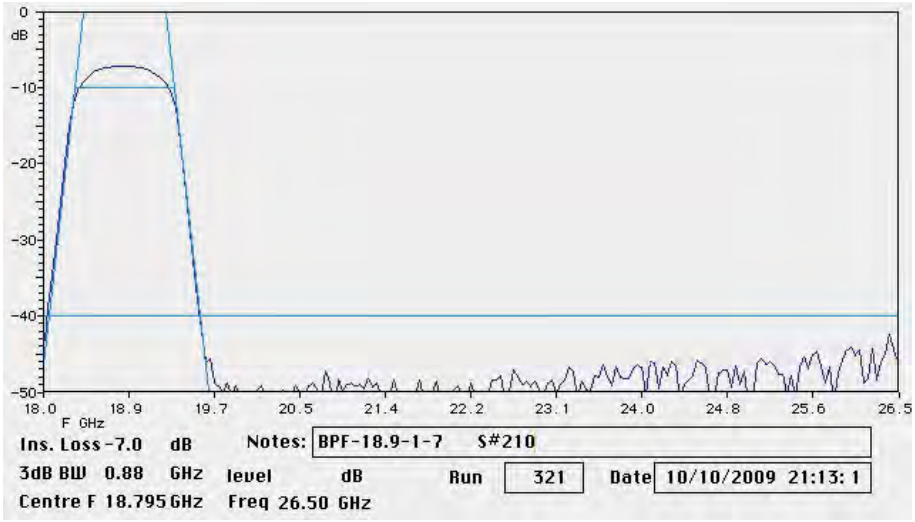

Figure B.0.9: 18.9 GHz spectrum analyser plot for filter serial number #210

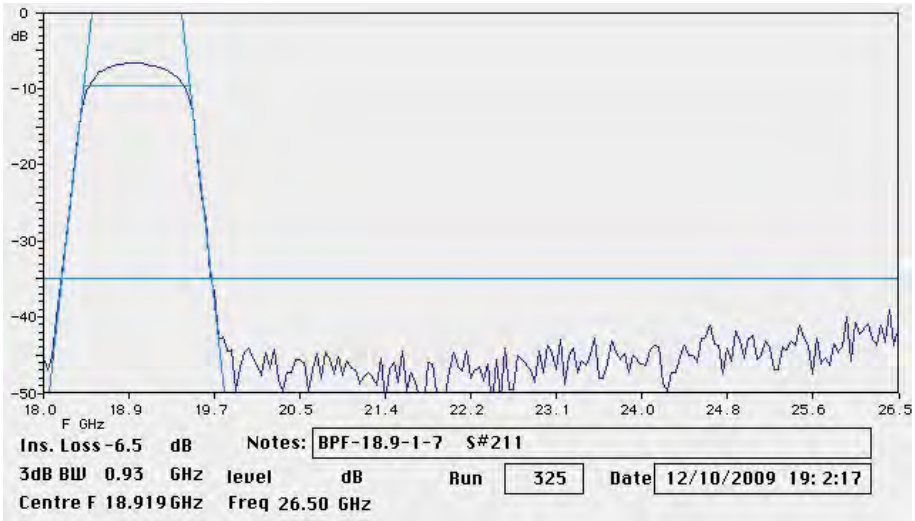

Figure B.0.10: 18.9 GHz spectrum analyser plot for filter serial number #211

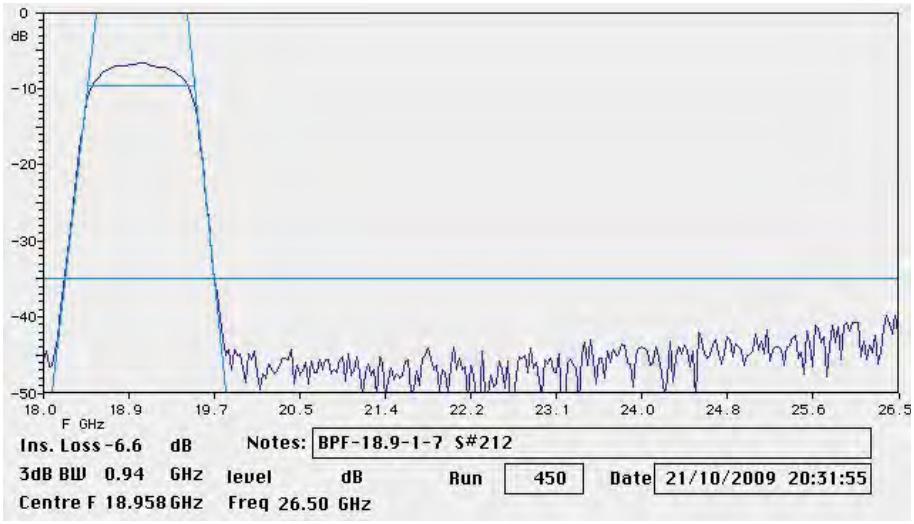

Figure B.0.11: 18.9 GHz spectrum analyser plot for filter serial number #212

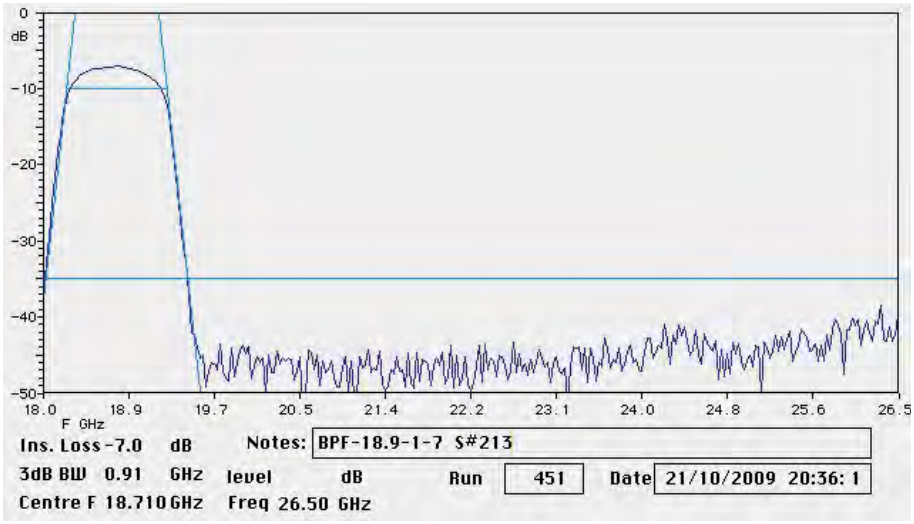

Figure B.0.12: 18.9 GHz spectrum analyser plot for filter serial number #213

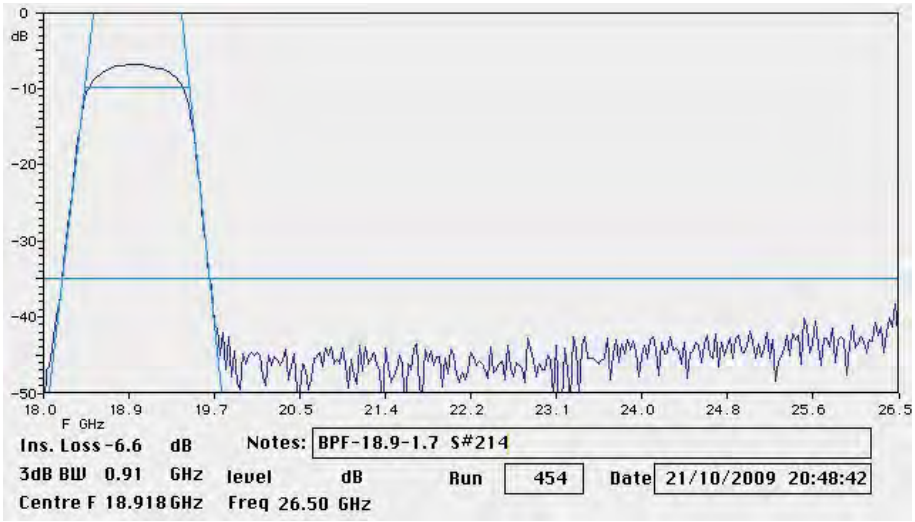

Figure B.0.13: 18.9 GHz spectrum analyser plot for filter serial number #214. And yet more text to make it wrap.

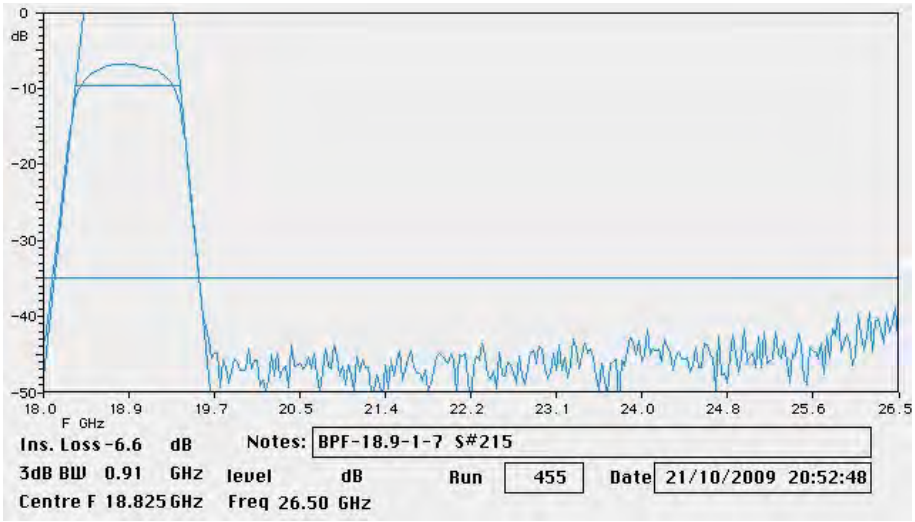

Figure B.0.14: 18.9 GHz spectrum analyser plot for filter serial number #215

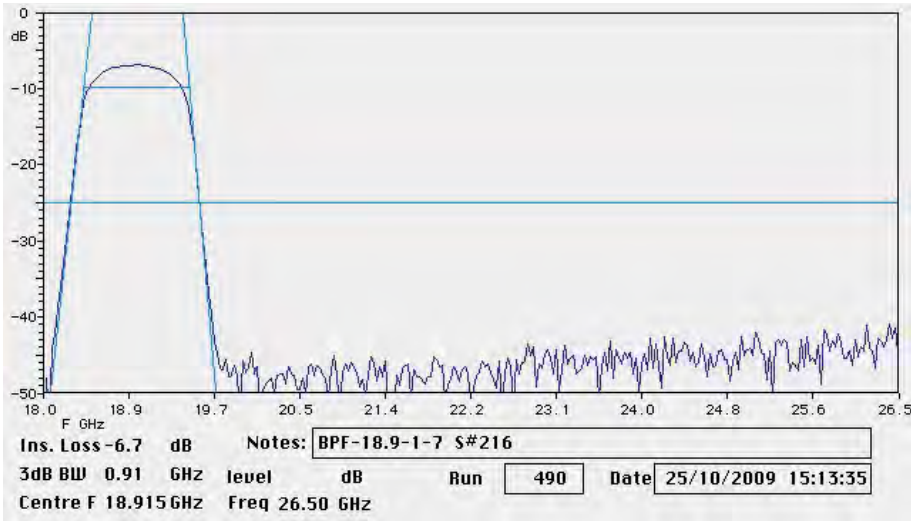

Figure B.0.15: 18.9 GHz spectrum analyser plot for filter serial number #216

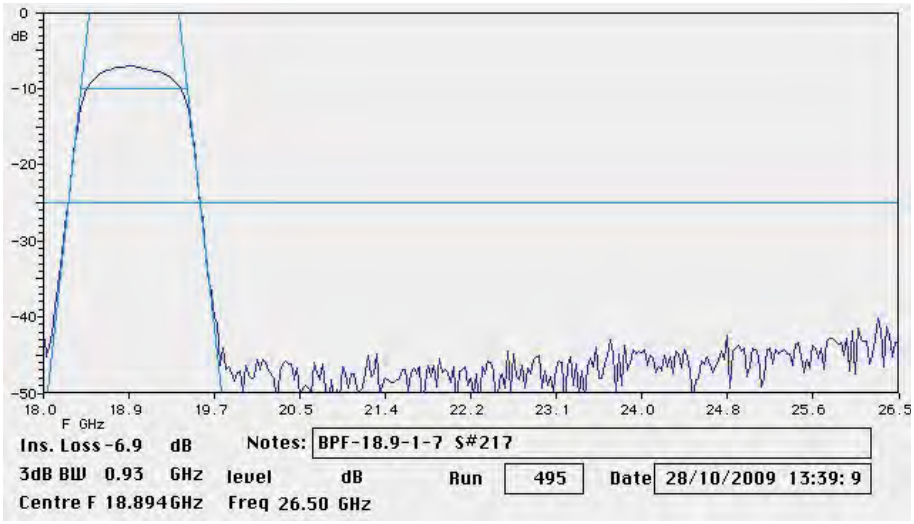

Figure B.0.16: 18.9 GHz spectrum analyser plot for filter serial number #217

B.0.4 22.9 GHz Filters

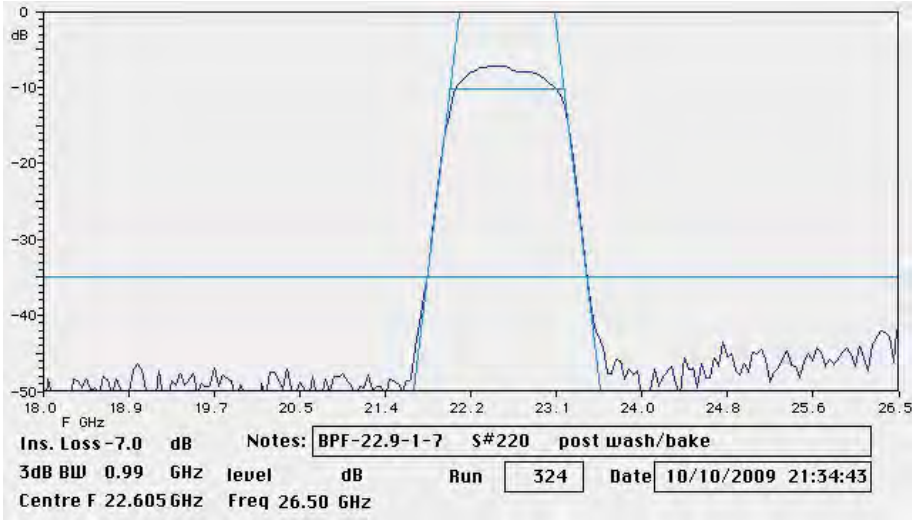

Figure B.0.17: 22.9 GHz spectrum analyser plot for filter serial number #220

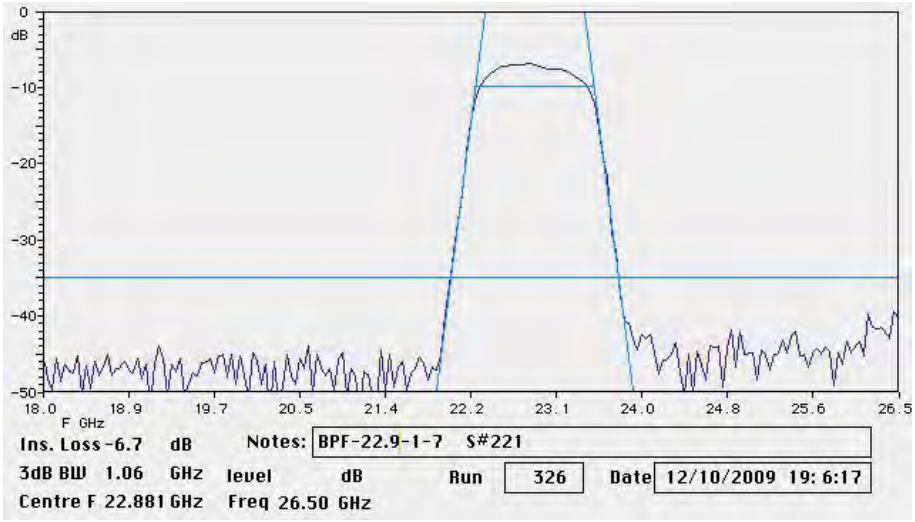

Figure B.0.18: 22.9 GHz spectrum analyser plot for filter serial number #221

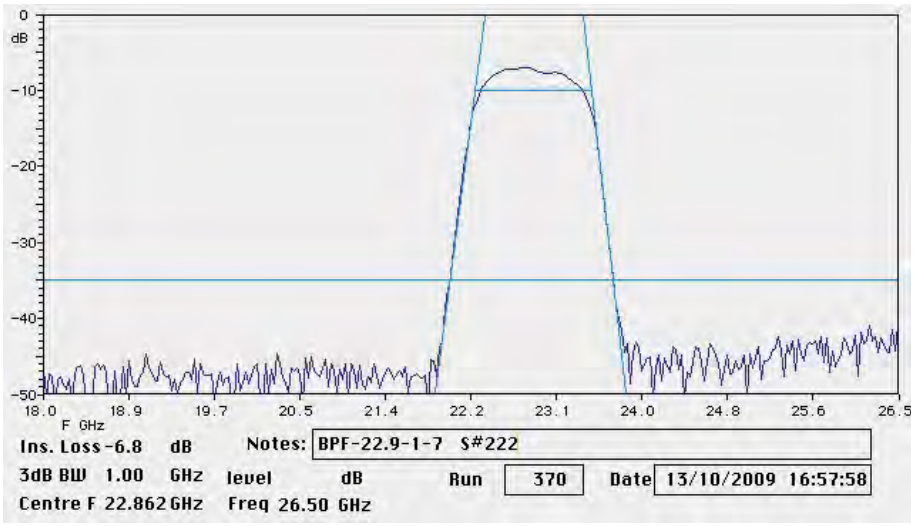

Figure B.0.19: 22.9 GHz spectrum analyser plot for filter serial number #222

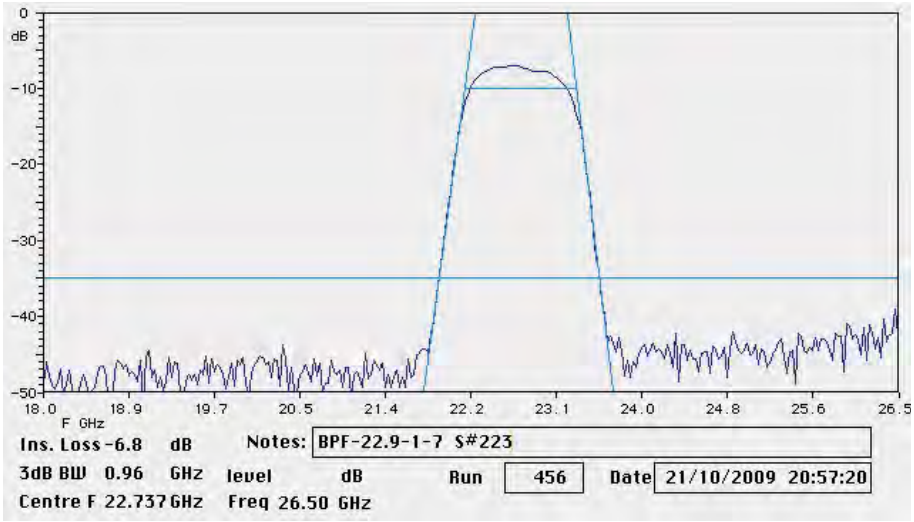

Figure B.0.20: 22.9 GHz spectrum analyser plot for filter serial number #223

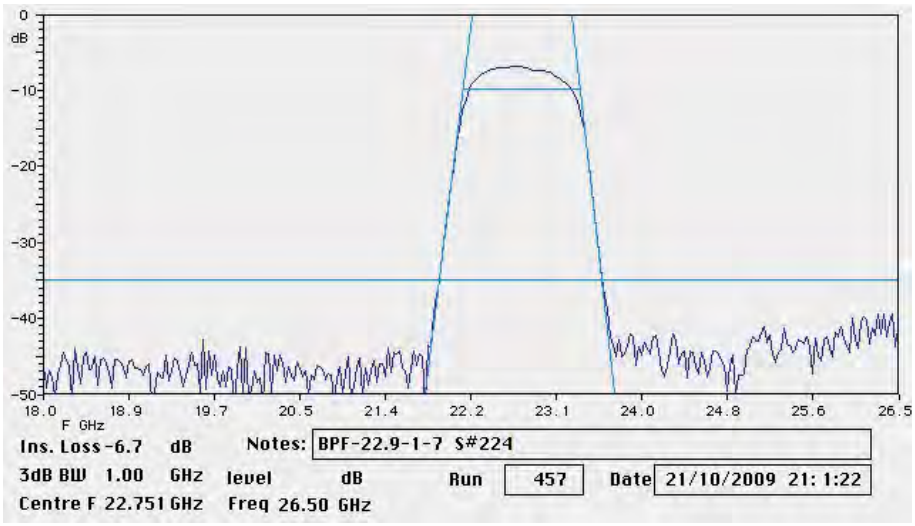

Figure B.0.21: 22.9 GHz spectrum analyser plot for filter serial number #224

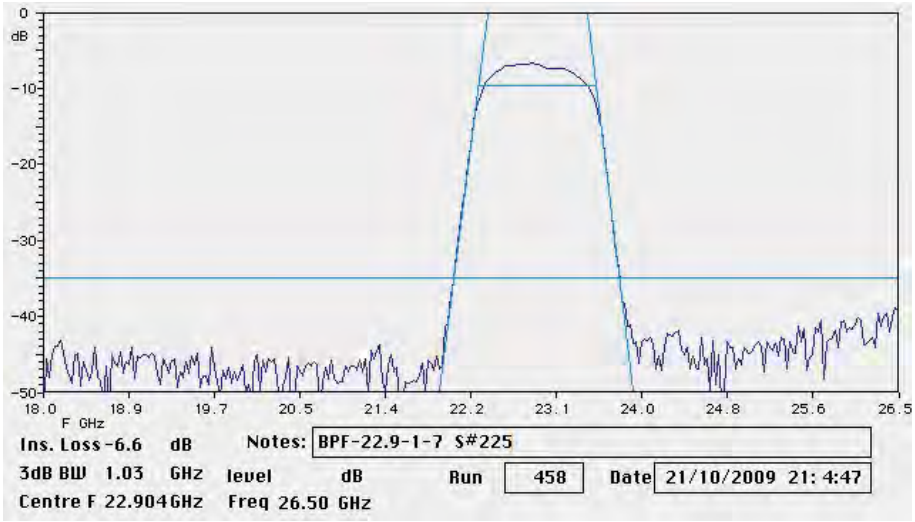

Figure B.0.22: 22.9 GHz spectrum analyser plot for filter serial number #225

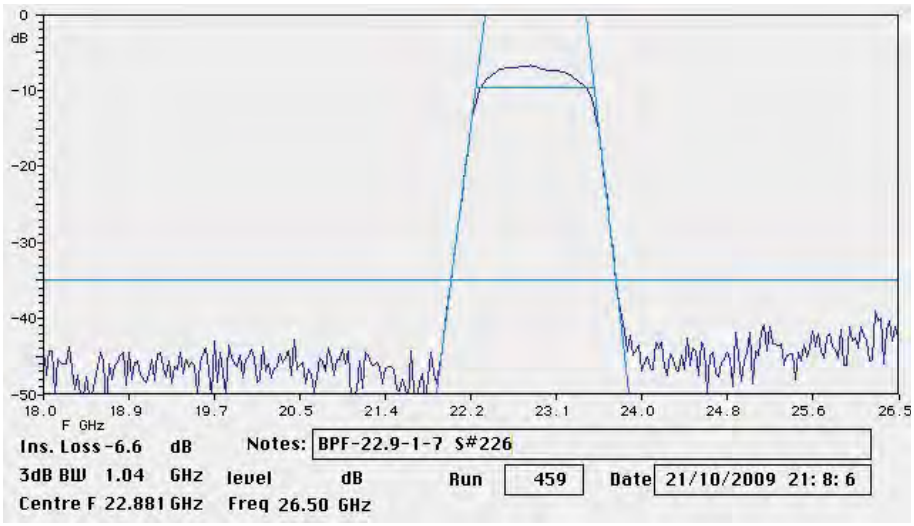

Figure B.0.23: 22.9 GHz spectrum analyser plot for filter serial number #226

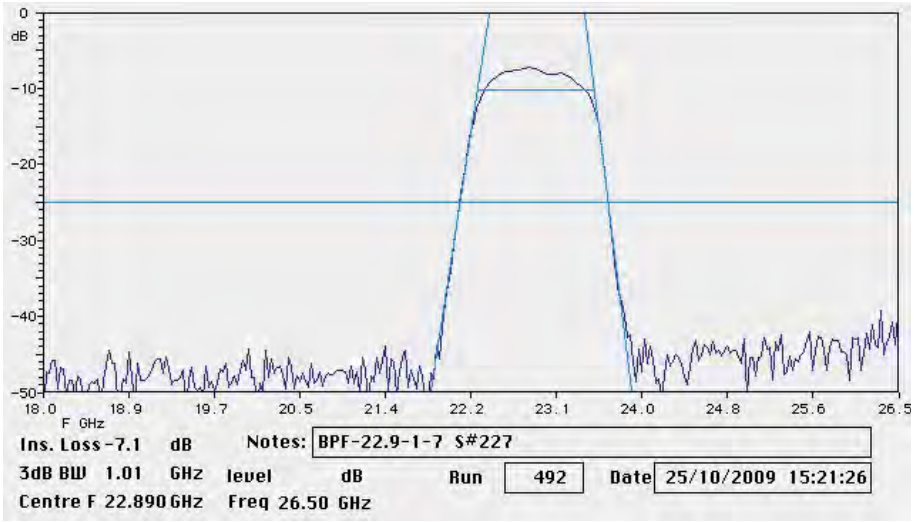

Figure B.0.24: 22.9 GHz spectrum analyser plot for filter serial number #227

B.0.5 25.5 GHz Filters

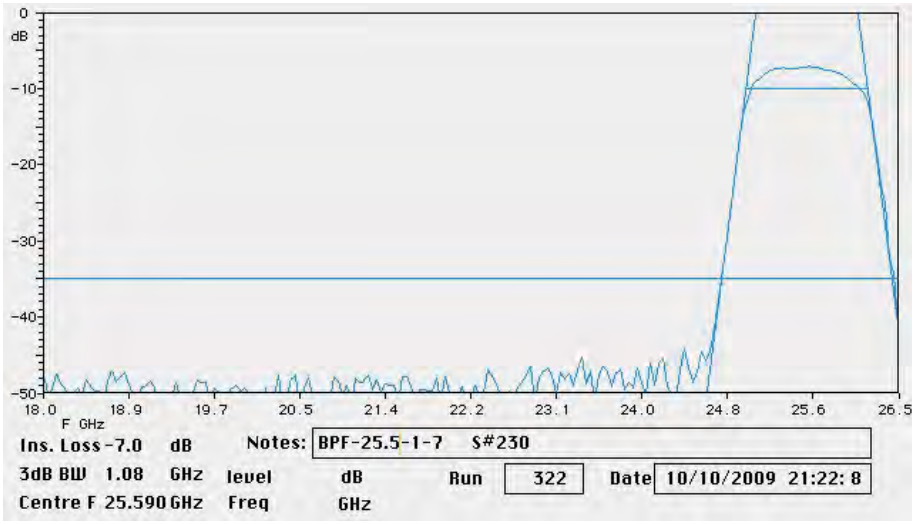

Figure B.0.25: 25.5 GHz spectrum analyser plot for filter serial number #230

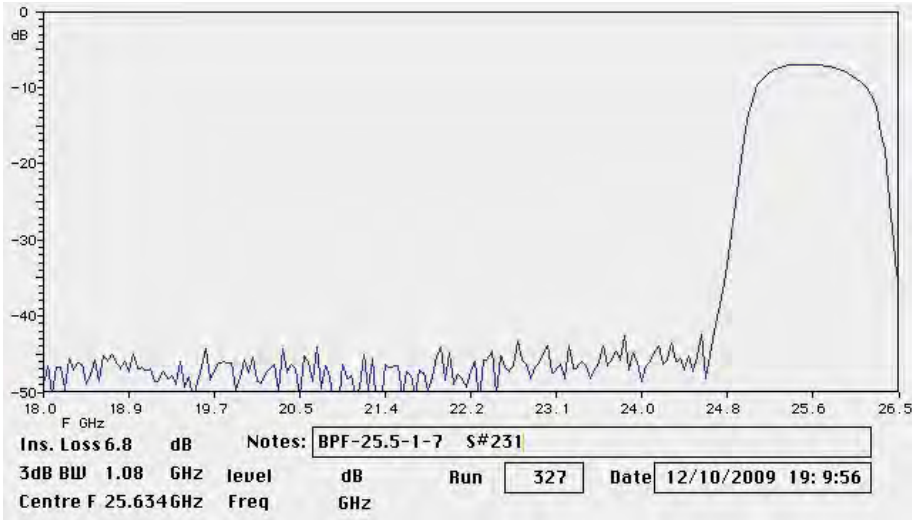

Figure B.0.26: 25.5 GHz spectrum analyser plot for filter serial number #231

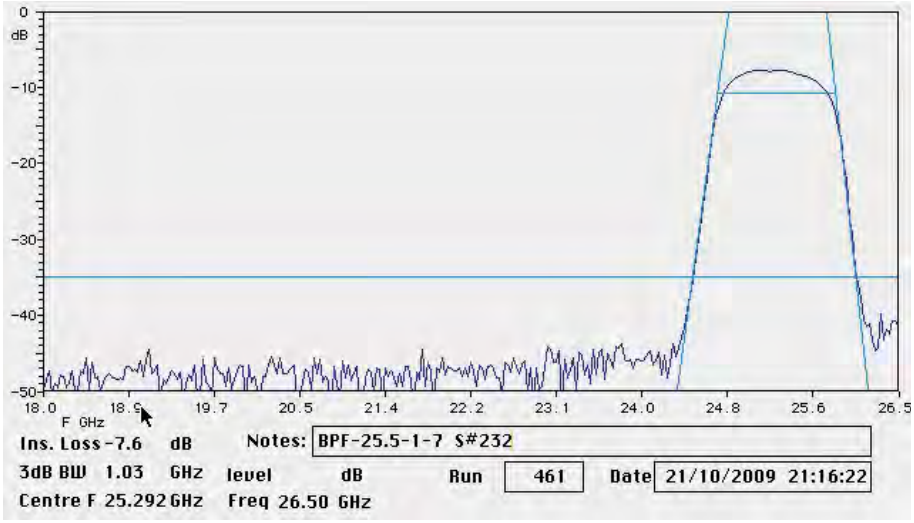

Figure B.0.27: 25.5 GHz spectrum analyser plot for filter serial number #232

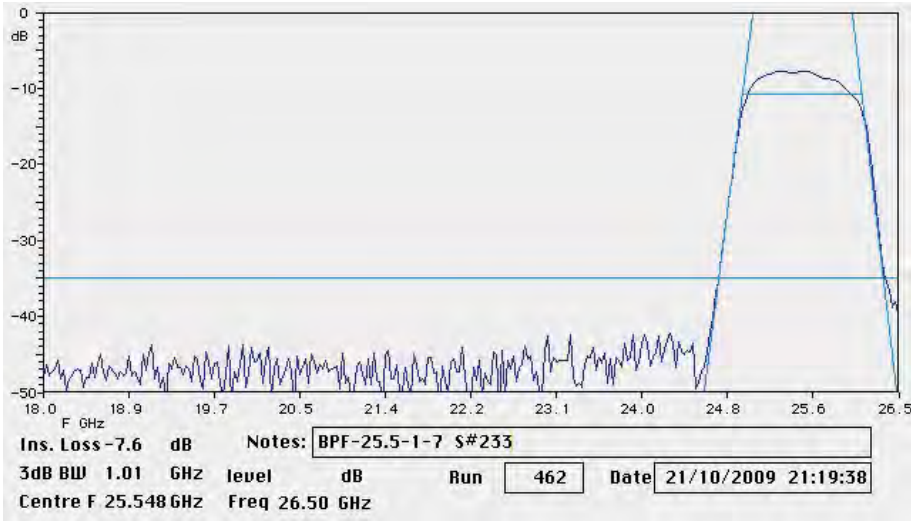

Figure B.0.28: 25.5 GHz spectrum analyser plot for filter serial number #233

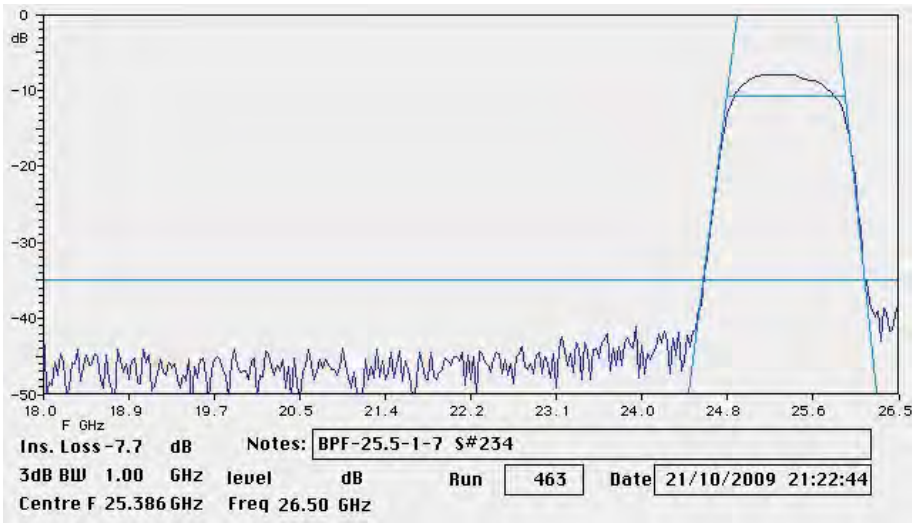

Figure B.0.29: 25.5 GHz spectrum analyser plot for filter serial number #234

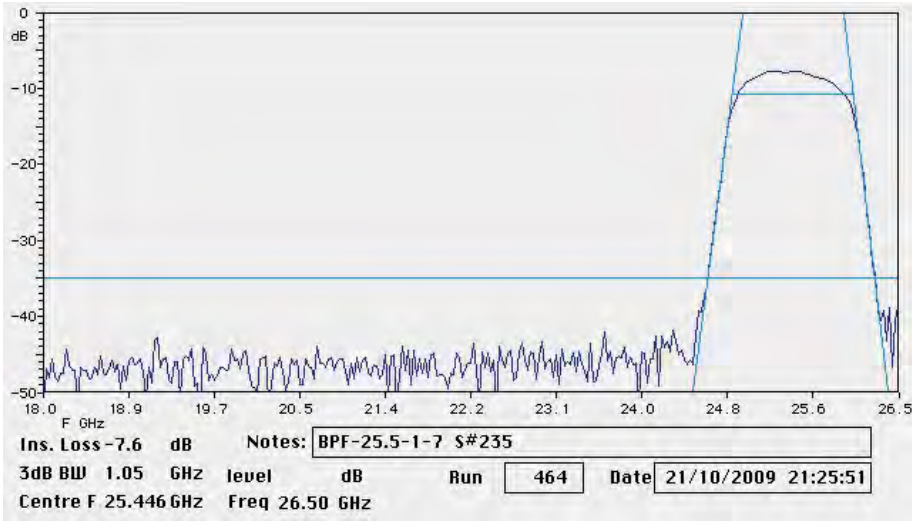

Figure B.0.30: 25.5 GHz spectrum analyser plot for filter serial number #235

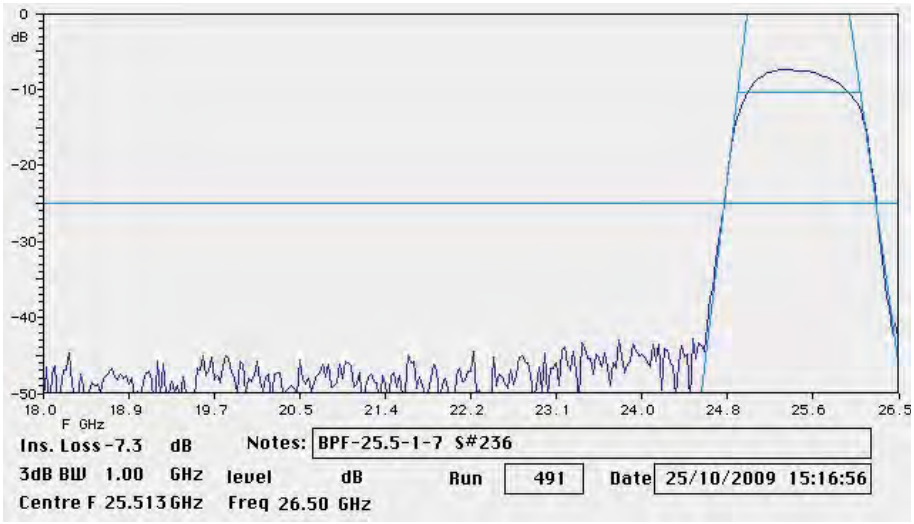

Figure B.0.31: 25.5 GHz spectrum analyser plot for filter serial number #236

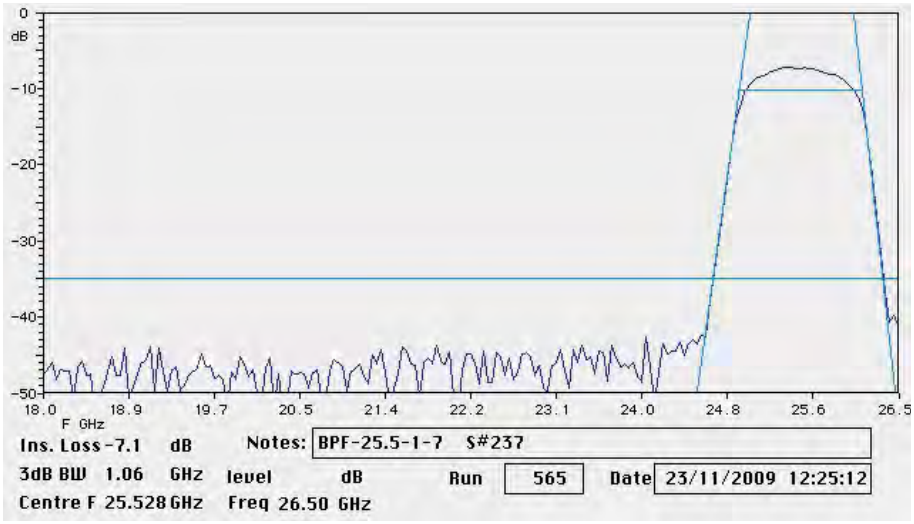

Figure B.0.32: 25.5 GHz spectrum analyser plot for filter serial number #237

Appendix C

Phase plots

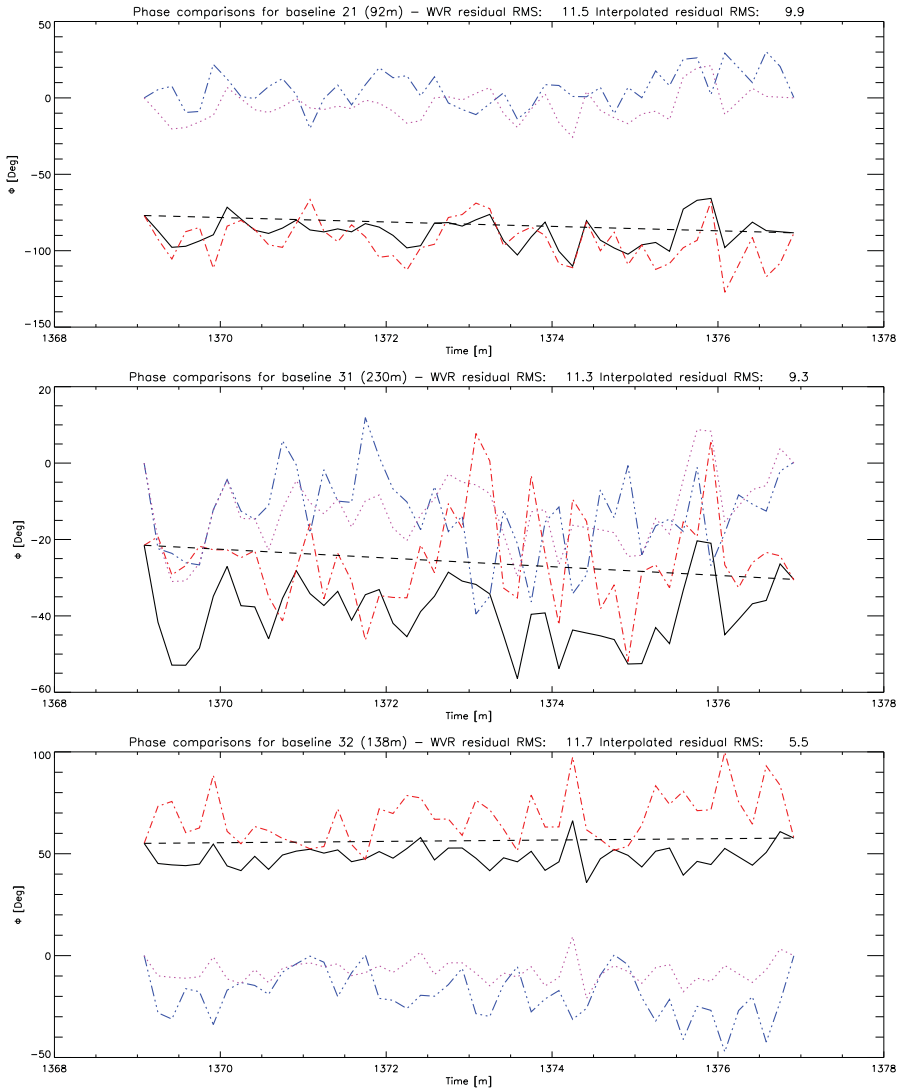

Figure C.0.1: Phase plots for baselines 21, 31, and 32: Solid (black) Calibrator phase, WVR derived phase, dash-dotted (red), Observed phase minus WVR phase Dash-dot-dot (blue) and Observed phase minus interpolated phase, dotted (magenta). Interpolated phase is shown with a dashed line between the bracketing calibrator observations. It is evident that on short baselines, noise dominates for the most part while on the long baselines we achieve correction.

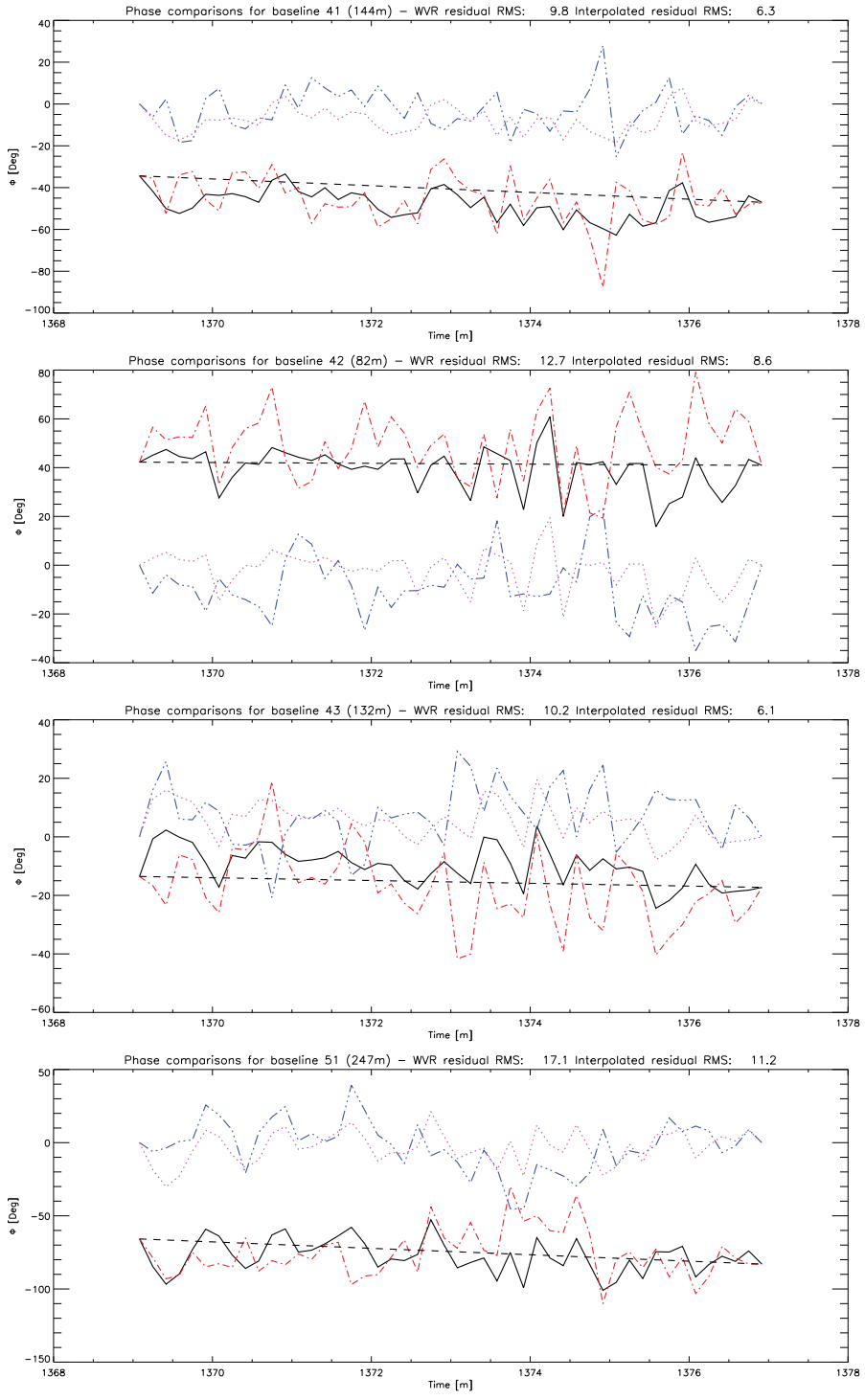

Figure C.0.1: Phase plots for baselines 41, 42, 43 and 51.

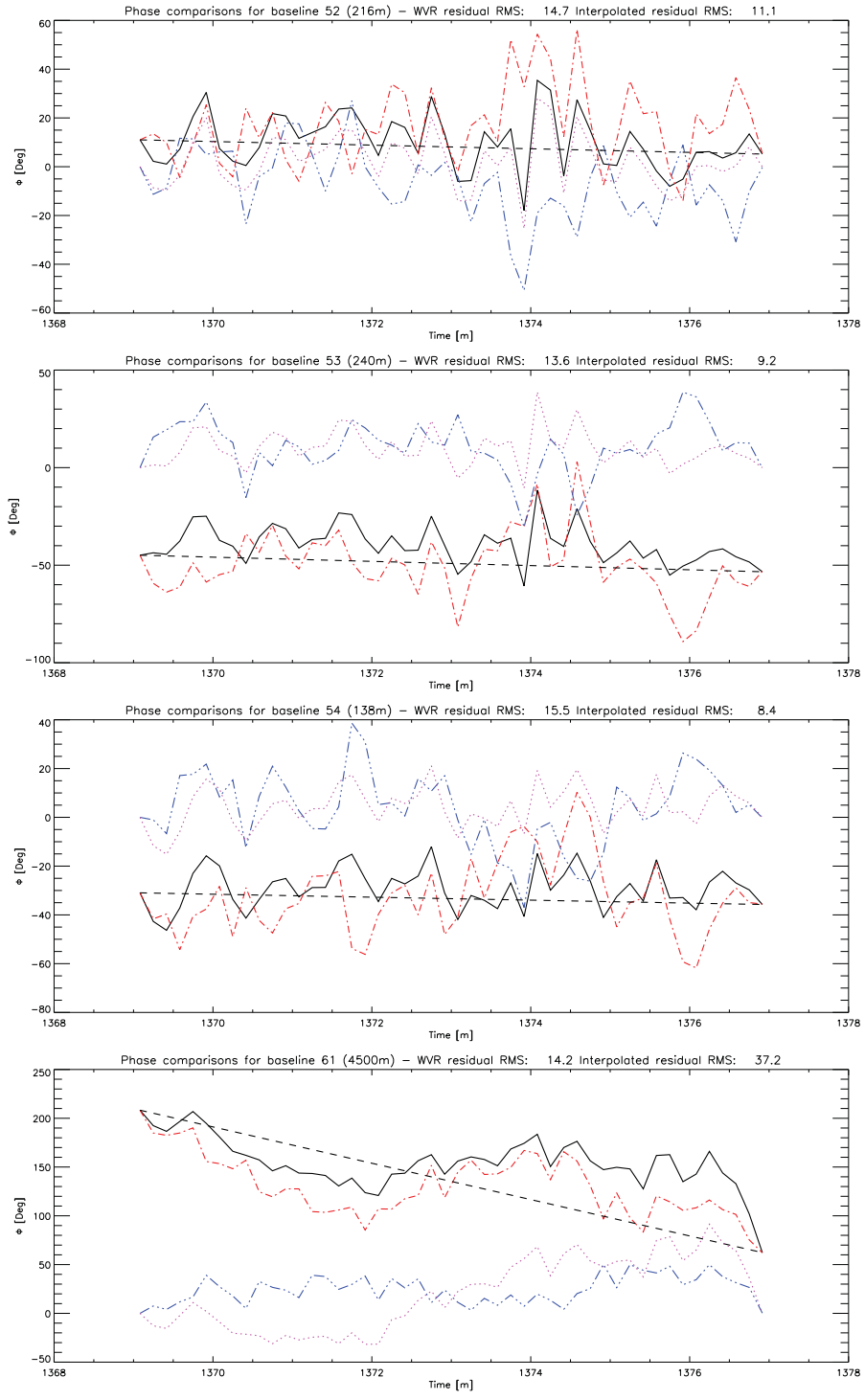

Figure C.0.1: Phase plots for baselines 52, 53, 54 and 61.

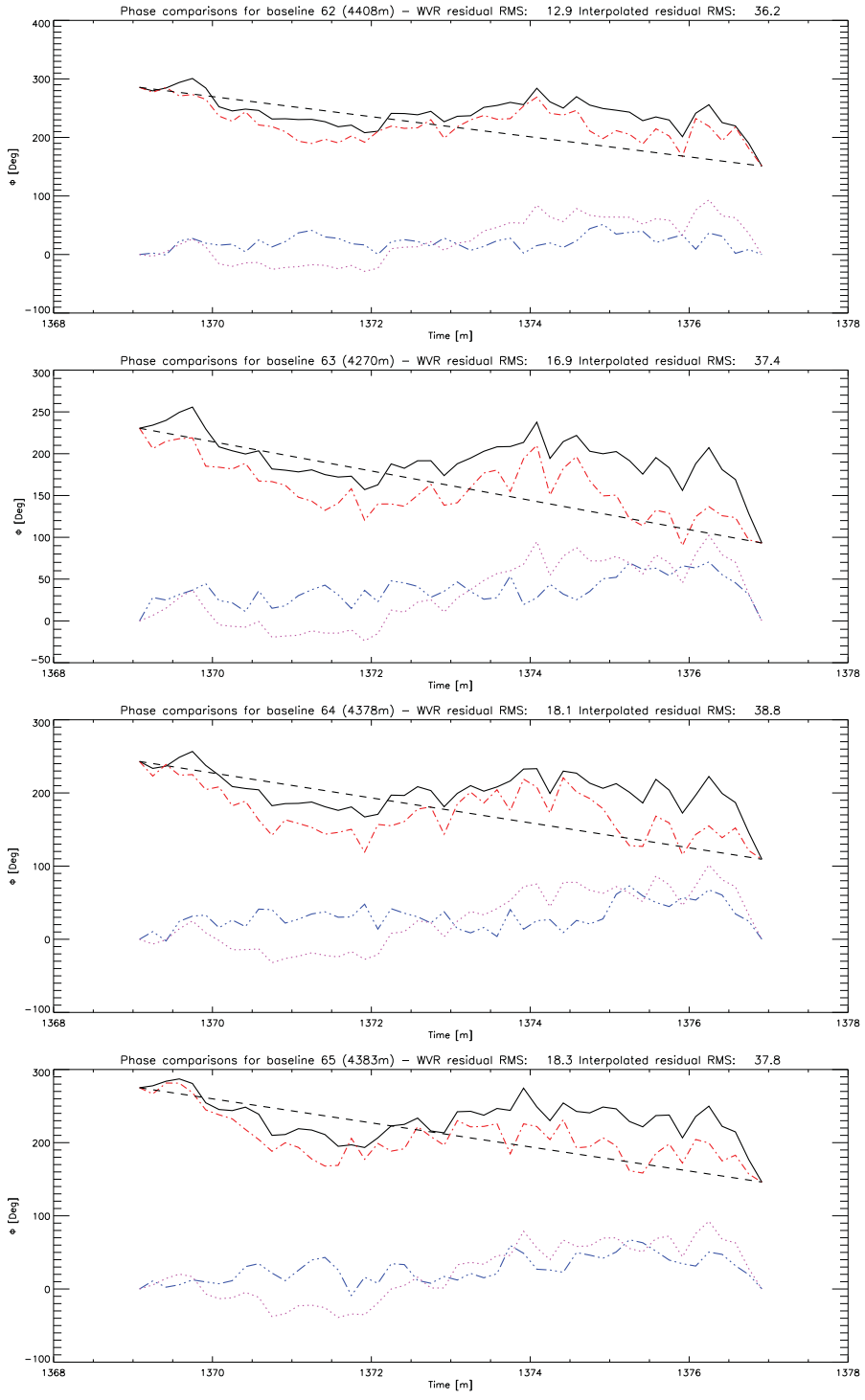

Figure C.0.1: Phase plots for baselines 62, 63, 64 and 65.

List of Figures

List of Tables

Bibliography

[1] Omnisys Instruments AB. http://www.omnisys.se/products/microwave-and-radiometers/alma-wvr.

[2] David Abbott and Peter Hall. A Stable Millimetre-wave Water Vapour Radiometer. *IREE*, 19(4):213–225, December 1999.

[3] J. B. Battat, R. Blundell, J. M. Moran, and S. Paine. Atmospheric Phase Correction Using Total Power Radiometry at the Submillimeter Array. *ApJ*, 616:L71–L74, November 2004.

[4] Bradford R. Bean and E. J. Dutton. *Radio Meteorology*. National Buerau of Standards Monograph 92. U.S. Government Printing Office, 1966.

[5] Ian A. Bonnell, Matthew R. Bate, and Hans Zinnecker. On the formation of massive stars. *MNRAS*, 298:93–102, 1998.

[6] Michael Bremer. Phase monitoring with cloud correction near the 22.2 GHz water line. *IRAM Working Report No 247*, 1997.

[7] Michael Bremer. Atmospheric Phase Correction. Presentation at 7th IRAM Millimeter Interferometry School, October 2010.

[8] C. L. Carilli, J. E. Carlstrom, and M. A. Holdaway. Millimeter Interferometry. In G. B. Taylor, C. L. Carilli, and R. A. Perley, editors, *Synthesis Imaging in Radio Astronomy II*, volume 180, pages 565–599. Astronomical Society of the Pacific, 1999.

[9] C. L. Carilli and M. A. Holdaway. Tropospheric Phase Calibration in Millimeter Interferometry. *Radio Science*, 34:817–840, 1999.

[10] C. J. Chandler, W. F. Brisken, B. J. Butler, R. H. Hayward, and B.E. Willoughby. Results of Water Vapour Radiometry Tests at the VLA. *EVLA Memo #73*, 2004.

[11] J.-F. Colomer and P. de Vicente, editors. *The Water Vapour Radiometer at Effelsberg*. Observatorio Astronomico Nacional of Spain, 2004.

[12] Australian Communications and Media Authority ACMA. http://www.acma.gov.au/.

[13] D. N. Cooper, G. L. James, B. F. Parsons, and D. E. Yabsley. The Antennas. *JEEA*, 12(2):121–135, 1992.

[14] Jonathan Crofts. Private Communication. August 2011.

[15] R. de L. Krönig. On the theory of the dispersion of X-rays. *J. Opt. Soc. Am.*, (12):547–556, 1926.

[16] P. Debye. *Polar Molecules*. Dover, New York, 1929.

[17] Jr. E. K. Smith and S. Weintraub. The Constants in the Equation for Atmospheric Refractive Index at Radio Frequencies. *Proc. IRE*, (41), 1953.

[18] Neal Erickson. A very low-noise single-sideband receiver for 200-260 ghz. MTT-33(11), November 1985.

[19] N Evans. Site properties and stringency. *ALMA Memo Series*, 471, 2003.

[20] Richard Gooch. Karma: a Visualization Test-Bed. In George H. Jacoby and Jeannette Barnes, editors, *Astronomical Data Analysis Software and Systems V*, volume 101 of *A.S.P. Conference Series*, page 80, 1996.

[21] T. Hill, M. G. Burton, V. Minier, M. A. Thompson, A. J. Walsh, M. Hunt-Cunningham, and G Garay. Millimetre continuum observations of southern massive star formation regions - I. SIMBA observations of cold cores. *MNRAS*, 363:405–451, 2005.

[22] Richard Hills. Estimated Performance of the Water Vapour Radiometers. *ALMA Memo Series*, (495), 2004.

[23] Brett Hiscock. Private Communication. August 2011.

[24] J. M. Hollis, F. J. Lovas, and P. R. Jewell. Interstellar glycolaldehyde: The first sugar. *ApJ*, 540:L107–L110, September 10 2000.

[25] Honeywell. *Forward Looking Windshear Detection/Weather Radar System User's Manual with Radar Operating Guidelines*. Number ACS-5082 / 006-18167-0000 / Rev 6 - 02/04. Honeywell, 2004.

[26] Felix R. Hoots, Ronald L. Roehrich, and TS Kelso. *Models for Propagation of NORAD Element Sets*. Number 3 in Spacetrack Report. Defence Documentation Center, Cameron Station, Alexandria VA 22314, USA, 1980.

[27] Balthasar Indermuehle. Cloudsat predictions for ATCA: http://www.narrabri.atnf.csiro.au/observing/cloudsat_atca.txt.

[28] Balthasar Indermuehle. Cloudsat predictions for Mopra: http://www.narrabri.atnf.csiro.au/mopra/cloudsat_mopra.txt.

[29] Balthasar Indermuehle. SatWhere - http://www.satwhere.com/.

[30] Hideharu Ishizaki and Seiichi Sakamoto. Velocity and Structure Function of Phase Screen aloft Chajnantor. *ALMA Memo Series*, (529), 2005.

[31] International Telecommunications Union ITU. http://www.itu.int/.

[32] A. N. Kolmogorov. *Dan.S.S.S.R.*, 30(4):229, 1941.

[33] H. A. Kramers. La diffusion de la lumière par les atomes. In *Transactions of Volta Centenary Congress*, number 2, pages 545–557, Como, 1927. Atti Cong. Intern. Fisica.

[34] J. D. Kraus. *Radio Astronomy*. McGraw-Hill, 1966.

[35] Hans J. Liebe. An updated model for millimetre wave propagation in moist air. *Radio Science*, 20(5):1069–1089, 1985.

[36] N. Lo, M.P. Redman, P.A. Jones, M.R. Cunningham, R. Chhetri, I. Bains, and M.G. Burton. Observations and radiative transfer modelling of a massive dense cold core in G333. *MNRAS*, 415, July 2011.

[37] Kevin B. Marvel and David P. Woody. Phase correction at millimeter wavelengths using observations of water vapor at 22 GHz. *Proc. SPIE*, 3357:442–452, 1998.

[38] Enno Middelberg, Robert J. Sault, and Michael J. Kesteven. The ATCA Seeing Monitor. *PASA*, 23(47), 2006.

[39] Nextlimit. http://www.maxwellrender.com.

[40] Bojan Nicolic. Inference of Coefficients for Use in Phase Correction I. *ALMA Memo Series*, (587), 2009.

[41] Bojan Nicolic. Inference of Coefficients for Use in Phase Correction II: Using the Observed Correlation Between Phase and Sky Brightness Fluctuations. *ALMA Memo Series*, (588), 2009.

[42] Bojan Nicolic, Richard Hills, and John Richer. Limits on Phase Correction Performance Due to Differences Between Astronomical and Water-Vapour Radiometer Beams. *ALMA Memo Series*, (573), 2007.

[43] Bojan Nicolic, John Richer, Rosie Bolton, and Richard Hills. Tests of Radiometric Phase Correction with ALMA. *The Messenger*, 143:11–15, March 2011.

[44] NORAD. https://www.space-track.org.

[45] J. R. Pardo, J. Cernicharo, and E. Serabyn. Atmospheric Transmission at Microwaves (ATM): An Improved Model for mm/submm Applications. *IEEE Transactions on Antennas and Propagation*, 49(12):1683–1694, 2001.

[46] R. A. Perley. Aperture Synthesis in Radio Astronomy II. San Francisco, 1998. PASP.

[47] H. M. Pickett, R. L. Poynter, E. A. Cohen, M. L. Delitsky, J. C. Pearson, and H. S. P. Muller. Submillimeter, millimeter, and microwave spectral line catalog. *J. Quant. Spectrosc. & Rad. Transfer*, 80:883–890, 1998.

[48] J. Ruze. Antenna Tolerance Theory – A Review. *Proc. IEEE*, (54):633–640, 1966.

[49] R. J. Sault, G. J. Carrad, P. J. Hall, and J. Crofts. Radio path length correction using water vapour radiometry. *ArXiv Astrophysics e-prints*, December 2007.

[50] Robert J. Sault, Peter J. Teuben, and Mel C. H. Wright. A retrospective view of Miriad. In R. Shaw, H. E. Payne, and J. J. E. Hayes, editors, *Astronomical Data Analysis Software and Systems IV*, volume 77 of *ASP Conference Series*, pages 433–436, 1995.

[51] Jamie Stevens and Robin Wark. ATCA user guide. http://www.narrabri.atnf.csiro.au/observing/users_guide, July 2011.

[52] Alison Stirling, Richard Hills, John Richer, and Juan Pardo. 183 GHz water vapour radiometers for ALMA: Estimation of phase errors under varying atmospheric conditions. ALMA Memo 496.1, July 2004.

[53] David A. Tahmoush and Alan E. E. Rogers. Correcting atmospheric path variations in millimeter wavelength very long baseline interferometry using a scanning water vapor spectrometer. *Radio Science*, 35(5):1241–1251, September-October 2000.

[54] V. I. Tatarski. *Wave propagation in a turbulent medium*. Dover, New York, 1961.

[55] G. I. Taylor. The spectrum of turbulence. *Proc. R. Soc.*, 132:476–490, 1938.

[56] W. F. Thi, E. F. van Dishoeck, G. A. Blake, G. J. van Zadelhoff, J. Horn, E. E. Becklin, V. Mannings, A. I. Sargent, M. E. van den Ancker, A. Natta, , and J. Kessler. H_2 and CO emission from disks around T Tauri and Herbig Ae Pre-main-sequence stars and from debris disks around young stars: Warm and cold circumstellar gas. *ApJ*, 561:1074–1094, November 10 2001.

[57] A. Richard Thompson, James M. Moran, and Jr. George W. Swenson. *Interferometry and Synthesis in Radio Astronomy*. Wiley-VCH Verlag GmbH & Co. KHaA, 2nd edition, 2001.

[58] John S. Toll. Causality and the Dispersion Relation: Logical Foundations. *Physical Review*, 104(6):1760–1770, 1956.

[59] R. N. Treuhaft and G. E. Lanyi. The Effect of the Dynamic Wet Troposphere on VLBI Measurements. *TDA Progress Reports*, (42-84):1–17, 1985.

[60] F. Ulaby, R. Moore, and A. Fung. *Microwave Remote Sensing Fundamentals and Radiometry*, volume 1. Artech House, 685 Canton Street, Norwood, MA 02062, USA, 1st edition edition, 1981.

[61] Serena Viti. Tracking the early stages of massive star formation. In D.C. Lis, G.A. Blake, and E. Herbst, editors, *Astrochemistry: Recent Successes and Current Challenges*, Proceedings IAU Symposium No. 231. IAU, 2005.

[62] A. J. Walsh and Michael G. Burton. Mopra observations of G305.2+0.2: massive star formation at different evolutionary stages? *MNRAS*, 365, 2006.

[63] J. W. Waters. Absorption and emission by atmospheric gases. In M. L. Meeks, editor, *Methods of Experimental Physics 12B*, New York, 1976. Academic Press.

[64] Martina Corinna Wiedner. *Atmospheric Water Vapour and Astronomical Millimetre Interferometry*. PhD thesis, University of Cambridge, 1998.

[65] W. Wilson. The Australia Telescope Compact Array Broadband Backend: Description and First Results. *MNRAS*, In Press((arXiv:1105.3532)), 2011.

[66] J. M. Winters and R. Neri. *An Introduction to the IRAM Plateau de Bure Interferometer*. Institut de Radio Astronomie Millimétrique, 300 Rue de la Piscine, F-38406 Saint Martin d'Hères, 2011.